Advanced fabrication strategies for functional soft materials: Plasma, Transient, and Electrochemical Approaches

Emma Louise Bowley

Submitted in fulfilment of the requirements for the Degree of Doctor of Philosophy

School of Chemistry

College of Science and Engineering

University of Glasgow

March 2026

Declaration of Authorship

I declare that, except where explicit reference is made to the contributions of others, this dissertation is the result of my own work and has not been submitted for any other degree at the University of Glasgow or any other institution.

Emma Louise Bowley

Abstract

Supramolecular soft materials derived from low molecular weight gelators (LMWG) have been widely prepared using pH-switching strategies, in which the method of inducing the pH change plays a critical role in determining material properties and applications. In this thesis, three distinct pH-switching approaches were explored. Although each approach relies on a change in pH, it has been demonstrated that they produce materials with significantly different behaviours, structures, and functionalities.

In chapter 2, plasma-induced gelation was investigated as a novel route for the *in situ* fabrication and 3D printing of supramolecular hydrogels. It was demonstrated that cold atmospheric plasma enables precise spatial and temporal control over gelation, allowing the formation of complex, patterned, and multilayered structures with defined geometries. Studies using Kineticolor showed that gelation is driven by plasma-induced pH changes. It was further demonstrated that this approach can be combined with the *in situ* formation of gold nanoparticles, enabling the fabrication of composite hydrogels with enhanced functionality.

In Chapter 3, transient pH-switching systems were explored by combining a urea/urease reaction with formate hydrolysis in DMSO/H_2O hydrogel systems. The scope of the system was expanded by incorporating a range of LMWGs, and it was demonstrated that variation of the ester component, including methyl, ethyl, and *n*-propyl formate, allows control over hydrolysis rates and thus temporal behaviour. The effects of temperature and ageing were also investigated, revealing complex, non-linear, and sometimes unpredictable dynamics that are important for practical applications.

In chapter 4, these pH triggers were further applied to a lipid-based system, where it was demonstrated that they can induce and control phase transitions in a monoolein-oleic acid mixture. Using flow-through small-angle X-ray scattering transitions, including *Pn3m-to-*H_{II}, H_{II}*-to-Im3m*, and H_{II}*-to-Im3m-to-*H_{II}*,* were successfully realised. It was shown that these nanoscale structural changes significantly influence the macroscopic properties of the materials, highlighting the versatility of transient pH control across different supramolecular systems.

Finally, in chapter 5, electrochemically induced gelation and polymerisation of carbazole-functionalised amino acid-based hydrogels were investigated. *In situ* electrochemical small-angle X-ray scattering was used to examine the dynamic processes of self-assembly and polymerisation, showing how subtle molecular changes govern structural evolution and material properties.

Overall, this thesis demonstrates that the choice of gelation method enables tailoring of material structure, dynamics, and functionality across multiple length scales.

Contents

Declaration of authorship 2

Abstract 3

Contents 5

Acknowledgements 10

List of publications arising from this PhD 12

List of abbreviations 13

Chapter 1 – Introduction 16

1.1. Gels 17

1.2. Low molecular weight gelators 18

1.3. Dipeptide gels 19

1.4. Gelation triggers 22

1.5. Solvent-triggered gelation 23

1.6. Temperature-triggered gelation 23

1.7. pH-triggered gelation 24

1.8. Electrochemical triggers 25

1.9. Transient gels 29

1.10. Ageing 32

1.11. Plasma-triggered gelation 34

1.12. Localised gelation 36

1.13. Gel 3D printing 38

1.14. Nanostructure of LMWGs 41

1.15. Characterising the properties of LMWG gels 43

1.16. Aims of thesis 53

1.17. References 54

Chapter 2 – Plasma-induced gelation and 3D printing of hydrogels 64

2.1. Introduction 66

2.2. Results and discussion 68

2.2.1. Plasma gelation 68
2.2.2. Plasma parameter optimisation 74
2.2.3. Kineticolor pH analysis 83
2.2.4. Plasma 3D printing 91
2.2.5. Plasma gel properties 93
2.2.6. Plasma gels containing nanoparticles 96
2.3. Conclusions 106
2.4. Experimental 107
2.4.1. Materials 107
2.4.2. Preparation of solutions 107
2.4.3. Plasma gelation 107
2.4.4. 3D printing 109
2.4.5. Nanoparticle gel 3D printing 109
2.5.6. pH measurements 109
2.4.7. HPLC 109
2.4.8. Small-angle X-ray scattering 110
2.4.9. Rheological measurements 110
2.4.10. Computer vision analysis with Kineticolor 111
2.4.11. Confocal microscopy 111
2.4.12. UV-Vis 112
2.4.13. TEM 112
2.5. References 112
Chapter 3 – Designing transient systems 116
3.1. Introduction 118
3.2. Results and discussion 120
3.2.1. Urea/urease/methyl formate transient gels 120
3.2.2. Control of transient gels via formate hydrolysis 132
3.2.3. Ageing of transient gels 139
3.2.4. Temperature control of transient systems 141
3.3. Conclusions 143

3.4. Experimental 144
3.4.1. Materials 144
3.4.2. Preparation of solutions 144
3.4.3. Preparation of Hydrogels 145
3.4.4. Rheological measurements 145
3.4.5. pH measurements 146
3.4.6. Confocal microscopy 146
3.4.7. Small-angle X-ray scattering 147
3.5. References 148
Chapter 4 - Temporal control of lipid phase transitions 150
4.1. Introduction 152
4.2. Results and discussion 154
4.2.1. Monoolein phase behaviour 154
4.2.2. *Pn3m-to-H$_{II}$* phase transition 155
4.2.3. *H$_{II}$-to-Im3m* phase transition 156
4.2.4. *H$_{II}$-to-Im3m-to-H$_{II}$* phase transition 158
4.2.5. Macroscopic properties 159
4.3. Conclusions 160
4.4. Experimental 161
4.4.1. Materials 161
4.4.2. Preparation of 10% OA/MO (w/w) matrix 161
4.4.3. Viscosity measurements 161
4.4.4. pH measurements 162
4.4.5. Small-angle X-ray scattering 162
4.5. References 164
Chapter 5 - Electrofabrication and electropolymerisation of carbazole-protected amino acids 166
5.1. Introduction 167
5.2. Results and discussion 170
5.2.1. Electrogelation and electropolymerisation 170

5.2.2. EC-SAXS Cell 174
5.2.3. In-situ SAXS of electrogelation 175
5.2.4. In-situ SAXS of electropolymerisation 192
5.3. Conclusions 205
5.4. Experimental 206
5.4.1. Materials 206
5.4.2. Preparation of solutions 206
5.4.3. pH measurements 207
5.4.4. Electrochemical gelation 207
5.4.5. Electropolymerisation of hydrogels 207
5.4.6. Electrochemical measurements 207
5.4.7. Rheological measurements 208
5.4.8. Small-angle X-ray scattering 208
5.5. References 210
Conclusions 213
Appendix 1 – Supplementary data for Chapter 2 216
1.1. Viscosity 217
1.2. pK_a 218
1.3. Hue calibration values for Kineticolor analysis 219
1.4. SAXS fitting parameters for nanoparticle plasma gels 223
Appendix 2 – Supplementary data for Chapter 3 225
2.1 Frequency sweeps 226
2.2. Heat-Cool cycles 227
2.3. SAXS data for DMSO-H_2O gels 228
2.4. SAXS fitting parameters for methyl formate transient systems 230
2.5. Images of the transient systems 236
2.6. SAXS fitting parameters for ethyl formate transient systems 239
2.7. SAXS fitting parameters for *n*-propyl formate transient systems 242
2.8. Ageing rheology 245
2.9. Temperature rheology 248

Appendix 3 – Supplementary data for Chapter 5 251
3.1. SAXS data for Carb-Ala electrogelation 252
3.2. SAXS data for Carb-Gly electrogelation 258
3.3. SAXS data for Carb-Val electrogelation 264
3.4. SAXS data for Carb-Leu electrogelation 268
3.5. Chronopotentiometry 274
3.6. SAXS data for Carb-Ala electropolymerisation 275
3.7. SAXS data for Carb-Gly electropolymerisation 282
3.8. SAXS data for Carb-Val electropolymerisation 289
3.9. SAXS data for Carb-Leu electropolymerisation 294

Acknowledgements

I would like to thank my supervisor, Prof. Dave Adams for giving me the opportunity to undertake a PhD. I really appreciate all the opportunities you have given me during my time in the group. Without you, I wouldn't be here, and your support and guidance have been invaluable

Thank you to the School of Chemistry and all the technicians who have helped me collect all sorts of weird and wonderful data.

I am incredibly grateful to the Adams group, old and new (Courtenay, Chloe, Max, Qingwen, Simona, Rui, Fin, Tejaswini, Helen, Hunter, Olivia, Daniel, Libby, Dipankar, Lucia, Sofia), you have defined this PhD, and I could not have asked for a better group to work alongside. You inspire me with your enthusiasm and knowledge, and I cannot wait to see what great things you all go on to achieve.

I also have to include the Draper group (Connor, Ellen, Matthew, Lineta, Rebbeca, Bart, Nick, Ziyao, Jakki, Jess) and the Loch group (Alex) in this. To me, we have always felt like one big group, and it would not have been the same without all of you.

Simona, as you once said, you feel like my academic sister. Thank you for being a wonderful source of humour and happiness, and of course, for taking me on all your beamline trips. Libby, thank you for your kindness and for answering all my questions, especially while I have been writing. Fin, thank you for being such a great sounding board for ideas and an excellent proofreader; I hope I have helped you as much as you have helped me. Connor, our catch-ups and trips to the library have kept me sane over these past few months, and I cannot believe it has been three and a half years since we met; it feels like yesterday we first started. Ellen, thank you for being such a wonderful source of moral support. You are a fantastic friend and an excellent scientist.

To all my friends who have had to listen to me talk about gels for the past few years, thank you for always being there for me. To James and Hannah, thank you for following me to Glasgow, for putting up with living with me, and for always making me laugh. To Leif, I miss you, and I cannot fully express how grateful I am for your friendship.

Sumanta, thank you for everything. I would never have finished this without you by my side, and I am so excited for our future together.

Finally, thank you to my family. I love you all. Tom and Lucy, thank you for keeping me grounded and making me laugh. Mum and Dad, thank you for always supporting me. I am the person I am today because of you, and I could not be more grateful for everything you have done. I hope I have made you proud.

List of publications arising from this PhD

(In order of publication)

"Designing and Controlling Transient Supramolecular Gels" **E.L. Bowley**, S. Bianco, F. Hallam Stewart, C. M. Wallace, R.E. Ginesi, A.S. Loch, M. Rosenthal, A.J. Smith, and D.J. Adams, 2024, *ChemSystemsChem*, e202400073 Advanced Article.

"Soft Materials with Time-Programmed Changes in Physical Properties through Lyotropic Phase Transitions Induced by pH-Changing Reactions" **E. Bowley**, W. Liu, D.J. Adams, and A.M. Squires, *ACS Appl. Mater. Interfaces*, 2024, 16(15), 19585–19593.

"Forging out-of-equilibrium supramolecular gels", S. Bianco, F. Hallam Stewart, S. Panja, A. Zyar, **E. Bowley**, M. Bek, R. Kádár, A. Terry, R. Appio, T. S. Plivelic, M. Maguire, H. Poptani, M. Marcello, R.R. Sonani, E.H. Egelman, and D.J. Adams, *Nature Synthesis*, 2024, 1-9.

"Cold plasma induced 3D printing of hydrogels" **E Bowley**, D. Ghosh, D. Padmanaban, M. Bieniek, C. Fyfe, T.J. McCabe, M. Reid, M. Vassalli, J.L. Walsh, M. Hasan and D.J. Adams. Submitted for publication.

List of abbreviations

Å	Angstrom
$\dot{\gamma}$	Shear rate
°C	Degrees Celsius
ΔE	Contrast change
θ	Scattering angle
φ	Half scattering angle
λ	Wavelength
µL	Microlitres
χ^2	Chi-squared
1D	One dimensional
2D	Two dimensional
3D	Three dimensional
10% OA/MO	10% Oleic acid/monoolein system
Ala	Alanine
Ag/AgCl	Silver/Silver chloride
aq	Aqueous
au.	Arbitrary units
Au	Gold
BQ	Benzoquinone
$CaCO_3$	Calcium carbonate
CAP	Cold atmospheric plasma
Carb	Carbazole
CD	Circular dichroism
CLogP	Calculated Log P
CM	Centimetre
CMC	Critical micellar concentration
CP	Cone-plate
Cyro-EM	Cryogenic-electron microscopy
CV	Cyclic voltammetry
Da	Dalton
DBD	Dielectric barrier discharge
DC	Direct current
DSC	Differential scanning calorimetry
DMSO	Dimethyl sulfoxide
e^-	Current
EC-SAXS	Electrochemical small-angle X-ray scattering

eq.	Equivalent
EtOH	Ethanol
Fmoc	Fluorenylmethoxycarbonyl protecting group
FTO	Fluorene-doped tin oxide
G′	Shear storage modulus
G″	Shear loss modulus
g	Gram
GdL	Glucono-δ-lactone
Gel-to-gel-to-gel	Gel to gel to gel
Gel-to-sol-to-gel	Gel to sol to gel
Gly	Glycine
GPC	Gel permeation chromatography
$HAuCl_4 \bullet 3H_2O$	Tetrachloroauric(III) acid trihydrate
HCl	Hydrochloric Acid
H_{II}	Inverse hexagonal phase
H_2O	Water
HPLC	High-performance liquid chromatography
Hrs	Hours
HQ	Hydroquinone
I	Intensity
Im3m	Primitive cubic phase
IR	Infrared spectroscopy
kV	Kilovolt
LPM	Litres per minute
LMWG	Low molecular weight gelator
LVR	Linear viscoelastic region
Leu	Leucine
M	Molar
mA	Milliamp
mg	Milligram
min	Minute
mL	Millilitre
mM	Millimolar
mm	Millimetre
mS	MilliSiemen
mV	Millivolt
MO	1-Monoolein

MO/EtOH	Monoolein/ethanol mixture
NaCl	Sodium chloride
NaOH	Sodium hydroxide
nm	Nanometre
NPs	Nanoparticles
OA	Oleic acid
Pa	Pascal
PBI	Perylene bisimide
PBS	Phosphate buffer solution
PLA	Polylactic Acid
Pn3m	Double diamond cubic phase
PP	Parallel plate
PTFE	Polytetrafluoroethylene
PXRD	Powder X-ray diffraction
q	Scattering vector
rad	Radian
ROI	Region of interest
RONS	Reactive oxygen and nitrogen species
s	Second
SANS	Small-angle neutron scattering
SAXS	Small-angle x-ray scattering
SEM	Scanning electron microscopy
SLD	Scattering length density
Sol-to-gel	Solution to gel
SPR	Surface plasmon resonance
Tanδ	Damping factor
TEM	Transmission electron microscopy
T_{gel}	Gelation temperature
uSAXS	Ultra small angle x-ray scattering
UV	Ultraviolet
UV-Vis	Ultraviolet-visible
WAXS	Wide angle x-ray scattering
w/w	Weight per weight
wt%	Weight percentage
V	Volts
Val	Valine
v/v	Volume per volume

Chapter 1 – Introduction

1.1. Gels

Gels are soft, semi-solid, or solid-like materials, composed of two or more components: a liquid phase and a three-dimensional (3D) network of interconnected molecules that traps the solvent.[1,2] This gel network provides the materials with viscoelastic properties, a combination of liquid and solid characteristics. Their solid network provides elasticity, whilst the solution trapped in the pores gives the viscous behaviour.[3,4] Generally, they exist in a steady state in which they exhibit solid-like rheological properties until higher strains are applied, after which they exhibit more liquid-like properties. This allows these materials to maintain their shape under stress, despite being predominantly composed of a solvent component, which often accounts for over 99% of the gel.[5,6]

There are various types of gels within this class of materials. Their solvent component classifies them; for example, the term hydrogel refers to materials formed in water, and the term organogel refers to materials formed in organic solvents.[2,4,6–8] When the solvent is removed from the gel network, the resulting material is classified as an aerogel or xerogel.[2,4,6–8] This wide variety of gel compositions yields materials with unique properties and, consequently, a broad range of applications.[2,9,10]

As suggested by the name, hydrogels are gels in which the solvent component is water, and they can be naturally occurring or made from synthetic materials.[6,11] This thesis is primarily focused on this class of gels. They have gained increasing popularity due to their biocompatibility and versatility, with applications in sensing, engineering, drug delivery, regenerative medicine, pharmaceuticals, environmental remediation, and electronics.[4,12–20]

Gels can be further categorised into two main types: chemical gels and physical/supramolecular gels, based on the kind of bonding between the polymer chains. 'Chemical' gels are cross-linked *via* covalent bonds and are formed irreversibly, whereas supramolecular ‘physical’ gels are self-assembled by non-covalent interactions, such as hydrogen bonding, π-π stacking, and hydrophobic forces (Figure 1.1).[5,6,21,22] Physical gels can be formed from polymer chains or Low molecular weight gelators (LMWGs) that self-assemble into one-dimensional (1D)

nanostructures; these chains/nanostructures then entangle in space to form the gel network.[4] Physical gels generally exhibit weaker mechanical properties and are more easily broken compared to their chemical counterparts, due to the non-covalent interactions which form them. Notably, however, these non-covalent interactions also allow supramolecular gels to be disassembled and reassembled in response to an external stimulus, unlike chemical gels.[4] This stimulus-responsiveness, along with their tuneable properties, makes them attractive materials [23,24]

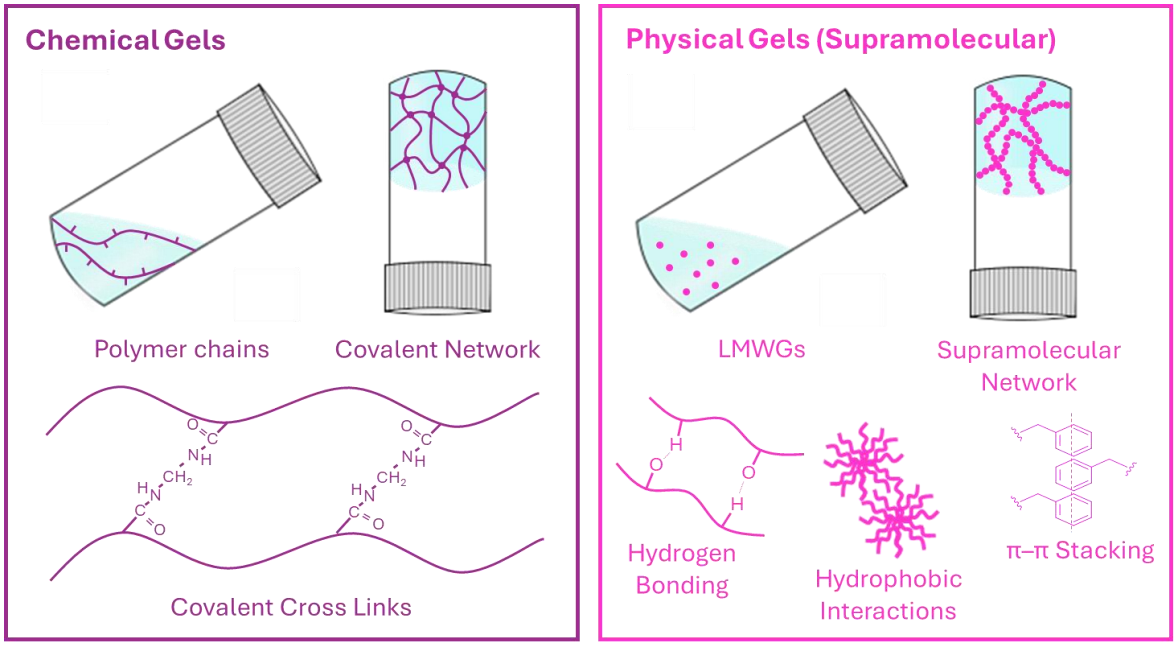

Figure 1.1. Schematic drawing representing the underlying network structure of chemical and supramolecular gels. Chemical gels are formed from polymer chains crosslinked by covalent bonds to create a covalent network. Supramolecular gels are formed from molecular chains that are crosslinked by non-covalent forces to create a supramolecular network.

1.2. Low molecular weight gelators

LMWGs are organic molecules with a molar mass ≤ 3000 Da, although they are usually much smaller and are generally referred to as gelators in this context.[25,26] These molecules are capable of self-assembling through non-covalent interactions and therefore can form gels.[25,27] Because of this, gels containing these molecules are supramolecular in nature and have attracted significant attention in recent years due to their advantages over chemical hydrogels: they are reversible, more sensitive to external stimuli, and often more flexible and adaptable.[25,28] LMWGs

are easily synthesised from commercially available materials, and their structure and function can be tailored through functionalisation of the molecule. There are many different examples of reported LMWGs, including peptides[29], modified fatty acids[30], nucleobases[31], surfactants[32], and functionalised sugars[33], to name a few.

LMWG gels are formed *via* supramolecular self-assembly when a gelation trigger is applied.[27,34] Initially, the LMWG is suspended in a solvent, and upon the application of the gelation trigger, the solubility of the LMWG is reduced, encouraging the formation of fibres.[26,29] These 1D structures entangle and continue to grow into a 3D network that traps water (or other solvent) and forms the gel (Figure 1.2).[27,29]

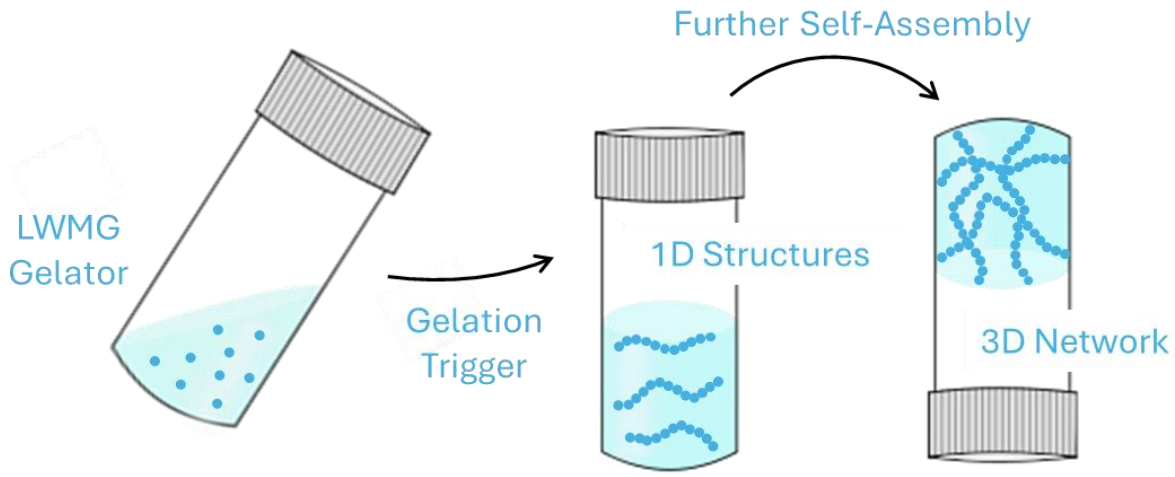

Figure 1.2. Mechanism of gelation of LWMGs. The application of a gelation trigger induces 1D structures to self-assemble into a 3D network, forming a gel.

Both the choice of LMWG and the gelation trigger affect the overall mechanical properties of the material produced, as they influence the self-assembly process and, in turn, the shape and arrangement of fibres within the network.[27,35–37] Many gelation triggers exist, including pH-, solvent-, temperature-, enzyme-, and salt-triggered gelation.[27,29,34,38] This thesis will focus on dipeptide LMWGs and pH- and enzyme-triggered gelation.

1.3. Dipeptide Gelators

Small peptides are a subclass of LMWGs that self-assemble into a variety of nanostructures and are known for their biocompatibility and ease of synthesis, making them ideal for forming gels.[27] Although larger peptides, such as octapeptides,[39] had previously been used to form gels, the first dipeptide-based

LMWGs were reported by Vegners *et al.* in 1995, using N-fluorenylmethoxycarbonyl (Fmoc)-based dipeptides that were carriers for antigen presentation.[40] Since Fmoc dipeptides have become increasingly common, with Zhang *et al.* reporting Fmoc dipeptides that respond to ligand–receptor interactions, temperature, and pH changes.[41] The same group also reported the first dipeptide LMWGs conjugated to 2-naphthoxyacetic acid (2Nap) in 2007.[42] Since then, these types of N-functionalised dipeptides have become widely used, with the properties of the resulting gel easily modifiable by changing capping group, linker, amino acid side chains, and the chirality of these side chains (Figure 1.3a).[38,43,44]

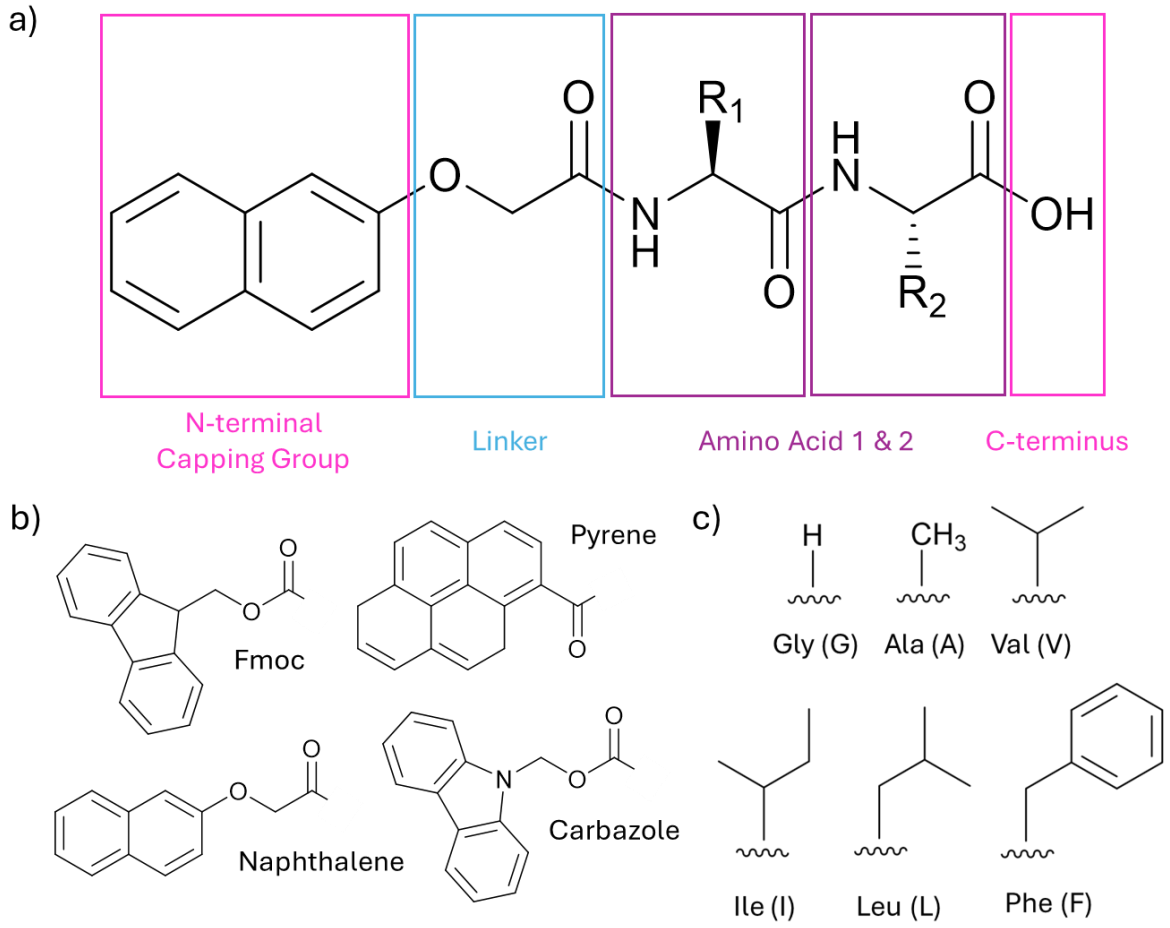

Figure 1.3. a) Chemical structure of N-functionalised dipeptide LMWG. b) Examples of various capping groups/linkers: Fmoc, naphthalene, pyrene, and carbazole. c) Examples of common amino acid side chains which are seen in dipeptide LMWGs used in this thesis.

Many capping groups can be selected, such as naphthalene, carbazole, pyrene, and Fmoc, all of which, along with various amino acid side chains, exhibit distinct hydrophilic and hydrophobic properties (Figure 1.3b). This is important because

the mechanical properties of the gel formed are partly determined by the hydrophobicity of the LMWG used. However, many other factors influence the mechanical properties, such as the size of the capping group, the presence of heteroatoms, and the flexibility of the peptide backbone.[45] In addition to altering hydrophobicity, capping group modifications can introduce additional non-covalent interactions.

When choosing the capping group for an LMWG, the linker connecting it to the peptide chain is equally important, as it can significantly influence self-assembly behaviour and the properties of the resulting gel.[46] The linker acts as a spacer, affecting the flexibility and conformation of the peptide backbone. Shorter linkers tend to restrict the movement and flexibility of the peptide chain, thereby limiting interactions within the gel network.[46] Linkers with lower rigidity or greater length provide more freedom for peptide segments to adopt configurations that favour interactions such as hydrogen bonding and π–π stacking.[42,46,47] By enabling more optimal alignment and stacking, such linkers increase the overall stability and mechanical strength of the gel network, thereby achieving the desired functionalities. [42,47] For example, Li *et al*. compared linkers from different groups and found that more flexible linkers were less restrictive during molecular packing; therefore, the corresponding hydrogels exhibited different properties.[48]

Peptide-based LMWGs can also be designed to offer a wide range of functionalities based on the choice of amino acid; many additional non-covalent interactions can be incorporated, such as hydrogen bonding from polar amino acids, hydrophobic interactions from non-polar amino acids, electrostatic interactions from charged side-chains and π-stacking from aromatic amino acids (Figure 1.3c).[45,49,50] Since 2003, the properties of hydrogels formed from N-functionalised dipeptides have been widely reported, and numerous experimental insights and inspirations from nature have informed the design of dipeptide gelators.[51,52] For example, aromatic side chains have been shown to facilitate gelation *via* π-π stacking, and these aromatic groups were later found to increase the stiffness of the resulting gel network.[53] Despite amino acid side chains being essential for supramolecular design, the peptide sequence alone cannot reliably predict whether a molecule will form a successful gel.[45,49,50] In practice, many successful gelators are discovered through experimentation or chance.[50]

To introduce amphiphilicity in the structures, the N-terminus or the C-terminus are not functionalised, which plays a key role in enabling gelation through changes in pH.[45] This is discussed further in section 1.7.

Due to their ease of preparation and modification, biocompatibility, and their ability to exhibit stimuli-responsive reversible sol–gel transitions, dipeptide gels are attractive for applications such as drug release, tissue engineering, energy storage, and sensing.[50,54–56]

1.4. Gelation triggers

There are various mechanisms for triggering gelation, including pH change[35,37,38], enzymatic reactions[57], solvent switch[37,58], thermal cycling[37,59], irradiation[59] and salt addition[60]. These methods share a common principle: the supramolecular gelation of LMWGs is induced by altering the environment from one in which the molecules are relatively soluble to one in which they are insoluble. Once the gel is formed, it exists in a kinetically trapped state.[61]

Within each gelation mechanism, there are different approaches to achieving the desired environmental changes. For example, for pH-triggered gels, various methods can be used to induce the pH changes, such as electrochemically[62] or hydrolysis induced[63] changes that exploit pH shifts in response to various external stimuli. This thesis explores these two gelation methods, as well as transient gels, in which the gel is initially formed *via* a solvent switch, with pH changes used to alter its properties.[64]

The choice of gelation trigger largely determines the type, properties, and morphology of the final gel.[65,66] A key factor determining these properties is the kinetics of gel formation, which can vary significantly depending on the method used.[63,66] For example, solvent switch gels form very rapidly, whereas pH-triggered gels with glucono-δ-lactone (GdL) take at least 16 hours to form.[63,65,66] Furthermore, when GdL is used to trigger gelation, its concentration controls the rate of pH decrease, which, in turn, controls the rate of gel formation and directly affects the mechanical strength of the final gel.[63]

1.5. Solvent-triggered gelation

Gels triggered by a solvent-switch mechanism are first dissolved in a water-miscible organic solvent, after which water is added to initiate gelation. For this method to work, the LMWG must be soluble in the organic solvent but insoluble in water.[67,68] The dilution of the organic solvent with water causes rapid self-assembly *via* nucleation points, where 1D fibres propagate to form spherulitic domains, resulting in gel formation almost immediately (Figure 1.4).[66,68] The ratio of organic solvent to water can be adjusted to influence the mechanical properties of the resulting gel by altering its microstructure.[68] A typical solvent combination is DMSO/water, although gels can be formed from various solvent/water systems, depending on the nature of the gelator molecule.[68,69] Our interest lies in tuning these solvent-switch systems by altering the LMWG's solubility *via* pH changes, as explored further in Chapter 3.

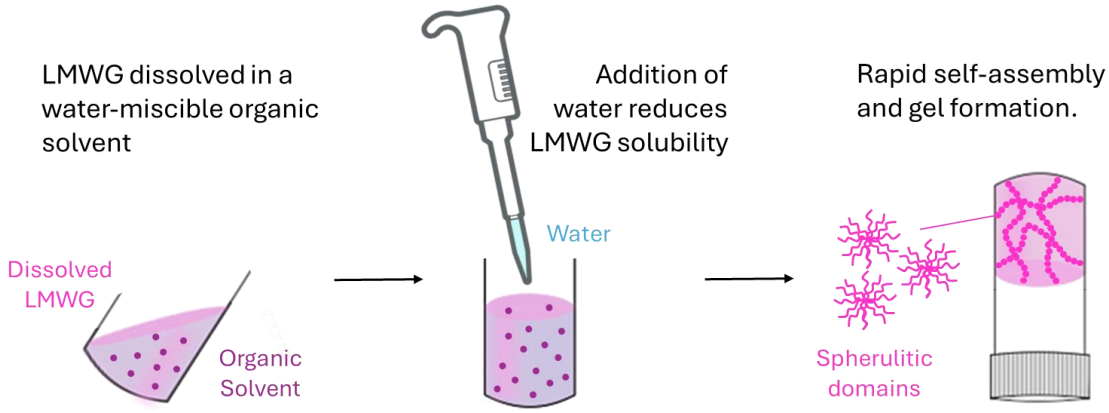

Figure 1.4. Schematic of solvent-triggered gelation. The LMWG is first dissolved in a water-miscible solvent, and water is subsequently added to induce gelation.

1.6. Temperature-triggered gelation

Temperature is often used to induce gelation, as it provides a simple means of altering solubility within the system and thereby driving self-assembly. This process works because the molecule is soluble in the solvent at high temperatures. As the temperature decreases, the solubility of the molecule decreases, triggering self-assembly once the gelation temperature T_{gel} is reached. T_{gel} is defined as the temperature at which a pre-gel solution transitions from a sol state to a gel state.[70] The most common method to achieve this type of gelation is a heat-cool cycle, in which a suspension is heated above the T_{gel} and then cooled.[70] It is

important to note that the heating and cooling rates influence the final properties of the gel.[71] Additionally, temperature affects gel properties in other gelation methods. Although this approach has been applied to various *N*-functionalised dipeptides, there are fewer studies on this method than on pH-triggered gelation (discussed in the next section). This is because many of these dipeptide LMWGs are not soluble until temperatures which exceed the solvent's boiling point.[72]

1.7. pH-triggered gelation

If an LMWG bears an ionisable group, such as a carboxylic acid, then pH changes can be employed to trigger gelation by protonating/deprotonating this group.[61,73,74] Many LMWG are amphiphilic, and their solubility in water can be altered by adjusting the pH to above or below the pK_a of the ionisable group, therefore inducing self-assembly.[45,61,74] In many cases, this occurs due to the neutralisation of pH-sensitive groups, which removes the electrostatic repulsion between charged groups within the gelator. As a result, the gelator becomes less soluble in water and reduces unfavourable interactions by self-assembling into a hydrogel network through non-covalent interactions.[61] For LMWGs, the pK_a of the molecule is influenced by interactions within the surrounding self-assembled network, and typically, the pK_a is higher in the assembled gel network than in solution; therefore, the pK_a of the gelator is often referred to as the "apparent" pK_a.[63,75] This shift is essential when targeting a specific final pH, as many pH-triggered dipeptides tend to have pK_a values below 7.

Multiple methods can be used to alter pH, including hydrolysis reactions, electrochemical reactions, direct addition of acids or bases, photoacids, and enzymatic triggers.[73,76–79] This versatility makes pH-triggered gelation a popular approach due to its accessibility and the ease with which gelation can be reversed by adjusting the pH in the opposite direction.[79,80] However, the homogeneity of the resulting gels can vary depending on the method, as the pH change can occur throughout the bulk solution or at a localised point.[79] If pH is reduced with the direct addition of acid, for example, then localised gelation occurs, and the resulting gel's properties are varied and not reproducible.[74] In 2009, Adams *et al.* demonstrated pH-triggered gelation by dissolving Fmoc dipeptides in water at high pH and using the hydrolysis of GdL to gradually reduce the pH from approximately pH 9 to pH 4 (Figure 1.5).[74] This method yielded more reproducible homogeneous

gels. [74,79] Notably, this reaction can be replaced with other reactions that gradually reduce the pH, such as the hydrolysis of other various anhydrides, thereby providing an alternative means of altering gel properties while using the same LMWG.[79]

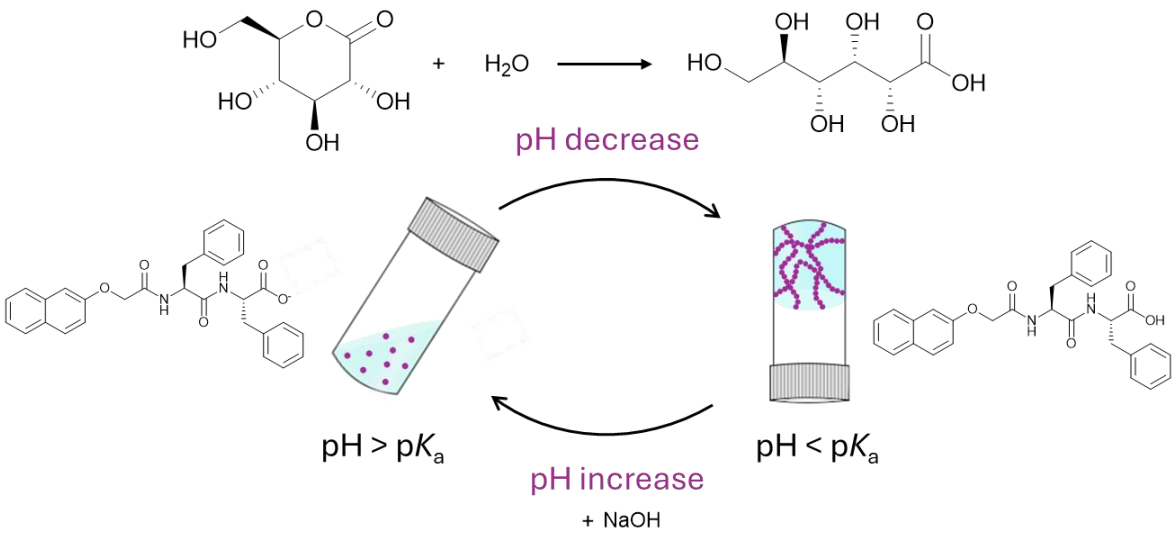

Figure 1.5. Schematic showing pH-triggered gelation *via* the addition of GdL and reversible gelation upon NaOH addition.

While these examples show gelation *via* a reduction in pH, it is also possible to form gels at high pH, as is the case with dipeptide LMWGs when a salt trigger is applied or with those containing an ionisable amino group.[60,76,81] This is demonstrated by Patterson *et al.*, who generated a pH gradient *via* electrochemical reduction of H_2O_2 to fabricate Fmoc-3 gels.[76]

1.8. Electrochemical triggers

Electrogelation, a subset of electrofabrication, refers to the fabrication of materials *via* electrochemical methods.[62] These include various methods for applying electrical signals to solutions of macromolecules/gelator molecules to form soft materials for practical applications.[62] Using electrofabrication to form hydrogels offers exciting prospects for developing bioactive and organic materials, with several advantages over other, more established biofabrication techniques.[82-84] For instance, electrofabrication is not limited by the long fabrication times of stereolithography or by clogging in layer-by-layer printing. No external photomasks, moulds, or laser sources are required to create patterns on a surface

or in a gel; therefore, cytotoxic and non-biocompatible photoinitiators and photoacids are often avoided.[84]

Electrofabrication techniques can be broadly classified into two categories: direct and indirect electrochemical approaches.[83] In direct electrofabrication, electron transfer between the electrode and reactants results in the direct formation of the desired product, such as metals, polymers, or oxides.[83] Indirect electrofabrication involves modifying the local environment by generating ions, altering pH, or producing catalysts, which induce self-assembly or precipitation of materials in the surrounding solution.[83]

Direct electrochemical approaches can also employ an applied electric field to form materials away from the electrode surface.[82,83] This method enables control of the movement, morphology, and direction of cells within a biomaterial. Several techniques fall under this category, such as electrophoresis, dielectrophoresis, and electrotaxis, with dielectrophoresis being the most widely used.[83] Other direct approaches that do not rely on an electric field include the direct formation or detachment of biomolecules from the electrode surface and electropolymerisation, the latter of which is most relevant to this thesis.[82,83] In this thesis, indirect methods are of particular interest, as this is the mechanism by which LMWGs are formed, analogous to the pH-switch mechanisms discussed in Section 1.7.

Indirect approaches allow for spatiotemporal control, as fabrication is exclusively at the electrode surface, leading to highly localised gelation.[83,84] There are many examples of biomaterials produced *via* indirect electrochemical approaches, including alginate, chitosan, agarose, and silk.[85–88] However, these materials have several limitations, including significant variation in material properties, increased risk of allergic reactions, and limited tunability of bulk mechanical properties. Batch-to-batch variation often results in inconsistencies in chemical composition, purity, and potential contamination.[83] Some of these issues can be mitigated by using synthetic gelators with a defined chemical composition. N-functionalised dipeptide LMWGs do not exhibit this batch-to-batch variation, forming highly reproducible hydrogels with easily tuneable mechanical properties.[84] A technique for generating hydrogels directly at or near a surface involves the localised gelation of LMWGs *via* electrochemically generated

pH/proton gradients.[83,84] This can be achieved by exploiting various electrochemical acid-base or redox reactions. The resulting localised pH change then initiates the self-assembly of the gelator molecules exclusively at the electrode surface, with excellent spatiotemporal control.[84]

The anodic neutralisation reaction of carbazole-protected dipeptide gelators *via* hydroquinone (HQ) oxidation is one such example, used in Chapter 4. In this method, gelation is triggered by applying a constant current to the electrode surface, leading to the electrochemical oxidation of hydroquinone to benzoquinone. As a result, protons are generated at the electrode-solution interface, forming a localised low pH gradient.[84] As the pH at the electrode surface decreases below the apparent pK_a, of the gelator, gelation occurs locally, whereas the bulk solution remains unaffected (Figure 1.6).[84,89] Johnson *et al.* first reported the formation of nanometre-thick dipeptide hydrogel films of the LMWG FmocLG using this method in 2011. They further expanded this work in 2013 by demonstrating the controlled growth of thin dipeptide gels on an electrode surface.[90,91] The gel volume increased with deposition time, and the rate of gel growth could be easily controlled by altering the applied current.[90,91]

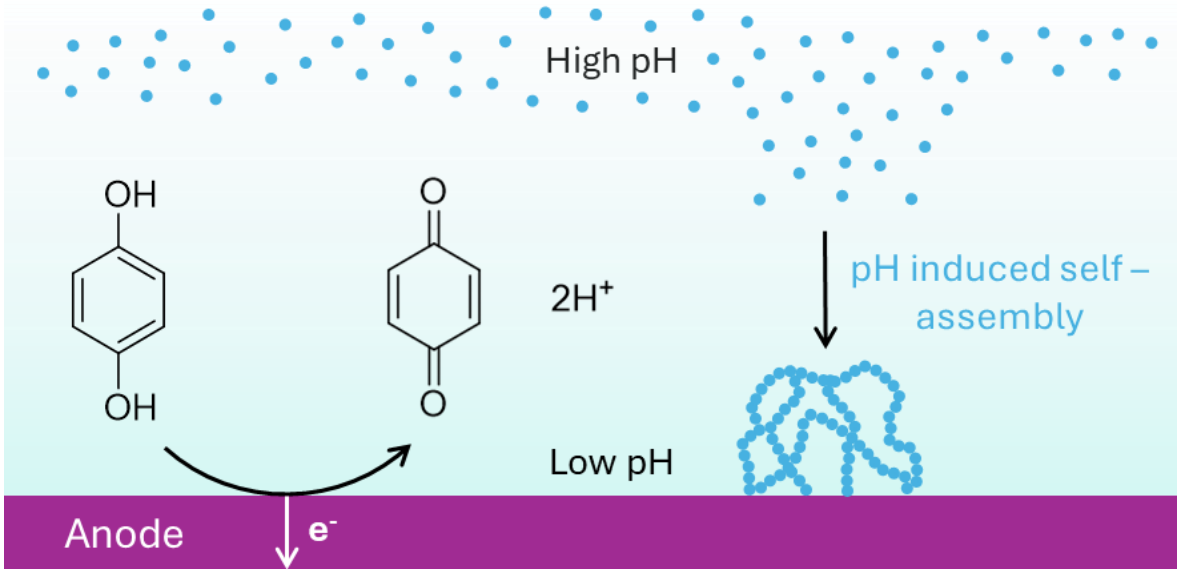

Figure 1.6. Schematic representation of electrochemical gelation *via* HQ oxidation. A constant current is applied to the electrode surface, electrochemically oxidising hydroquinone to benzoquinone, which generates protons at the electrode-solution interface, resulting in a localised pH drop at the electrode surface and inducing gel formation.

As mentioned previously, local pH reduction *via* electrochemical reduction of H_2O_2 was used to fabricate Fmoc-3 gels. This method applies to any LMWG which is capable of gelling at high pH.[76] Other electrochemically induced gelation methods include: electrochemical generation of Ca^{2+} ions from $CaCO_3$ particles *via* water electrolysis, which induces Ca^{2+} cross-linking, and electrochemical generation of oxidising agents, both of which can be used to gel chitosan (Figure 1.17).[92,93]

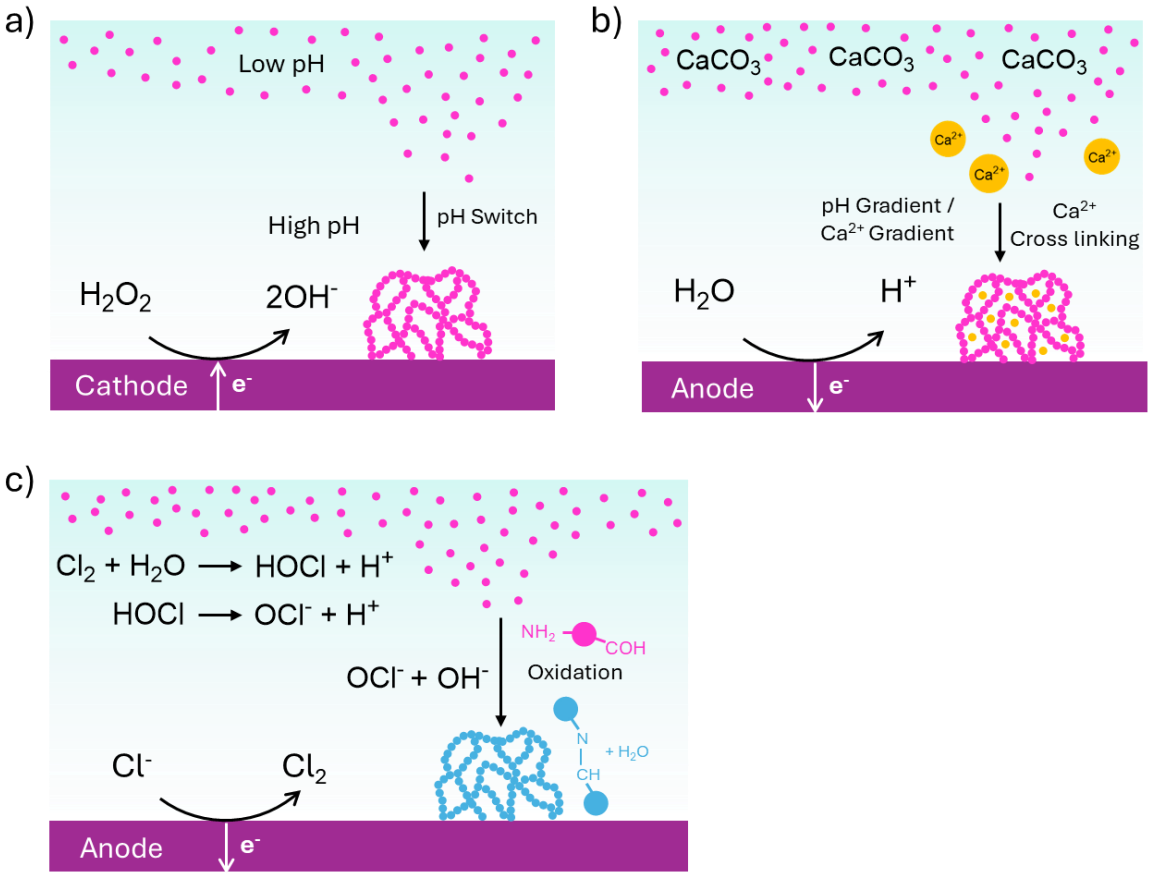

Figure 1.7. Schematic representation of various examples of indirect electrochemical: a) pH-triggered gelation with H_2O_2, b) electrochemical generation of Ca^{2+} from $CaCO_3$ particles *via* water electrolysis, c) electrochemical generation of oxidising agents.

The supramolecular network in hydrogels is sensitive to external stimuli; therefore, these materials often exhibit reversible, dynamic properties.[6,92] Therefore, when hydrogels are formed electrochemically, subsequent electrochemical processes can be applied to access materials with novel morphologies. Carbazole-protected amino acids, for example, can undergo electrochemical polymerisation to form redox-active polymers.[94] Kubiak *et al.* reported the electropolymerisation of amino acid Carb-Ala gels. The polymers

produced had a unique morphology, with a more open, fibrous structure than the polymer formed directly from the Carb-Ala monomer, demonstrating the use of electrochemical processes on gels as a stepping stone to unique materials

1.9. Transient gels

Supramolecular transient gels are soft condensed materials that are dynamic in nature. Most conventional supramolecular LMWG gels discussed so far are prepared so that their properties don't change with time. However, supramolecular transient gels can be designed to be dynamic, exhibiting changes in mechanical properties and even phase transitions over time.[95,96] Various stimuli, including pH, enzyme reactions, temperature, and redox reactions, can trigger these changes.[95,97–100] The dynamic behaviour of these materials enables the formation of gels that would otherwise be unattainable by conventional methods.[101] Additionally, these processes enable temporal control of changes, allowing systems to be managed over time with specific applications in mind.[64] As a result, interest in transient gels has grown, with inspiration often drawn from self-assembled biological systems found in nature.[102]

Boekhoven *et al.* reported the first transient self-assembled system to exhibit a sol-to-gel-to-sol phase transition driven by a chemical reaction.[97] This was achieved using an LMWG with an anionic carboxylate group. Through carboxylate alkylation, a methyl ester was formed, altering the charge of the gelator and inducing the sol-to-gel transition. The methyl ester then undergoes spontaneous hydrolysis in aqueous conditions, allowing the system to regenerate the negative charge and drive the reverse gel-to-sol transition.[97] Since this work was published, there have been numerous examples of transient systems driven by altering the system's equilibrium. In most cases, a chemical fuel is used to alter the gelator environment, thereby changing the gel network.[102]

One example of such a system is a chemical reaction network that converts dicarboxylates into metastable anhydrides by irreversibly consuming carbodiimide fuels. The anhydrides rapidly hydrolyse back to the original dicarboxylates and can self-assemble into hydrophobic colloids, hydrogels or inks (Figure 1.8).[95] These chemical fuel systems have a tuneable lifetime, which can be adjusted by varying the amount of fuel, and, as expected, this affects the properties of the materials

produced at each stage.[95,102] The system's kinetics can also be used to alter the transition rate.

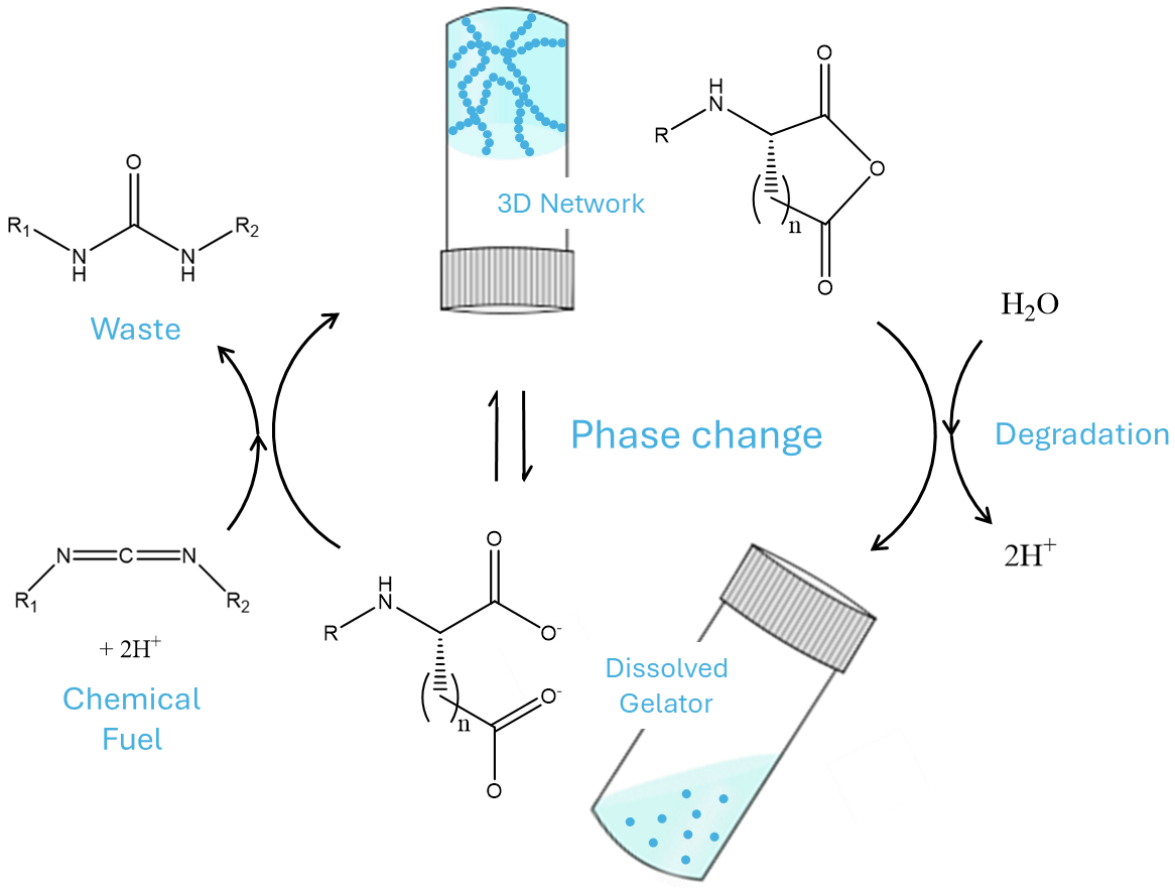

Figure 1.8. Mechanism of phase change in a transient system *via* fuel-driven formation of a transient anhydride bond.

Enzymes are a popular choice for achieving transient changes; for example, α-chymotrypsin was the first enzyme used to induce transient self-assembly. The enzyme catalysed the formation of a peptide bond, thereby generating a metastable dipeptide which could self-assemble into a gel. The system was tuneable by varying the enzyme concentration, since the enzyme directly modifies the precursor blocks, as shown in Figure 1.9a.[104,105] Another widely used enzyme reaction is the autocatalytic urea–urease reaction, which gradually increases pH through ammonia production and enables temporally programmable self-assembly.[106] One advantage of this reaction is the bell-shaped behaviour of its kinetics at different pH values. This reaction can therefore be paired with a chemical fuel that lowers the pH, forming a pH-responsive transient system. [101]

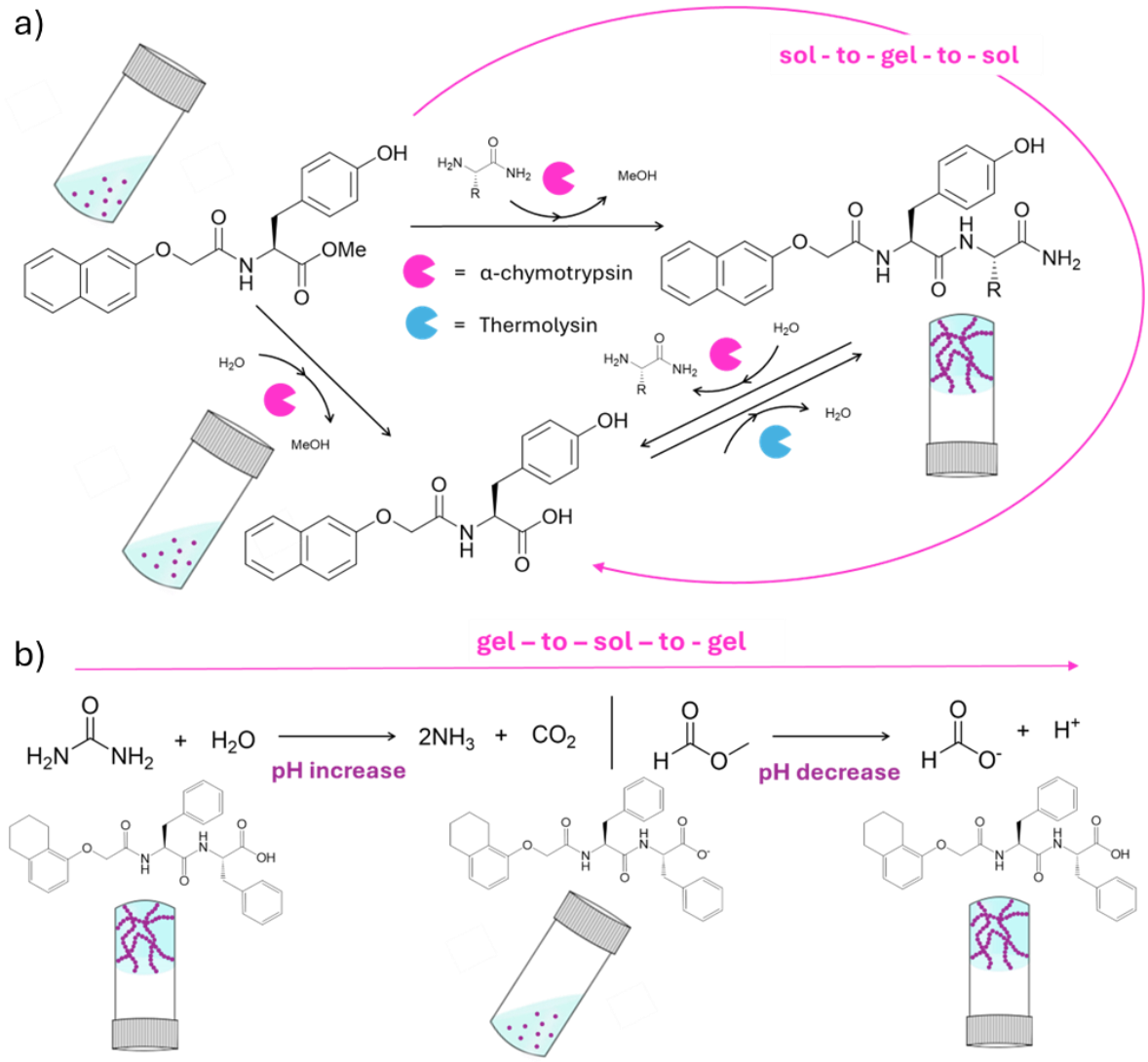

Figure 1.9. Reaction scheme of a) the enzyme α-chymotrypsin and b) the urea-urease reaction with methyl formate, with arrows illustrating the transient self-assembly processes they induce.

The Adams group used this urea–urease reaction, combined with methyl formate hydrolysis, to form pre-programmable transient gels with a controlled increase followed by a decrease over time.[64,100,107] When these reactions were combined with a solvent-triggered DMSO/H_2O hydrogel formed with the functionalised dipeptide gelator 1ThNapFF, a gel-to-sol-to-gel transition occurred (Figure 1.9b). Within these systems, the choice of counter-trigger significantly affects the time the system remains a solution and its properties after re-gelation.[64,107]

There are now several examples of pre-programmable reaction networks, such as the sol-to-gel-to-sol systems first presented by Boekhoven *et al*. The initial sol-to-gel transition can be programmed either by the pH method described above or by

adding a chemical fuel that converts a non-gelator into a gelator; once the fuel is depleted, the system reverses to the sol state.[99,108] Additionally, a gel-to-gel-to-gel transition can be induced by pH changes that alter the gel network structure.[109] This tunability expands the functional catalogue of hydrogels, enabling adaptive materials that respond to environmental stimuli or user input, which is essential for creating next-generation smart biomaterials and soft robotics. Such control over the assembly and disassembly of gels, or over their structure, is crucial for applications such as controlled drug delivery, tissue engineering scaffolds, or self-healing materials, where materials need to function, then degrade, and reform.[97,100]

1.10. Ageing

One of the most underexplored aspects of LMWG hydrogels is the phenomenon of gel ageing. In the context of LMWG systems, ageing refers to the time-dependent evolution of structural, mechanical, or functional properties that occurs after gel formation. These changes can manifest over timescales ranging from minutes to days, depending on the gelator chemistry and environmental conditions. Typical symptoms of ageing include fibre thickening, network densification, increased stiffness, phase separation, or structural rearrangement.[27,110–114] Such transformations do not necessarily indicate chemical degradation or gel breakdown, but they represent the slow progression toward thermodynamic equilibrium or a kinetically trapped state.[111,112]

Many LMWG gels form through rapid, kinetically controlled processes in which molecules aggregate into fibrous networks.[27] Over time, these networks can reorganise into more ordered, lower-energy configurations. Such reorganisation may proceed *via* mechanisms such as Ostwald ripening, fibre fusion or bundling, or the gradual alignment of gelator molecules within the supramolecular framework.[110,112,113] These processes can lead to significant shifts in gel morphology and viscoelastic behaviour, which in turn alter macroscopic properties.[113]

Time-dependent evolution in these systems can lead to either desirable improvements in stability and performance or unwanted structural drift that limits reproducibility.[110–113] For example, in drug delivery or tissue engineering,

mechanical integrity is critical, and time-dependent stiffening or contraction may alter the diffusion of therapeutic molecules or compromise performance. Although systems that exhibit time-tuneable mechanical or optical properties, such as the transient system discussed previously, can exploit ageing as a design feature when controlled release, adaptive stiffness, or self-healing is desired.[114–116]

Several studies have reported distinct ageing phenomena in specific LMWG systems, which LMWG hydrogels are particularly susceptible to, due to the reversible nature of supramolecular self-assembly.[110,115] Fmoc-derivatised amino acids and peptides, for example, frequently exhibit structural evolution over time, in which initially thin fibres gradually bundle into thicker aggregates, increasing the network's rigidity.[115,117] Shi *et al.* investigated a small library of phenylalanine-based hydrogels and observed that a cinnamoyl-capped phenylalanine derivative formed opaque gels that transitioned to clear gels after ten days. This optical change suggested a gradual reorganisation of gelator molecules, leading to a more homogeneous, ordered structure.[118] Similarly, Draper *et al.* reported that a 2-thiophene-diphenylalanine LMWG transformed from a turbid to a transparent gel over three days. SEM revealed a morphological shift from large spherical aggregates to interconnected fibrous networks, suggesting that ageing promoted fibre rearrangement and refinement. This process was found to be influenced by carbonate concentration.[110]

One of the most considerable changes supramolecular gels exhibit is syneresis, or spontaneous shrinkage, which is an expulsion of solvent from the gel matrix over time.[119–121] This process can arise from increased hydrophobic interactions or network densification and can significantly alter the volume and mechanical properties of a gel.[121] Duraisamy *et al.* reported a self-shrinking hydrogel formed *via* a temperature-triggered process, which contracted and expelled buffer solution within 30 minutes, driven by changes in molecular packing.[119] Despite many LMWGs being reported as highly hydrophobic, syneresis does not always occur, and when it does, the time frame of the change can vary widely. A triphenylalahenine-based hydrogel, for example, was shown to self-shrink over seven days, driven by its high hydrophobicity.[120] To date, there is no comprehensive explanation of why syneresis occurs, and it can be a barrier to the use of hydrogels in applications.

The mechanistic understanding of ageing remains limited, primarily because of the many parameters that can contribute, including solvent composition, ionic strength, temperature, gelator concentration, and assembly kinetics. Many papers choose to ignore ageing, and when it is reported in studies not focused on ageing, the coverage can be inconsistent or incomplete.

1.11. Plasma-triggered gelation

Recently, there has been a growing interest in using plasma to trigger gelation, where electronic species generated by a plasma, namely electrons, ions, and reactive oxygen and nitrogen species (RONS), are used to enhance self-assembly.[122] Cold atmospheric plasma (CAP), in particular, has been shown to be a sustainable, cost-effective and tuneable trigger for self-assembly.[123] However, relatively few studies have been published in this area to date.

CAP has previously been used to modify proteins, offering a sustainable method to improve their gelling functionality for plant-based food applications. It was applied as a non-thermal pretreatment to enhance the gelation of oat and pea proteins.[124,125] Treatment of oat protein dispersions with CAP effectively modified their structure, and the dispersions were subsequently gelled via a heat–cool process. CAP exposure enhanced protein hydrophobicity and induced structural rearrangements *via* oxidation and peptide bond cleavage, resulting in gels with increased viscoelastic moduli and improved stability.[124] For pea protein, plasma treatment partially unfolded the protein structure, which again increased surface hydrophobicity and promoted oxidation-driven aggregation.[125] This led to gelation at lower temperatures, and these gels exhibited higher compressive strength, elasticity, and water-holding capacity, supported by the formation of a more homogeneous and interconnected protein network.[125]

A dielectric barrier discharge (DBD) plasma has also been used to induce *in situ* gelation with the biopolymer chitosan.[126] DBD was employed to gel chitosan solutions *in situ* without the use of chemical initiators or toxic crosslinkers.[126] As with electrofabrication, the plasma treatment generated reactive species that induced oxidation, leading to partial cleavage of ß-(1→4)-glycosidic bonds and aldehyde generation, leading to Schiff base crosslinking between chitosan chains.[126] The crosslinking density and swelling behaviour of the resulting

hydrogels were tuneable by varying the plasma exposure time and chitosan concentration.[126]

Recently, Basumatary *et al.* presented the first instance of plasma-induced self-assembly of LMWG using a helium gas plasma jet.[122] They proposed that CAP alters the molecular environment, leading to the self-assembly and structural transformation of Fmoc-F and Fmoc-W, which were dissolved in phosphate-buffered saline (PBS) at physiological pH (Figure 1.10).[122] These changes were driven by enhanced non-covalent interactions, which stabilised the resulting 3D network.[122] This technique is advantageous because gelation is fast, tuneable and nonthermal, as CAP can operate at ambient temperature and pressure.[122]

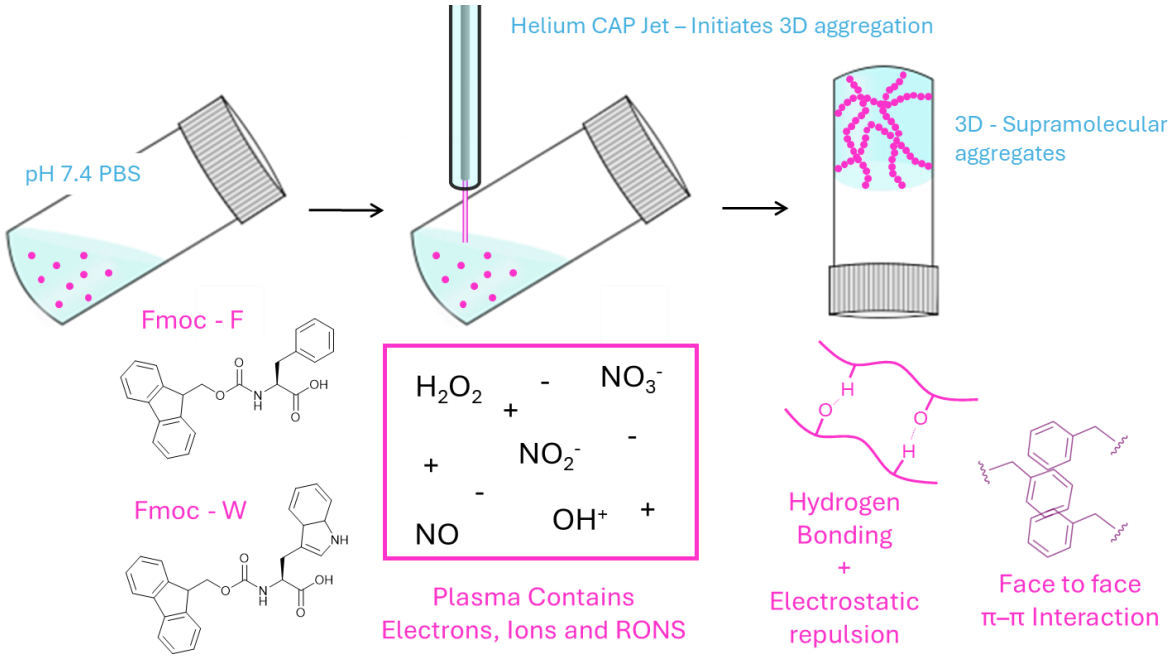

Figure 1.10. Schematic of the plasma-induced self-assembly of Fmoc-F and Fmoc-W proposed by Basumatary *et al.* The dipeptides are dissolved in PBS buffer, and the application of a He plasma jet initiates 3D aggregation.

Building on this, Bhatt *et al.* presented a proposed mechanism for the self-assembly of Fmoc peptides *via* CAP.[123] In particular, CAP-generated RONS induced molecular aggregation through the modification of Fmoc-Y. Oxidation, hydroxylation, and nitration occurred, enhancing self-assembly by increasing hydrogen-bonding potential and promoting supramolecular interactions (Figure 1.11).[123] Additionally, the modifications shielded the amine group, thereby altering the molecule's hydrophobicity. Using this method, the authors successfully produced 3D fibrous Fmoc-Y structures. [123]

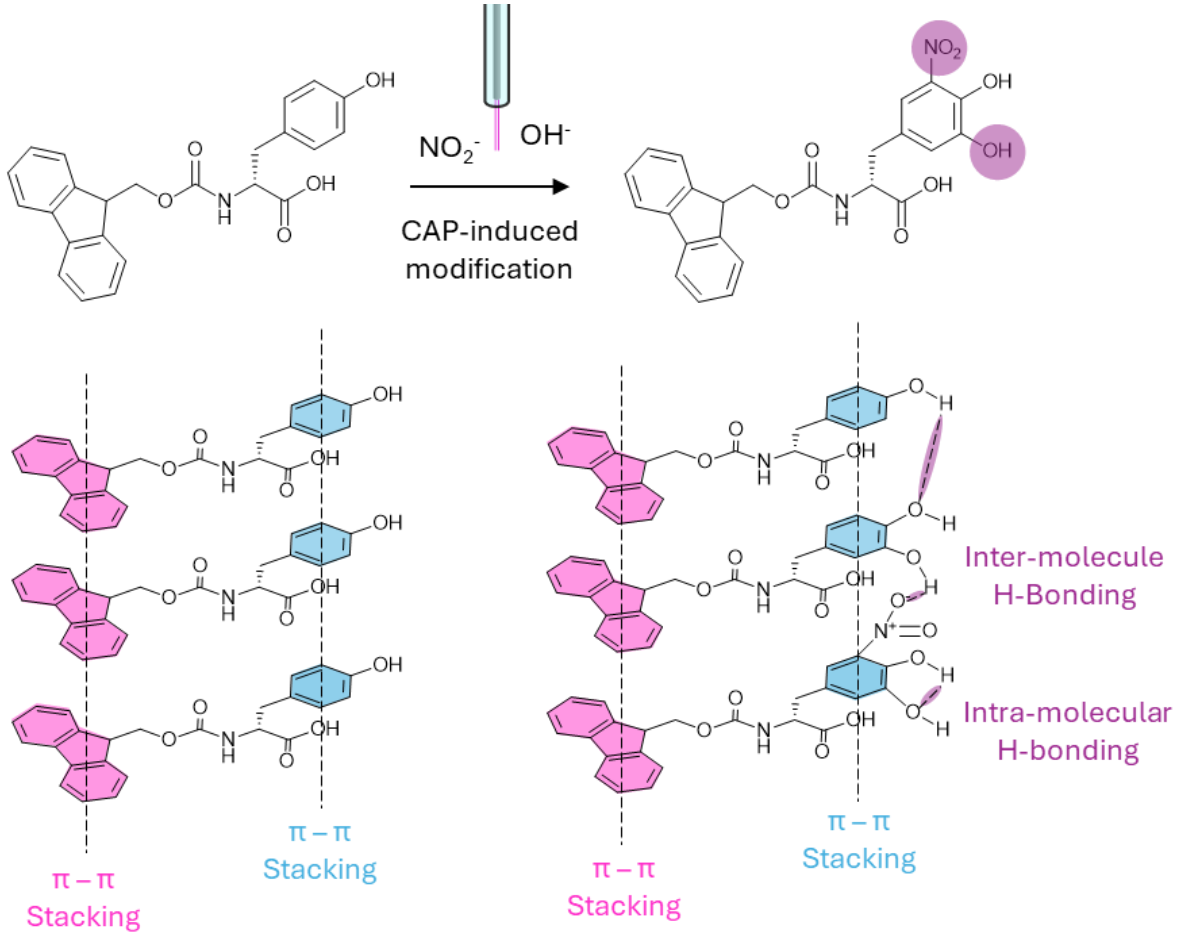

Figure 1.11. Schematic of the suggested mechanism of CAP-induced chemical modification leading to the increase in H-bond potential and the promotion of supramolecular interactions from Bhatt *et al.*

Despite its promise, the CAP-triggered self-assembly approach faces several challenges and open questions. The connection between specific RONS-induced modifications and aggregation remains weak as the relative abundance, kinetics, and structural roles of identified additions are not quantified. Moreover, the individual contributions of different reactive species are not isolated, leading to ambiguity. The reproducibility and scalability of CAP treatment for plasma gelation are also insufficiently explored, given the sensitivity of plasma–liquid systems to operational parameters such as power, distance, gas composition, and exposure time.[127,128] Plasma-induced gelation is explored further in Chapter 2.

1.12. Localised gelation

Controlling gelation at increasingly smaller length scales is needed for spatial precision across applications such as tissue engineering, drug delivery, soft

robotics, and 3D bioprinting. Bulk gelation methods are limited in spatial resolution, whereas more localised gelation techniques allow the formation of gels that can be shaped or patterned in complex architectures.

As discussed in section 1.8, electrofabrication can be used to form localised self-assembled hydrogels on surfaces by creating a pH gradient that can be spatio-temporally controlled.[84] Plasma gelation can also be used in a similar manner by varying the amount and position of plasma application to form well-defined gel structures and to tune their properties, as explored further in Chapter 2. [122,129] In addition to these two methods, several other techniques enable the localised self-assembly of gels with high spatial resolution.

Photoacid generators are a method for achieving spatially and temporally controlled gelation.[6] These compounds can release protons upon light irradiation, enabling precise pH tuning, or release cations, forming salt-triggered gels.[130,131] When these compounds are incorporated into LMWG systems, patterned light exposure results in gel formation only in the specifically illuminated regions.[131] This approach has significant implications for bio-fabrication and cell encapsulation, where minimising chemical exposure and maximising spatial resolution are essential.[132] The light can also be applied at a micrometre-scale resolution and from a distance.[131] The materials formed have a somewhat transient nature, as they can be subsequently collapsed when a counter-trigger is applied, although this is not preprogrammed. However, this technique typically requires a photomask to define illuminated regions, limiting its flexibility and scalability.[131]

Supramolecular gel noodles can also be formed, which are 1D macroscopic fibres with specific structures.[132] They have attracted attention for their ability to achieve internal fibrillar alignment, cross-sectional patterning, and programmable shape-memory performance.[132–134] In these systems, gelator solutions are injected into a medium containing the triggering agent, for example, a low-pH or multivalent cation solution, resulting in immediate fibre formation.[133,134] Despite these promising advantages, the gel noodles are limited by their restricted functionality and by the fact that the materials formed are often flexible or mechanically sound but not both, so the materials are possible but practically

unusable.[134] There have been recent techniques to overcome this, such as twisting the gel fibres into gel noodles to combine multiple LMWG properties.[134]

Finally, a more recent method is gel 3D printing, in which LMWG precursors are deposited onto a surface in a defined shape, and gelation is triggered during or after deposition.[135] This method enables the fabrication of intricate structures that have attracted interest across fields ranging from medicine to soft electronics, and is further discussed in the following section.[136,137]

1.13. Gel 3D printing

3D gel printing is a relatively recent localised gelation method used to fabricate tissue scaffolds for biomedical applications and functional devices, such as biosensors and strain sensors.[137–139] These printed structures can be designed to replicate both the mechanical properties and geometries of biological tissues.[137,140] To achieve this, high spatial precision and reproducibility are essential. Hydrogels, particularly supramolecular hydrogels, are well-suited for these applications owing to their biocompatibility, tuneable physical and chemical properties, and high water content.[135,138–141]

Many polymeric hydrogels have been used in 3D bioprinting, where the gel precursors are typically extruded as solutions that subsequently undergo gelation via external triggers such as temperature changes, UV photocuring, exposure to crosslinking agents, or printing into reactive solutions or pre-existing gels.[138,139] However, LMWGs have emerged more recently as a promising alternative.[135,140] Their ability to undergo reversible gelation and self-healing enables them to be pre-gelled and extruded directly, rather than being formed post-printing.[135,142,143] In theory, this allows the final material properties to be determined by the gel before extrusion, assuming that the gel is printable and that the extrusion process does not significantly alter its properties.[135]

The most common way to 3D print these materials is extrusion-based 3D printing, where material is deposited layer by layer through a nozzle or syringe, forming programmable geometries analogous to conventional 3D printing (Figure 1.12).[142,144] Many successful 3D-printed LMWGs have been reported, and materials with multilayer structures containing property gradients or domains with varied properties/uses have been produced.[140,144,145] These multilayer gels can remain

independent of adjacent material even when deposited in close proximity.[144] This technique is cost-effective, accessible, and well-suited for printing viscous materials. However, extrusion-based systems are limited by relatively low resolution and slow printing speeds.

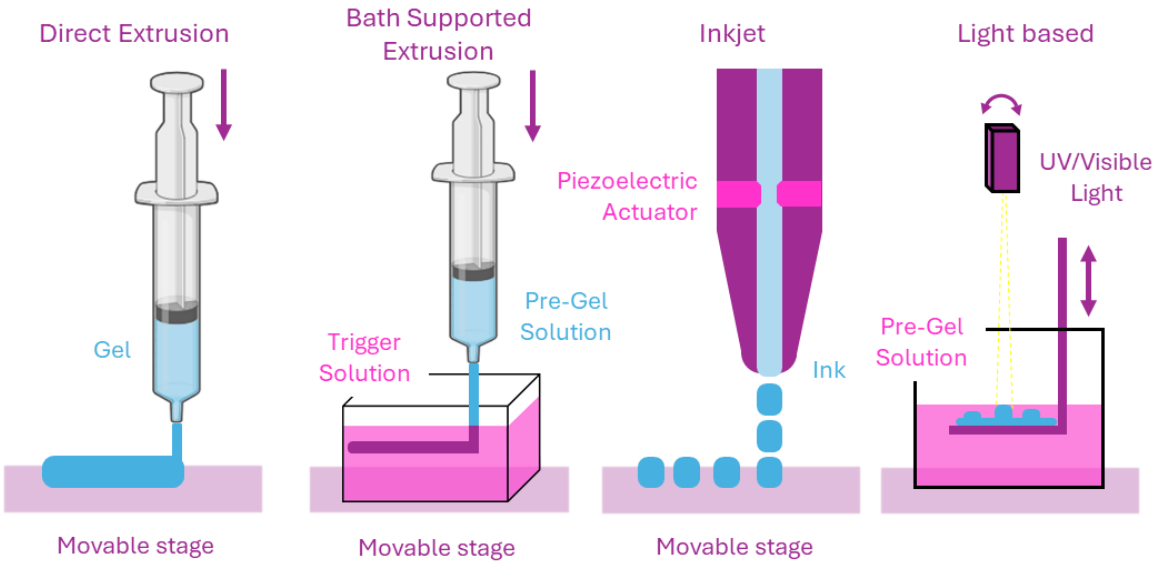

Figure 1.12. Schematic of the different 3D printing methods: Direct extrusion, bath-supported extrusion, inkjet, and light-based methods (left to right).

Studies characterising LMWGs before and after extrusion have shown that the printing process can alter their structural and mechanical properties.[142] Although recent work has proposed methods to mimic the 3D printing process on a rheometer, allowing more rapid material screening, developing a system in which the gel's properties remain unaltered during printing would be highly advantageous, particularly for applications requiring specific functional requirements.[142]

Studies have established that LMWGs forming spherulitic domains print more effectively than gels containing fibrous networks, as spherulitic structures better withstand the shear stress during extrusion.[135] This highlights the influence of supramolecular morphology on printability. Apart from this factor, gelator concentration, needle diameter, nozzle-to-surface distance, and flow rate also significantly affect the final printed gel, emphasising the complexity of achieving reproducible and stable LMWG-based structures with this method.[135,142,144]

A complementary approach to direct extrusion is solvent-switch printing, where LMWG-containing organic solutions are printed directly into a coagulation bath

(Figure 1.12).[146] Rapid solvent exchange triggers gelation, producing well-defined filaments. This printing method enables printing of LMWGs gels that are not thixotropic and would otherwise disintegrate under extrusion shear forces.[146] For example, sugar-based LMWGs have been printed using DMSO as the solvent and water as the coagulation medium, resulting in rapid formation of biocompatible hydrogel filaments.[146] Following this, Jian *et al.* developed a support bath-free 3D printing system based on two oppositely charged N-functionalised dipeptides.[141] Electrostatic interactions between the cationic and anionic side chains of these dipeptides enabled *in situ* gelation during printing, resulting in self-supporting hydrogel scaffolds.[141] By varying the composition and concentration of the two LMWGs, the mechanical strength and degradation rate of the printed shapes could be controlled.[141]

Despite these achievements, challenges remain in the rational design and prediction of printable LMWG systems. Current successes are primarily the result of trial-and-error approaches rather than systematic material design. There is still a limited understanding of why certain LMWGs print effectively, while others fail.[135,144] While many LMWG 3D-printed gels demonstrate biocompatibility, issues such as residual solvent toxicity and mechanical instability can limit their practical applications.[141,146] Consequently, developing an approach that preserves gel properties during printing would represent a significant step forward. This concept is further explored in Chapter 2 through plasma-induced *in situ* 3D printing of hydrogels.

Beyond extrusion printing, inkjet and light-based printing are two additional techniques for 3D printing gels, typically operating at smaller scales compared to bulk extrusion-based methods (Figure 1.12).[147,148] Inkjet printing relies on the controlled ejection of small droplets of low-viscosity gel precursors, or bioinks, *via* thermal or piezoelectric actuation. This enables rapid, highly precise deposition, enabling spatially controlled patterning or mixing of multiple materials.[148] However, the technique is constrained by its requirement for low-viscosity formulations and droplet drying/merging, which is not ideal for LMWG solutions.

Light-based printing encompasses several photopolymerisation-based techniques, such as stereolithography and digital light processing.[147,149] These methods use

focused UV or visible light to photopolymerise hydrogel precursors layer by layer, producing spatially resolved, smooth-surface materials. [147,149] While digital light processing enables faster fabrication by curing entire layers simultaneously, both techniques require photopolymerisable materials, which can limit the choice of gelators.

1.14. Nanostructure of LMWGs

The self-assembly of LMWGs is a hierarchical process spanning multiple length scales. The interactions during self-assembly drive the formation of 1D nanostructures.[6] The type and shape of the fibres formed within the 3D network significantly impact the morphology, mechanical properties, and stability of the resulting gel, as well as the micellar structures present in the pre-gel solution.[72] Therefore, when designing LMWG systems, it is essential to consider the resulting nanostructures, as they directly influence properties such as stiffness and elasticity. There has been extensive work on understanding the relationship between nanostructure and macroscopic properties to explain macroscopic phenomena.[72,150] In transient gels, differences between the initial and final gel states often arise from nanoscale structural evolution.

In pre-gel solutions, LMWGs can form micelles of various shapes and sizes, which influence the self-assembly process and the properties of the final gels.[71,72,150,151] Micelles form spontaneously in solution to minimise interactions between the hydrophobic core and the solvent above the critical micelle concentration (CMC). They can often vary in size and shape within the same solution due to dynamic conditions.[71,152] Factors such as pH, salt addition, and temperature influence micellar growth, and the same LMWG can exhibit different micelles depending on the conditions.[71,72,150,151,153] Dipeptide-based LMWGs have previously been shown to form spherical micelles, worm-like micelles, and hollow-cylinder fibres upon reaching the CMC (Figure 1.13).[27,72] Before this point, the LMWGs exist as dispersed molecules.[32] Among these micelle architectures, the “worm-like micelle” is particularly interesting; these micelles are cylindrical fibres with a high degree of flexibility and are considered viscoelastic.[71] Cardoso *et al.* demonstrated a concentration-dependent transition from spherical to worm-like micelles, with two CMC values: one for spherical micelle formation and another for the subsequent transition to worm-like structures. A defining feature of worm-

like micelles is that they are continuously "breaking" and reforming when shear is applied, making them uniquely viscoelastic. They also show shear-thinning induced by alignment.[154] Ikeda *et al.* investigated the effect of these micellar shapes on the hydrogel network structure using a glutamic acid-based organogelator, finding that worm-like micelles produced gels with higher yield stress than those formed from spherical micelles.[151]

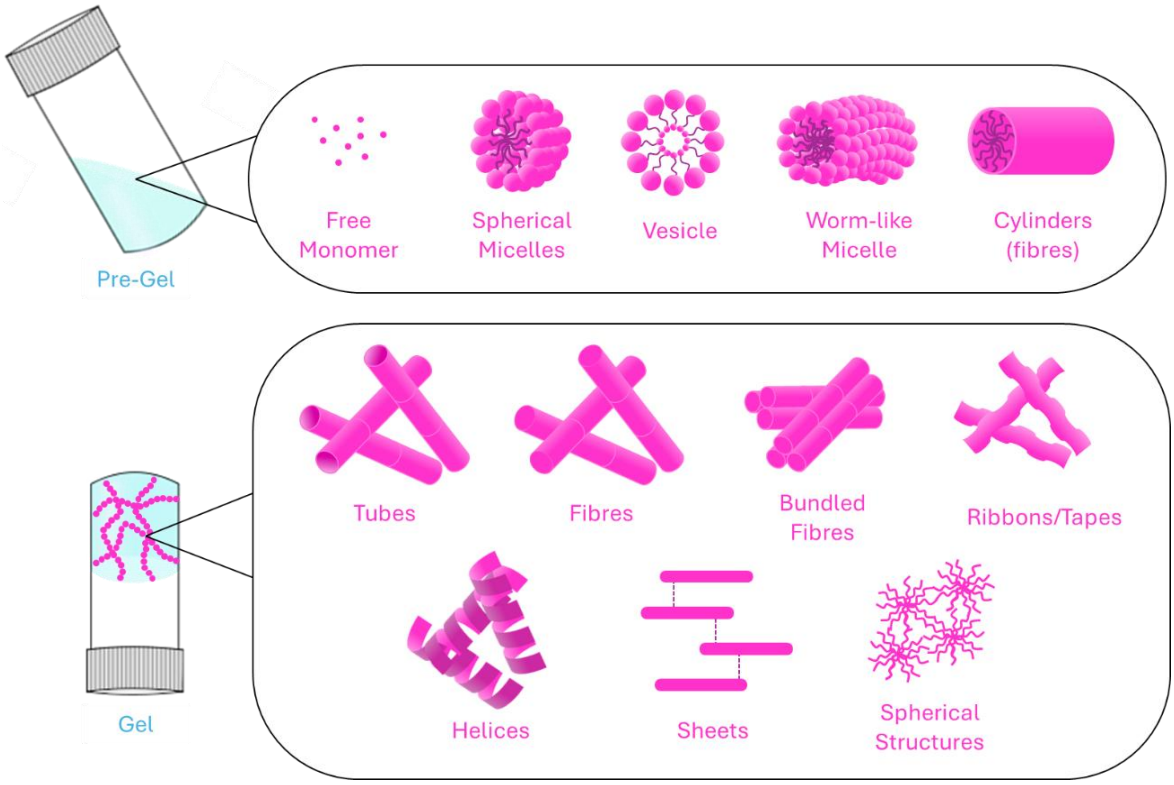

Figure 1.13. Schematic showing the different self-assembled structures reported in pre-gel solutions (top) and gels (bottom).

Various nanostructures have been reported in dipeptide gels, including tapes, nanotubes, fibres, spherical structures, helices, and two-dimensional (2D) films (Figure 1.13).[42,150,153,155,156] These assemblies have hierarchical organisation, forming larger 3D networks through secondary interactions.[63] Distinct physical properties can result from different nanostructures even when the same short peptide is used, for example, the stereoisomers LL-2NapFF and LD-2NapFF both form nanotubes.[150] However, the LL-2NapFF nanotubes have a radius of 80 Å compared to the much larger LD-2NapFF nanotubes, which have a radius of 300 Å.[150]

Even small changes in the gel environment or gelation kinetics can alter the nanostructure formed. In pH-switch gels, fibres formed at lower pH values are more rigid compared to those formed at higher pH values and are less able to withstand large deformation.[63,71,153] The increase in rigidity is due to tighter molecular packing and more ordered nanostructures. The pH of the pre-gel can also affect the nanostructures, as demonstrated by Nanda *et al.*, who used naphthalene-based LMWG to form hydrogels in buffer solutions of differing pH.[153] Depending on pH, the nanofibers' morphology varied: they were helical at pH < 12 but became tape-like above this. Additionally, gels formed at the higher pH values in the 7-12 range exhibited wider fibres.[153] On the same note, Ginesi *et al*. also showed pH dependence of perylene bisimide (PBI) gels, finding that both the starting and final pH impacted the resulting gel. The worm-like micelles formed from adjusting the PBI solution from pH 9 to pH 6 resulted in the formation of different worm-like micelles than the worm-like micelles formed directly at pH 6. The gels formed from the pH 6 solutions had thicker, flatter, and shorter cylindrical fibres than those formed from the pH 9 solutions, resulting in gels which had different mechanical properties.[157]

To characterise these nanostructures, many studies employ multiple advanced characterisation techniques, such as electron microscopy and small-angle scattering, which are discussed in the next section.[158]

1.15. Characterising the properties of LMWG gels

Characterising the properties of LMWG gels is crucial for understanding their behaviour and enabling their use in various applications. In this section, several techniques commonly used to probe the structural and mechanical properties of gels are reviewed. These include scattering techniques, such as small-angle X-ray scattering (SAXS), small-angle neutron scattering (SANS), wide-angle X-ray scattering (WAXS), and ultra-small-angle X-ray Scattering (uSAXS). Techniques for measuring mechanical properties, such as rheology (including cavitation rheology and viscosity measurements) and nanoindentation, and for imaging, such as confocal microscopy, scanning electron microscopy (SEM), transmission electron microscopy (TEM), and cryogenic TEM (Cryo-TEM). Many of these techniques are employed throughout this thesis, and a combination can provide a comprehensive view of LMWG gel properties across multiple length scales (Figure 1.14).

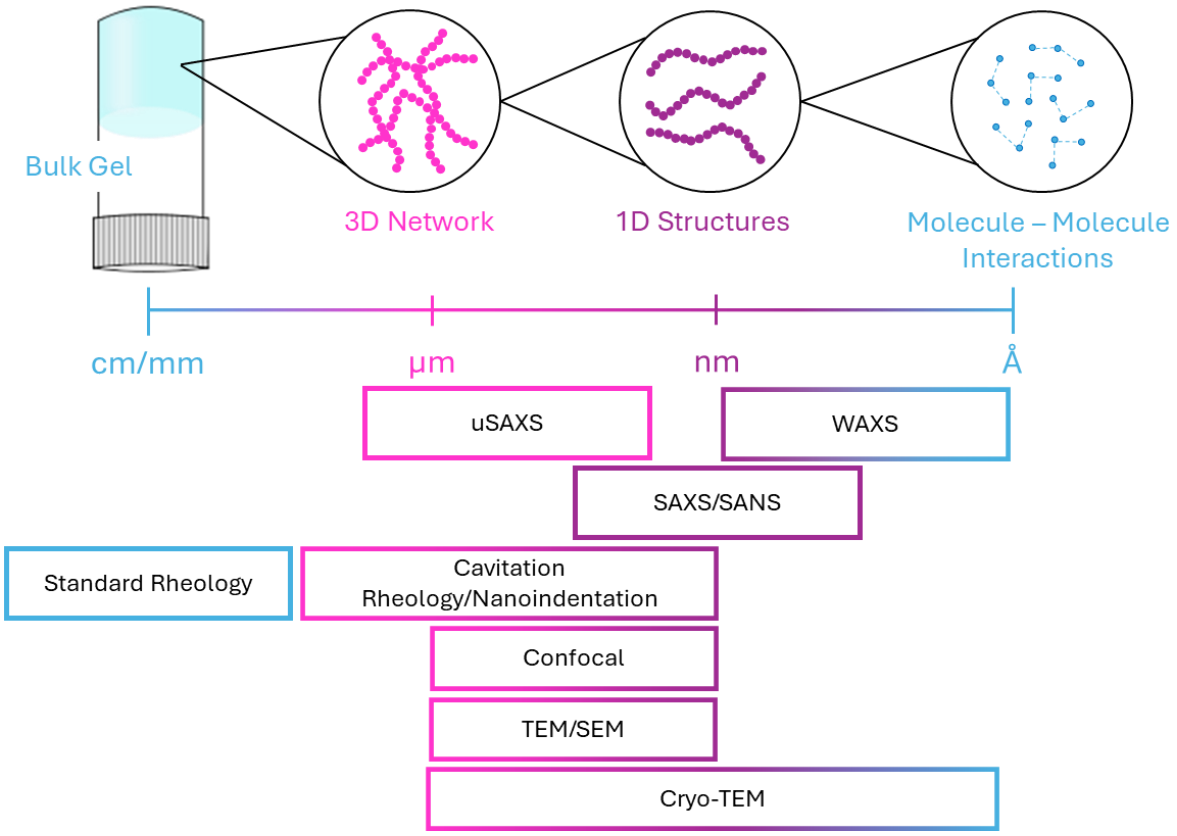

Figure 1.14. Schematic indicating the different length scales associated with LMWGs and the corresponding characterisation techniques suitable for each scale.

Infrared spectroscopy (IR) and circular dichroism (CD) have also been used to understand molecular packing by comparison with known systems, although structural motifs observed in one system may not directly translate to dipeptides, and comparisons remain ambiguous. CD data reported in the literature are often inconsistent and contradictory, as is the case for FmocFF.[159-161] Finally, powder X-ray diffraction (PXRD) data are often collected to correlate a molecule's crystal structure with its gel self-assembled structure.[162] However, this approach has limitations, as crystal structures are often obtained from dried samples or in a solvent different from that used in the gel.

SAXS, SANS, WAXS and uSAXS are scattering techniques used to probe the nanoscale structure of many different materials, and, relevant to this work, provide insight into the fibres within a gel network (Figure 1.15). They offer the advantage that samples can be measured in their hydrated state, as no drying is required, ensuring that the actual structure is preserved during data collection.[158,163] These methods are non-destructive and allow for *in situ*

measurements, which can be used to study the formation and evolution of gels over time, especially useful for transient systems.[158,163]

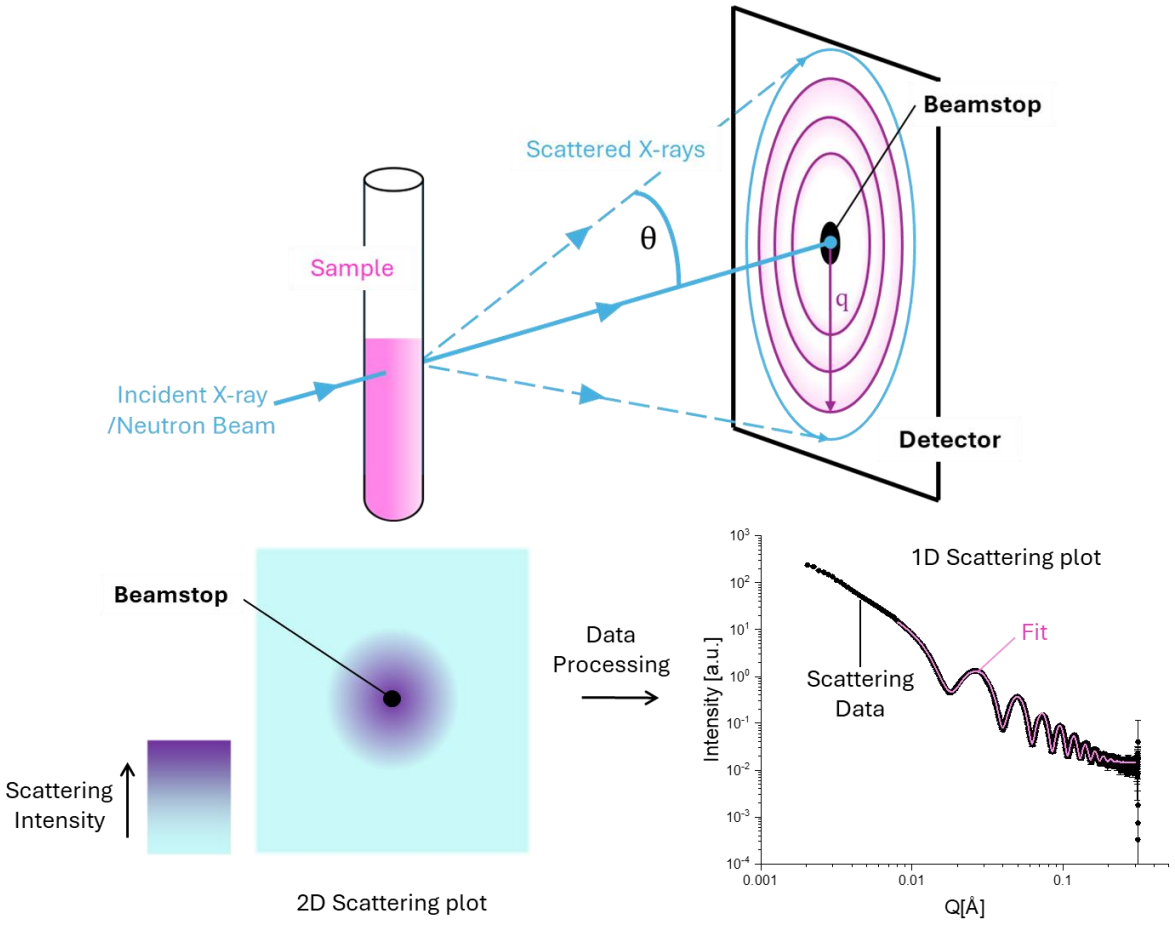

Figure 1.15. Schematic showing a typical scattering experiment. A beam is directed at the sample, and the resulting scattered intensity is collected as a 2D scattering pattern. The 2D data are integrated to produce a 1D scattering plot, which can be fitted using an appropriate model.

SAXS, WAXS and uSAXS measure the scattering of X-rays, while SANS uses neutrons, with each offering distinct advantages depending on the system being studied.[158,163,164] X-ray scattering is sensitive to electron-density contrast, making it well suited to studying systems with inorganic components or dense structures.[158,164] It is also significantly faster than neutron-based techniques, making it useful for hydrogels and dynamic processes.[158] In contrast, SANS is especially useful for studying soft matter and biological samples, as it can exploit isotopic substitution, such as hydrogen/deuterium contrast, to highlight specific parts of complex systems.[158,163] This difference arises because X-rays scatter off electrons in the sample, whereas neutrons scatter off atomic nuclei.[158,163,164]

In scattering experiments, the beam is directed at a sample, and the elastic-scattering intensity is collected at small angles, typically between 0.1° and 10°.[164] The majority of the beam passes through the sample, while a small proportion interacts with the sample and is scattered.[164] Scattering intensity is measured as a function of the scattering vector, q, defined by the following equation:

$$q = \frac{4\pi \sin \varphi}{\lambda} \quad (1)$$

Where φ is half the scattering angle, and λ is the wavelength of the beam.[164] The scattering angle is inversely proportional to the object's size, meaning that larger structures scatter at smaller angles.[164] Typical measurable length scales are in the order of 1–100 nm for SAXS, 0.1–1 nm for WAXS, 20–3000 nm for uSAXS, and 2–200 nm for SANS.[158]

The scattering pattern provides information about variations in electron density (SAXS, WAXS, uSAXS) or nuclear density (SANS) within the sample.[158,163,164] The variations reflect the size, shape, and distribution of the nanostructures, such as fibres, pores, or aggregates.[158,165] It must be noted that the observed scattering is an average over all materials along the beam path, including the solvent, fibres, air, and sample holder, so background subtraction is necessary to isolate the sample scattering.[164]

For effective scattering measurements, there must be a significant contrast between the scattering length density (SLD) of the solvent and the object, in our case, the LMWGs.[164] In this thesis, the LMWGs used have SLD values ranging from 13.5×10^{-6} - 14.1×10^{-6} Å^{-2}, while the background (water) SLD is 9.469×10^{-6} Å^{-2}.[166] This difference provides enough contrast for SAXS to be effectively used for the gels studied.

Once the scattering pattern is collected, it is processed from a 2D to a 1D plot, which can then be fitted to an appropriate model to obtain the structural parameters. For LMWGs, the model and parameters provide information about the shape, length, radius, and flexibility of the fibres in the gel or pre-gel solution.[163,165] The anisotropy in the original 2D scattering can also reveal the degree of fibre alignment within the gel.[167] Since the micelles and fibres formed during self-assembly strongly influence the macroscopic properties of the gel, as discussed in Section 1.14, understanding these structural parameters is essential.

The scattering pattern is an average of all the structures in the sample; therefore, scattering data might be ambiguous if no knowledge of the structures is known, or the sample is very polydisperse, which is why, often, complementary techniques are necessary to understand the nanostructures clearly.

Scattering experiments are ideal for monitoring the structural evolution of gel networks, both during their initial formation and their evolution over time, through *in situ* measurements. Many studies have used these techniques to gain insights into the mechanisms underlying gel formation, behaviour, and ageing. External stimuli, such as changes in temperature, pH, electrochemical processes, light, or shear, can be applied to a sample while measurements are collected, allowing real-time observation of structural responses and dynamic processes as they occur. For example, time-resolved and *in situ* SAXS has been used to follow the effects of pH, temperature, shear, gelation kinetics, and internal fracture process of gels.[38,168–170]

Scattering experiments can also be combined with complementary characterisation techniques to correlate time points. SAXS can be combined with rheology, polarised light imaging, differential scanning calorimetry (DSC) and CD. By integrating these techniques, a further understanding of gel systems that would be impossible to obtain from a single static measurement is possible, capturing both the temporal and structural evolution of the material.

At a similar length scale, microscopy techniques such as SEM and TEM are commonly used to obtain information on the nanoscale/microscale structure of gels.[158] These imaging techniques provide insight into the 3D network morphology through visual evidence of the fibrous or porous architecture characteristic of gels.[158,171] However, artefacts are often introduced during sample preparation, as drying is required, which can alter the observed morphologies, leading to significant structural discrepancies between the imaged morphology and that of the hydrated gel.[158,163,171] Furthermore, since *in situ* images cannot be collected with these techniques, scattering methods that can be used are often preferable for more accurate data.

Both techniques use a focused electron beam. In TEM, a high-energy beam is transmitted through an ultrathin sample, where the electrons are scattered or absorbed depending on the material's density and thickness, producing contrast

in the resulting image. Electromagnetic lenses focus the transmitted electrons to form a magnified image on a fluorescent screen or digital detector.[172]

SEM images the surface of a material by scanning the electron beam across its exterior.[172] The electrons interact with atoms at or near the surface, causing the emission of secondary electrons. These electrons are detected to form high-resolution, 3D images of the surface topography. SEM typically requires conductive samples or a thin conductive coating to prevent charging under the electron beam.[172] Unlike TEM, SEM samples can be bulkier and thicker; however, both require a high vacuum to prevent electron scattering by air molecules, which means samples must be dried before imaging, introducing uncertainty about whether the observed morphology accurately reflects the hydrated gel state.[171,172]

Cyro-EM can be used to overcome the drying issues associated with conventional TEM and to resolve structures on a much smaller length scale, down to near-atomic resolution.[150] By rapidly vitrifying the sample, the self-assembled nanostructures are preserved, allowing direct observation of the fundamental packing in the gel fibres without artefacts.[150]

Confocal laser scanning microscopy has also gained popularity for imaging gels, as it is a non-destructive technique that allows high-resolution imaging in their hydrated state and enables 3D imaging *via* z-stacks. [27,158,173,174] Images are acquired by scanning a focused laser beam through a pinhole aperture across a sample, thereby detecting only light from a specific focal plane to produce high-resolution, often 3D images (Figure 1.16).[173,174] By adding fluorescence tags or dyes to the gel, visual information on the distribution and organisation of fibres within the gel network can be obtained, and the homogeneity of the network can be observed.[144,173] *In situ* images can also be taken during a gel's structural evolution during gelation.[175] In the biological field, confocal microscopy is a well-established technique that has been used to image protein aggregation, cellular structures, and dynamic processes within live cells.[174] Although the spatial resolution of confocal microscopy is lower than that of SEM or TEM due to the diffraction limit of light, it offers a significant advantage in enabling imaging of hydrated, dynamic systems.[144,174]

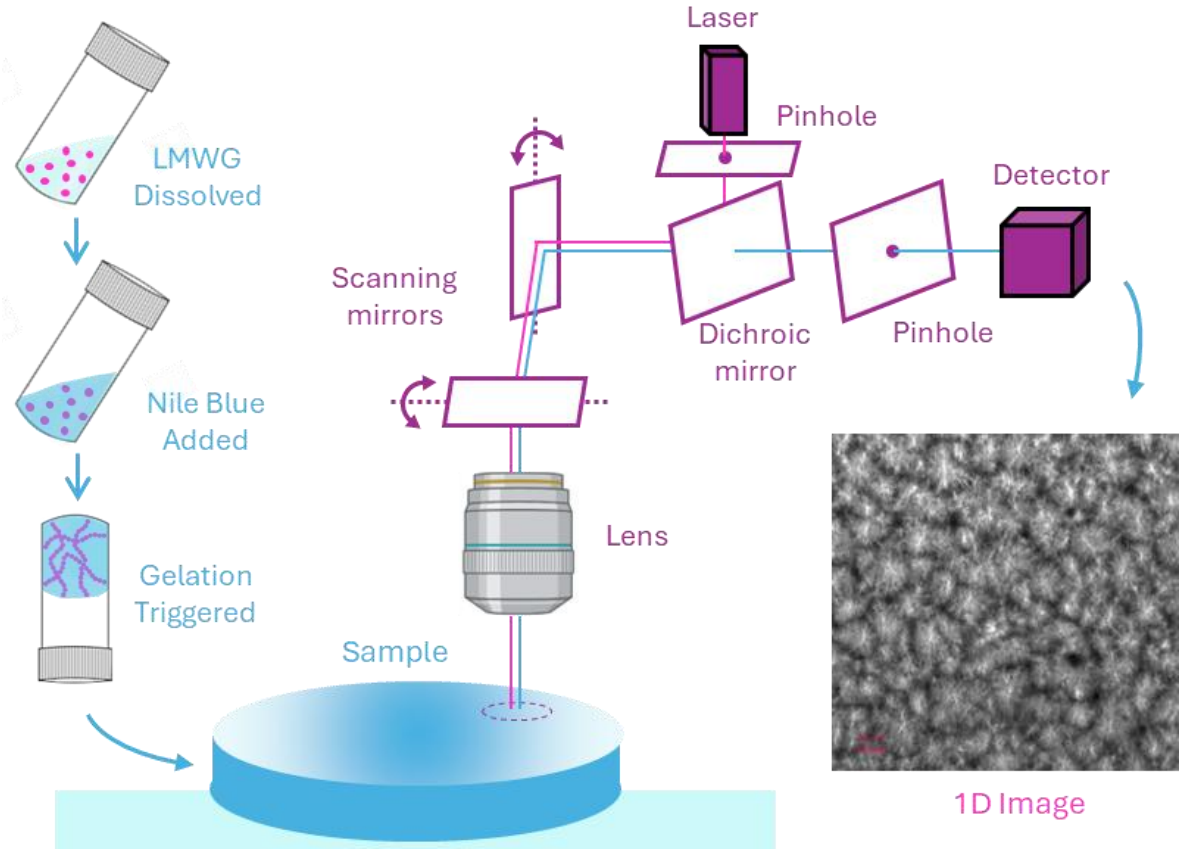

Figure 1.16. Schematic of a confocal microscopy experiment used to study LMWG gels. A focused laser beam scans the gel containing a dye, and the fluorescence signals are collected to generate images of the self-assembled network.

Confocal microscopy typically requires the addition of a dye or fluorophore during gel preparation/synthesis, and the method chosen can influence data quality. If a dye is selected, it must successfully integrate into the gel network during formation.[143,174] Alternatively, a fluorophore can be attached to the LMWG, ensuring uniform distribution throughout the network; however, this approach carries the risk of altering the self-assembly behaviour, as the fluorophore can affect the molecular interactions.[176] Similar but typically less pronounced effects can also occur when small-molecule dyes are introduced. In this work, although the capping groups naphthalene and Fmoc are fluorescent, their emission profiles can be quenched or altered upon gelation.[177] Therefore, nile blue A was selected as the fluorescent probe for all confocal imaging experiments due to its strong contrast and its previous reliable integration into the LMWG network without significantly disrupting the gelation process.[143,144]

The primary interest in gels for practical applications lies in their macroscopic properties, particularly their viscoelastic behaviour, which can be measured

through rheological measurements.[178] Standard rheology provides information about the gel's stiffness, elasticity, and flow behaviour by measuring its deformation and flow response under an applied force, which can be correlated to its macroscopic performance.[179]

Rheology is typically measured using a rheometer, an instrument that applies controlled deformations or stresses to a material and measures its mechanical response.[180] The most common approach for gels is oscillatory shear rheology, in which a small-amplitude sinusoidal strain is applied to a sample, and the resulting stress response is recorded.[180] The sample is placed between two geometries, such as parallel plates, a cone-and-plate, or a cup-and-vane (Figure 1.17a-b), with a carefully controlled gap to measure uniform deformation.[179,180]

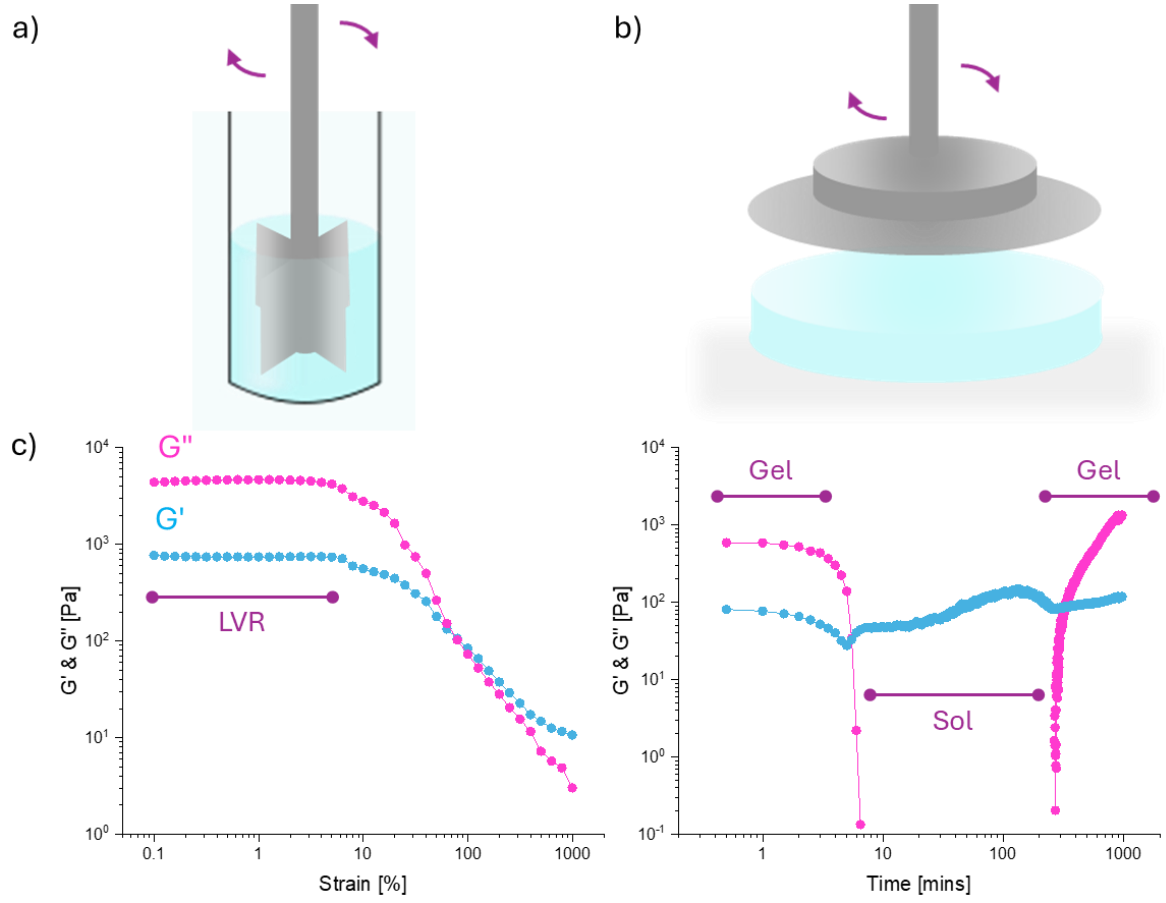

Figure 1.17. Schematic of cup and vane (a) and parallel plate/cone plate (b) geometries used for rheological measurements. c) Example of a typical strain sweep and typical time sweeps (right), showing the LVR and gel phases.

The cup-and-vane geometry is preferred because it minimises loading artefacts and slippage during measurements and allows full penetration into the gel,

providing more information on a material's bulk properties than plate geometries do. However, depending on the gel preparation method, it is not always possible to prepare gels within a vial; in such cases, plate geometries are preferred to avoid transferring or disturbing the material.[181,182]

The shear storage modulus (G′) and the loss modulus (G″) are obtained, where G′ is an indication of the stiffness of a material and is a measure of the energy stored during deformation.[180] G″ is an indication of how viscous a gel is, often called the liquid-like behaviour of a gel, and is a measure of the energy dissipated by a gel during shear.[178,179] When considered together, if G′ > G″, the gel behaves more as an elastic solid, and if G′ < G″, the gel behaves more as a viscous liquid.[178,179] The ratio of G″ to G′ is defined as the damping factor (tanδ) and quantifies the viscoelastic nature of the gel.[180] A true gel is defined as a system where tanδ ≤ 0.1, indicating that G′ is approximately an order of magnitude greater than G″ and that the material behaves primarily as an elastic solid.[179]

Rheology can be monitored as a function of strain, frequency, or time, each providing insight into different aspects of gel behaviour.[180] For instance, the linear viscoelastic region (LVR), in which G′ and G″ are independent of strain, can be observed when G′ and G″ are measured as functions of strain (Figure 1.17c).[180] Within the LVR, the gel structure remains undisturbed, and the measured G′ and G″ values reflect the material's properties.[179,180] True gels show frequency-independent behaviour if the strain is kept within this region.[178]

The rheological measurements described above are most suitable for non-transient hydrogels, where the structure remains stable during analysis. However, when applied to transient gels, such measurements provide only a snapshot of the gel's properties at a given time and fail to capture the system's dynamic evolution.[95,183] To address this, time-sweep rheology is employed to monitor the evolution of mechanical properties during gelation or structural transitions over time (Figure 1.17c). Bianco *et al*. demonstrated that performing time-sweep rheology on a transient system can be an effective tool for monitoring mechanical properties and phase changes.[183] G′ and G″ are recorded under constant values of angular frequency and applied strain over time, where values of angular frequency and applied strain can be determined from regular strain and frequency

sweeps.[183,184] This method has shown reliable results and correlates visually with the point at which the gel becomes self-supporting.[183]

In addition to oscillatory tests, steady shear experiments can be performed to measure viscosity and yield stress by applying a constant shear rate or stress and recording the resulting flow behaviour.[180] Although viscosity measurements are applied to pre-gel solutions rather than gels, they provide complementary information.[184,185] Viscosity data can indicate the type of nanostructures present in the pre-gel solutions. Spherical micelles typically exhibit low viscosity, whereas worm-like micelles display significantly higher viscosity and exhibit shear-thinning behaviour.[71,185]

Beyond conventional rheology, cavitation rheology provides a method of probing local mechanical properties of soft materials at smaller length scales.[186,187] This technique is advantageous when gels are too small to be measured using a standard rheometer or when transferring the sample would disrupt its structure.[186] A fine needle is inserted into the material, and air is injected at a controlled rate to form a cavity. As internal pressure increases, the material initially deforms elastically until a critical pressure is reached, at which point cavitation occurs. This critical pressure is directly related to the material's elastic modulus and toughness, allowing estimation of local stiffness.[186] Unlike bulk rheology, which measures an average response across the entire sample, cavitation rheology provides spatially resolved measurements, allowing the analysis of heterogeneous or small gels.[186,187] It can also reveal the gel's response to internal stresses, which is difficult to capture using standard rheological methods.[187]

Another complementary method is nanoindentation, which, like cavitation rheology, is a localised technique suited to micron-scale, one-dimensional samples where bulk rheology is impractical.[188] It is often used to probe the hardness and elasticity of gel networks at a much smaller length scale, providing data on the local modulus of the gel and how mechanical properties vary across different regions of the sample.[79,188] Similar to cavitation rheology, this method is particularly beneficial for small or highly heterogeneous gels.

1.16. Aims of thesis

There are various methods for forming supramolecular hydrogels, which yield novel materials with properties useful for a wide range of applications. However, difficulties in designing LMWGs systems for a particular application pose an undeniable challenge. This thesis aims to further expand the understanding of three methods of forming different materials.

In Chapter 2, we establish plasma-induced *in situ* 3D printing of hydrogels. The CAP parameters are investigated, and using Kineticolor and HPLC, the mechanism of plasma-induced gelation is shown to be pH-driven. Complex, patterned, and layered hydrogels are printed, and their mechanical properties are characterised. Finally, plasma-induced gelation and plasma-induced formation of gold nanoparticles are combined to simultaneously form hydrogels containing gold nanoparticles.

In Chapter 3, we explore the design and control of transient hydrogels using DMSO/H_2O gels containing urea/urease and methyl formate to induce a pH-induced state change. The scope of the system is expanded by testing different LMWGs. Methyl formate is also substituted with ethyl and *n*-propyl formate to control state transitions *via* slower formate hydrolysis. Finally, the temperature effects and ageing of the system are measured to gain further insight into the applicability of these materials for applications.

In Chapter 4, the same urea/urease and methyl formate pH triggers used in Chapter 3 are incorporated into a monoolein/oleic acid system to trigger a phase change. Using flow-through SAXS, the following transitions were successfully realised: *Pn3m*-to-H_{II}, H_{II}-to-*Im3m*, and H_{II}-to-*Im3m*-to-H_{II}, and the effect of the phase transitions on the materials' macroscopic properties is investigated.

Finally, in Chapter 5, we fabricate carbazole-functionalised amino acid-based hydrogels using electrogelation, and the resulting materials are electropolymerised. These electrochemical processes of self-assembly and polymerisation are examined using *in situ* EC-SAXS.

1.17. References

1 K. Almdal, J. Dyre, S. Hvidt and O. Kramer, *Polym. Gels Netw.*, 1993, **1**, 5–17.

2 J. Stergar and U. Maver, *J. Solgel Sci. Technol.*, 2016, **77**, 738–752.

3 A. Tirella, G. Mattei and A. Ahluwalia, *J. Biomed. Mater. Res. A*, 2014, **102**, 3352–3360.

4 M. Bustamante-Torres, D. Romero-Fierro, B. Arcentales-Vera, K. Palomino, H. Magaña and E. Bucio, *Gels*, 2021, **7**, 182.

5 T. Rossow and S. Seiffert, in *Supramolecular Polymer Networks and Gels*, 2015, vol. 268, pp. 1–46.

6 L. Thomson and D. J. Adams, in *Chemoresponsive Materials*, The Royal Society of Chemistry, 2nd edn., 2022, pp. 96–128.

7 M. C. Bavya, L. George, R. Srivastava and V. Rohan K, in *Encyclopedia of Smart Materials*, Elsevier, 2019, pp. 113–144.

8 D. Gräbner and H. Hoffmann, in *Cosmetic Science and Technology*, Elsevier, 2017, pp. 471–488.

9 B. Rieß and J. Boekhoven, *ChemNanoMat*, 2018, **4**, 710–719.

10 D. Zhang, B. Ren, Y. Zhang, L. Xu, Q. Huang, Y. He, X. Li, J. Wu, J. Yang, Q. Chen, Y. Chang and J. Zheng, *J. Mater. Chem. B*, 2020, **8**, 3171–3191.

11 Z. Liu, X. Ma, J. Liu, H. Zhang and D. Fu, *Int. J. Pharm.*, 2025, **672**, 125323.

12 Y. Hong, H. Song, Y. Gong, Z. Mao, C. Gao and J. Shen, *Acta Biomater.*, 2007, **3**, 23–31.

13 L. Zeng, X. Lin, P. Li, F.-Q. Liu, H. Guo and W.-H. Li, *Prog. Org. Coat.*, 2021, **159**, 106417.

14 M. de Loos, B. L. Feringa and J. H. van Esch, *Eur. J. Org. Chem.*, 2005, **2005**, 3615–3631.

15 Z. Zhang, D. J. Young, Z. Li and X. J. Loh, *Small Methods*, 2019, **3**, 1800270.

16 B. O. Okesola and D. K. Smith, *Chem. Soc. Rev.*, 2016, **45**, 4226–4251.

17 S. Cascone and G. Lamberti, *Int. J. Pharm.*, 2020, **573**, 118803.

18 B. V. Slaughter, S. S. Khurshid, O. Z. Fisher, A. Khademhosseini and N. A. Peppas, *Adv. Mater.*, 2009, **21**, 3307–3329.

19 M. Hamidi, A. Azadi and P. Rafiei, *Adv. Drug Deliv. Rev.*, 2008, **60**, 1638–1649.

20 M. Humenik, T. Preiß, S. Gödrich, G. Papastavrou and T. Scheibel, *Mater. Today Bio*, 2020, **6**, 100045.

21 G. Fichman and E. Gazit, *Acta Biomater.*, 2014, **10**, 1671–1682.

22 M. Patenaude, N. M. B. Smeets and T. Hoare, *Macromol. Rapid Commun.*, 2014, **35**, 598–617.

23 X. Y. Liu, in *Low Molecular Mass Gelator. Topics in Current Chemistry*, Springer, 2005, vol. 256, pp. 1–37.

24 B. N. Narasimhan, G. S. Deijs, S. Manuguri, M. S. H. Ting, M. A. K. Williams and J. Malmström, *Nanoscale Adv.*, 2021, **3**, 2934–2947.

25 T. Saydé, O. El Hamoui, B. Alies, K. Gaudin, G. Lespes and S. Battu, *Nanomaterials*, 2021, **11**, 481.

26 M. J. Webber, E. A. Appel, E. W. Meijer and R. Langer, *Nat. Mater.*, 2016, **15**, 13–26.

27 E. R. Draper and D. J. Adams, *Chem*, 2017, **3**, 390–410.

28 R. Dong, Y. Pang, Y. Su and X. Zhu, *Biomater. Sci.*, 2015, **3**, 937–954.

29 J. Raeburn and D. J. Adams, *Chem. Commun.*, 2015, **51**, 5170–5180.

30 F. Delbecq, R. Nguyen, E. Van Hecke and C. Len, *J. Mol. Liq.*, 2019, **295**, 111708.

31 G. M. Peters and J. T. Davis, *Chem. Soc. Rev.*, 2016, **45**, 3188–3206.

32 K. Trickett and J. Eastoe, *Adv. Colloid Interface Sci.*, 2008, **144**, 66–74.

33 S. Datta and S. Bhattacharya, *Chem. Soc. Rev.*, 2015, **44**, 5596–5637.

34 R. N. Mitra, D. Das, S. Roy and P. K. Das, *J. Phys. Chem. B*, 2007, **111**, 14107–14113.

35 B. Ding, Y. Li, M. Qin, Y. Ding, Y. Cao and W. Wang, *Soft Matter*, 2013, **9**, 4672.

36 C. Colquhoun, E. R. Draper, R. Schweins, M. Marcello, D. Vadukul, L. C. Serpell and D. J. Adams, *Soft Matter*, 2017, **13**, 1914–1919.

37 J. Raeburn, A. Zamith Cardoso and D. J. Adams, *Chem. Soc. Rev.*, 2013, **42**, 5143.

38 D. J. Adams, L. M. Mullen, M. Berta, L. Chen and W. J. Frith, *Soft Matter*, 2010, **6**, 1971.

39 T. C. Holmes, S. de Lacalle, X. Su, G. Liu, A. Rich and S. Zhang, *Proc. Natl. Acad. Sci. U. S. A.*, 2000, **97**, 6728–6733.

40 R. Vegners, I. Shestakova, I. Kalvinsh, R. M. Ezzell and P. A. Janmey, *J. Pept. Sci.*, 1995, **1**, 371–378.

41 Y. Zhang, H. Gu, Z. Yang and B. Xu, *J. Am. Chem. Soc.*, 2003, **125**, 13680–13681.

42 Z. Yang, G. Liang, M. Ma, Y. Gao and B. Xu, *J. Mater. Chem.*, 2007, **17**, 850–854.

43 P. Dastidar, *Chem. Soc. Rev.*, 2008, **37**, 2699.

44 K. McAulay, B. Dietrich, H. Su, M. T. Scott, S. Rogers, Y. K. Al-Hilaly, H. Cui, L. C. Serpell, A. M. Seddon, E. R. Draper and D. J. Adams, *Chem. Sci.*, 2019, **10**, 7801–7806.

45 S. R. S. Veloso, M. Rosa, C. Diaferia and C. Fernandes, *Gels*, 2024, **10**, 507.

46 S. Fleming, S. Debnath, P. W. J. M. Frederix, T. Tuttle and R. V. Ulijn, *Chem. Commun.*, 2013, **49**, 10587.

47 S. M. M. Reddy, P. Dorishetty, G. Augustine, A. P. Deshpande, N. Ayyadurai and G. Shanmugam, *Langmuir*, 2017, **33**, 13504–13514.

48 L. Li, L. Xie, R. Zheng and R. Sun, *Front. Chem.*, 2021, **9**, 739791.

49 A. L. Ferguson and J. D. Tovar, *Langmuir*, 2022, **38**, 15463–15475.

50 D. J. Adams, *Macromol. Biosci.*, 2011, **11**, 160–173.

51 K. Tao, A. Levin, L. Adler-Abramovich and E. Gazit, *Chem. Soc. Rev.*, 2016, **45**, 3935–3953.

52 L. Chen, S. Revel, K. Morris, L. C. Serpell and D. J. Adams, *Langmuir*, 2010, **26**, 13466–13471.

53 A. M. Smith, R. J. Williams, C. Tang, P. Coppo, R. F. Collins, M. L. Turner, A. Saiani and R. V. Ulijn, *Adv. Mater.*, 2008, **20**, 37–41.

54 X. Du, J. Zhou, J. Shi and B. Xu, *Chem. Rev.*, 2015, **115**, 13165–13307.

55 D. M. Ryan and B. L. Nilsson, *Polym. Chem.*, 2012, **3**, 18–33.

56 Y. Tian, J. Li, A. Wang, Q. Li, H. Jian and S. Bai, *Macromol. Biosci.*, 2023, **23**, 2300171.

57 Z. Yang, G. Liang and B. Xu, *Acc. Chem. Res.*, 2008, **41**, 315–326.

58 A. Mahler, M. Reches, M. Rechter, S. Cohen and E. Gazit, *Adv. Mater.*, 2006, **18**, 1365–1370.

59 J. H. Collier, B. Hu, J. W. Ruberti, J. Zhang, P. Shum, D. H. Thompson and P. B. Messersmith, *J. Am. Chem. Soc.*, 2001, **123**, 9463–9464.

60 L. Chen, T. O. McDonald and D. J. Adams, *RSC Adv.*, 2013, **3**, 8714.

61 E. R. Draper and D. J. Adams, in *Chemoresponsive Materials: Stimulation by Chemical and Biological Signals*, The Royal Society of Chemistry, 2015, pp. 332–363.

62 N. Raßmann, M. Weber, R. E. J. Glaß, K. Kreger, N. Helfricht, H.-W. Schmidt and G. Papastavrou, *Langmuir*, 2023, **39**, 17190–17200.

63 L. Chen, K. Morris, A. Laybourn, D. Elias, M. R. Hicks, A. Rodger, L. Serpell and D. J. Adams, *Langmuir*, 2010, **26**, 5232–5242.

64 S. Panja, C. Patterson and D. J. Adams, *Macromol. Rapid Commun.*, 2019, **40**, 1900251.

65 V. Nele, J. P. Wojciechowski, J. P. K. Armstrong and M. M. Stevens, *Adv. Funct. Mater.*, 2020, **30**, 2002759.

66 J. Raeburn, G. Pont, L. Chen, Y. Cesbron, R. Lévy and D. J. Adams, *Soft Matter*, 2012, **8**, 1168–1174.

67 N. A. Dudukovic and C. F. Zukoski, *Soft Matter*, 2014, **10**, 7849–7856.

68 L. Chen, J. Raeburn, S. Sutton, D. G. Spiller, J. Williams, J. S. Sharp, P. C. Griffiths, R. K. Heenan, S. M. King, A. Paul, S. Furzeland, D. Atkins and D. J. Adams, *Soft Matter*, 2011, **7**, 9721.

69 H. Zhang, P. Ren, H. Wei, S. Halila, A. R. Osi, Y. Zhou, Z. Dai, R. Wang and J. Chen, *Soft Matter*, 2020, **16**, 8647–8654.

70 S. Roldán-Vargas, F. Smallenburg, W. Kob and F. Sciortino, *Sci. Rep.*, 2013, **3**, 2451.

71 E. R. Draper, H. Su, C. Brasnett, R. J. Poole, S. Rogers, H. Cui, A. Seddon and D. J. Adams, *Angew. Chem. Int. Ed.*, 2017, **56**, 10467–10470.

72 A. Z. Cardoso, L. L. E. Mears, B. N. Cattoz, P. C. Griffiths, R. Schweins and D. J. Adams, *Soft Matter*, 2016, **12**, 3612–3621.

73 S. C. Bremmer, A. J. McNeil and M. B. Soellner, *Chem. Commun.*, 2014, **50**, 1691.

74 D. J. Adams, M. F. Butler, W. J. Frith, M. Kirkland, L. Mullen and P. Sanderson, *Soft Matter*, 2009, **5**, 1856.

75 C. Tang, A. M. Smith, R. F. Collins, R. V. Ulijn and A. Saiani, *Langmuir*, 2009, **25**, 9447–9453.

76 C. Patterson, S. Panja, W. Liu, A. R. Mount, A. Squires and D. J. Adams, *Mater. Chem. Front.*, 2023, **7**, 2671–2675.

77 J. Zhang, K. Jin, Y. Xiao, Y. Feng, D. Lu, M. Chen, M. Sun, D. Wang, C. Jin, Z. Li and Y. Wang, *Macromol. Rapid Commun.*, 2025, **46**, 2401156.

78 S. Sutton, N. L. Campbell, A. I. Cooper, M. Kirkland, W. J. Frith and D. J. Adams, *Langmuir*, 2009, **25**, 10285–10291.

79 E. R. Draper, L. L. E. Mears, A. M. Castilla, S. M. King, T. O. McDonald, R. Akhtar and D. J. Adams, *RSC Adv.*, 2015, **5**, 95369–95378.

80 A. Aggeli, M. Bell, L. M. Carrick, C. W. G. Fishwick, R. Harding, P. J. Mawer, S. E. Radford, A. E. Strong and N. Boden, *J. Am. Chem. Soc.*, 2003, **125**, 9619–9628.

81 A. Mata, L. Hsu, R. Capito, C. Aparicio, K. Henrikson and S. I. Stupp, *Soft Matter*, 2009, **5**, 1228.

82 J. Li, S. Wu, E. Kim, K. Yan, H. Liu, C. Liu, H. Dong, X. Qu, X. Shi, J. Shen, W. E. Bentley and G. F. Payne, *Biofabrication*, 2019, **11**, 032002.

83 K. Ino, F. Ozawa, N. Dang, K. Hiramoto, S. Hino, R. Akasaka, Y. Nashimoto and H. Shiku, *Adv. Biosyst.*, 2020, **4**, 1900234.

84 C. Patterson, B. Dietrich, C. Wilson, A. R. Mount and D. J. Adams, *Soft Matter*, 2022, **18**, 1064–1070.

85 Q. Lu, Y. Huang, M. Li, B. Zuo, S. Lu, J. Wang, H. Zhu and D. L. Kaplan, *Acta Biomater.*, 2011, **7**, 2394–2400.

86 K. Yan, Y. Xiong, S. Wu, W. E. Bentley, H. Deng, Y. Du, G. F. Payne and X.-W. Shi, *ACS Appl. Mater. Interfaces*, 2016, **8**, 19780–19786.

87 Y. Cheng, X. Luo, J. Betz, G. F. Payne, W. E. Bentley and G. W. Rubloff, *Soft Matter*, 2011, **7**, 5677.

88 Y. Liu, Y. Cheng, H.-C. Wu, E. Kim, R. V. Ulijn, G. W. Rubloff, W. E. Bentley and G. F. Payne, *Langmuir*, 2011, **27**, 7380–7384.

89 K. McAulay, L. Thomson, L. Porcar, R. Schweins, N. Mahmoudi, D. J. Adams and E. R. Draper, *Org. Mater.*, 2020, **2**, 108–115.

90 E. K. Johnson, D. J. Adams and P. J. Cameron, *J. Mater. Chem.*, 2011, **21**, 2024–2027.

91 E. K. Johnson, L. Chen, P. S. Kubiak, S. F. McDonald, D. J. Adams and P. J. Cameron, *Chem. Commun.*, 2013, **49**, 8698.

92 Y. Zou, Y. Zhong, H. Li, F. Ding and X. Shi, *Curr. Med. Chem.*, 2020, **27**, 2610–2630.

93 K. M. Gray, B. D. Liba, Y. Wang, Y. Cheng, G. W. Rubloff, W. E. Bentley, A. Montembault, I. Royaud, L. David and G. F. Payne, *Biomacromolecules*, 2012, **13**, 1181–1189.

94 P. S. Kubiak, S. Awhida, C. Hotchen, W. Deng, B. Alston, T. O. McDonald, D. J. Adams and P. J. Cameron, *Chem. Commun.*, 2015, **51**, 10427–10430.

95 M. Tena-Solsona, B. Rieß, R. K. Grötsch, F. C. Löhrer, C. Wanzke, B. Käsdorf, A. R. Bausch, P. Müller-Buschbaum, O. Lieleg and J. Boekhoven, *Nat. Commun.*, 2017, **8**, 15895.

96 P. Innocenzi, *The Sol to Gel Transition*, Springer International Publishing, 1st edn., 2016, pp. 1-6.

97 J. Boekhoven, W. E. Hendriksen, G. J. M. Koper, R. Eelkema and J. H. van Esch, *Science*, 2015, **349**, 1075–1079.

98 A. D. Drozdov, *Int. J. Eng. Sci.*, 2018, **128**, 79–100.

99 S. Dhiman, K. Jalani and S. J. George, *ACS Appl. Mater. Interfaces*, 2020, **12**, 5259–5264.

100 S. Panja, K. Boháčová, B. Dietrich and D. J. Adams, *Nanoscale*, 2020, **12**, 12840–12848.

101 S. Panja and D. J. Adams, *Chem. Commun.*, 2019, **55**, 10154–10157.

102 B. Rieß, R. K. Grötsch and J. Boekhoven, *Chem*, 2020, **6**, 552–578.

103 M. Reches and E. Gazit, *Nat. Nanotechnol.*, 2006, **1**, 195–200.

104 C. G. Pappas, I. R. Sasselli and R. V. Ulijn, *Angewandte Chemie*, 2015, **127**, 8237–8241.

105 S. Debnath, S. Roy and R. V. Ulijn, *J. Am. Chem. Soc.*, 2013, **135**, 16789–16792.

106 E. Jee, T. Bánsági, A. F. Taylor and J. A. Pojman, *Angewandte Chemie*, 2016, **128**, 2167–2171.

107 S. Panja, A. M. Fuentes-Caparrós, E. R. Cross, L. Cavalcanti and D. J. Adams, *Chem. Mater.*, 2020, **32**, 5264–5271.

108 M. Kumar, D. Sementa, V. Narang, E. Riedo and R. V. Ulijn, *Chem. A Eur. J.*, 2020, **26**, 8372–8376.

109 S. Panja and D. J. Adams, *Giant*, 2021, **5**, 100041.

110 E. R. Draper, T. O. McDonald and D. J. Adams, *Chem. Commun.*, 2015, **51**, 6595–6597.

111 J. R. Moffat and D. K. Smith, *Chem. Commun.*, 2008, 2248.

112 F. Rodríguez-Llansola, J. F. Miravet and B. Escuder, *Chem. Commun.*, 2009, 209–211.

113 M. M. Smith and D. K. Smith, *Soft Matter*, 2011, **7**, 4856.

114 M. Lescanne, P. Grondin, A. d'Aléo, F. Fages, J.-L. Pozzo, O. M. Monval, P. Reinheimer and A. Colin, *Langmuir*, 2004, **20**, 3032–3041.

115 S. Panja and D. J. Adams, *Chem. Soc. Rev.*, 2021, **50**, 5165–5200.

116 L. H. El-Qarra, N. Cosottini, C. Tangsombun and D. K. Smith, *Chem. Eur. J.*, 2024, **30**, e202402530.

117 N. A. Dudukovic and C. F. Zukoski, *J. Chem. Phys.*, 2014, **141**, 164905.

118 J. Shi, Y. Gao, Z. Yang and B. Xu, *Beilstein J. Org. Chem.*, 2011, **7**, 167–172.

119 D. K. Duraisamy, P. D. Sureshbhai, P. Saveri, A. P. Deshpande and G. Shanmugam, *Chem. Commun.*, 2022, **58**, 13377–13380.

120 S. Basak, N. Nandi, S. Paul, I. W. Hamley and A. Banerjee, *Chem. Commun.*, 2017, **53**, 5910–5913.

121 A. M. Castilla, M. Wallace, L. L. E. Mears, E. R. Draper, J. Doutch, S. Rogers and D. J. Adams, *Soft Matter*, 2016, **12**, 7848–7854.

122 D. Basumatary, P. Bhatt and K. Sankaranarayanan, *Langmuir*, 2025, **41**, 12052–12063.

123 P. Bhatt, P. Das and K. Sankaranarayanan, *Phys. Chem. Chem. Phys.*, 2025, **27**, 24969-24985.

124 G. Eazhumalai, R. G. T. K. and U. S. Annapure, *Sustain. Food Technol.*, 2025, **3**, 1203–1217.

125 S. Zhang, W. Huang, E. Feizollahi, M. S. Roopesh and L. Chen, *Innov. Food Sci. Emerg. Technol.*, 2021, **67**, 102567.

126 R. Molina, P. Jovancic, S. Vilchez, T. Tzanov and C. Solans, *Carbohydr. Polym.*, 2014, **103**, 472–479.

127 F. Rezaei, P. Vanraes, A. Nikiforov, R. Morent and N. De Geyter, *Mater.*, 2019, **12**, 2751.

128 T. F. de Melo, L. C. Rocha, R. P. Silva, R. S. Pessoa, A. M. P. Negreiros, R. Sales Júnior, M. B. Tavares and C. Alves Junior, *Mater.*, 2022, **15**, 4854.

129 Z. Chen and R. E. Wirz, *in Cold Atmospheric Plasma (CAP) Technology and Applications*, Morgan and Claypool, 2021, 71-82.

130 J. Raeburn, T. O. McDonald and D. J. Adams, *Chem Commun.*, 2012, **48**, 9355.

131 D. J. Cornwell, O. J. Daubney and D. K. Smith, *J. Am. Chem. Soc.*, 2015, **137**, 15486–15492.

132 P. R. A. Chivers and D. K. Smith, *Nat. Rev. Mater.*, 2019, **4**, 463–478.

133 X. Le, W. Lu, J. Zheng, D. Tong, N. Zhao, C. Ma, H. Xiao, J. Zhang, Y. Huang and T. Chen, *Chem. Sci.*, 2016, **7**, 6715–6720.

134 D. Ghosh, R. Huang, N. Mahmoudi, L. Matthews, C. Patterson, C. Holland, M. Vassalli and D. J. Adams, *Mol. Syst. Des. Eng.*, 2025, **10**, 922–932.

135 M. C. Nolan, A. M. Fuentes Caparrós, B. Dietrich, M. Barrow, E. R. Cross, M. Bleuel, S. M. King and D. J. Adams, *Soft Matter*, 2017, **13**, 8426–8432.

136 Y. Hui, Y. Yao, Q. Qian, J. Luo, H. Chen, Z. Qiao, Y. Yu, L. Tao and N. Zhou, *Nat. Electron.*, 2022, **5**, 893–903.

137 M. E. Prendergast and J. A. Burdick, *Adv. Mater.*, 2019, **32**, 1902516.

138 A. C. Dell, G. Wagner, J. Own and J. P. Geibel, *Pharmaceutics*, 2022, **14**, 2596.

139 E. Mancha Sánchez, J. C. Gómez-Blanco, E. López Nieto, J. G. Casado, A. Macías-García, M. A. Díaz Díez, J. P. Carrasco-Amador, D. Torrejón Martín, F. M. Sánchez-Margallo and J. B. Pagador, *Front. Bioeng. Biotechnol.*, 2020, **8**, 776.

140 F. Andriamiseza, D. Bordignon, B. Payré, L. Vaysse and J. Fitremann, *J. Colloid Interface Sci.*, 2022, **617**, 156–170.

141 H. Jian, M. Wang, Q. Dong, J. Li, A. Wang, X. Li, P. Ren and S. Bai, *ACS Appl. Mater. Interfaces*, 2019, **11**, 46419–46426.

142 R. E. Ginesi, J. Doutch and E. R. Draper, *Faraday Discuss.*, 2025, **260**, 347–359.

143 M. J. S. Hill, A. M. Fuentes-Caparrós and D. J. Adams, *Biomacromolecules*, 2023, **24**, 4253–4262.

144 M. J. S. Hill and D. J. Adams, *Soft Matter*, 2022, **18**, 5960–5965.

145 N. Zhang, Y. Wang, J. Zhang, J. Guo and J. He, *Acta Biomater.*, 2021, **135**, 304–317.

146 A. Chalard, M. Mauduit, S. Souleille, P. Joseph, L. Malaquin and J. Fitremann, *Addit. Manuf.*, 2020, **33**, 101162.

147 X. Mu, J. K. Sahoo, P. Cebe and D. L. Kaplan, *Polymers (Basel).*, 2020, **12**, 2936.

148 B. Derby, *Annu. Rev. Mater. Res.*, 2010, **40**, 395–414.

149 Z. Wang, H. Kumar, Z. Tian, X. Jin, J. F. Holzman, F. Menard and K. Kim, *ACS Appl. Mater. Interfaces*, 2018, **10**, 26859–26869.

150 R. R. Sonani, S. Bianco, B. Dietrich, J. Doutch, E. R. Draper, D. J. Adams and E. H. Egelman, *Cell Rep. Phys. Sci.*, 2024, **5**, 101812.

151 N. Ikeda and K. Aramaki, *J. Oleo Sci.*, 2023, **72**, ess23011.

152 R. S. Tu and M. Tirrell, *Adv. Drug Deliv. Rev.*, 2004, **56**, 1537–1563.

153 J. Nanda, A. Biswas and A. Banerjee, *Soft Matter*, 2013, **9**, 4198.

154 C. A. Dreiss, *Soft Matter*, 2007, **3**, 956.

155 M. Takeuchi, M. Iriguchi, M. Hattori, E. Kim, A. Ichikawa, Y. Hasegawa, Q. Huang and T. Fukuda, *Biomed. Mater.*, 2020, **15**, 055001.

156 L. F. McGarry, O. El-Zubir, P. G. Waddell, F. Cucinotta, A. Houlton and B. R. Horrocks, *Soft Matter*, 2023, **19**, 8386–8402.

157 R. E. Ginesi, N. R. Murray, R. M. Dalgliesh, J. Doutch and E. R. Draper, *Chem. Eur. J.*, 2023, **29**, e202301042.

158 C. R. M. MacDonald and E. R. Draper, *Beilstein J. Org. Chem*, 2024, **20**, 2608–2634.

159 E. Hughes, N. S. O'Neill and R. Schweitzer-Stenner, *J. Phys. Chem. B*, 2025, **129**, 260–272.

160 Md. M. Hassan, A. D. Martin and P. Thordarson, *J. Mater. Chem. B*, 2015, **3**, 9269–9276.

161 C. Gila-Vilchez, M. C. Mañas-Torres, J. A. González-Vera, F. Franco-Montalban, J. A. Tamayo, F. Conejero-Lara, J. M. Cuerva, M. T. Lopez-Lopez, A. Orte and L. Álvarez de Cienfuegos, *Polym. Chem.*, 2021, **12**, 6832–6845.

162 E. R. Draper, K. L. Morris, M. A. Little, J. Raeburn, C. Colquhoun, E. R. Cross, Tom. O. McDonald, L. C. Serpell and D. J. Adams, *CrystEngComm*, 2015, **17**, 8047–8057.

163 L. L. E. Mears, E. R. Draper, A. M. Castilla, H. Su, Zhuola, B. Dietrich, M. C. Nolan, G. N. Smith, J. Doutch, S. Rogers, R. Akhtar, H. Cui and D. J. Adams, *Biomacromolecules*, 2017, **18**, 3531–3540.

164 H. Schnablegger and Y. Singh, *The SAXS Guide*, Anton Paar GmbH, 4th edn., 2017.

165 I. W. Hamley and V. Castelletto, *Adv. Colloid Interface Sci.*, 2023, **318**, 102959.

166 https://www.ncnr.nist.gov/resources/activation/.

167 S. Bianco, F. Hallam Stewart, S. Panja, A. Zyar, E. Bowley, M. Bek, R. Kádár, A. Terry, R. Appio, T. S. Plivelic, M. Maguire, H. Poptani, M. Marcello, R. R. Sonani, E. H. Egelman and D. J. Adams, *Nat. Synth.*, 2024, **3**, 1481–1489.

168 K. Fukao, T. Nakajima, T. Nonoyama, T. Kurokawa, T. Kawai and J. P. Gong, *Macromolecules*, 2020, **53**, 1154–1163.

169 M. Chalal, F. Ehrburger-Dolle, I. Morfin, F. Bley, M.-R. Aguilar de Armas, M.-L. López Donaire, J. San Roman, N. Bölgen, E. Pişkin, O. Ziane and R. Casalegno, *Macromolecules*, 2010, **43**, 2009–2017.

170 G. Ben Messaoud, P. Le Griel, D. Hermida-Merino and N. Baccile, *Soft Matter*, 2020, **16**, 2540–2551.

171 E. R. Draper and D. J. Adams, *Chem. Soc. Rev.*, 2018, **47**, 3395–3405.

172 B. J. Inkson, in *Materials Characterization Using Nondestructive Evaluation (NDE) Methods*, Elsevier, 2016, pp. 17–43.

173 R. Kubota, W. Tanaka and I. Hamachi, *Chem. Rev.*, 2021, **121**, 14281–14347.

174 A. R. Hibbs, *Confocal Microscopy for Biologists*, Springer US, Boston, MA, 1st edn., 2004.

175 E. L. Bowley, S. Bianco, F. H. Stewart, C. M. Wallace, R. E. Ginesi, A. S. Loch, M. Rosenthal, A. J. Smith and D. J. Adams, *ChemSystemsChem*, 2024, **7**, e202400073.

176 J. Zhong, T. Zhao and M. Liu, *NPG Asia Mater.*, 2022, **14**, 38.

177 C. Tang, R. V. Ulijn and A. Saiani, *Eur. Phys. J. E*, 2013, **36**, 111.

178 C. Yan and D. J. Pochan, *Chem. Soc. Rev.*, 2010, **39**, 3528.

179 A. Dawn and H. Kumari, *Chem. Eur. J*, 2018, **24**, 762–776.

180 T. G. Mezger, in *The Rheology Handbook For users of rotational and oscillatory rheometers*, Vincentz, 3rd edn., 2011.

181 H. A. Barnes and Q. D. Nguyen, *J. Nonnewton. Fluid Mech.*, 2001, **98**, 1–14.

182 R. Akhtar, E. R. Draper, D. J. Adams and J. Hay, *J. Mater. Res.*, 2018, **33**, 873–883.

183 S. Bianco, S. Panja and D. J. Adams, *Gels*, 2022, **8**, 132.

184 M. Kretschmer, B. Winkeljann, B. A. K. Kriebisch, J. Boekhoven and O. Lieleg, *Commun. Mater.*, 2021, **2**, 97.

185 L. Thomson, D. McDowall, L. Marshall, O. Marshall, H. Ng, J. Homer, E. Theodosiou, P. Topham, L. Serpell, R. Poole, A. Seddon and D. Adams, *ACS Nano*, 2022, **16**, 20497–20509.

186 J. A. Zimberlin, N. Sanabria-DeLong, G. N. Tew and A. J. Crosby, *Soft Matter*, 2007, **3**, 763.

187 A. M. Fuentes-Caparrós, B. Dietrich, L. Thomson, C. Chauveau and D. J. Adams, *Soft Matter*, 2019, **15**, 6340–6347.

188 G. Ciccone, M. Azevedo Gonzalez Oliva, N. Antonovaite, I. Lüchtefeld, M. Salmeron-Sanchez and M. Vassalli, *J. Vis. Exp.*, 2022, **179.**

Chapter 2 – Plasma-induced gelation and 3D printing of hydrogels

This chapter is adapted from the following paper submitted for publication:

“Cold plasma induced 3D printing of hydrogels”

Emma Bowley, Dipankar Ghosh, Dilli Padmanaban, Matthew Bieniek, Calum Fyfe, Timothy. J. McCabe, Marc Reid, Massimo Vassalli, James L. Walsh, Mohammad Hasan and Dave J. Adams

E.L. Bowley performed the rheology, viscosity, UV-vis spectroscopy, confocal microscopy, video and pH experiments. The plasma generation equipment was built by J. Walsh (University of York). D.J. Adams (University of Glasgow) synthesised the gelators under investigation. Kineticolor analysis was performed by C. Fyfe and T.J. McCabe (University of Strathclyde). L. Marshall (University of Glasgow) ran the HPLC samples. H. Futty, D Harris, and T. Maurya (University of Glasgow) and A.J. Smith (Diamond Light Source) collected and processed the SAXS data. M. Mullin (University of Glasgow) collected the TEM images.

2.1. Introduction

Supramolecular hydrogels can be formed by low molecular weight gelators (LMWGs) that self-assemble into a three-dimensional (3D) network.[1,2] Gelation is often initiated by changes in environmental conditions, such as pH.[1,3] Both the choice of LMWG and the gelation trigger influence the overall mechanical properties of the resulting material, such as stiffness, by affecting the self-assembly process and, consequently, the fibre arrangement within the network.[4–6] Various gelation triggers exist, including pH-, solvent-, temperature-, enzyme-, and salt-triggered gelation.[1–3,6–10]

New techniques for forming and shaping gels are continuously being explored to develop novel materials. Because the properties of hydrogels are determined by the underlying network, controlling this network is essential for tuning material properties and, by extension, their applications.[2,11] Achieving spatial control over gelation allows these highly adaptable materials to be fabricated into precise shapes, providing an additional level of control. This capability has driven the adoption of 3D printing in the field of hydrogels, although several other approaches for localised gelation have also been developed.[12–14] Precise gel formation at small scales is critical for many applications requiring spatial accuracy.

3D gel printing is a recent, localised gelation technique which has been used to fabricate tissue scaffolds for biomedical applications and functional devices such as biosensors and strain sensors.[15,16] Several 3D printing methods for gels exist, including direct extrusion, bath-supported extrusion, inkjet, and light-based methods, as discussed in Chapter 1.[12,14,17,18] However, these systems are limited by relatively low resolution and slow printing speeds, changes in structural and mechanical properties during printing, and low predictive accuracy for successful gelation.[12,19,20] In this chapter, plasma 3D printing is introduced as a method for forming gels *in situ*, preserving chemical properties during printing while also offering improved resolution. The gelation mechanism is pH-triggered, a process that has been extensively explored in the literature. This suggests that many known gelators could be adapted for printing with this technique if they are capable of forming pH-switch gels.

Plasma, often referred to as the fourth state of matter, is generated when a significant amount of energy is applied to a gas. In this process, electrons are detached from atoms, allowing positive and negative charges to move more freely. These electrons are then rapidly accelerated, producing additional electrons *via* collisions. When the number of free electrons becomes sufficiently high to affect the gas's electrical properties, the system is considered a plasma, or an ionised gas.[21] Plasmas can vary widely, with significant differences in temperature and density depending on the type.[21–23]

Cold atmospheric plasma (CAP) is a weakly ionised gas that can be generated at ambient temperature and pressure.[21,23] CAP is a non-equilibrium state of matter in which electrons have high energies, while ions and neutral species remain close to ambient temperature.[21,23] The plasma contains electrons, ions, radicals and reactive oxygen and nitrogen species (RONS). The most common radicals and RONS include: •O, •H, •N, •OH, •NO, H_2O_2, and O_3.[22] Because of this mix of reactive species, plasma has previously been used to drive oxidative and reductive chemical transformations, polymerisation reactions, and the controlled modification of aqueous solutions.[24,25]

CAP has been demonstrated to be a sustainable, cost-effective, and tuneable trigger for self-assembly.[26] The first instance of plasma-induced self-assembly of LMWG was reported in 2024.[23] In the current literature, plasma-mediated gelation is proposed to arise from chemical changes that alter the molecular environment, thereby enhancing non-covalent interactions and promoting self-assembly.[23,26] Plasma has been used to modify proteins, improving their properties when subsequently gelled.[27,28] In contrast, this chapter uses CAP to induce localised gelation *via* a pH-switch mechanism. When CAP is applied to a gelator solution, the resulting decrease in pH triggers gelation. These plasma-induced changes provide a means to control solution pH spatially and temporally, enabling the gelation of many chemical or physical hydrogel systems *via* pH reduction.

In this chapter, we introduce a lab-based plasma jet as a localised pH trigger to induce gelation, enabling the *in situ* 3D printing of LMWG gels. This technique is also applied to fabricate gold nanoparticle-containing gels by simultaneously processing the nanoparticles and triggering gelation.

2.2. Results and discussion

2.2.1. Plasma gelation

Initial gelation experiments were conducted using four gelators: 2NapFF, 2NapFV, 6BrNapAV, and 2NapVG. The chemical structures of these gelators are shown in Figure 2.1. Stock solutions of each gelator were prepared by dissolving the appropriate amount in deionised water containing 1 equivalent of NaOH (0.1 M), then stirring for 16 hours to obtain the desired concentration. After this period, the solutions were adjusted to pH 7 using 1 M HCl or 1 M NaOH as required.

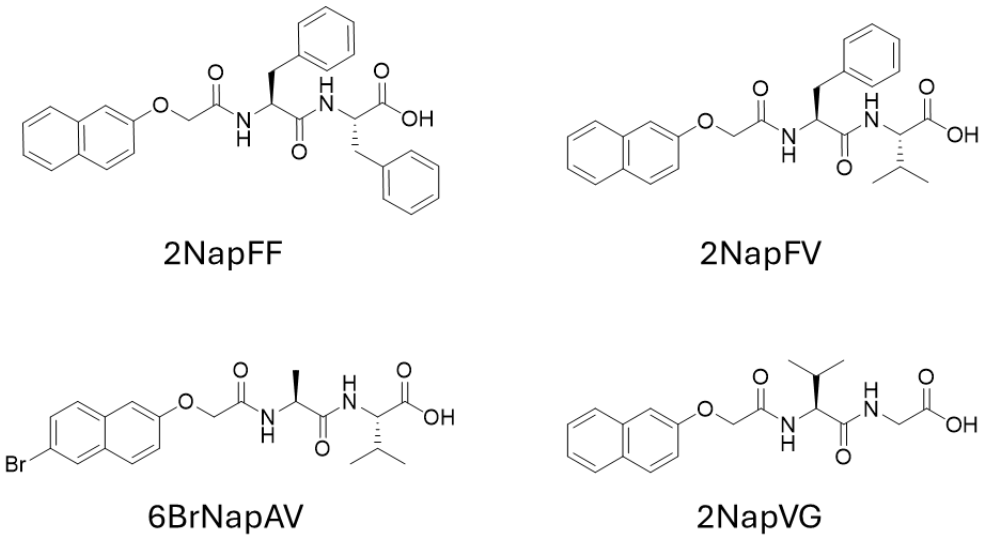

Figure 2.1. Structure of the low molecular weight gelators used in this chapter and their corresponding acronyms.

For plasma treatment, 1.5 mL of the pre-gel solution was transferred to a petri dish. The pin electrode was positioned approximately 5 mm above the solution surface, and an argon gas flow rate of 0.5 LPM (litres per minute) was used. Successful gelation was observed for 2NapFF, 2NapFV, and 6BrNapAV across all investigated concentrations. Gelation was not observed for 2NapVG under the same conditions at any concentration. Instead, the solution gradually changed from a pale yellow (due to the methyl red indicator) to a pale brown colour upon exposure to plasma for 30 minutes, in contrast to the rapid gelation observed with the other three gelators. The apparent pK_a for 2NapVG occurs at a lower pH than the other three gelators (Figure 2.2); therefore, the lack of gelation is probably because the pH has not been lowered sufficiently below the pK_a to initiate self-assembly.

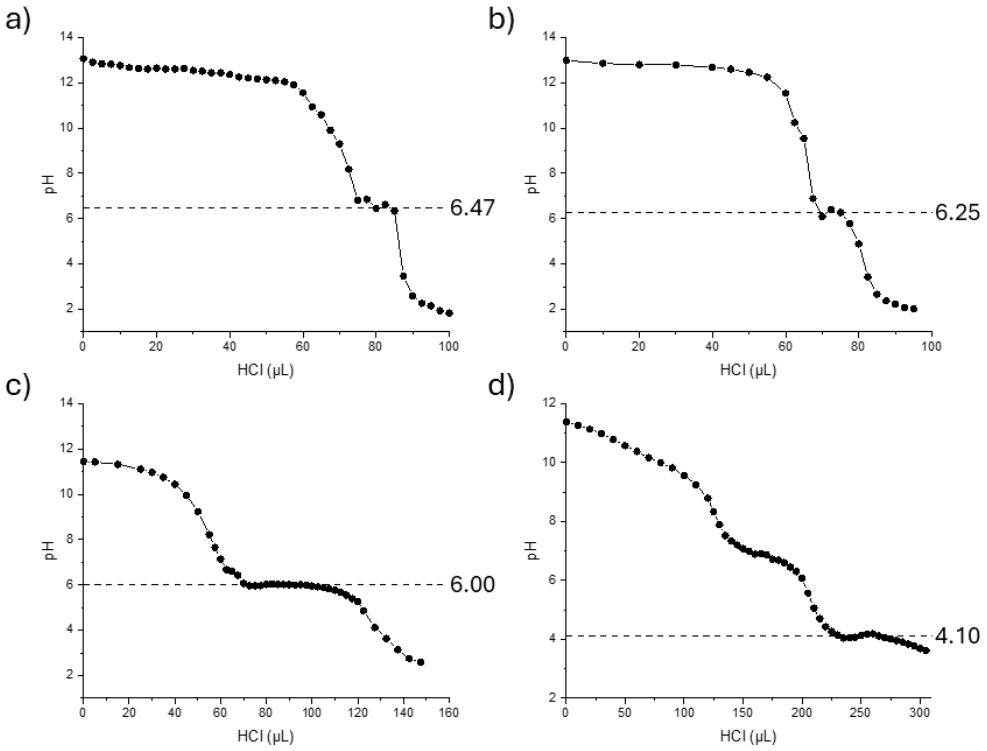

Figure 2.2. Apparent pK_a measurements for a) 2NapFF, b) 2NapFV, c) 6BrNapAV, and d) 2NapVG at 5 mg/mL and 25 °C.

It is proposed that this gelation is induced by a localised decrease in pH resulting from the flux of species generated by the plasma. Therefore, this plasma gelation mechanism is analogous to conventional pH-switching methods. All gelators used in this chapter contain a terminal carboxylic acid group, which is deprotonated at pH values above the apparent pK_a of the gelator, rendering the molecules soluble in water. At high pH, the gelators form micellar aggregates.[1] Reducing the pH below the apparent pK_a protonates the carboxylate group, triggering self-assembly into extended one-dimensional structures that subsequently form a 3D gel network.[3]

The gelators were selected based on their pre-gel aggregation states, at high pH: 2NapFF and 2NapFV form nanotubes/worm-like micelles, whereas 6BrNapAV and 2NapVG form non-persistent spherical micelles.[29–32]

For gelators that form viscous solutions containing worm-like micelles (2NapFF and 2NapFV), the plasma generated electron, ions, and RONS species interact with the solution at the plasma-liquid interface.[22] This induces a localised decrease in pH below the apparent pK_a at the plasma–solution interface, leading to the self-

assembly of worm-like micelles into extended fibrillar structures and, consequently, rapid gelation at the site of plasma exposure. (Figure 2.3).

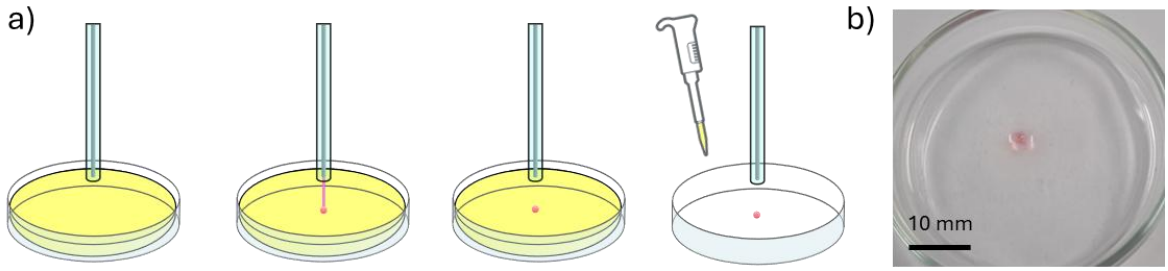

Figure 2.3. a) Schematic illustrating gelation of worm-like micellar gelator solutions. Plasma application induces localised gelation at the point of contact. Following gelation, the remaining solution can be removed with a pipette, leaving the gel behind. b) An image of gel produced from 2NapFF (5 mg/mL) with methyl red is shown.

2NapFF exhibited more rapid gelation compared to 2NapFV. This difference is attributed to the higher apparent pK_a of 2NapFF (6.47) compared to 2NapFV (6.25). As the apparent pK_a of 2NapFF is closer to the initial solution pH, a smaller decrease in pH is required to trigger protonation and subsequent self-assembly, resulting in faster gelation. The apparent pK_a values of the gelators investigated are shown in Figure 2.2.

In contrast, for gelators that form free-flowing solutions containing spherical micelles, a pink region was observed at the point of plasma contact with the solution surface. This colour change, caused by the presence of the methyl red indicator, indicates a localised decrease in pH. However, because these solutions have low viscosity, the low-pH region rapidly disperses throughout the bulk solution *via* diffusion and convection, resulting in a uniform reduction in bulk pH. As plasma exposure continued, the pH gradually decreased below the apparent pK_a of 6BrNapAV (6.00), enabling the transition from spherical micelles to worm-like micelles and eventually to a gel.

Initially, gelation proceeded slowly but accelerated as the local solution pH decreased, and diffusion and convection were limited by the self-assembled structures. This process produced a gel with an “egg-like” shape, where the gel is thicker in the middle, as demonstrated in Figure 2.4. However, adjusting the initial solution pH to a value closer to the apparent pK_a of the gelator yields more

controlled and precise gelation, similar to that observed in wormlike micellar gelator solutions. This minimises the time required to reach the critical pH, leading to faster gelation and a reduction in the pronounced "egg-like" shape.

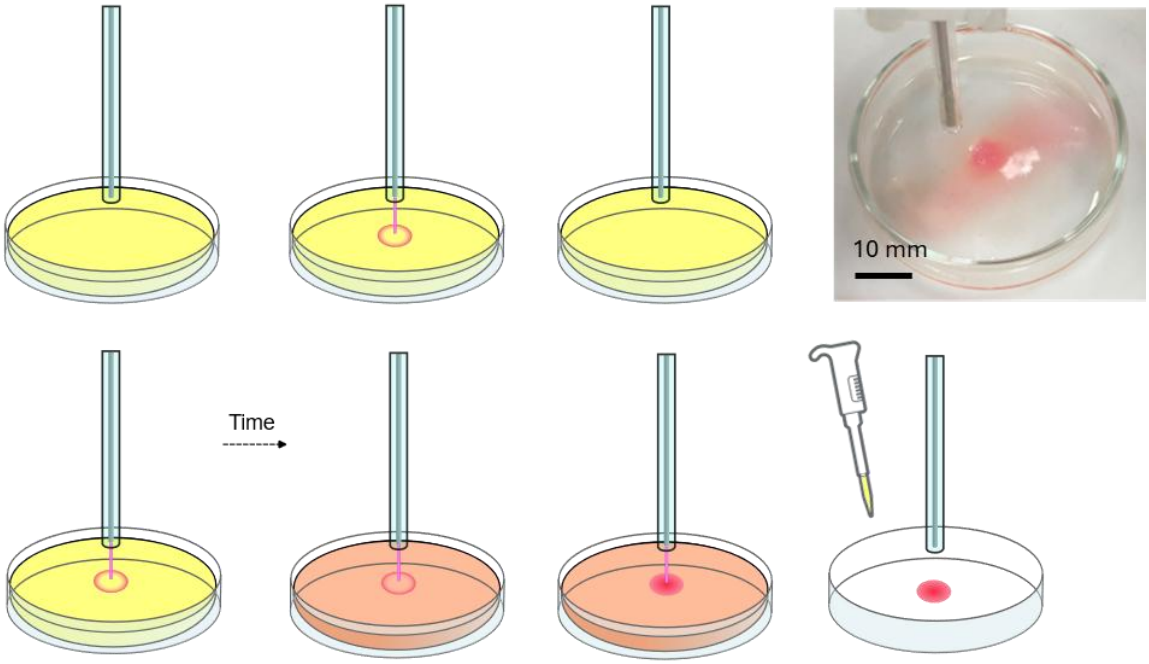

Figure 2.4. Schematic illustrating gelation of spherical micelle gelator solutions. Plasma application induces a localised decrease in pH and a corresponding colour change at the plasma–solution interface, which disperses when the plasma is switched off. Prolonged plasma exposure results in a sufficiently low pH to trigger gelation. Following gelation, the remaining solution can be removed with a pipette, leaving behind the "egg-like" gel. An image of gel produced from 6BrNapAV (5 mg/mL) with methyl red is shown.

Previous publications by Basumatary *et al.* and Bhatt *et al.* have suggested that plasma-induced gelation proceeds *via* CAP-mediated chemical modification of the gelator, thereby increasing hydrogen bonding potential and promoting supramolecular interactions that initiate 3D aggregation.[23,26] For the CAP plasma used in this chapter, the process is pH-induced, with no chemical modification or degradation of the gelator, except under prolonged plasma exposure. This conclusion was supported by high-performance liquid chromatography (HPLC) performed by Libby Marshall (University of Glasgow), which showed that both the gelator powder and the freeze-dried plasma-treated gel exhibited identical retention times (Figure 2.5a).

Multiple plasma exposure durations were examined, and the retention time remained unchanged, with no additional peaks observed after up to 4 plasma passes. After 5 plasma passes, additional peaks appeared in the HPLC chromatograms, consistent with macroscale observations. During extended plasma application, the gel exhibited visible burning, and the final gel was partially burnt away (Figure 2.5b). Although a small section of the 4x pass sample appeared dried on the gel surface, no corresponding changes were detected in the HPLC data. These results support the conclusion that plasma-triggered gelation under the conditions used in this study does not proceed *via* chemical modification of the gelator.

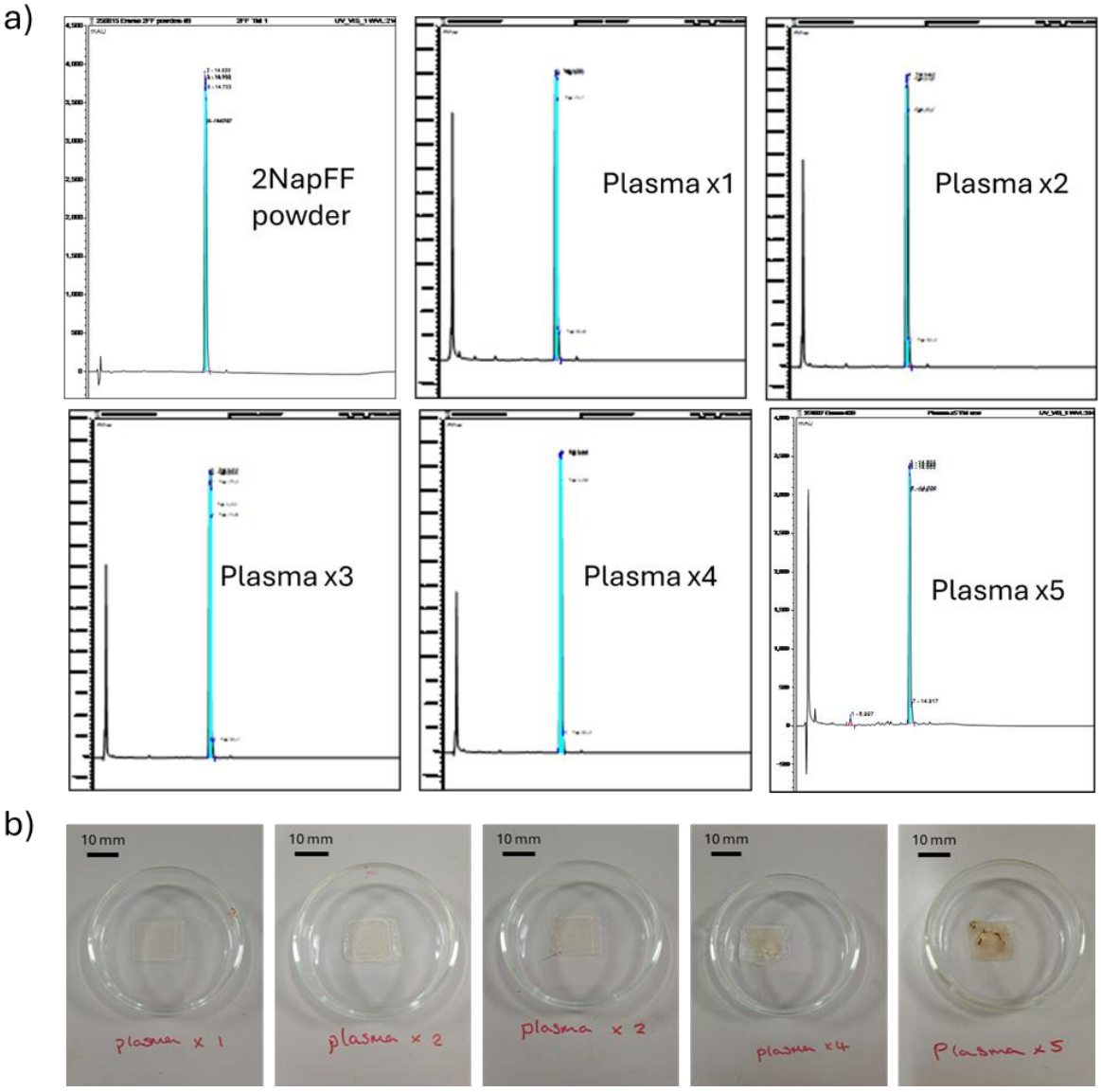

Figure 2.5. a) HPLC chromatograms of 2NapFF powder and plasma-triggered gels, with the number of plasma applications indicated. b) Images of 15 x 15 mm plasma-printed squares for HPLC analysis.

SAXS data were collected from gels formed from plasma-induced and pH-switch (GdL hydrolysis) gelation using the same stock gelator solution (Figure 2.6), during experiment SM41059-1 by Helen Futty, Daniel Harris, and Tejaswini Maurya (University of Glasgow).[3] The data indicate that the fibres formed during plasma-induced and pH-switch gelation are structurally similar. In both cases, the gels contained cylindrical fibres with comparable radii: 55 Å for the gel formed using plasma and 57 Å for the gel formed using GdL. These finding further supports a pH-triggered gelation mechanism for the plasma-induced gels. Although the scattering intensity of the GdL gel was lower than that of the plasma gel, this difference is likely attributed to variations in sample loading. The GdL gels were formed directly in the capillary, whereas the plasma gel had to be inserted, resulting in sample compression.

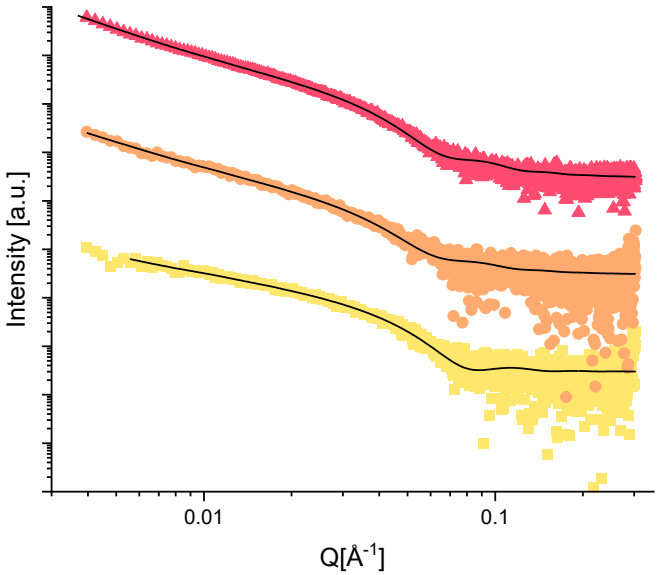

Figure 2.6. SAXS Data of 2NapFF (5 mg/mL) solution (yellow), GdL Gel (orange), and Plasma Gel (red).

This plasma-triggered gelation mechanism enables precise spatial control over gel formation, making the technique well-suited for applications such as 3D printing of defined gel structures. This is presented in more detail in Section 2.2.3.

Table 2.1. Parameters of cylinder with a power-law model for 2NapFF: a) 5 mg/mL solution, b) GdL Gel, and c) Plasma Gel. * indicates parameters that were not permitted to vary during fitting.

Sample	Background*	Scale A	Radius	Length*	B Scale	Power Law	χ^2
2NapFF Solution	0.03	$8.44 \times 10^{-4} \pm 4.8 \times 10^{-5}$	44.2± 0.8	1000	$5.25 \times 10^{-6} \pm 2.10 \times 10^{-5}$	2.36 ± 0.8	0.17
2NapFF GdL Gel	0.03	$4.48 \times 10^{-4} \pm 2.8 \times 10^{-5}$	57.3 ± 1.2	1000	$7.35 \times 10^{-5} \pm 2.1 \times 10^{-5}$	2.25 ± 0.05	0.20
2NapFF Plasma Gel	0.03	$8.63 \times 10^{-4} \pm 1.9 \times 10^{-5}$	55.2 ± 0.4	1000	$7.86 \times 10^{-5} \pm 8.07 \times 10^{-6}$	2.40 ± 0.02	0.24

2.2.2. Plasma parameter optimisation

The plasma setup used in the lab was provided by Prof. James Walsh (University of York). It comprised a benchtop DC power supply connected to a plasma generator fitted with a pin electrode, from which the plasma was generated (Figure 2.7). The pin electrode was enclosed within a quartz tube, through which an inert gas was supplied to generate the plasma. For all experiments detailed in this chapter, argon served as the inert gas. However, alternative inert gases, such as helium, can also be used. The choice of gas influences the plasma composition and impacts the gelation process, resulting in variations in mechanical properties and pH changes.

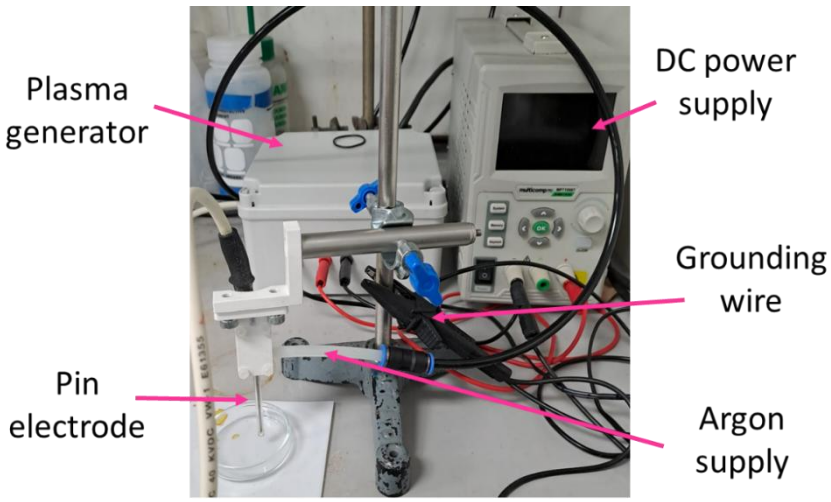

Figure 2.7. Static plasma jet set up with key components indicated: Plasma generator, pin electrode, DC power supply, grounding wire, and argon supply.

CAP was generated using a pin electrode connected to a DC power supply and a plasma generator box (provided by Prof. James Walsh) by ionising argon gas under a highly non-uniform electric field. The plasma generator converts a low-voltage DC input (20–50 V) into a high-voltage kHz output. The generator consists of a switch-mode power supply based on a half-bridge topology, using two MOSFET switches that operate 180 degrees out of phase. This converts the DC input into a square wave at the desired operating frequency. The square wave is then applied across the primary winding of a ferrite-cored transformer, which has a large number of turns on the secondary winding to step up the voltage. The inductance of the transformer secondary, with its self-capacitance and the capacitance of the plasma-generating electrode, forms a resonant circuit. The switching frequency of the power supply is adjusted to match this resonant frequency, allowing very high voltages, on the order of several kV, to be generated from a relatively low input voltage.

When a sufficiently high voltage was applied to the pin electrode, an intense electric field developed at the electrode tip. This localised field accelerates free electrons in the surrounding gas, enabling them to gain sufficient energy between collisions to ionise neutral gas molecules *via* electron-impact ionisation. The resulting avalanche of charged species initiates and sustains a plasma discharge at atmospheric pressure without the need for vacuum conditions.

Positive ions formed within the discharge drift toward the cathode, while electrons and negative ions are driven toward the opposing electrode or liquid surface, allowing continuous current flow. The pin electrode geometry confines the discharge to a small region, promoting stable plasma formation at relatively low currents and gas temperatures, thereby maintaining non-thermal conditions characteristic of CAP. Reactive species generated within the plasma, including RONS, are subsequently transported downstream by the gas flow, forming a plasma jet suitable for interactions with surfaces and liquids.

To ensure safe operation, a crocodile-clip grounding wire was attached to the clamp stand supporting the pin electrode, and the plasma was applied over an insulated material. These safety measures were implemented to moderate plasma intensity and reduce the risk of electrical shock to the operator.

Plasma generation is influenced by multiple factors that can affect both the composition and strength of the plasma produced and, therefore, the gelation process. To determine the optimal conditions for the setup described above, a series of parameter-optimisation experiments was conducted to produce the most uniform and robust gels. The parameters investigated included the input voltage, gas flow, the air gap between the solution surface and the pin electrode, the conductivity of the gelator solution, and the solution volume. For all optimisation experiments, 2NapFF at 5 mg/mL (pH 7) was used in a 5 mm diameter petri dish. In these experiments, methyl red (10 mg/mL in ethanol) was added as a pH indicator to facilitate visual observation of pH changes during plasma treatment and gelation. At pH 7, methyl red is yellow, and transitions to orange at a pH of 6.2 and red at a pH of 4.4.

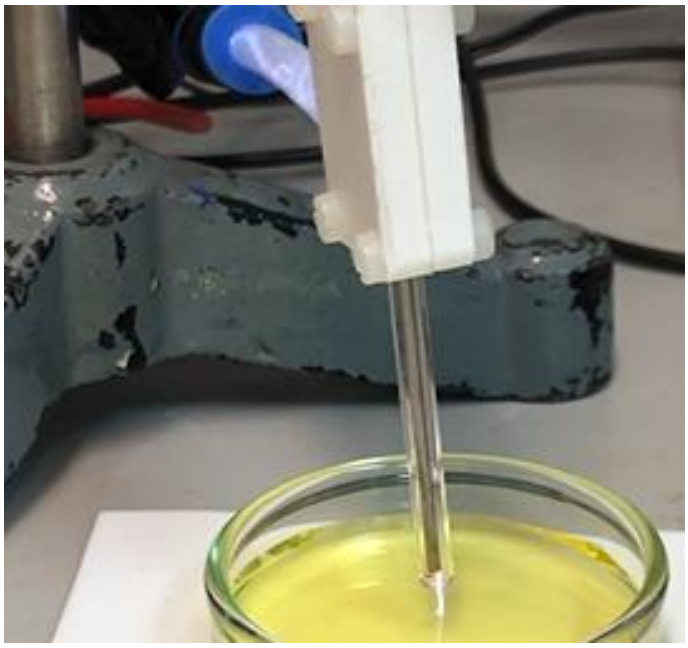

Figure 2.8. Plasma forming in the argon supply tubing.

The effects of input voltage on the plasma jet and gelation were examined at 20 V, 30 V, 40 V, and 50 V, keeping the air gap, gas flow, and solution volume constant. Voltages below 20 V were insufficient to reach the plasma's breakdown voltage, and thus no plasma was generated. The voltage was capped at 50 V because higher voltages caused argon in the supply tubing to form a plasma, triggering the power supply to shut off. When plasma is generated in the air supply tubing, it is still generated at the electrode, as shown in Figure 2.8. However, plasma can damage the tubing and pose a greater hazard to the user, so it was avoided.

As shown in Figure 2.9, increasing the input voltage enhanced the plasma's stability and intensity by increasing the density of charged particles. Higher voltage also accelerated plasma drying or burning of the gel, meaning gelation was also accelerated. Since rapid and precise pH reduction and gel formation are advantageous for 3D printing, 50 V was chosen for all subsequent experiments.

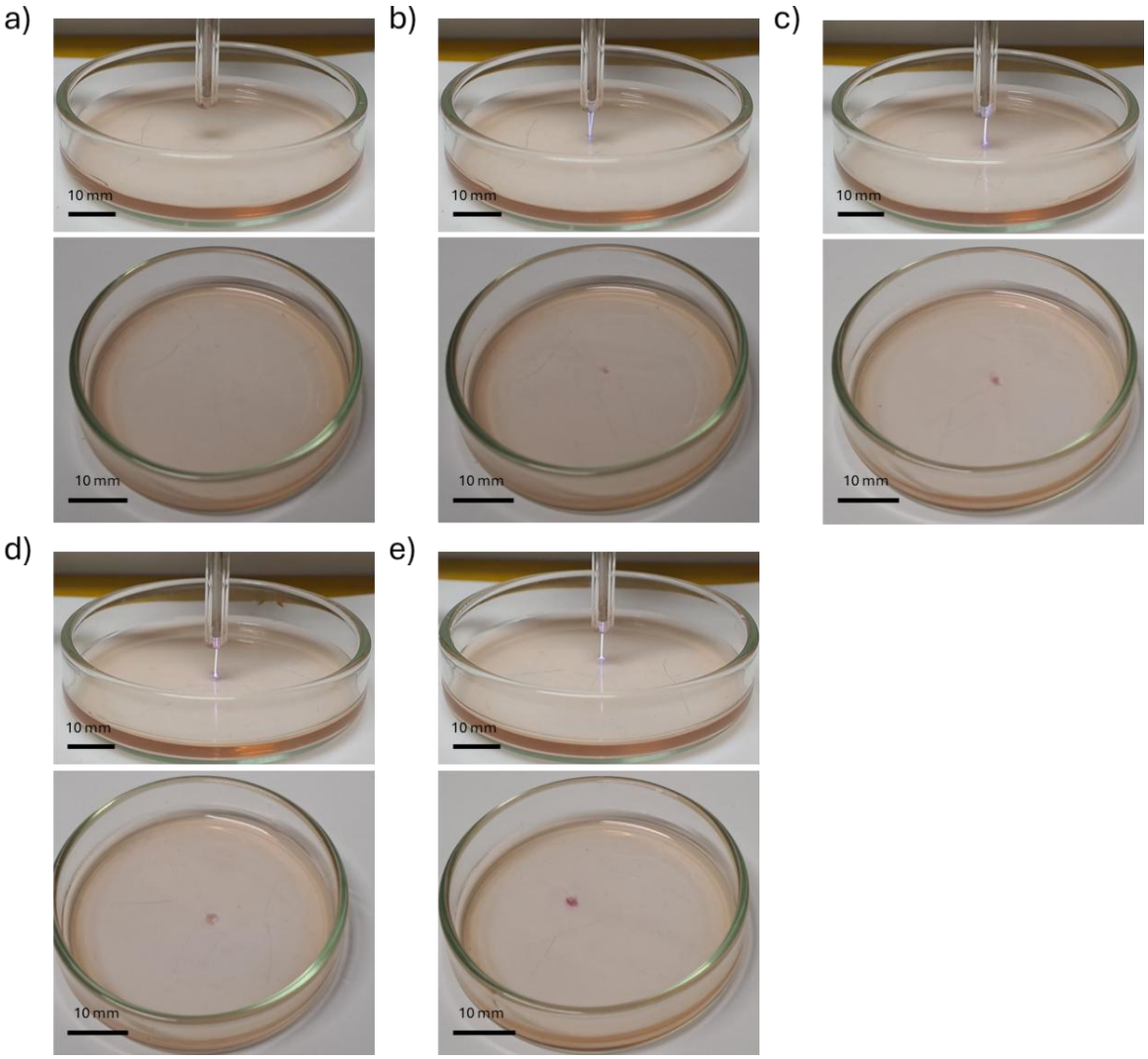

Figure 2.9. Images of the plasma jet and gel produced after 5 s from 2NapFF (5mg/mL) containing methyl red at a) 10 V, b) 20 V, c) 30 V, d) 40 V, and e) 50 V.

Argon gas flow was varied from 0.2, 0.4, 0.6, and 0.8 LPM, while keeping voltage, air gap, and solution volume constant. At low gas flow rates, the stream is weak, so the plasma is unstable and jumps around across the liquid surface, producing an uneven gel (Figure 2.10). Increasing gas flow initially stabilised the plasma jet by increasing the charged-particle density; however, above 0.6 LPM, the gas flow spreads the solution too much, creating a spot with no solution directly beneath

it. This causes a ring-shaped gel to form. At 0.8 LPM, turbulence destabilised the jet, causing it to split into multiple streams. An gas flow of 0.5 LPM was found to maximise gelation rate while maintaining jet stability, and was therefore used in subsequent experiments.

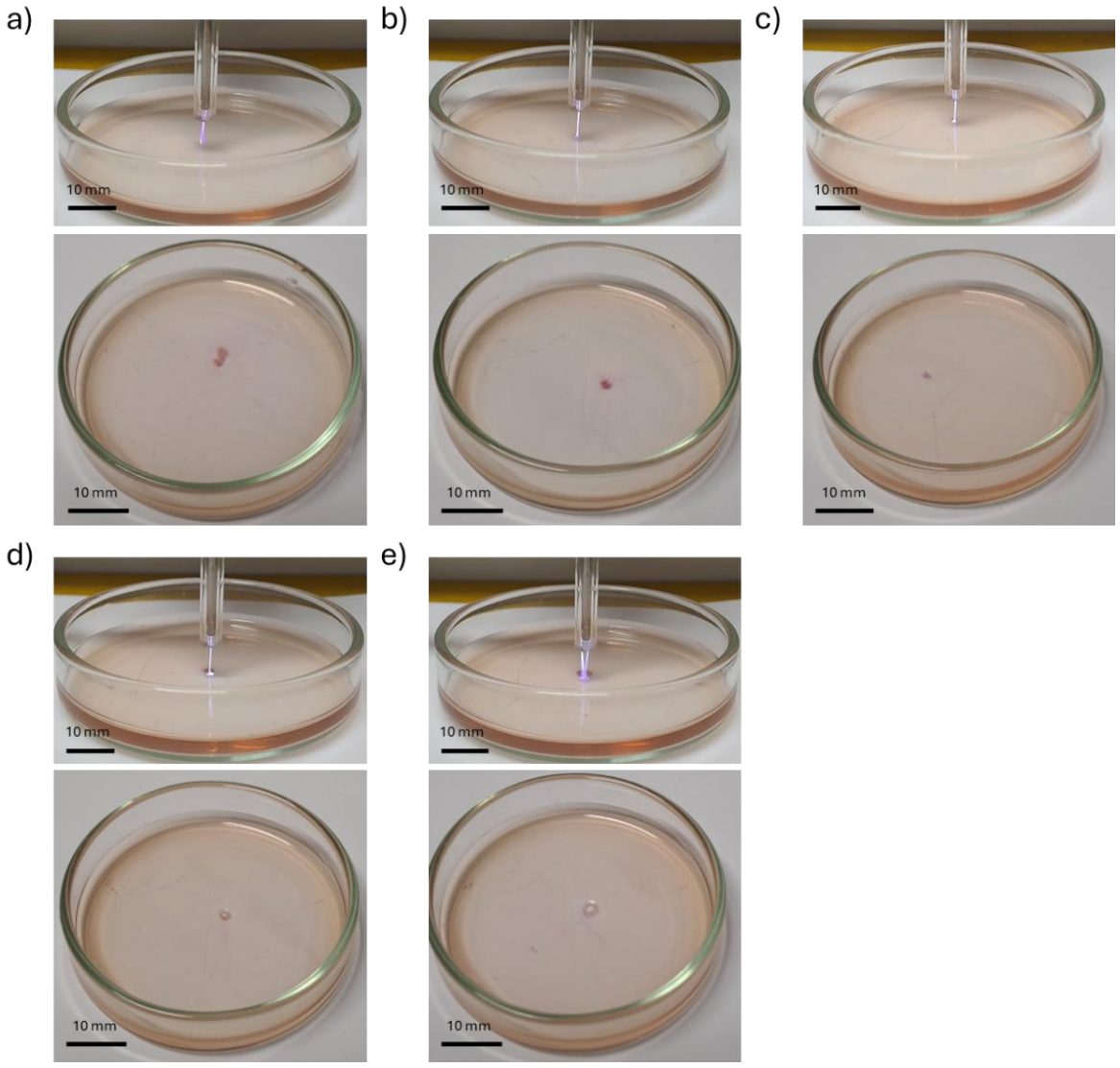

Figure 2.10. Images of the plasma jet and gel produced after 5 s from 2NapFF (5mg/mL) containing methyl red at a) 0.2 LPM, b) 0.4 LPM, c) 0.5 LPM, d) 0.6 LPM, and e) 0.8 LPM.

The air gap between the pin electrode and the liquid surface was varied from 5 mm to 20 mm (5, 10, 15, and 20 mm) while keeping other parameters constant (Figure 2.11). Small gaps allowed capillary action to draw the solution into the quartz tube, preventing plasma formation, so for experimental ease 5 mm was chosen as the smallest gap. As the air gap increases, the plasma weakens due to a reduced electric field strength, which reduces electron acceleration and

ionisation efficiency. The longer gap also increases energy losses due to collisions and charge recombination in the air, while reducing the stabilising influence of the liquid surface on the discharge. As a result, the plasma becomes weaker, less dense, and more unstable. Therefore, an air gap of 5 mm was chosen, as it was close enough to the solution to generate a stable plasma stream, leading to more precise gelation while minimising the risk of solution-electrode contact.

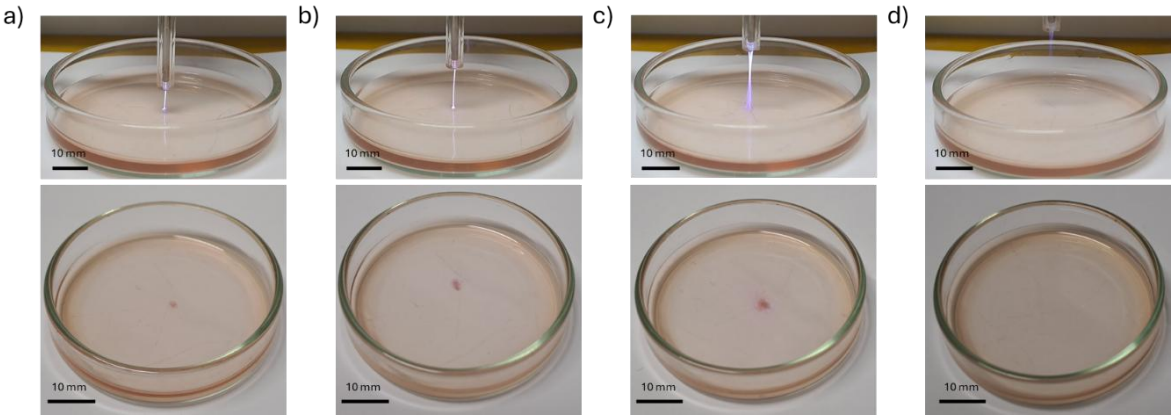

Figure 2.11. Images of the plasma jet and gel produced after 5 s from 2NapFF (5 mg/mL) containing methyl red, with an air gap of: a) 5 mm, b) 10 mm, c) 15 mm, d) 20 mm.

The effects of varying solution volume were investigated at 0.5 mL, 1 mL, 1.5 mL, 2.0 mL, and 2.5 mL, while keeping other parameters constant. As mentioned previously, the same petri dish was used for all experiments, with a 5 mm diameter. At low volumes, the argon stream pushed the solution away from the electrode, creating a spot of no gelator solution directly below it, disrupting uniform plasma application and producing patchy, ring-shaped gels (Figure 2.12). The plasma jet formed a different shape, spreading out at the end into multiple streams to meet the edge of the liquid. Increasing the volume above 1 mL reduced this effect, allowing uniform gel formation directly under the electrode. Once the solution volume exceeded 2 mL, the gels did not adhere to the bottom of the petri dish and were susceptible to floating away from the plasma stream. Therefore, 1.5 mL of solution was chosen as the ideal volume, as the gel forms directly under the electrode and remains there during the experiment, which is vital for precise gelation and 3D printing with these materials.

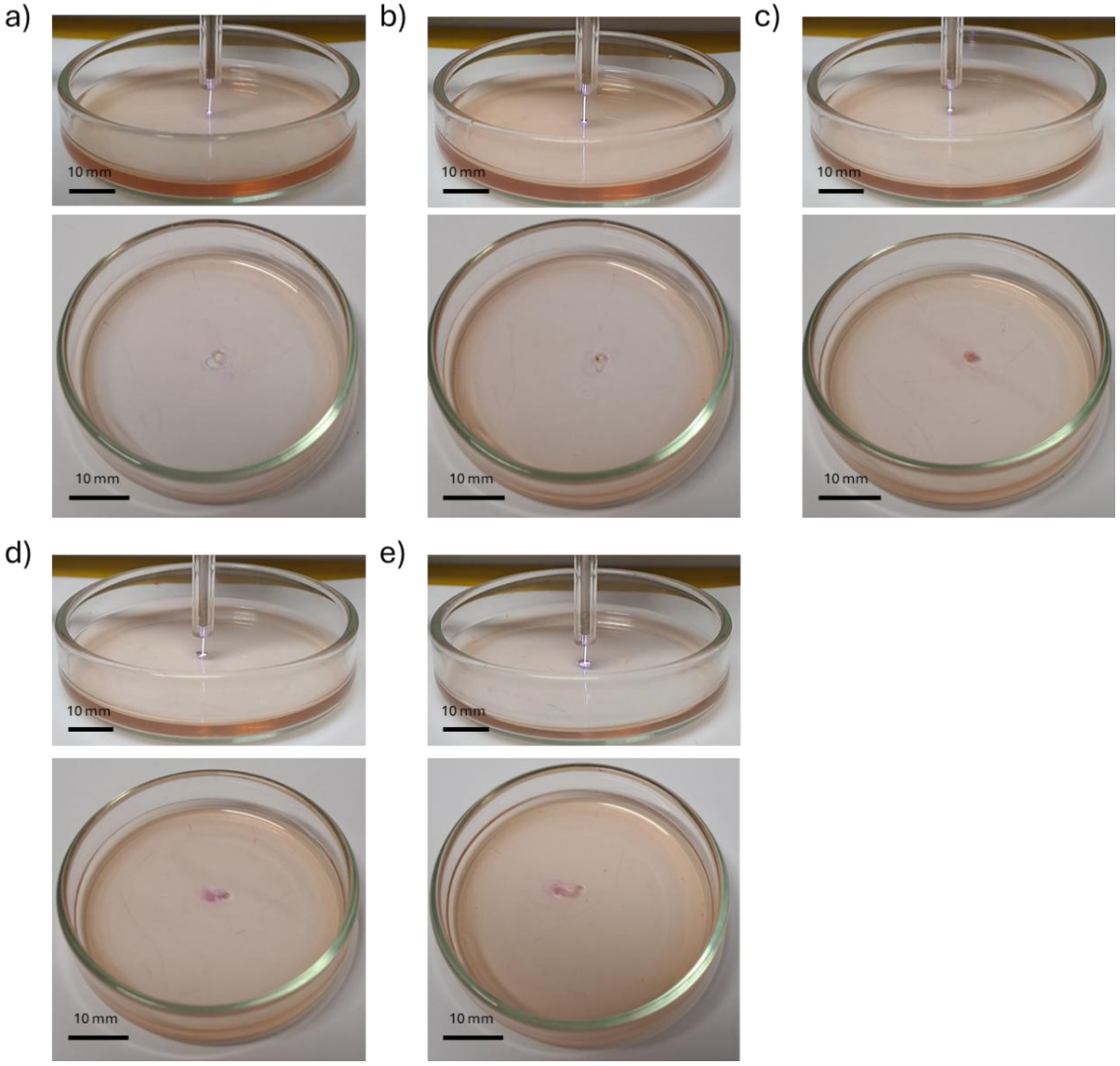

Figure 2.12. Images of the plasma stream and the gel it produced after 10 s from 2NapFF (5 mg/mL) containing methyl red with solution volumes of a) 0.5 mL, b) 1 mL, c) 1.5 mL, d) 2.0 mL, and e) 2.5 mL.

The viscosity of the gelator solutions was measured at the 3 concentrations tested (Figure 2.13). As expected, for each gelator, solutions at 2 mg/mL exhibited the lowest viscosity, whereas those at 10 mg/mL were the most viscous.[1] In addition, solutions forming worm-like micelles were more viscous than those forming spherical micelles. Within these micellar categories, gelators with higher apparent pK_a values generally exhibited slightly higher viscosities; 2NapFF was more viscous than 2NapFV, and 6BrNapAV was more viscous than 2NapVG. These viscosity differences significantly influenced gelation. Solutions at 2 mg/mL required longer plasma exposure to form gels, likely because fewer gelator molecules were available for assembly. Whereas 10 mg/mL solutions, particularly 2NapFF and

2NapFV, on timescales similar to those of the 5 mg/mL solutions, were highly viscous and often disrupted the gel structure during solution removal. Based on these observations, a concentration of 5 mg/mL was selected for all subsequent experiments.

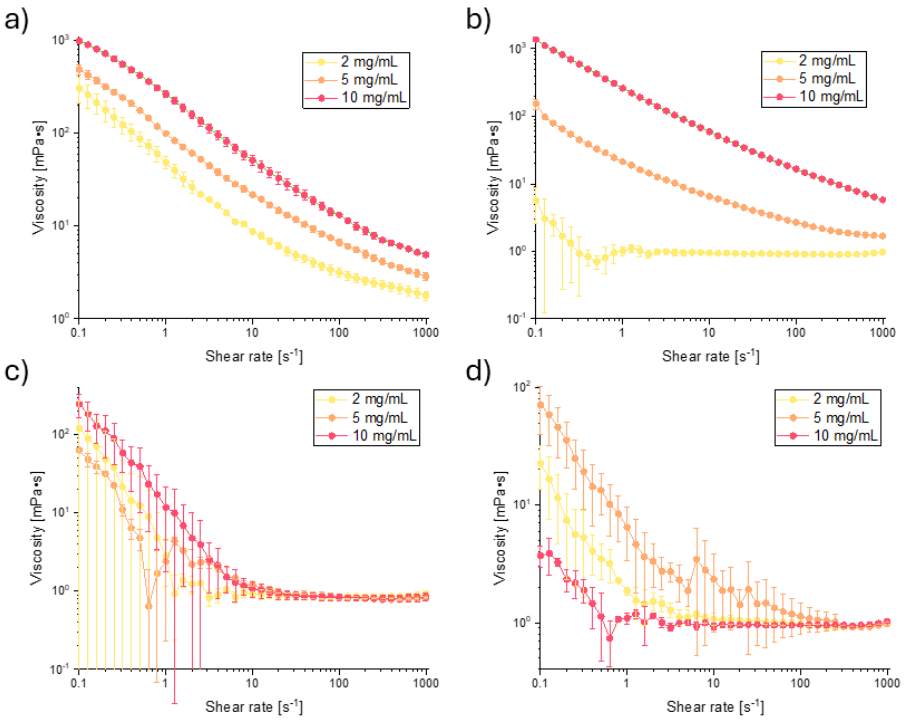

Figure 2.13. Viscosity sweep for a) 2NapFF, b) 2NapFV, c) 6BrNapAV, and d) 2NapVG solutions at 2 mg/mL (orange), 5 mg/mL (yellow), and 10 mg/mL (red) at pH 7. Samples were collected in triplicate and averaged. Error bars show the standard deviation between samples.

To verify that the addition of methyl red (10 mg/mL in ethanol; 2 µL per mL of gel) and nile blue (0.1 wt% aqueous solution, 2 µL per mL of gel, section 2.2.5.) did not affect the nanostructures in the gelator solutions, viscosity measurements were performed (Appendix 1.1). The presence of the additives did not cause any significant changes in viscosity for the worm-like micellar molecules, 2NapFF and 2NapFV, suggesting that the micellar structures remain intact. Therefore, the behaviour observed in dye-containing solutions can be considered representative and directly comparable to that in dye-free gelator solutions. For the spherical micelles, 2NapVG is unaffected; however, for 6BrNapAV, the addition of methyl red reduces the viscosity. However, the behavioural observations of 6BrNapAV plasma gelation with and without methyl red remain consistent, and since methyl

red is used solely as a pH indicator rather than for characterisation, confidence in the comparison is maintained.

In addition, the apparent pK_a values of all gelator solutions containing methyl red and nile blue were determined and compared with those of the regular solutions (Appendix 1.2). While the addition of these dyes caused slight shifts in the apparent pK_a values, especially for the more viscous gelators, these changes were minor and are not expected to impact the plasma-induced gelation process.

The effect of conductivity on the gelation process was investigated by adding NaCl to the 2NapFF gelator solution (Table 2.2). Changes in the gel were visually observed, and the corresponding images are shown in Figure 2.14. As the conductivity increased, the rate of gelation also accelerated. This may be due to the increased ion density, which enhances electrostatic forces under the electric field.[33] This increased ion density facilitates plasma jet formation, as the self-repulsion of excess ions reduces surface tension.[33] Consequently, the solution's pH decreases more rapidly, accelerating gelation. However, as the conductivity increased, so did the formation of a yellow/brown discolouration in the gel. This could indicate the formation of new species in the gel, side reactions, or burning of the gel by the plasma jet. To maintain gel composition and avoid these effects, all subsequent experiments were conducted under low-conductivity conditions without added NaCl.

Table 2.2. Conductivity of the gelator solutions with different NaCl concentrations.

[NaCl] (M)	Conductivity (mS)
0	1.82
0.05	7.38
0.10	10.62
0.20	19.56
0.50	41.01

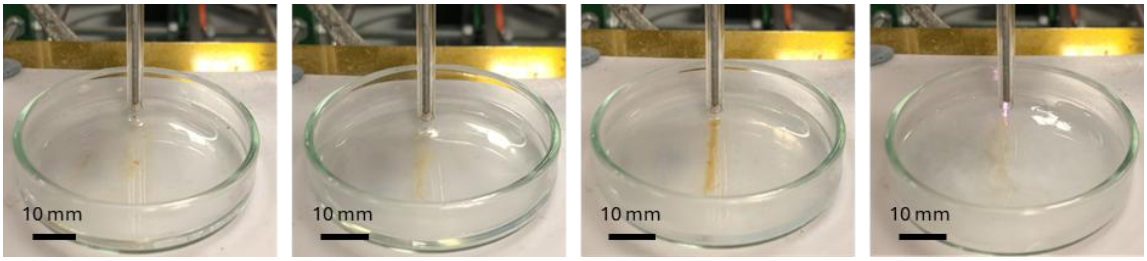

Figure 2.14. Images of the gel formed after plasma treatment of the solution are shown. The NaCl concentrations in the solution, from left to right, were 0.05 M, 0.1 M, 0.2 M, and 0.5 M. The plasma was passed over the solution once in a line.

2.2.3. Kineticolour pH analysis

The pH of the plasma gelation was investigated using Kineticolor, a computer vision software that performs colour-based kinetic analysis on video recordings. This software is suitable for non-contact monitoring of bulk systems that exhibit visual changes and has been used to analyse a variety of systems, including peptide synthesis, electrochromic films, catalyst activity, and mixing analysis.[34–37] As plasma-induced gelation was hypothesised to be triggered by a change in pH, universal indicator was used to visualise changes in the gels, which were then captured on video. Videos were recorded of plasma being applied to NaCl and 2NapFF solutions containing universal indicator (20 µL/mL), and the videos were analysed in Kineticolor by Calum Fyfe and Timothy J. McCabe (University of Strathclyde). The software calculated the colour compositions of the solutions over time in RGB, HSV, and L*a*b* colour models. These optical parameters can be collected from reflection spectra or other commercial systems, but Kineticolor combines optical analysis with temporally and spatially resolved metrics and is suited to unusual experimental setups that are not feasible with these more conventional techniques.

pH values were correlated with hue values (the HSV metric that captures pure colour) by photographing solutions at specified pH values from pH 10 to pH 2 in increments of 0.5. Kineticolor single-image analysis was then used to extract colour values from each image, and an average hue value was calculated within an ROI (region of interest) of each image (Figure 2.15). The hue values and standard deviations are provided in Appendix 1.3. These measurements were taken separately for each solution type to account for any colour changes arising

from the inclusion of the gelator. It is worth noting that there was minimal change in hue at pH values below 4 due to the indicator's range. For each solution type, two initial pH conditions (7 and 10) were recorded in a Petri dish and in a cuvette to observe pH changes radially around the plasma solution interface and vertically within the solution, respectively.

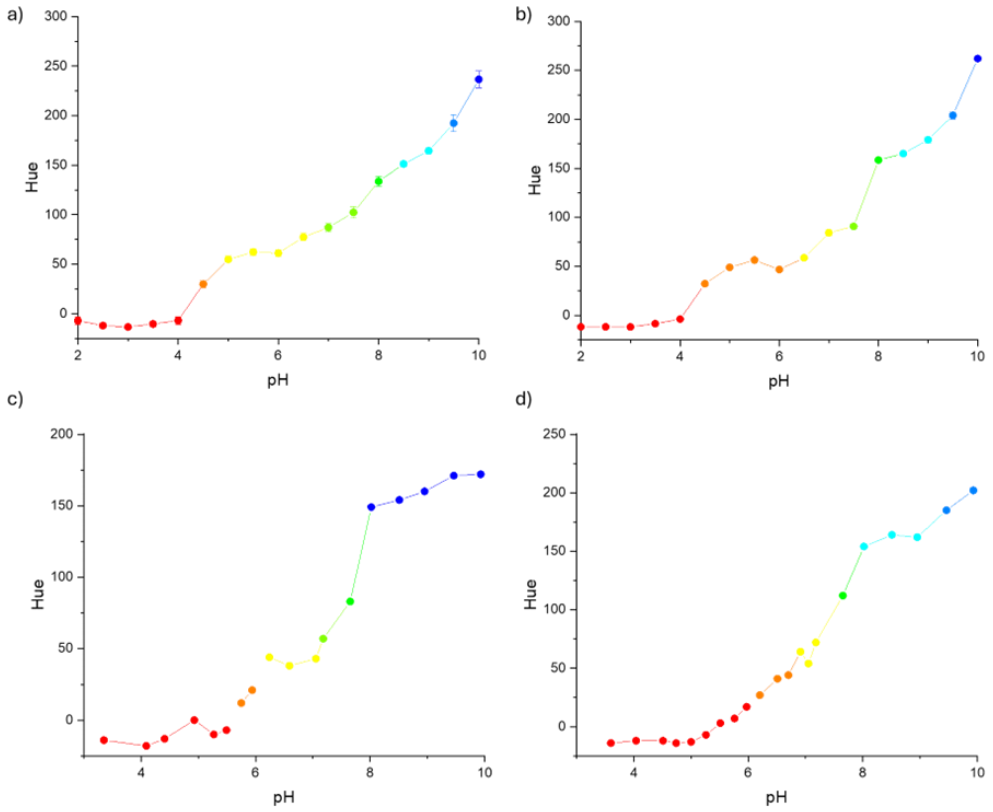

Figure 2.15. Calibration curves for a) NaCl solution in a Petri dish, b) NaCl solution in a cuvette, c) 2NapFF solution in a Petri dish, and d) 2NapFF solution in a cuvette. The point colours indicate the indicator's colour at that pH. Error bars indicate the standard deviation between the hue values of individual pixels within the image ROI.

To obtain a quantitative measure of the colour change and, therefore, the change in pH over time, the contrast change (ΔE) derived from the Euclidean distance in the L*a*b* colour space was used (Figure 2.16). This value provided a measure of pH variation over time within a defined ROI, derived from video recordings of the solutions during plasma application.

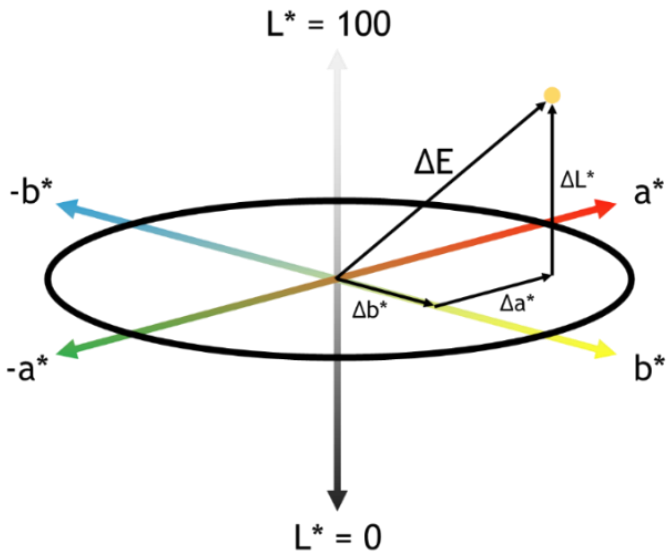

Figure 2.16. L*a*b* colour space illustrates the quantitative relationship of colours across three axes: a* and b* (chromaticity coordinates), and L* (lightness). The Euclidean distance (ΔE) within the L*a*b* colour space is a measure of contrast change.

From the ΔE graphs in Figure 2.17, the difference in pH evolution between the salt solutions and the gelator solutions is evident. For the salt solutions starting at pH 10 and pH 7, the ΔE values show a significant decrease in pH over time, with pH dropping from the initial value to below 4, as evidenced by the green-to-red colour change. For these videos, the plasma was switched off once no further colour changes were observed. In contrast, for the gelator solutions, the plasma was applied until the gel began to burn; at this point, no colour change was seen in the remaining gelator solution. A red gel formed only at the site where the plasma was applied, as indicated by the universal indicator. As shown in Figure 2.17, there was little to no change in the average contrast change within the ROI, indicating that the pH change was localised at the plasma-solution interface. The formation of the gel confined the low-pH region to a localised area, preventing it from spreading further into the bulk solution. This trend was consistent across both initial pH conditions and for experiments performed in both the Petri dish and the cuvette.

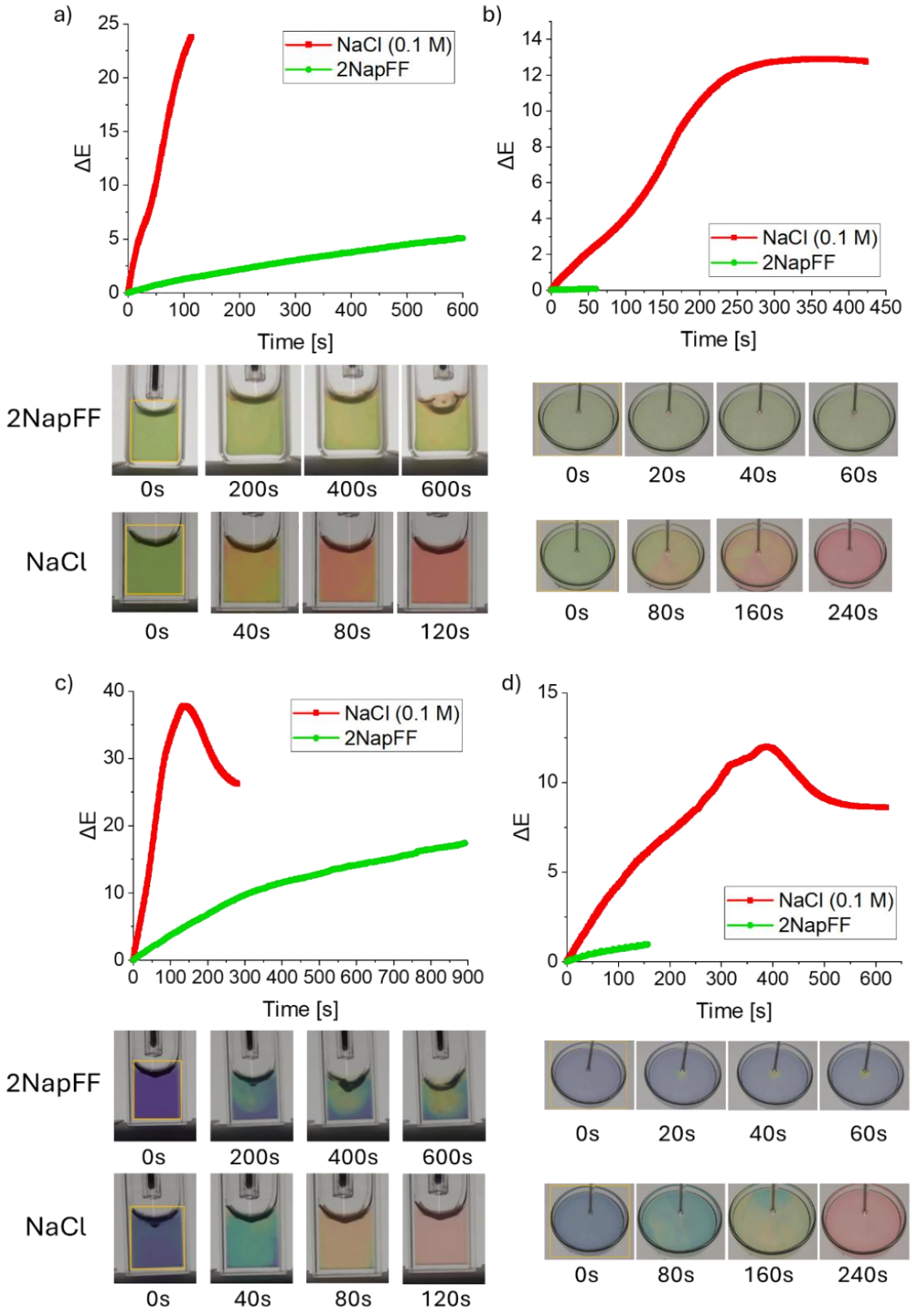

Figure 2.17. ΔE vs time plots for NaCl (red) and 2NapFF (green) in a) a cuvette with an initial starting pH of 7, b) a Petri dish with an initial starting pH of 7, c) a cuvette with an initial starting pH of 10, and d) a Petri dish with an initial starting pH of 10. The yellow box indicates the ROI where the analysis was performed.

However, the timing of each pH change differed between the NaCl solutions and the gelator solutions. For the NaCl solutions, the cuvette experiment took twice as long to reach a pH below 4 compared to the petri dish experiment, due to the larger solution volume in the petri dish. For the gelator solutions, the gel formed and started to burn in the Petri dish within 60 s, whereas in the cuvette, the gel took longer to form and was less uniform in shape, not burning until 600 s (10 min) of plasma application. This disparity is likely due to solution evaporation, as the plasma jet raises the temperature of the surrounding air, indicated by a reduction in the experimental volume of the cuvette (Figure 2.17a).

To further investigate the pH change at the gelation point, spatially resolved ΔE changes were measured using multiple smaller ROIs to compare the rates of pH decrease at different points in the cuvette videos. The original ROI was divided into five rows (Row 1 at the bottom to Row 5 at the top). The graphs present the overall contrast change for each row, rather than the average across the entire ROI, as previously illustrated. For the gelator solution, the overall change was minimal (ΔE ≈ 2), indicating a very subtle and localised effect. The largest ΔE was observed in row 5 (closest to the plasma source). Conversely, the smallest occurred in row 1 (farthest from the plasma source), aligning with the visual observation that the colour change was mainly concentrated at the top of the cuvette (Figure 2.23a). In the absence of the gelator, the ΔE change was larger (ΔE ≈ 30) and more uniformly distributed throughout the whole solution. The overlapping ΔE values for each row indicate that the colour change occurred simultaneously throughout the cuvette when using the salt solutions (Figure 2.18b).

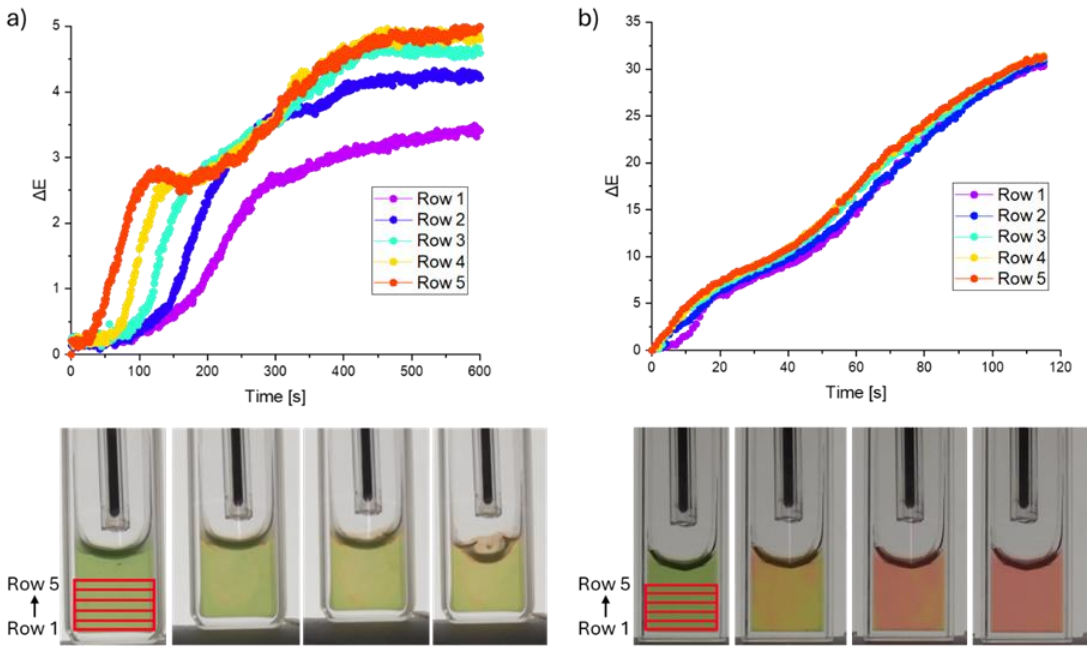

Figure 2.18. ΔE overtime plots for a) 2NapFF and b) NaCl in a cuvette for 5 ROIs indicated by the red boxes, where row 1 is the bottom row and row 5 is the top row.

As well as quantifying colour change Kineticolor was used for contact analysis to measure the pH evolution over time. Contact analysis is a binary image-processing method that transforms complex videos with numerous colour changes into quantitative measurements *via* perimeter-based calculations. Three-channel HSV thresholding was used to tune the contact to specific pH ranges, and five separate pH ranges were investigated: 10–9, 8.5–7.5, 6.5–5.5, and > 4. When combined, this yielded a contact plot showing pH evolution over time (Figure 2.19). For the plasma solutions, this analysis quantified the decrease in the solution's pH. Because the pH range was smaller for the pH 7 solutions, only solutions with an initial pH of 10 were analysed using this method.

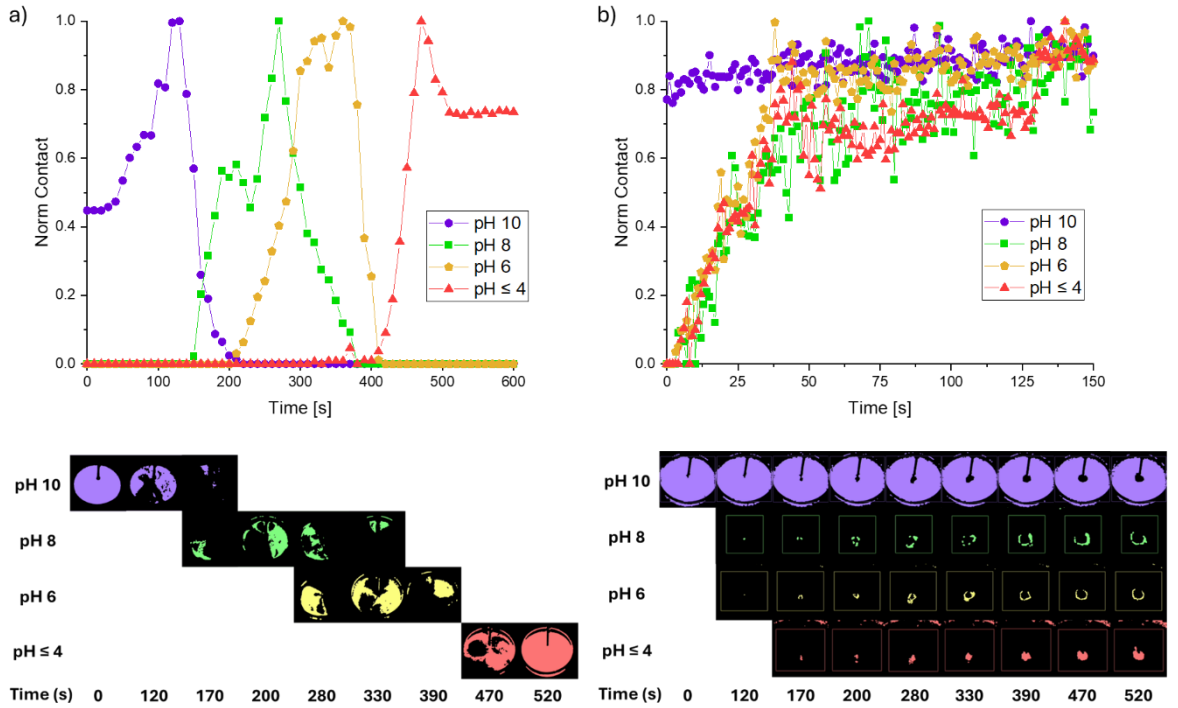

Figure 2.19. Combined contact plot of pH values 10, 8, 6, and >4 showing pH evolution over time for the plasma applied (top) and images indicating the thresholding (below) for a) 7.5 mL of NaCl 0.1M solution, b) 7.5 mL of 2NapFF (5 mg/mL) solution, both start at pH 10 and contain universal indicator (20 µL/mL).

For the NaCl solution, the pH began at 10 and decreased approximately linearly across each pH range, then plateaued at a pH < 4 (Figure 2.19a). In contrast, for the 2NapFF solution, the pH started at 10, and contact increased across each pH range, with no subsequent decrease, unlike in the NaCl solutions. The blue colour indicating pH 10 remained constant, while colours corresponding to lower pH values, pH 8 (green), pH 6 (orange/yellow), and pH 4 (red), appeared quickly. This is due to the colour gradient in the gelator solutions. At the plasma-solution interface, the colour is red (lower pH), which transitions to the outer solution region, where the colour is blue (pH 10). The gelator restricts the low-pH region to just below the plasma jet, unlike in NaCl solution.

The difference in timescales further highlights how the pH decrease is faster in the gelator solution at the plasma solution interface, likely due to restricted diffusion, compared to the NaCl solution, where regions of pH less than 4 are not observed until 500 s. Whereas, in the gelator solution, regions of pH less than 4 start to appear almost immediately (Figure 2.19b)

Finally, shape analysis of plasma gelation was performed without universal indicator, showing the increase in gel area over time for both pH 10 and pH 7 solutions. By applying a binary threshold to the image based on the slight colour change between the solution and the gel, the gel area (in pixels) was measured (Figure 2.20). In both videos, at the beginning, there is a short 'induction period' in the data (the first 10 s), indicating the time when no plasma is applied.

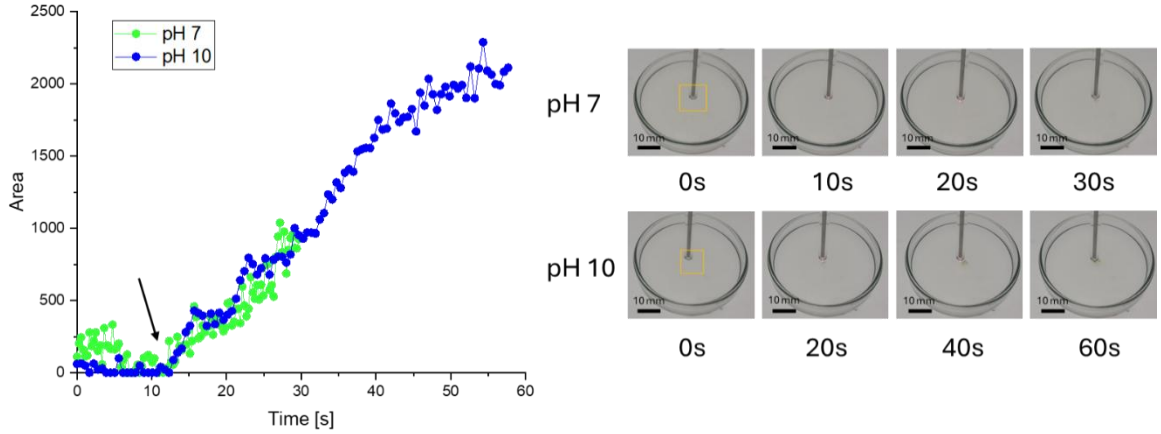

Figure 2.20. Graph of the gel growth over time for gelator solutions at an initial pH of 7 and 10; the arrow indicates the point on the graph when the plasma was switched on.

As shown in Figure 2.20, the gel area increases immediately upon plasma activation for both pH conditions. This growth continued linearly until the gel began to burn, at which point the plasma was switched off. This burning occurred much more rapidly in the pH 7 solution, as expected, because less pH reduction is needed than in the pH 10 solution, so the gel formed, dried, and burned more quickly. Additionally, in the pH 10 solution, the gel area continued to increase beyond that observed in pH 7. The formed gel was not anchored to the bottom of the Petri dish, so it floated on the solution's surface and moved around. This is because the viscosity of the pH 10 solution is lower than that of the pH 7 solution, in which no movement was observed; thus, more of the solution has the plasma applied to it in the pH 10 solution than in the pH 7 solution, resulting in a larger gel.

2.2.4. Plasma 3D printing

This plasma-triggered pH-gelation enables precise spatial and temporal control over gelation, making the technique suitable for applications such as 3D printing of defined gel structures. A 3D printer (RepRap Huxley) was modified by Dr Bart Dietrich (University of Glasgow) to allow 3D printing using the plasma setup. The 3D printer setup is shown in Figure 2.21. The quartz tube was attached to a modified 3D printer, and the pin electrode was positioned approximately 0.5 cm above the liquid surface of a petri dish containing 1.5 mL of pre-gel solution. The 3D printer and the plasma jet were activated simultaneously, enabling direct 3D printing of plasma gels.

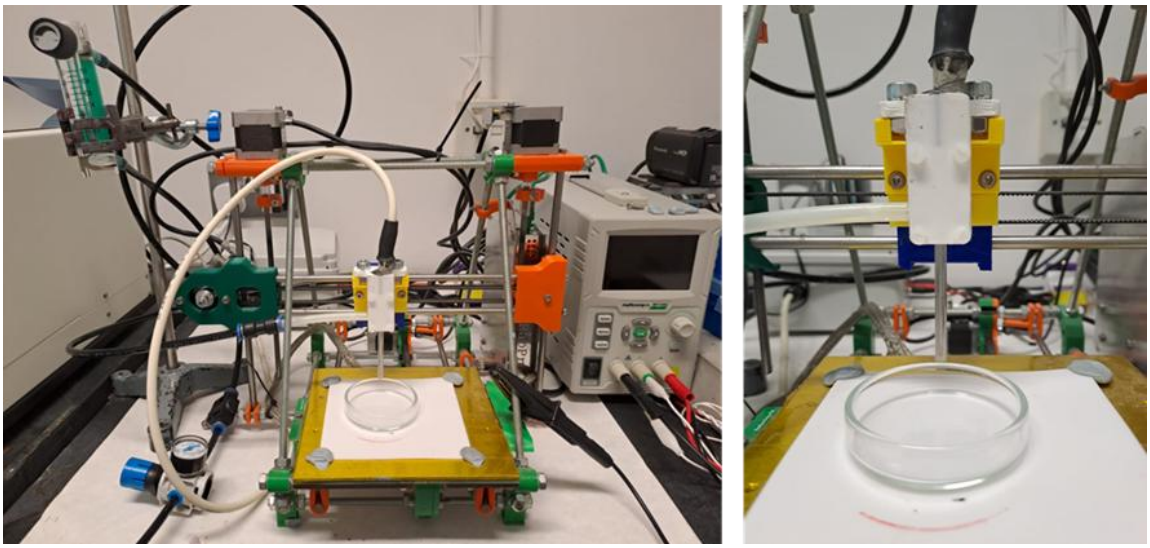

Figure 2.21. 3D printer plasma jet setup.

When the plasma stream is applied across the solution, localised gelation is triggered, directly beneath the pin electrode. After gelation, the solution can be removed with a pipette, leaving only the 3D-printed gel (Figure 2.22a). Using this setup, precise 3D-printed shapes can be fabricated, as shown in Figure 2.22b. This technique enables resolution at the millimetre scale; the printer can be precisely controlled in 1 mm increments. Furthermore, the printing process is rapid, and the plasma can be switched on and off during printing to generate complex geometries.

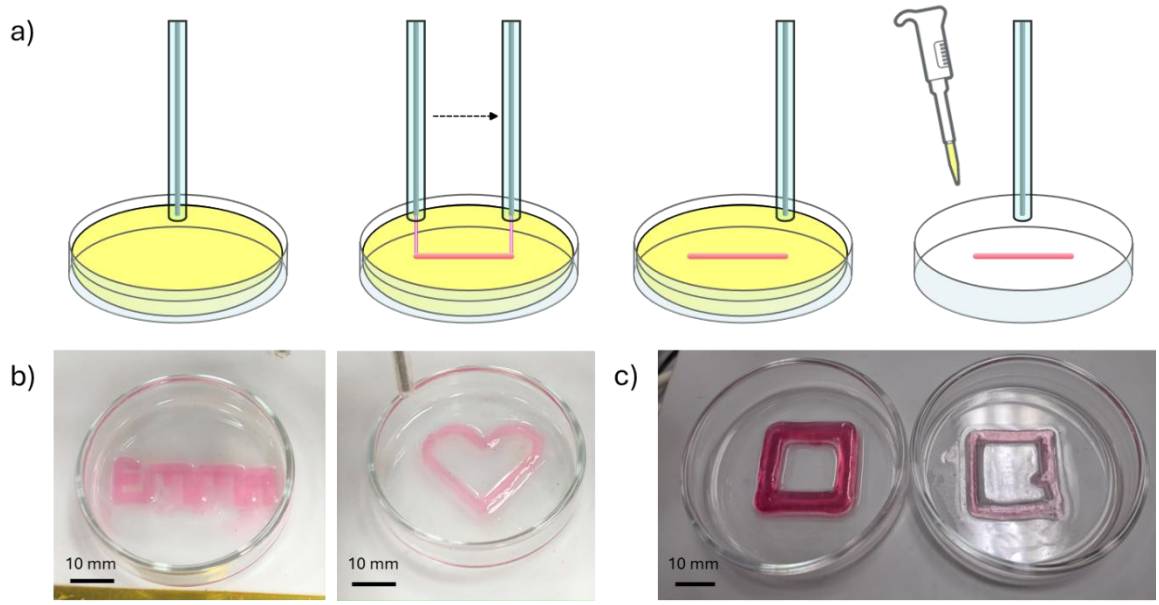

Figure 2.22. a) Schematic illustrating 3D printing of gels using plasma. When the plasma stream is applied across the solution, localised gelation is triggered. After gelation, the solution can be removed with a pipette, leaving only the 3D-printed gel. b) Images of 3D printed gels from 2NapFF (5 mg/mL) containing methyl red. c) Images of a 3D-printed gel square from 2NapFF (5 mg/mL) containing methyl red. The structure on the left consists of 5 layers, while that on the right consists of a single layer.

Multiple layers can be printed sequentially to produce larger gel structures by adding more gelator solution and printing the same shape on top of existing layers (Figure 2.22c). Using this approach, gels composed of different gelators can also be fabricated in distinct, precisely defined layers. In this method, a single gel shape is first printed, and the remaining gelator solution is then removed. A second gelator solution is then added and plasma-printed in the same shape. Removal of the excess solution leaves a gel with well-defined layers of different gelators, as illustrated in Figure 2.23.

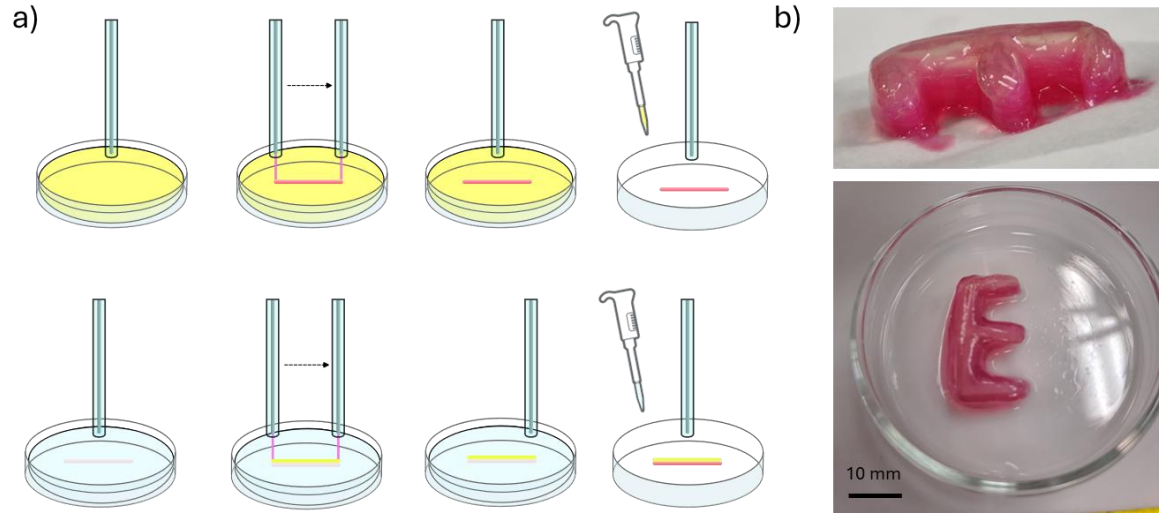

Figure 2.23. a) Schematic illustrating 3D printing of gel layers using plasma. After the gelation of the first layer, the remaining solution can be removed with a pipette, leaving only the printed gel. A different gelator solution can then be added to the Petri dish, and the same shape can be plasma printed on top of the first. Removal of the excess solution results in a gel with two distinct layers. b) Images of 3D-printed gel with bottom layers composed of 2NapFV (5 mg/mL) containing methyl red, and top layers formed from 2NapFF (5 mg/mL).

2.2.5. Plasma gel properties

The rheological properties of the gels were explored by printing a 15 x 15 mm gel square, which was used to record strain- and frequency-sweep data for each gelator. The square was printed using plasma applied once and twice to examine how the plasma dose affects the mechanical properties. The rheological data indicate that increased plasma application results in a stiffer gel (Figure 2.24). This is likely due to a further decrease in pH, resulting in a denser, more entangled network. The magnitude of stiffening between one and two plasma passes depends on the gelator. Larger increases are observed for 6BrNapAV and 2NapFV, whereas 2NapFF shows a smaller change. This trend is consistent with differences in the apparent pK_a of the individual gelators. Gelation of 2NapFF occurs at higher pH and is largely complete after a single plasma exposure, whereas 6BrNapAV and 2NapFV require further pH reduction to fully develop their networks. Since the rheological data were measured using a parallel-plate geometry directly on the petri dish and the gel's surface was uneven, the values may not accurately reflect the properties of the gel, which explains the relatively high values.

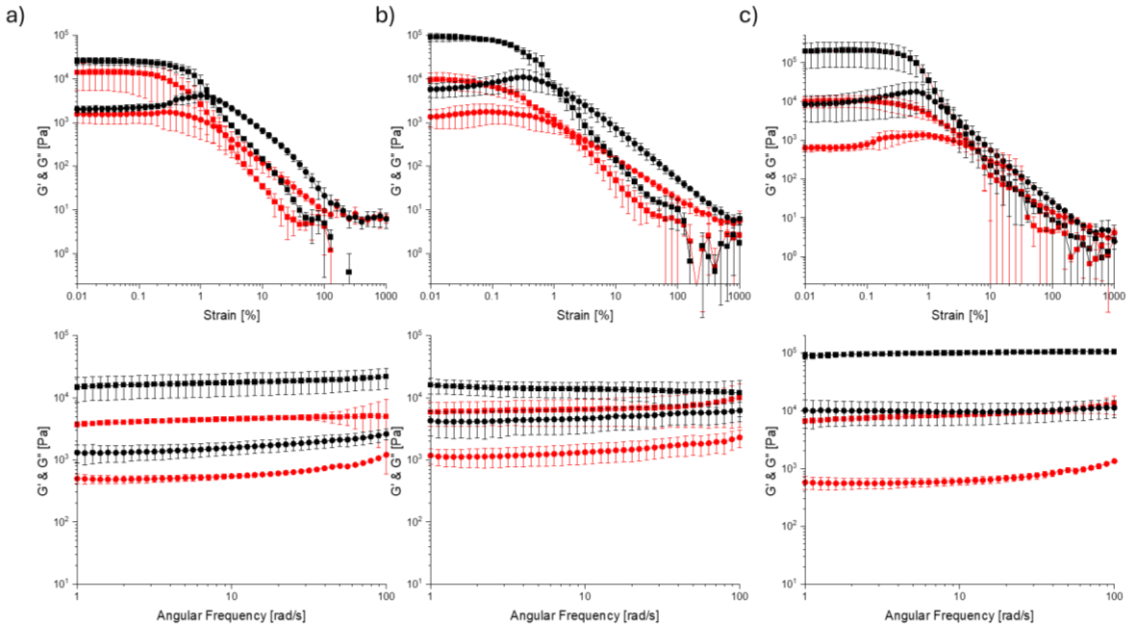

Figure 2.24. Strain (top) and frequency sweeps (bottom) for a) 2NapFF, b) 2NapFV, and c) 6BrNapAV of 15 x 15 mm plasma-printed squares, where the plasma was applied once (red) and twice (black) in a square shape. Samples were measured in triplicate and averaged. Error bars show the standard deviation between samples.

Confocal images were obtained to probe the structural properties of plasma-gel networks and the effects of different gelators on morphology. 2NapFF, 2NapFV, and 6BrNapAV (5 mg/mL) solutions were prepared as previously described, and nile blue (2 µL/mL) was added prior to pH adjustment. As previously mentioned, the apparent pK_a and viscosity of the solutions were measured to detect any changes, but no significant differences were observed between the regular solutions and those containing nile blue (Appendix 1.1-1.2).

Images were taken from both the centre and the edge of each gel, as shown in Figures 2.25-2.27. The 2NapFF gel exhibited a well-defined edge and larger fibres than those of the other gelators tested. The fibres also appear to be more aligned; this backs up the macroscale observations: the 2NapFF gel is more spatially defined, whereas 2NapFV is less so, and 6BrNapAV even less so. Again, this is consistent with the pK_a values of the gelator. The 2NapFV gel also shows a well-defined network of fibre-like structures, similar to that observed for 2NapFF. However, the edge of the gel was less defined than that of 2NapFF, and the fibres were smaller. In contrast, the 6BrNapAV gels lack these defined fibres; instead, they contain spherical structures with indistinct edges that are hard to determine.

These observations suggest that the structure and quality of the gel network formed under plasma-induced gelation depend heavily on the gelator molecule. As expected, owing to immediate localised gelation, the worm-like micellar solutions exhibit more well-defined gels due to minimal pH diffusion, making them more effective for 3D printing. The degree of fibre alignment and network definition appears to be most pronounced in the 2NapFF gel, while 2NapFV and 6BrNapAV exhibited less spatially defined gels.

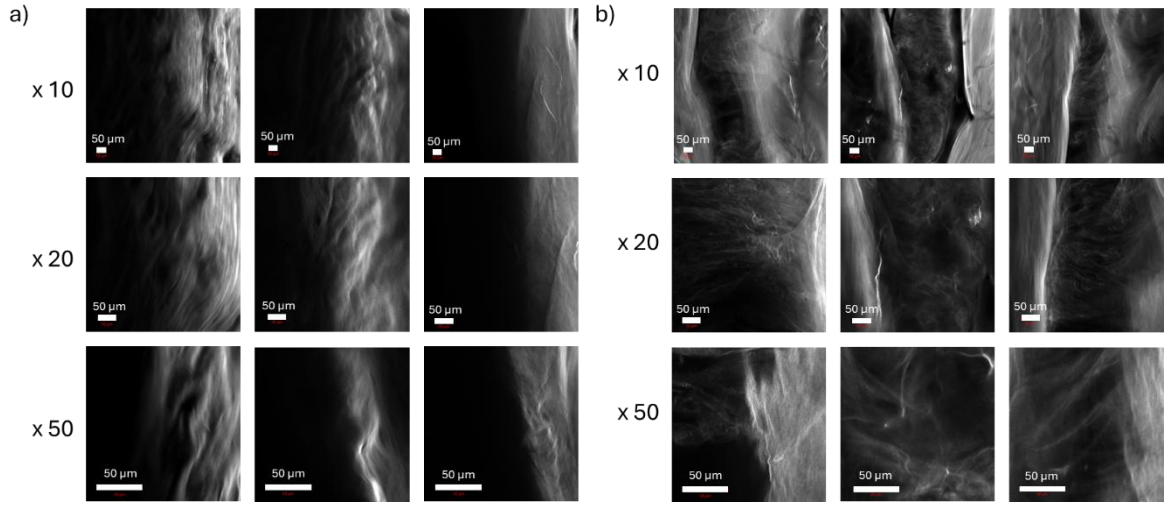

Figure 2.25. Confocal images of the a) edge and b) middle of 2NapFF (5 mg/mL) plasma gels. The plasma was passed over the solution once in a line. Scale bars (white) represent 50 µm.

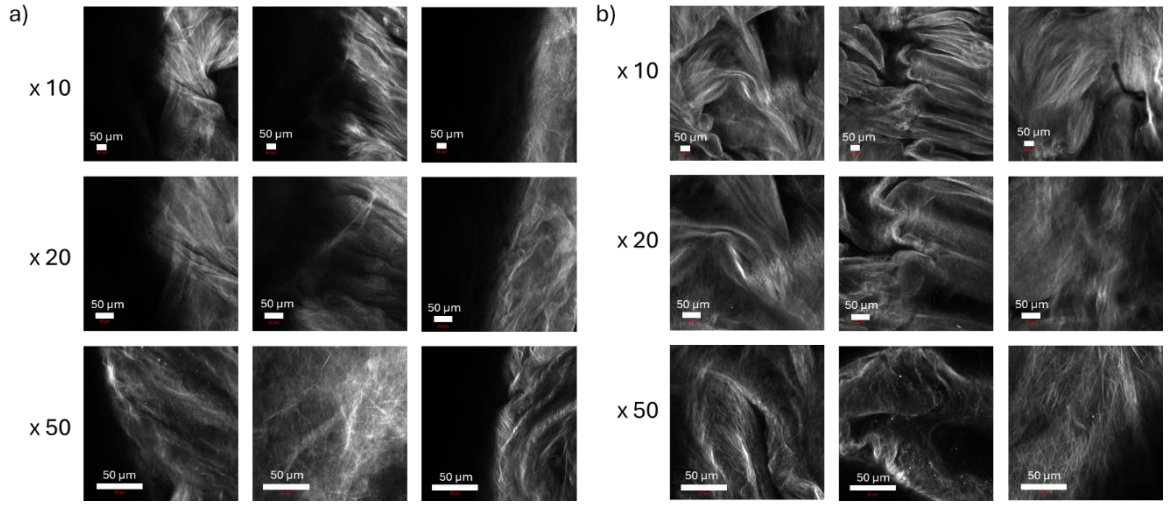

Figure 2.26. Confocal images of the a) edge and b) middle of 2NapFV (5 mg/mL) plasma gels. The plasma was passed over the solution once in a line. Scale bars (white) represent 50 µm.

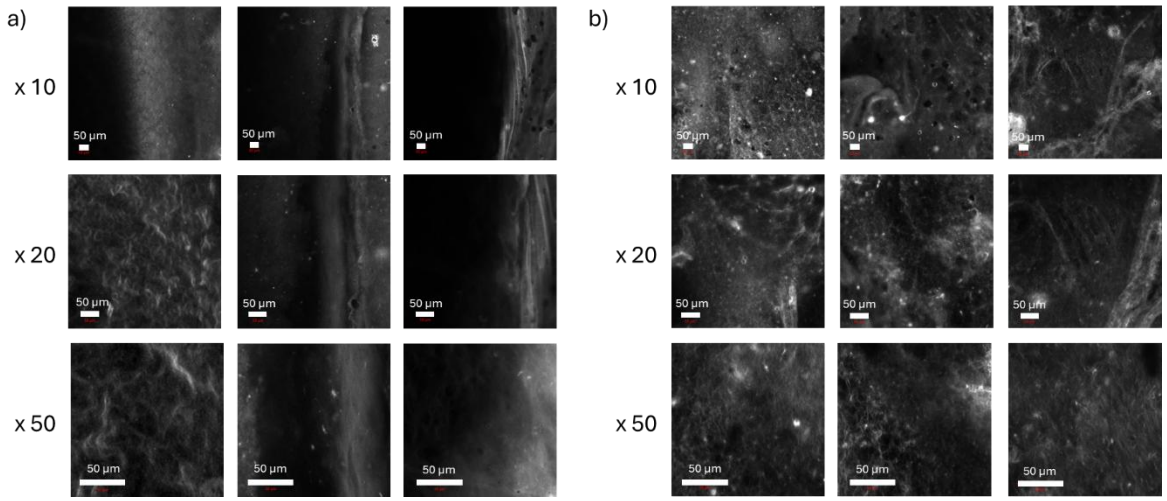

Figure 2.27. Confocal images of the a) edge and b) middle of 6BrNapAV (5 mg/mL) plasma gels. The plasma was passed over the solution once in a line. Scale bars (white) represent 50 µm.

2.2.6. Plasma gels containing nanoparticles

Incorporating nanoparticles into gels offers numerous potential benefits, such as the inherent antimicrobial and antioxidant properties of gold nanoparticles, as well as their unique optical, electrical, and photothermal properties.[38-40] By modifying the size, shape, and surface charge of these nanoparticles, they can be tailored to serve specific functions, thereby making nanoparticle-containing gels highly versatile for applications across diverse fields, including medicine, food, and sensor design.[41-43] Recent advances in plasma-based synthesis tools have improved the design of nanogold, particularly in production time and size control.[43-45] Chantaramethakul *et al*. used solution plasma sputtering with two Au wire electrodes as the Au source in a pyrex glass reactor.[45] They achieved control over the particle size of spherical gold nanoparticles, ranging from 5–20 nm. Olenki *et al*. demonstrated that varying the starting concentration of tetrachloroauric (III) acid trihydrate ($HAuCl_4 \bullet 3H_2O$) enabled the controlled synthesis of nanogold with different sizes and shapes using a laboratory-based CAP plasma jet. As discussed above, gels can be formed using a plasma source. Therefore, combining these two techniques makes it possible to produce gels containing nanoparticles *in situ*.

Dipeptide gels containing nanoparticles have previously been reported, but the formation of nanoparticle-containing gels has involved multiple steps: initially

forming a gel, then forming the nanoparticles.[46–48] For example, Adole *et al.* prepared FmocFF solvent-switch gels containing Au^{3+} ions, which were reduced to Au^0 nanoparticles *via* thermal annealing.[48] This method relies on the thermal durability of the FmocFF fibres and is therefore not applicable to other gelators that are less thermally stable. Notably, the FmocFF fibres acted as stabilising scaffolds for the nanoparticles.[48] FmocFF salt-triggered gels have also been prepared using $HAuCl_4$ and silver nitrate; these gels were then exposed to sunlight, which induced the formation of gold and silver nanoparticles.[47] However, no method has been reported that simultaneously forms a gel and the nanoparticles. Additionally, the gels have only been produced in bulk, with limited spatial control.

As mentioned above, the starting concentration of $HAuCl_4 \bullet 3H_2O$ enabled the controlled synthesis of nanogold with various sizes and shapes, achieved using a CAP plasma source like that used in this chapter.[43] Replication of this nanogold synthesis was attempted using our lab-based plasma source. A stock solution of aqueous $HAuCl_4 \bullet 3H_2O$ was used to prepare 0.1 mM and 0.5 mM working solutions, to which different plasma treatment times were subsequently applied. The formation of nanogold during this process was monitored using UV-Vis spectroscopy. (Figure 2.28).

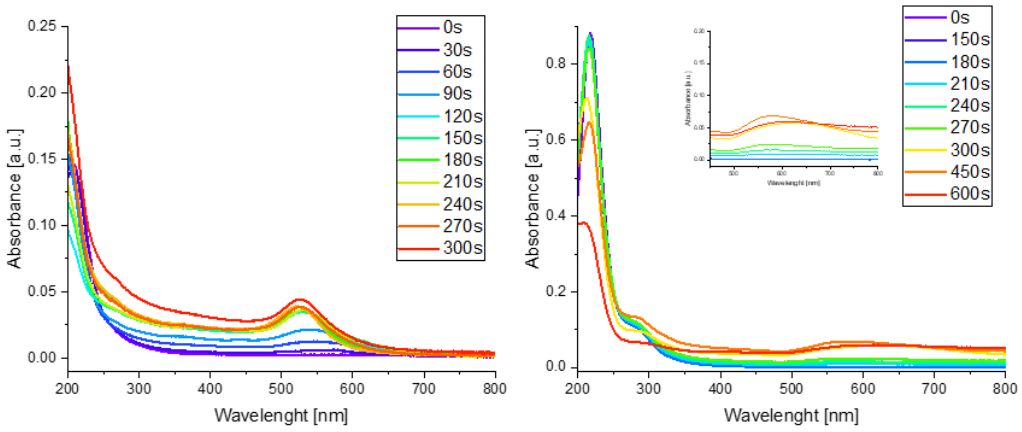

Figure 2.28. UV-vis absorbance spectra of 0.1mM (left) and 0.5mM (right) concentration of $HAuCl_4 \bullet 3H_2O$ after different plasma treatment times.

The absorption spectra of the untreated $HAuCl_4 \bullet 3H_2O$ solution exhibit a clear peak between 270 and 300 nm, indicative of non-reduced gold ions. [43] This peak is visible in the 0.5 mM solution but too small to be detected in the 0.1 mM solution. As plasma treatment time increased, the peak in the 0.5 mM solution decreased,

indicating a reduction in the concentration of gold ions. Additionally, the characteristic surface plasmon resonance (SPR) peak of Au nanoparticles at 520 nm was observed for the 0.1 mM solution, confirming the production of gold nanoparticles. As treatment time increased, the peak shifted to shorter wavelengths, indicating a reduction in nanogold particle size. The plasmon peak was absent in the 0.5 mM solution and was replaced by a broad peak at longer wavelengths, suggesting that at this concentration our plasma treatment primarily produces planar nanogold particles rather than spherical ones, as previously observed.[43]

The solutions, which initially appeared clear, became increasingly pink as plasma treatment time increased, further indicating nanoparticle formation.

Having successfully produced nanogold particles from $HAuCl_4 \bullet 3H_2O$ in water, the same precursor was added to 2NapFF and 6BrNapAV gelator solution to form *in situ* nanoparticle-containing gels. When plasma was applied to these gelator/$HAuCl_4 \bullet 3H_2O$ solutions, simultaneous reduction of Au^{3+} to Au^0 nanoparticles and gel formation were observed, yielding a gel containing AuNPs. Multiple concentrations of $HAuCl_4 \bullet 3H_2O$ were tested, and successful nanoparticle-containing 3D-printed 2NapFF gels were detected with the following $HAuCl_4 \bullet 3H_2O$ concentrations: 0.25 mM, 0.5 mM, 1.0 mM, 2.5 mM, and 5.0 mM (Figure 2.29).

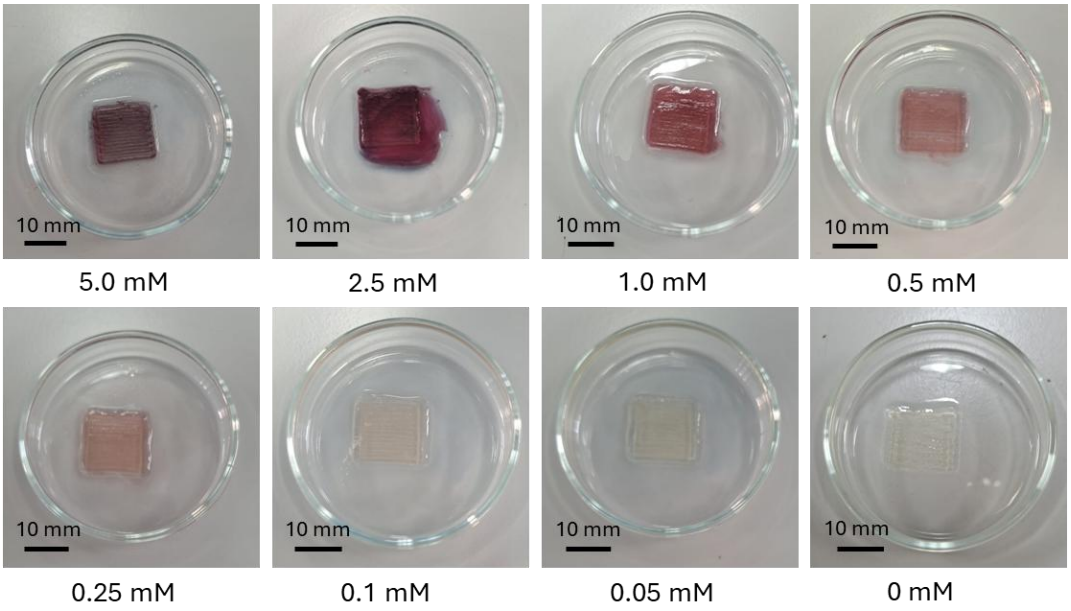

Figure 2.29. Images of the 15 x 15 mm 2NapFF gels plasma printed with 0 mM, 0.05 mM, 0.1 mM, 0.25 mM, 0.5 mM, 1.0 mM, 2.5 mM, and 5.0 mM $HAuCl_4 \bullet 3H_2O$. The plasma was passed over the solution in a square once.

From Figure 2.29, it is evident that the gels, which are usually colourless/transparent, became increasingly pink and then purple with increasing concentrations of $HAuCl_4 \bullet 3H_2O$. This colour change indicates the formation of gold nanoparticles, consistent with observations by Olenki *et al.*[43]

UV-Vis absorption measurements were performed before and after plasma treatment to further confirm the presence of AuNPs. The characteristic SPR band in the 530-540 nm range was observed for concentrations of $HAuCl_4 \bullet 3H_2O$ above 0.25 mM (Figure 2.30). The intensity of this SPR peak increased with higher concentrations of $HAuCl_4 \bullet 3H_2O$, likely indicating an increase in the number of nanoparticles formed. The peak position was similar across all concentrations, suggesting that nanoparticle size remained consistent across the tested concentrations. Although no SPR peak was observed at 1.0 mM, the gels exhibited a pink colour change, suggesting that nanoparticles formed, though not enough to be detected by UV-Vis. No colour change was observed for the 0.05 mM $HAuCl_4 \bullet 3H_2O$ gel (Figure 2.29).

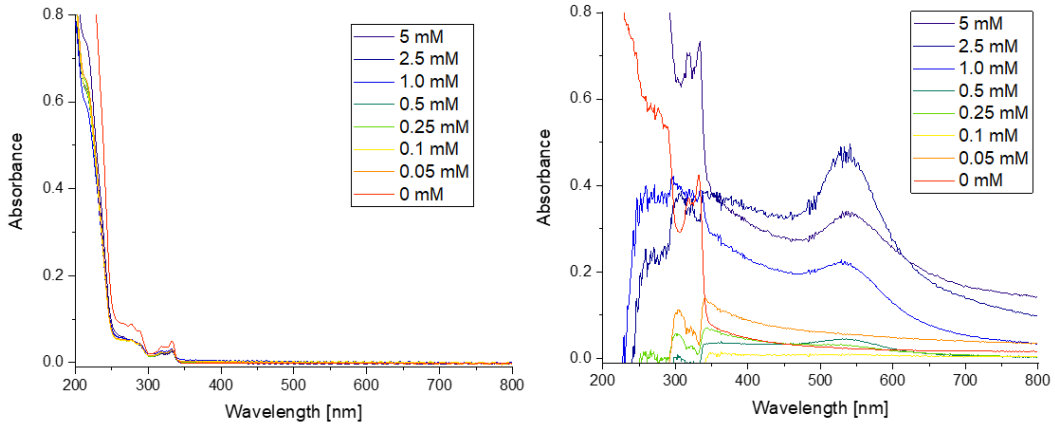

Figure 2.30. UV-Vis of 2NapFF (5 mg/mL) with 0 mM, 0.05 mM, 0.1 mM, 0.25 mM, 0.5 mM, 1.0 mM, 2.5 mM, and 5.0 mM $HAuCl_4 \bullet 3H_2O$ before (left) and after (right) plasma treatment/gelation.

These nanoparticle-containing gels, like the previous, can be 3D-printed into intricate shapes without nanoparticle diffusion into the solution, for worm-like micelle gelators. The gold nanoparticles only form at the interface where the plasma interacts with the solution, as illustrated in Figure 2.31a. This controlled formation allows the creation of multi-layered gel structures, in which nanoparticles can be selectively embedded in different layers (Figure 2.31b).

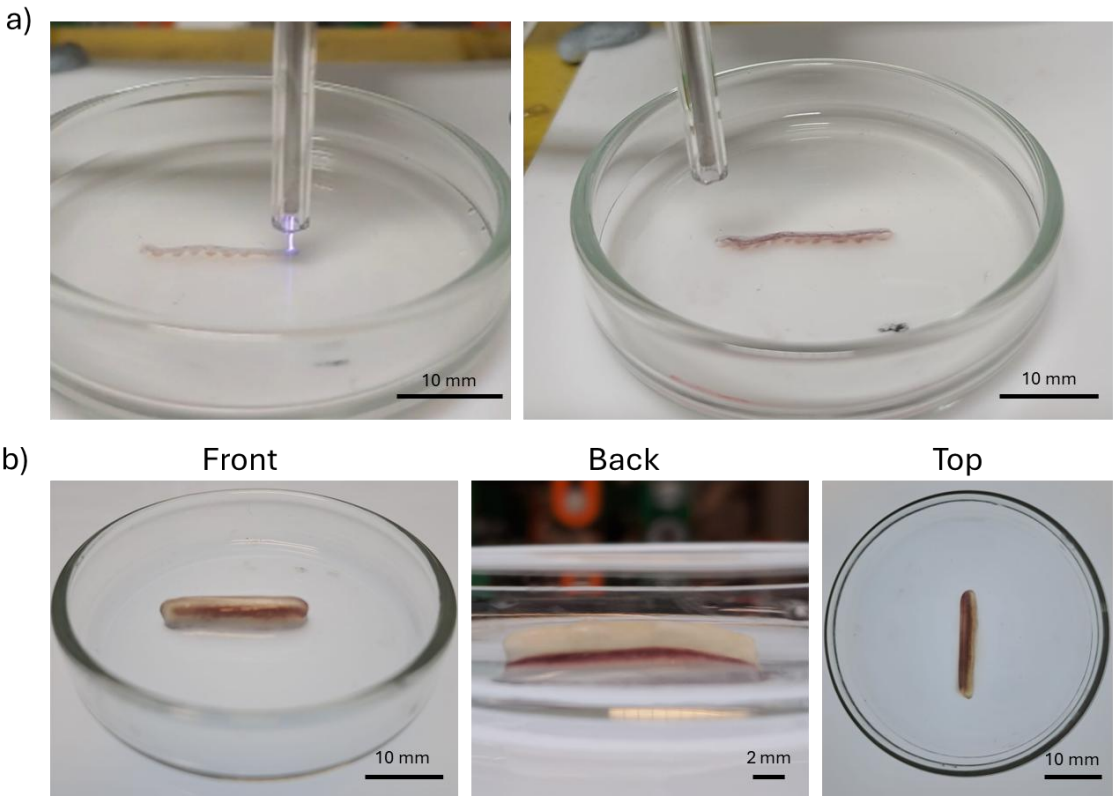

Figure 2.31. a) Images of plasma printed line of 2NapFF (5 mg/mL) with 2.5 mM $HAuCl_4 \cdot 3H_2O$, the plasma was passed over the solution twice in a straight line. b) Images of plasma printed line with three layers of 2NapFF (5 mg/mL) with the middle layer containing 2.5 mM $HAuCl_4 \cdot 3H_2O$.

To further confirm the presence of gold nanoparticles and determine the particle size, TEM images were collected by Margaret Mullin (University of Glasgow) from a 2NapFF plasma gel with 2.5 mM HAuCl4•3H2O and from a 2NapFF plasma gel without HAuCl4•3H2O. Comparing the two sets of images confirmed the presence of nanoparticles (Figures 2.32 and 2.33). The nanoparticles appear to be evenly distributed throughout the gel sample and aggregate onto the gel fibres, although this cannot be fully confirmed because the samples are soft, preventing the isolation of individual sections.

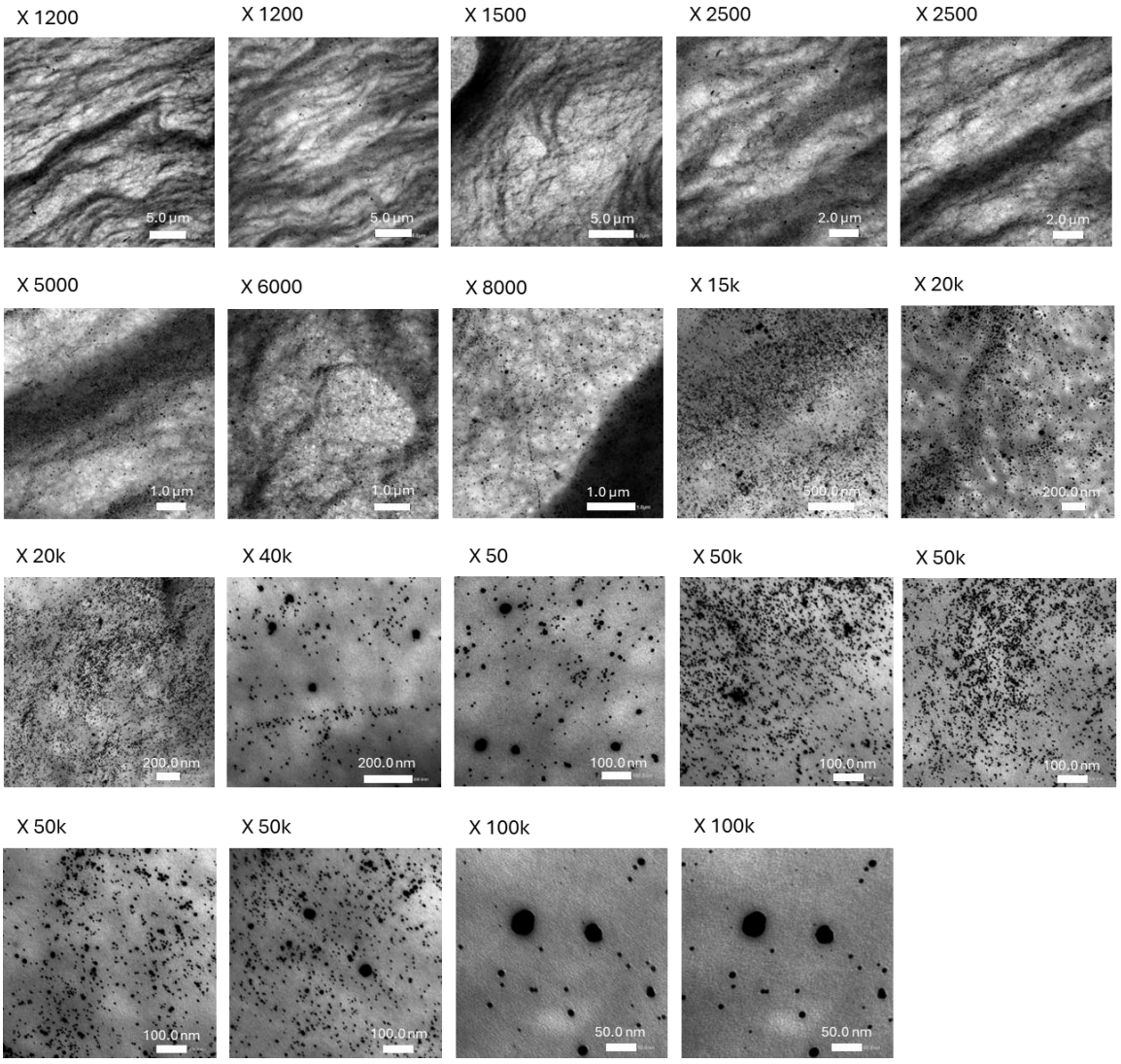

Figure 2.32. TEM images of the 2NapFF (5 mg/mL) plasma gels. The plasma was passed over the solution in a square twice, and multiple positions were imaged. The magnification of each image is indicated above.

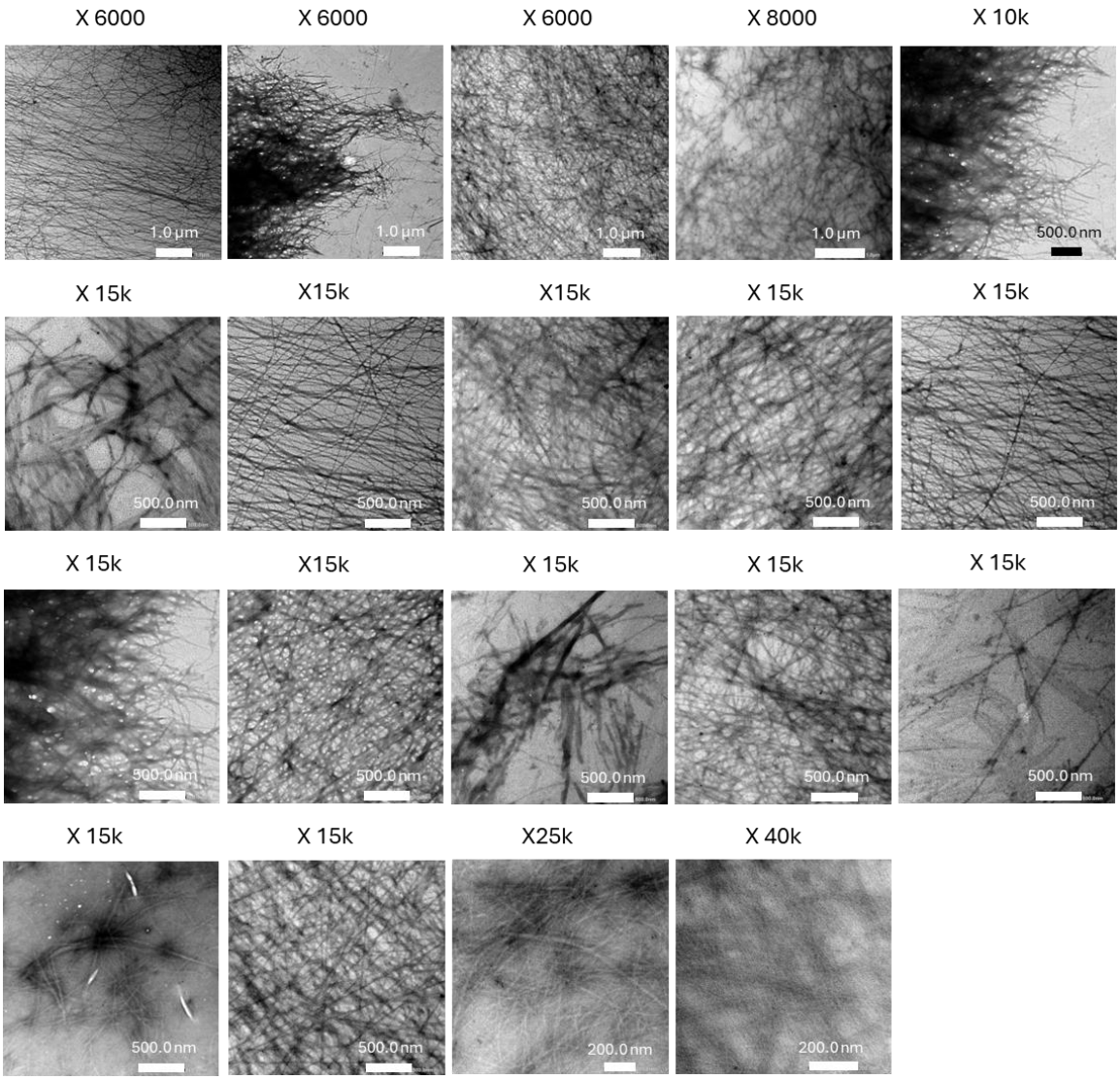

Figure 2.33. TEM images of the 2NapFF (5 mg/mL) plasma gels with $HAuCl_4 \bullet 3H_2O$ (2.5 mM). The plasma was passed over the solution in a square twice, and multiple positions were imaged. The magnification of each image is indicated above.

Image analysis was performed on the clearest images using ImageJ (Figure 2.34). The nanoparticles ranged in size from 2.5 nm to 230 nm, although the larger particles may have resulted from nanoparticle aggregation, as these particles in the images are not perfectly spherical. In the literature, the gold nanoparticles typically range in size from about 1 nm to 100 nm, and nanoparticles produced from a CAP plasma jet are approximately 20-90 nm with various shapes having been reported, including spherical, rod, triangular, star, cubic, or branched, depending on the synthesis method.[43,49]

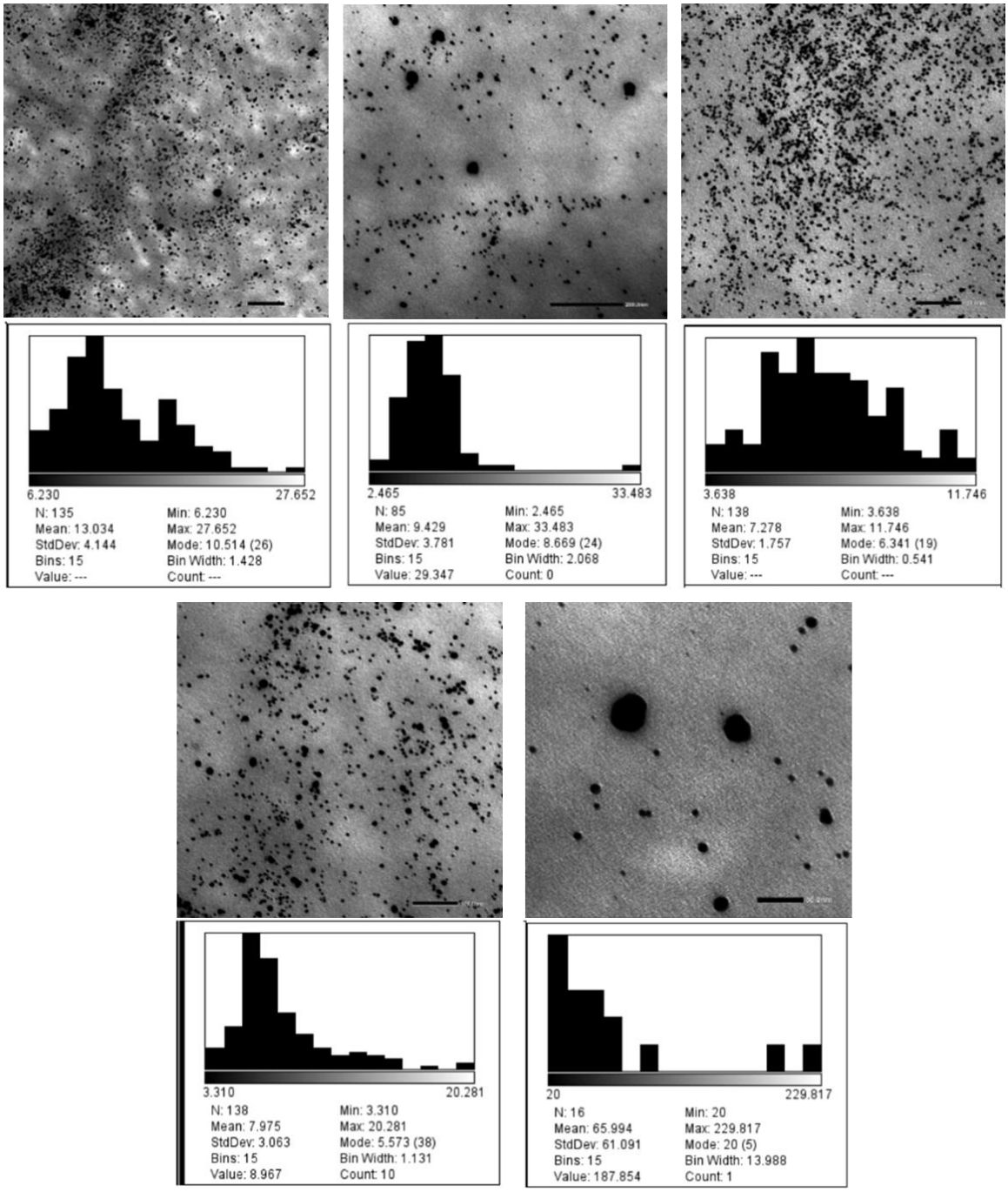

Figure 2.34. Image analysis of TEM images of the 2NapFF (5 mg/mL) plasma gels with $HAuCl_4 \bullet 3H_2O$ (2.5 mM). The magnification of each image is indicated above, and the image analysis below.

This method of simultaneously fabricating gels and producing nanoparticles was also tested with the 6BrNapAV gelator at $HAuCl_4 \bullet 3H_2O$ concentrations of 0.25 mM, 0.5 mM, 1.0 mM, 2.5 mM, and 5.0 mM. As with 2NapFF, successful nanoparticle-containing 3D-printed 6BrNapAV gels were produced. As shown in Figure 2.35, like the 2NapFF gels, the gels formed became increasingly pink and then purple as the $HAuCl_4 \bullet 3H_2O$ concentration increased. The pre-gel solution surrounding the final

gel also changed colour, indicating that it also contained gold nanoparticles. This is a natural consequence of localised gelation with different micellar solutions, as discussed previously. Because spherical micellar solutions do not gel immediately upon plasma application, but nanoparticles do form instantly, some nanoparticles are naturally dispersed in the solution.

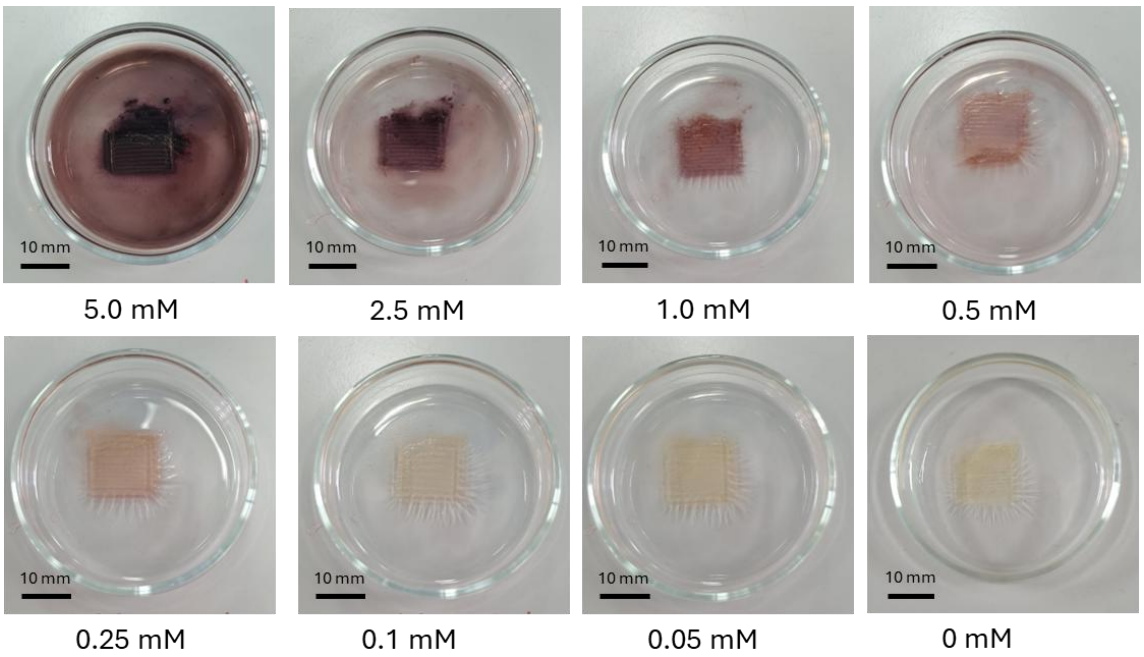

Figure 2.35. Images of the 15 x 15 mm 6BrNapAV gels plasma printed with 0 mM, 0.05 mM, 0.1 mM, 0.25 mM, 0.5 mM, 1.0 mM, 2.5 mM, and 5.0 mM $HAuCl_4 \bullet 3H_2O$. The plasma was passed over the solution in a square once.

Again, UV-Vis absorption measurements were performed before and after plasma treatment to confirm the presence of AuNPs. The characteristic SPR band was observed in the 530-550 nm range for concentrations above 0.25 mM, and the intensity of the SPR peak increased with higher concentrations of $HAuCl_4 \cdot 3H_2O$ (Figure 2.36). The peak position shifted to longer wavelengths at higher $HAuCl_4 \cdot 3H_2O$ concentrations (2.5 mM and 5.0 mM), suggesting that nanoparticle size increased with increasing $HAuCl_4 \cdot 3H_2O$ concentration.

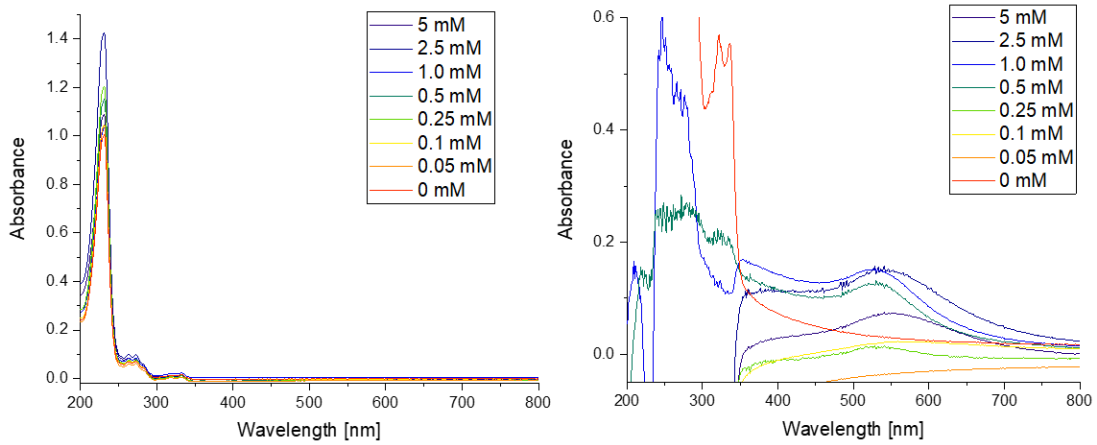

Figure 2.36. UV-Vis of 6BrNapAV (5 mg/mL) with 0 mM, 0.05 mM, 0.1 mM, 0.25 mM, 0.5 mM, 1.0 mM, 2.5 mM, and 5.0 mM $HAuCl_4 \cdot 3H_2O$ before (left) and after (right) plasma treatment/gelation.

SAXS data were also collected for 2NapFF plasma gels containing gold nanoparticles with initial $HAuCl_4 \cdot 3H_2O$ concentrations of 0.1 mM, 0.5 mM, 2.5 mM, and 5.0 mM. For the 0.1, 0.5, and 2.5 mM samples, the SAXS data were fitted to models of a flexible elliptical cylinder combined with a sphere and a power law. These data support the conclusion that the 0.1 mM sample contained nanoparticles, as indicated by a colour change but not by UV-vis. The radius of the sphere component in the model indicates gold nanoparticle sizes of 26.6 Å, 36.2 Å, and 36.4 Å for the 0.1, 0.5, and 2.5 mM samples, respectively. Notably, this radius increased with increasing $HAuCl_4 \cdot 3H_2O$ concentration, as observed by Olenki *et al.* in water.[43] The radii fall within the range observed in the TEM images; however, it should be considered that these samples are hydrated, unlike TEM samples.

The 5.0 mM gel was best fit by a flexible elliptical cylinder with an ellipsoid and power-law model, although its χ^2 value was still higher than those of the other fits. As CAP plasma can modify nanoparticle shape during gold nanoparticle formation, shifting it from spherical to plate-like geometries, this shift in the model for the highest concentration suggests that at 5.0 mm, the nanoparticles may have transitioned to a plate-like shape, although this has not been observed in TEM images, and there is no definitive model for this plate-like geometry, so it could not be confirmed.

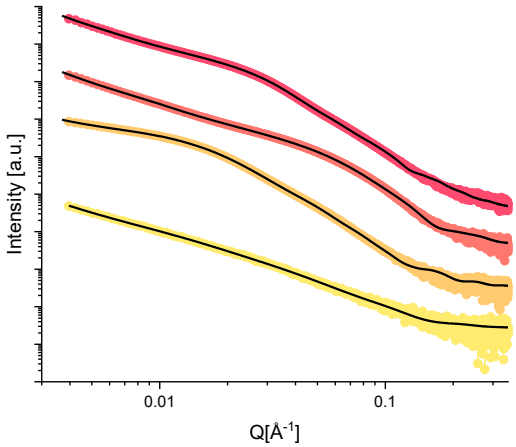

Figure 2.37. SAXS Data of 2NapFF (5 mg/mL) plasma gels containing from top to bottom 0.1 mM, 0.5 mM, 2.5 mM, and 5.0 mM $HAuCl_4 \bullet 3H_2O$.

All SAXS data also showed that the addition of nanoparticles altered the fibres from cylindrical to flexible elliptical cylinders. This is possibly due to nanoparticles disrupting self-assembly and aggregating onto fibres, leading to this change in fibre shape. The Kuhn length also increased with higher $HAuCl_4 \bullet 3H_2O$ concentrations, as more gold nanoparticles were produced, thereby reducing the network's flexibility. All parameter values for the SAXS fits are provided in Appendix 1.4.

2.3. Conclusions

This chapter has demonstrated that CAP can serve as an external trigger for gelation in LMWG hydrogels, with high spatial and temporal control. The mechanism of plasma-induced gelation was shown to be pH-driven, and this process was successfully visualised and quantified using Kineticolor analysis. A systematic exploration of plasma parameters established the conditions required to optimise gelation behaviour and enable reliable plasma-assisted 3D printing.

By integrating the plasma source directly onto a 3D printer, it was shown that patterned hydrogels and multilayer architectures with defined geometries can be fabricated. Furthermore, local mechanical properties of the gels can be tuned by varying plasma exposure. This highlights plasma printing's ability not only to control structure but also to locally modulate material properties within a single structure. In addition, this approach enables the simultaneous *in situ* formation of gold nanoparticles and gels, expanding the functional scope of plasma-printed hydrogels.

Looking ahead, a pulsed plasma source, rather than the sinusoidal plasma used in this work, offers significant potential for greater control. Pulsed plasmas can be operated at lower effective power, and variations in pulse parameters provide an additional means of tuning plasma chemistry and energy delivery. This increased level of control is expected to translate directly into control over gelation kinetics and mechanical properties.

Overall, this work establishes plasma as a versatile and powerful tool for the controlled fabrication of structured, tuneable, and functional gels.

2.4. Experimental

2.4.1. Materials

The gelators were synthesised by Prof. Dave Adams (University of Glasgow) as previously described, using established methods.[3,30] Tetrachloroauric (III) acid trihydrate ($HAuCl_4 \bullet 3H_2O$) was purchased from Thermo Fisher Scientific. Methyl red was purchased from Fluka Analytical. Universal indicator was purchased from Fisher Scientific. nile blue A dye, and sodium hydroxide were purchased from Sigma Aldrich. Hydrochloric acid was purchased from Honeywell. Deionised water was used in all experiments.

2.4.2. Preparation of solutions

To prepare the gelator stock solutions, the gelator was dissolved in H_2O at high pH and stirred for 16 hours to obtain concentrations of 2 mg/mL, 5 mg/mL, and 10 mg/mL, as required. After 16 hours, the solutions were pH-adjusted with HCl (1 M) and NaOH (1 M). For the methyl red gelator solutions, methyl red (10 mg/mL in ethanol) was added directly (2 µL/mL) to the gelator solution, and the pH was adjusted to pH 7. For the universal indicator gelator solutions, universal indicator (20 µL/mL) was added directly to the gelator solution, and the pH was adjusted to pH 7.

2.4.3. Plasma gelation

The Plasma generation equipment provided by Prof James Walsh (University of York) included a high-voltage power source capable of generating a sinusoidal output at a frequency of approximately 12 kHz, with amplitudes exceeding 5 kV.

A Tektronix DPO 5054 Digital Phosphor Oscilloscope was used to record the discharge current and voltage using a Pearson 7655 current monitor and a Tektronix P6015A (P-Series) high-voltage probe. The plasma-generating electrode unit contained a tungsten rod, 1.5 mm in diameter, connected to the power source's high-voltage output and fixed within a quartz capillary (outer diameter = 4 mm, inner diameter = 2 mm). A 3D-printed housing was fabricated to hold the electrode at the centre of the capillary, allowing gas to flow through the quartz capillary and exit past the tip of the electrode rod. In all cases, argon gas (99.9% purity) was used and supplied *via* mass flow controller at a rate of 0.5 LPM. The quartz capillary exit was oriented vertically downward towards the sample. For plasma gelation, the pre-gel solution was transferred into a 5 cm diameter petri dish. The pin electrode was positioned approximately 0.5 cm above the liquid surface. In all experiments, argon flow was initiated 30 s prior to plasma generation to ensure that air within the quartz tube was removed. All experiments were performed at a fixed operating frequency.

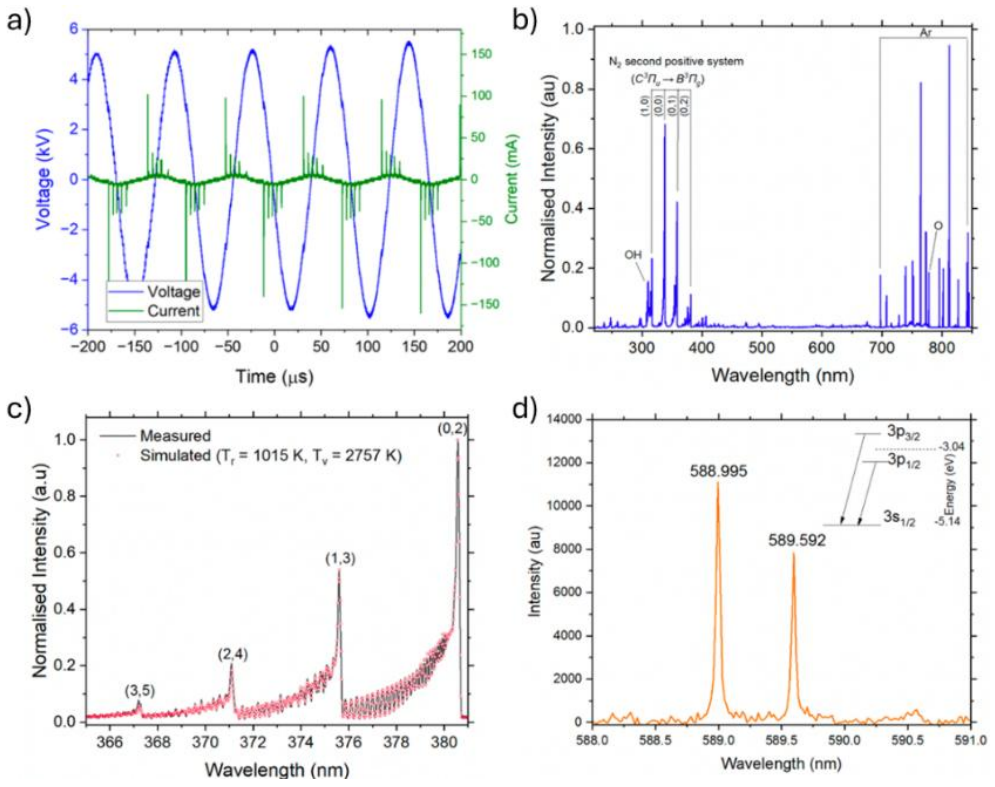

Figure 2.40. a) Measured voltage and current recorded during plasma generation, b) low-resolution optical emission spectra from 250 to 850 nm, c) high-resolution spectra of Nitrogen second positive system overlaid with simulated spectra at Tr = 1015 K and Tv = 2757 K, and d) characteristic Na emission that is observed after prolonged treatments.

2.4.4. 3D printing

A 3D printer (RepRap Huxley) was modified by Dr Bart Dietrich (University of Glasgow) to allow 3D printing using the plasma setup. The quartz tube was attached to the 3D printer and positioned approximately 0.5 cm above the liquid surface. The pre-gel solution was transferred to a Petri dish (5 cm in diameter) positioned below the quartz tube. The 3D printer commands and the plasma were turned on simultaneously. The printer head speed was set to 100 mm/min.

2.4.5. Nanoparticle gel 3D printing

For the gold nanoparticle gels, aqueous tetrachloroauric (III) acid trihydrate ($HAuCl_4 \bullet 3H_2O$) stock solutions (50 mM or 100 mM) were added to 2NapFF (5 mg/mL) solutions to achieve the desired $HAuCl_4 \bullet 3H_2O$ concentration. These $HAuCl_4 \bullet 3H_2O$ gelator solutions were adjusted to pH 7 with NaOH (1M) and transferred to petri dishes for printing. Gels were formed using the 3D plasma setup described above. After exposure, the excess solution was removed using a pipette, leaving the printed gel containing nanoparticles.

2.4.6. pH measurements

pH measurements were performed using a HANNA FC200 pH probe with a 6 mm × 10 mm conical tip. Unless specified, the measurements were taken at ambient temperature. The pH values were accurate to ±0.1.

The pK_a values of the gelator systems were determined by titration *via* the addition of 2.5 µL aliquots of 0.1 M HCl solution to the hydrogels containing 1 molar equivalence of 0.1 M NaOH at 25°C. The temperature was controlled using a circulating water bath. The system was stirred between recording the pH values and during HCl addition. The system was left to equilibrate overnight before the titration.

2.4.7. HPLC

30 x 30 mm gel squares were plasma-printed using the 3D printer plasma setup described above. The samples were frozen and then freeze-dried in a Labogene ScanVac CoolSafe over 16 hours. These samples were then dissolved in

H_2O/acetonitrile (90/10 %) with 1 eq. of NaOH (1 M) to give a concentration of 1 mg/mL and stirred for 16 hrs. These samples were measured using a Thermo Scientific UltiMate 3000 by Libby Marshall (University of Glasgow). The injection volume was 20 µL, with a gradient from 40% to 90% acetonitrile in H_2O over 20 min. The temperature was set to 40 °C.

2.4.8. Small-angle X-ray scattering

Plasma gel SAXS measurements were collected using the X-ray beam of the I22 beamline (Diamond Light Source, Oxfordshire, UK) during experiment SM41059-1 by H. Futty, D Harris, and T. Maurya (University of Glasgow) and A.J. Smith (Diamond Light Source). The I22 beamline operates at an energy of 12.4 keV and a camera length of 5.832 m, resulting in a Q range of 0.0040–0.304 $Å^{-1}$. 15 x 15 mm plasma gels were prepared as described above from 2NapFF (5 mg/mL, pH 7.0) and loaded into glass capillaries using a 2 mL syringe with a 21G plastic needle. The raw data were processed using the Dawn Science software (version 2.27).[50] As part of the processing, the backgrounds were subtracted from the raw 2D SAXS data, and an azimuthal integration between 45° and -45° was performed to reduce the data to an I vs q plot. The plots were then fitted to structural models in SASView 6.0.1.[51] To calculate the X-ray scattering length densities (SLDs) for all samples, the NIST neutron activation and scattering calculator was used, assuming a density of 1.55 g/cm^3 for all gelators.[52]

2.4.9. Rheological measurements

Rheological experiments were conducted using an Anton Paar Physica MCR 301 rheometer. Viscosity measurements were taken with a 75 mm cone plate geometry (CP75, cone angle 1°) at a measuring distance of 0.05 mm. Frequency and strain sweeps were performed using a 12.5 mm parallel-plate geometry (PP12.5). The measuring distance was manually lowered until a force of 0.01 N was recorded. The measurements were taken at a constant temperature of 25°C. Viscosity sweeps were performed over 0.1 s^{-1} to 1000 s^{-1} shear rate. Strain sweeps were performed over 0.01 % to 1000 % strain at a frequency of 10 rad/s. Frequency sweeps were performed at 0.5% strain, increasing the frequency from 1 rad/s to 100 rad/s. 15 x 15 mm gel squares were plasma-printed using the 3D printer

plasma setup described above, and the samples were used immediately. Samples were collected in triplicate. As the hydrogel was not removed from the surface of the petri dish after gelation, no damage occurred. The rheometer set up is shown in Figure 2.41.

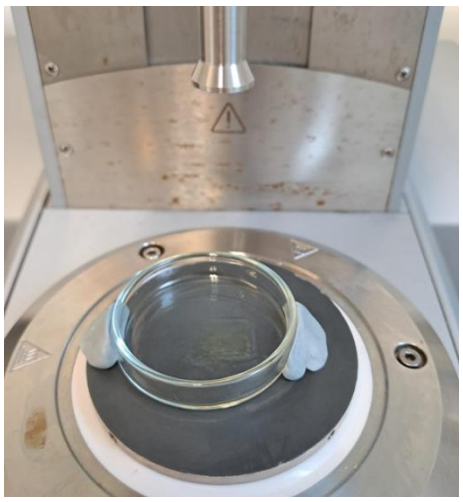

Figure 2.41. Rheometer set up for strain and frequency sweeps.

2.4.10. Computer vision analysis with Kineticolor

All analysis videos were recorded with a Panasonic HC-V180 at 720p and 25 frames per second. All videos were recorded with manual focus and no auto white balance. These settings maintained focus and video quality throughout each experiment. All videos were recorded in front of an LED light panel in a dark room to minimise the effects of ambient light, ensure the setup was well-lit, and achieve good-quality video output. Still images of the solutions were taken using the same video camera. The resulting video and photo files were uploaded to Kineticolor and processed by Calum Fyfe and Timothy. J. McCabe (University of Strathclyde). The analytical workflow has been published.[53]

2.4.11. Confocal microscopy

For imaging, nile blue A dye (0.1 wt% aqueous solution, 2 µL per mL of gel) was incorporated into gels to allow for observation by confocal fluorescence microscopy using a Zeiss LSM 710 confocal microscope fitted with Zeiss N-Achroplan 10×, LD Plan- NEUFLUAR 20× (0.4 Korr Ph 2), and LD EC Epiplan NEUFLUAR 50× (0.55 DIC) objectives. Lines of gel were plasma printed as described above. The excess solution was removed by pipette, and the gels were washed

with water to remove any residual solution. The gels were then imaged immediately in the Petri dish to prevent any damage.

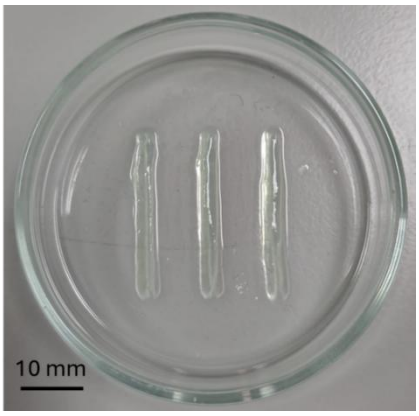

Figure 2.42. 3D printed gel line for confocal microscopy. Gels were imaged in the petri dish, so no damage occurred.

2.4.12. UV-Vis

Absorption spectra were recorded on an Agilent Cary 60 UV-Vis spectrophotometer using a quartz cuvette with 0.1 mm path length. 15 mm × 15 mm plasma gel samples were prepared as above and used immediately. The gel was placed on one side of the cuvette, and the other slide was pressed onto it to trap the gel. UV-Vis spectroscopy of the gel without $HAuCl_4 \bullet 3H_2O$ was used as the background for gels containing $HAuCl_4 \bullet 3H_2O$ after data collection.

2.4.13. TEM

TEM images were captured on a JEOL 1400 Flash TEM operating at 80 kV, using TEM Centre software version 1.7.26.3016 on a CCD camera by Margaret Mullin (University of Glasgow). Samples were imaged on 400-mesh carbon-coated copper grids, which were discharged prior to use. Gel samples containing gold nanoparticles were prepared as described above, and the grids were placed on top of the gel for 30 minutes. Afterwards, the grids were removed from the gel, leaving a small amount of gel attached, which was allowed to dry before imaging. Image analysis was performed on the TEM images using ImageJ.

2.5. References

1 E. R. Draper and D. J. Adams, *Chem.*, 2017, **3**, 390–410.

2 M. de Loos, B. L. Feringa and J. H. van Esch, *Eur. J. Org. Chem.*, 2005, **2005**, 3615–3631.

3 L. Chen, K. Morris, A. Laybourn, D. Elias, M. R. Hicks, A. Rodger, L. Serpell and D. J. Adams, *Langmuir*, 2010, **26**, 5232–5242.

4 V. Nele, J. P. Wojciechowski, J. P. K. Armstrong and M. M. Stevens, *Adv. Funct. Mater.*, 2020, **30**, 2002759.

5 J. Raeburn, G. Pont, L. Chen, Y. Cesbron, R. Lévy and D. J. Adams, *Soft Matter*, 2012, **8**, 1168–1174.

6 J. Raeburn, A. Zamith Cardoso and D. J. Adams, *Chem. Soc. Rev.*, 2013, **42**, 5143.

7 L. Chen, T. O. McDonald and D. J. Adams, *RSC Adv.*, 2013, **3**, 8714.

8 S. C. Bremmer, A. J. McNeil and M. B. Soellner, *Chem. Commun.*, 2014, **50**, 1691.

9 E. R. Draper, H. Su, C. Brasnett, R. J. Poole, S. Rogers, H. Cui, A. Seddon and D. J. Adams, *Angew. Chem. Int. Ed.*, 2017, **56**, 10467–10470.

10 E. K. Johnson, D. J. Adams and P. J. Cameron, *J. Mater. Chem.*, 2011, **21**, 2024–2027.

11 X. Y. Liu, in *Low Molecular Mass Gelator. Topics in Current Chemistry*, Springer, 2005, vol. 256, pp. 1–37.

12 M. J. S. Hill and D. J. Adams, *Soft Matter*, 2022, **18**, 5960–5965.

13 F. Andriamiseza, D. Bordignon, B. Payré, L. Vaysse and J. Fitremann, *J. Colloid Interface Sci.*, 2022, **617**, 156–170.

14 A. Chalard, M. Mauduit, S. Souleille, P. Joseph, L. Malaquin and J. Fitremann, *Addit. Manuf.*, 2020, **33**, 101162.

15 A. C. Dell, G. Wagner, J. Own and J. P. Geibel, *Pharmaceutics*, 2022, **14**, 2596.

16 M. E. Prendergast and J. A. Burdick, *Adv. Mater.*, 2019, **32**, 1902516.

17 X. Mu, J. K. Sahoo, P. Cebe and D. L. Kaplan, *Polymers (Basel).*, 2020, **12**, 2936.

18 B. Derby, *Annu. Rev. Mater. Res.*, 2010, **40**, 395–414.

19 R. E. Ginesi, J. Doutch and E. R. Draper, *Faraday Discuss.*, 2025, **260**, 347–359.

20 M. C. Nolan, A. M. Fuentes Caparrós, B. Dietrich, M. Barrow, E. R. Cross, M. Bleuel, S. M. King and D. J. Adams, *Soft Matter*, 2017, **13**, 8426–8432.

21 H. Conrads and M. Schmidt, *Plasma Sources Sci. Technol.*, 2000, **9**, 441–454.

22 X. Lu, G. V. Naidis, M. Laroussi, S. Reuter, D. B. Graves and K. Ostrikov, *Phys. Rep.*, 2016, **630**, 1–84.

23 D. Basumatary, A. Gaikhe, P. Radhakrishnanand and K. Sankaranarayanan, *J. Phys. D Appl. Phys.*, 2024, **57**, 285402.

24 T. F. de Melo, L. C. Rocha, R. P. Silva, R. S. Pessoa, A. M. P. Negreiros, R. Sales Júnior, M. B. Tavares and C. Alves Junior, *Mater.*, 2022, **15**, 4854.

25 F. Judée, S. Simon, C. Bailly and T. Dufour, *Water Res.*, 2018, **133**, 47–59.

26 P. Bhatt, P. Das and K. Sankaranarayanan, *Phys. Chem. Chem. Phys.*, 2025, **27**, 24969-24985.

27 S. Zhang, W. Huang, E. Feizollahi, M. S. Roopesh and L. Chen, *Innov. Food Sci. Emerg. Technol.*, 2021, **67**, 102567.

28 G. Eazhumalai, R. G. T. K. and U. S. Annapure, *Sustain. Food Technol.*, 2025, **3**, 1203–1217.

29 R. R. Sonani, S. Bianco, B. Dietrich, J. Doutch, E. R. Draper, D. J. Adams and E. H. Egelman, *Cell Rep. Phys. Sci.*, 2024, **5**, 101812.

30 K. McAulay, B. Dietrich, H. Su, M. T. Scott, S. Rogers, Y. K. Al-Hilaly, H. Cui, L. C. Serpell, A. M. Seddon, E. R. Draper and D. J. Adams, *Chem. Sci.*, 2019, **10**, 7801–7806.

31 E. R. Draper, B. Dietrich, K. McAulay, C. Brasnett, H. Abdizadeh, I. Patmanidis, S. J. Marrink, H. Su, H. Cui, R. Schweins, A. Seddon and D. J. Adams, *Matter*, 2020, **2**, 764–778.

32 M. J. S. Hill, A. M. Fuentes-Caparrós and D. J. Adams, *Biomacromolecules*, 2023, **24**, 4253–4262.

33 S.-Y. Ryu and S.-Y. Kwak, *J. Nanosci. Nanotechnol.*, 2013, **13**, 4193–4202.

34 C. Yan, C. Fyfe, L. Minty, H. Barrington, C. Jamieson and M. Reid, *Chem. Sci.*, 2023, **14**, 11872–11880.

35 N. R. Murray, T. J. D. McCabe, M. Reid and E. R. Draper, *J. Mater. Chem. C Mater.*, 2024, **12**, 12483–12490.

36 C. Yan, M. Cowie, C. Howcutt, K. M. P. Wheelhouse, N. S. Hodnett, M. Kollie, M. Gildea, M. H. Goodfellow and M. Reid, *Chem. Sci.*, 2023, **14**, 5323–5331.

37 H. Barrington, A. Dickinson, J. McGuire, C. Yan and M. Reid, *Org. Process Res. Dev.*, 2022, **26**, 3073–3088.

38 R. Geethalakshmi and Sarada, *Int. J. Nanomedicine*, 2012, 5375.

39 M. M. Kemp, A. Kumar, S. Mousa, T.-J. Park, P. Ajayan, N. Kubotera, S. A. Mousa and R. J. Linhardt, *Biomacromolecules*, 2009, **10**, 589–595.

40 R. Sardar, A. M. Funston, P. Mulvaney and R. W. Murray, *Langmuir*, 2009, **25**, 13840–13851.

41 S. Paidari and S. A. Ibrahim, *Gold Bull.*, 2021, **54**, 31–36.

42 G. Pasparakis, *WIREs Nanomed. Nanobiotechnol.*, 2022, **14**, e1817.

43 J. Olenik, V. Shvalya, M. Modic, D. Vengust, U. Cvelbar and J. L. Walsh, *ACS Sens.*, 2025, **10**, 387–397.

44 A. Izadi and R. J. Anthony, *Plasma Process. Polym.*, 2019, **16**, e1800212.

45 J. Chantaramethakul, N. Choophun, C. Chokradjaroen, A. Watthanaphanit, N. Saito and G. Panomsuwan, *J. Phys. Chem C*, 2023, **127**, 3184–3193.

46 R. N. Mitra and P. K. Das, *J. Phys. Chem C*, 2008, **112**, 8159–8166.

47 S. Mukherjee, M. Núñez-Martínez, S. Illescas-Lopez, A. Jeyakumar, M. T. Lopez-Lopez, J. M. Cuerva, V. Bhatia, J. A. Gavira, L. Álvarez de Cienfuegos and J. Haldar, *Biomater. Sci.*, 2025, **13**, 6818–6836.

48 V. V. Adole, G. Mishra and P. Chakraborty, *ACS Appl. Nano Mater.*, 2025, **8**, 19535–19548.

49 H. Duman, E. Akdaşçi, F. Eker, M. Bechelany and S. Karav, *Nanomaterials*, 2024, **14**, 1805.

50 M. Basham, J. Filik, M. T. Wharmby, P. C. Y. Chang, B. El Kassaby, M. Gerring, J. Aishima, K. Levik, B. C. A. Pulford, I. Sikharulidze, D. Sneddon, M. Webber, S. S. Dhesi, F. Maccherozzi, O. Svensson, S. Brockhauser, G. Náray and A. W. Ashton, *J. Synchrotron Radiat.*, 2015, **22**, 853–858.

51 http://www.sasview.org/ .

52 https://www.ncnr.nist.gov/resources/activation/.

53 N. Bugeja, C. Oliver, N. McGrath, J. McGuire, C. Yan, F. Carlysle-Davies and M. Reid, *Digit. Discovery*, 2023, **2**, 1143–1151.

This chapter is adapted from the following publications:

“Designing and Controlling Transient Supramolecular Gels”

ChemSystemsChem, 2024, 7(2), e202400073.

E.L. Bowley, S. Bianco, F. Hallam Stewart, C. M. Wallace, R.E. Ginesi, A.S. Loch, M. Rosenthal, A.J. Smith, and D.J. Adams.

E.L. Bowley performed the rheology, confocal microscopy and pH experiments. D.J. Adams and A.D. Loch (University of Glasgow) synthesised the gelators under investigation. S. Bianco, F. Hallam Stewart, C. M. Wallace, R.E. Ginesi (University of Glasgow), M. Rosenthal (ESRF), and A.J. Smith (Diamond Light Source) aided the collection and processing of SAXS data.

3.1. Introduction

Supramolecular gels present a promising approach for creating novel materials by mimicking natural out-of-equilibrium systems.[1,2] These dynamic systems can undergo changes in state or properties in response to internal or external stimuli, such as pH, temperature, enzymatic reactions, strain, light, or redox processes.[2-10] While much of the current research has focused on changes triggered by external factors, this chapter builds on current transient systems that enable programmable, time-dependent changes in material properties through internal triggers.[3,11] By programming these materials to exhibit specific behaviours under different conditions, they hold vast potential for applications ranging from drug delivery to material development.[12-15]

As discussed previously, among the various external triggers, pH has garnered significant attention in the development of stimuli-responsive materials due to its ease of control and broad application potential.[16,17] Numerous systems have been designed to respond to pH changes, including polymer systems with charged or ionisable groups that swell at specific pH values, and gels that form, change, or dissolve in response to pH fluctuations.[18,19] While these systems exhibit impressive responsiveness, they generally require an external trigger to induce the desired change, thereby limiting their functionality to simple pH-responsive behaviours rather than to programmable, time-dependent transformations.

The introduction of temporal control into these systems opens up new opportunities for advanced applications. For example, programmed changes in diffusion properties could enable the controlled release of drugs or fragrances at specific intervals, while programmed switching of transparency could serve as indicators of product expiration.[20,21] Incorporating temporal control is essential for designing complex systems with dynamic functionality and underscores the importance of temporal programming in developing next-generation materials with adaptive, life-like behaviours.

As discussed in section 1.9, Boekhoven *et al.* reported the first transient self-assembled system fuelled by a chemical reaction that facilitated a sol-to-gel-to-sol transition.[2] Since then, numerous examples of transient systems driven by

changes in the equilibrium of gel networks have been developed.[5] In most of these systems, the addition of a chemical fuel alters the self-assembly equilibrium, leading to changes in the gel state or network structure.[1,2,15] For instance, the transient system this chapter replicates combines a urea/urease reaction with methyl formate hydrolysis. Combining these pH triggers results in an initial increase in pH, followed by a decrease over time, thereby driving a gel-to-sol-to-gel transition. The urease-induced hydrolysis of urea generates ammonia, which initially raises the system's pH; thereafter, the hydrolysis of methyl formate becomes dominant, producing protons that lower the pH (Figure 3.1).[11,22,23]

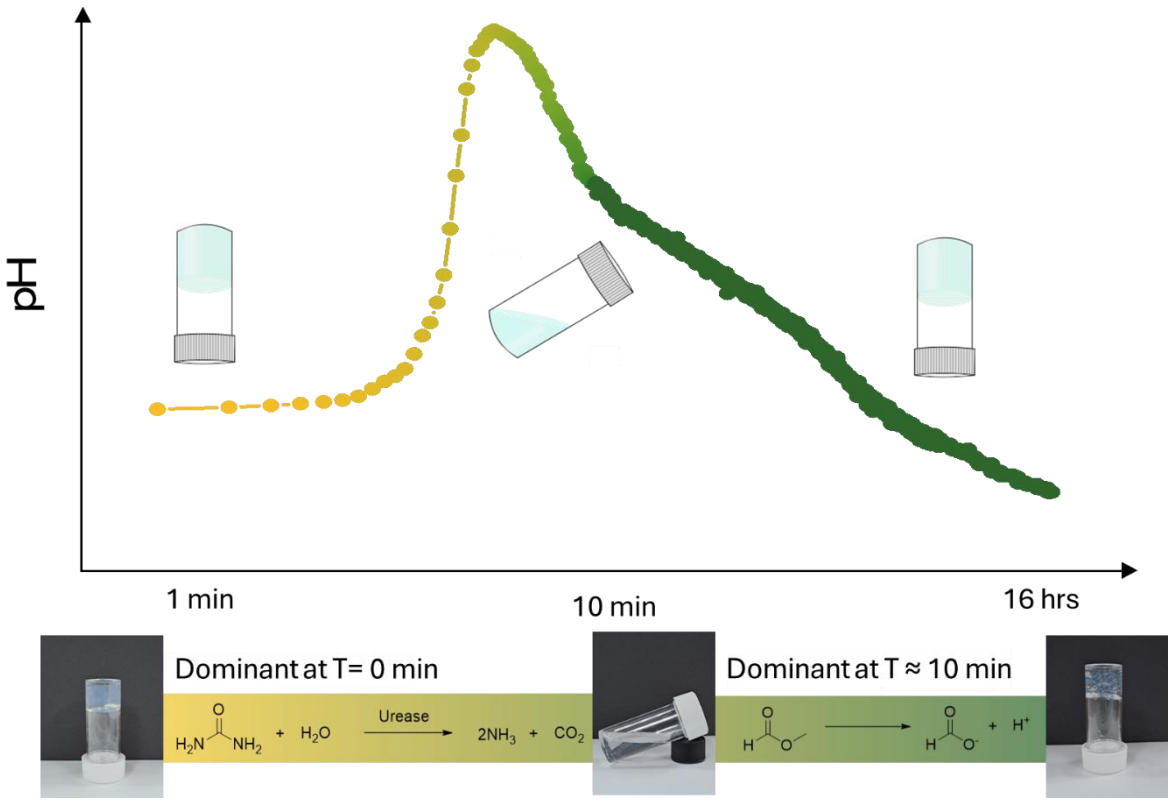

Figure 3.1. Urea/Urease and methyl formate reactions and the resulting change in pH, with images showing the gel-to-sol-to-gel transitions.

Supramolecular transient systems formed from low molecular weight gelators (LMWG) offer high tunability and dynamic behaviour. This transient nature provides access to novel materials that would otherwise be unattainable by conventional methods. Consequently, it is vital to understand how to design these pre-programmable systems to unlock their full potential. Despite the growing body of work on transient gel systems, many studies provide limited insight into the diversity of gelators, chemical fuels, and experimental conditions under which

these systems are studied, with much of the gelator choice being down to chance. It is also often suggested that these systems can be applied to a broad range of gelators and conditions, yet only one ideal system is presented, casting doubt on these claims. Finally, rheological measurements, which are essential for understanding their mechanical properties, are rarely reported. In many cases, the properties of the "final gel" are reported based on data collected 24 hours after triggering, typically when the system's pH has reached a plateau.[23,24] However, this time point may not represent the moment at which the system has fully stabilised or ceased to evolve.

In this chapter, the urea/urease/methyl formate transient system is further examined by investigating a broad library of LMWG and assessing the influence of various pH triggers across a range of temperatures. The effect of replacing methyl formate with ethyl formate and *n*-propyl formate on modulating the rate of pH decrease is also explored. Finally, system ageing is examined by measuring mechanical properties over 1 month, providing valuable insights into long-term stability and evolution.

3.2. Results and discussion

3.2.1. Urea/urease/methyl formate transient gels

The Adams group has previously reported a transient gel system that undergoes a gel-to-sol-to-gel transition using the 1ThNapFF gelator.[11,22,23] This system consisted of a DMSO/H_2O(20/80 v/v) mixture containing 1ThNapFF at 2 mg/mL, along with urea/urease and methyl formate. Initially, a gel forms at low pH, following a standard solvent-switch hydrogel mechanism. However, after approximately five minutes, the gel transitions into a sol due to the urea-urease reaction, which increases the pH above the pK_a. This deprotonates the terminal carboxylic acid, increasing the solubility and yielding a sol phase containing worm-like micelles. Once the hydrolysis of methyl formate becomes more dominant than the urea/urease reaction, the pH decreases again. When the pH drops below the apparent pK_a, the system transitions back to a gel state as the gelator is again protonated, reducing solubility. This reduces fibre repulsion and enhances the hydrophobic effect, thus forming a gel.

Notably, there is no reason this system should be restricted to the 1ThNapFF gelator, although the triggers have never been applied to other gelators or materials. Therefore, to explore this, a library of readily available LMWGs was examined to broaden the system's scope (Figure 3.2). The goal was to understand the scope of the methyl formate and urea/urease transient system and explore the range of achievable properties. Throughout this chapter, the 1ThNapFF DMSO/H_2O static gel is used as a non-transient analogue for comparison.

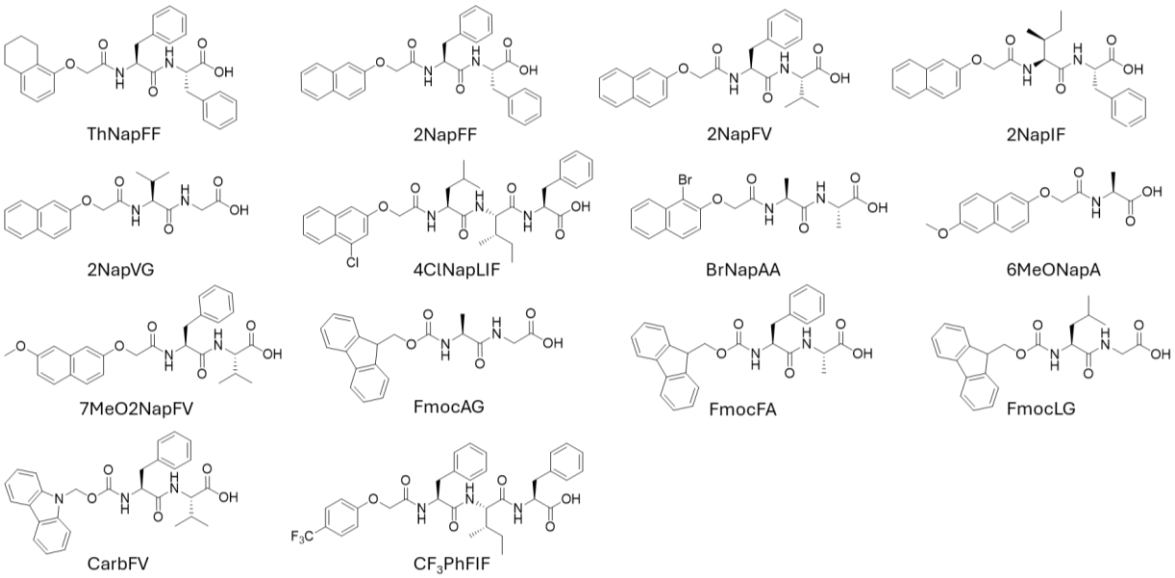

Figure 3.2. Structure of the LMWGs examined in this chapter and the acronyms used.

Initially, all selected gelators were tested for gelation in the DMSO/H_2O solvent-switch system at a constant 20/80 v/v ratio, as used for 1ThNapFF. The solvent-switch gels were left for 16 hours after mixing to determine whether a hydrogel formed. The results, summarised in Table 3.1, indicate that gelators with higher hydrophobicity, characterised by calculated logP values (clogP) greater than 2.10, were more likely to form successful gels. The hydrophobicity of each gelator was estimated from predicted clogP values calculated using an online prediction program.[25] However, this cannot be used as a definitive method for predicting whether an LMWG will gel, as evidenced by the molecule 4ClNapLIF, which has a clogP of 3.94 but did not form a gel. This is because hydrophobic interactions alone are not sufficient to induce self-assembly; additional bonding interactions are required to form the network structures that yield a gel.

It was also observed that different gelators exhibited varying gelation times, which can be attributed to differences in the network structures formed and in gelator solubility in DMSO and water, thereby affecting the rate of gelator aggregation.

Table 3.1. Results of the solvent-switch gelator test at 1 minute and 16 hours after mixing. ✓ indicates gel formation, and x indicates no gel formation. The clogP values of each gelator are included.

Gelator	Gel 1 minute after mixing	Gel 16 hours after mixing	c(logP) [a]
1ThNapFF	✓	✓	2.74
2NapFF	✓	✓	2.76
2NapIF	x	✓	2.58
2NapFV	x	x	2.08
2NapVG	x	x	0.83
4ClNapLIF	x	x	3.94
BrNapAA	x	x	0.62
6MeONapA	x	x	0.44
7MeONapFV	✓	✓	2.11
FmocAG	x	✓	2.87
FmocFA	✓	✓	4.11
FmocLG	✓	✓	4.18
CarbFV	✓	✓	4.75
CF_3PhFIF	✓	✓	3.19

[a] clogP calculated using an online prediction program and represents the predicted hydrophobicities.[25]

The rheological properties of successful hydrogels were also measured (Figure 3.3). Despite clogP values indicating whether a gelator might gel, no such link exists between the hydrophobicity of the gelator and the strength of the resulting gel. Again, attributed to differences in network structure and fibre formation.

It is worth noting that although 7MeO2NapFV and FmocAG appeared to form a gel, they did not maintain gel-like behaviour at frequencies above ≈ 30 rad/s, suggesting frequency-dependent network breakdown. These materials are therefore not true gels. The frequency sweeps for the DMSO/H_2O gels are provided in Appendix 2.1.

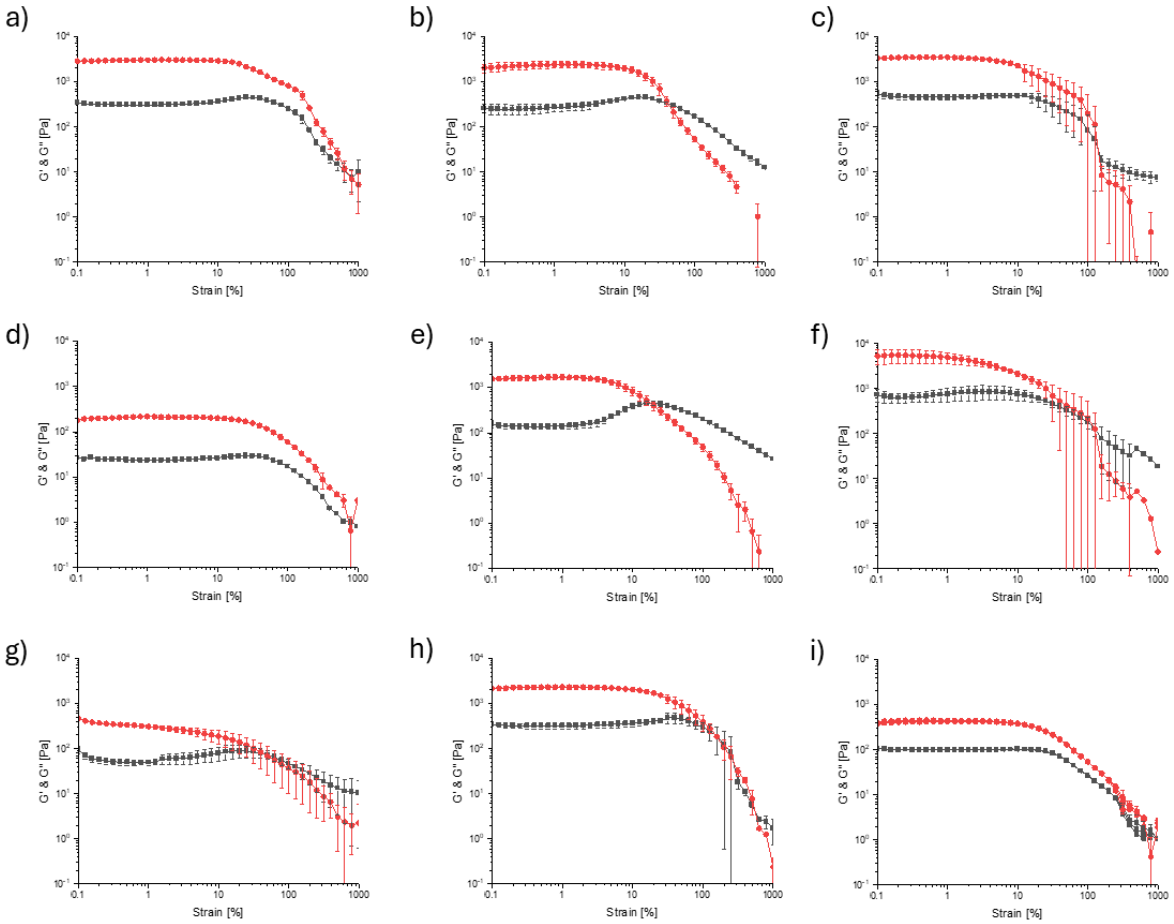

Figure 3.3. Strain sweeps of a) 1ThNapFF, b) 2NapFF, c) 2NapIF, d) 7MeO2NapFV, e) CarbFV, f) CF_3PhFIF, g) FmocAG, h) FmocFA, and I) FmocLG. The red symbols represent G′, the black symbols G″. Samples were collected in triplicate and averaged. Error bars show the standard deviation between samples.

In this chapter, T_{gel} is defined as the temperature at which a pre-formed gel melts, rather than the temperature at which a pre-gel solution transitions from a sol to a gel state, as discussed in Chapter 1. T_{gel} values of the successful solvent-switch gels were collected to assess their thermal stability, measured using a heat-cool cycle on a rheometer; the values are included in Table 3.2. The T_{gel} value of a gel was taken as the temperature at which the mechanical properties (G′ and G″) decreased to 95% of their initial values.

Table 3.2. T_{gel} values of gelators. The values were calculated from the heat-cool cycles provided in Appendix 2.2.

Gelator	T_{gel} (°C)
ThNapFF	> 90
2NapFF	79.2
2NapIF	73.0
7MeO2NapFV	35.9
FmocAG	34.9
FmocFA	31.7
FmocLG	73.0
CarbFV	38.9
CF_3PhFIF	51.4

T_{gel} values provide insight into the thermal robustness of the supramolecular network. As temperature increases, non-covalent interactions responsible for network formation are progressively weakened. Therefore, the temperature at which a significant drop in G′ and G″ occurs reflects the point at which the network begins to disassemble. A higher T_{gel} value indicates stronger intermolecular interactions and a more thermally stable network structure, whereas a lower T_{gel} value suggests a more weakly associated or dynamic assembly.

No correlation was observed between clogP values and the recorded T_{gel} values, suggesting that hydrophobicity alone does not dictate thermal stability in this system. Instead, T_{gel} is likely determined by a balance of multiple competing intermolecular interactions and the specific packing arrangement within the fibres. For all gels tested, T_{gel} values were above 25 °C, the temperature at which all previous rheological measurements were recorded. Confirming that the gels were measured well below their T_{gel}, and that the mechanical data reported earlier correspond to fully formed, thermally stable networks.

Although all gels were stable at 25 °C, distinctions are more apparent at higher temperatures. This is important for the gelators, whose temperature behaviour in their transient systems is analysed in Section 3.2.4. 1ThNapFF and CarbFV

exhibited T_{gel} above 35 °C, but FmocFA displayed a T_{gel} below 35 °C. Therefore, when the FmocFA transient system is measured at 35 °C, temperature effects on the state change cannot be excluded.

The following gelators were then examined with urease, urea, and methyl formate under the same conditions as those used for the 1ThNapFF transient system described previously: 2NapFF, 2NapIF, 7MeO2NapFV, FmocAG, FmocFA, FmocLG, CarbFV, and CF_3PhFIF. These gelators were chosen because they formed hydrogels within approximately 1 minute. The gelators that did not gel within this timeframe would not form a gel initially, as the initial urea- and urease-induced pH increase would already have raised the pH above the pK_a, and thus no gel-to-sol transition would be observed. To form the transient gels, urea and methyl formate were added to the DMSO gelator solution in that order to reduce the time that the methyl formate has to undergo hydrolysis when not in the gel state. Gelation was triggered by the immediate addition of the urease solution.

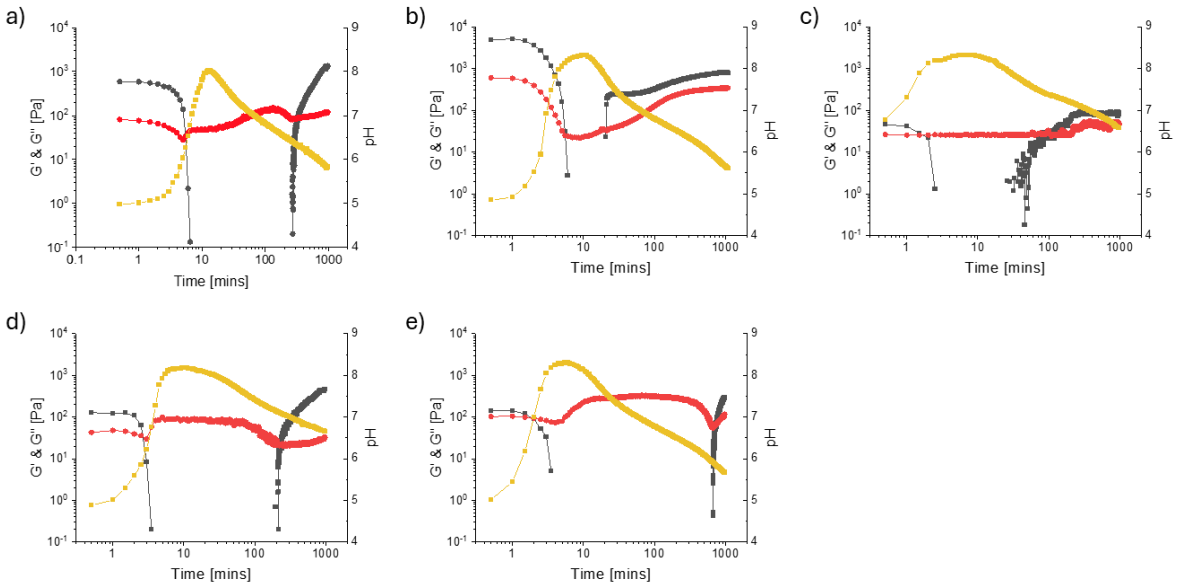

Figure 3.4. Variation of G′ (black), G″ (red), and pH (orange) over time for a) 1ThNapFF, b) FmocFA, c) CarbFV, d) 2NapFF, and e) 7MeO2NapFV, at a frequency of 50 rad/s over time in the presence of urea-urease reaction and methyl formate, with a final gelator concentration of 2 mg/mL. pH and rheology measurements were performed with two different vials under identical conditions.

Of the gelators tested, 2NapFF, FmocFA, CarbFV, and 7MeO2NapFV all underwent a successful gel-to-sol-to-gel transition in the presence of urea, urease, and methyl formate, as shown in Figure 3.4. 1ThNapFF was also measured with the

same triggers as a control. All systems underwent the initial transition from gel to sol within 10 minutes of gelation; the second transition from sol to gel was more variable, with CarbFV the quickest at approximately 20 minutes, and 7MeO2NapFV taking nearly the full 16 hours.

The apparent pK_a values of each system were measured to assess whether the gelator will successfully transition from gel-to-sol-to-gel when pH triggers are included. The apparent pK_a values of the tested gelators are listed in Table 3.3. Some gelators exhibit two apparent pK_a values because different supramolecular structures form at different pH values, each with a distinct local environment for the same carboxyl group, resulting in multiple buffering regions in the titration curve.[26] In cases where such structural transitions do not occur or occur minimally, only a single apparent pK_a is observed.

Table 3.3. Apparent pK_a values. The values were calculated from the pK_a titrations in Figure 3.5.

Gelator	Apparent pK_a values
ThNapFF	6.35
2NapFF	6.46
2NapIF	7.18, 5.42
7MeO2NapFV	8.08, 6.91
FmocAG	7.87
FmocFA	8.00, 5.88
FmocLG	7.62, 4.81
CarbFV	8.08
CF_3PhFIF	8.54

The gel formed from CF_3PhFIF did not transition to a sol state as pH increased. The gelators that did not transition to a sol state had an apparent pK_a above the system's maximum pH (≈ 8.1). The pH did not reach a sufficiently high value to deprotonate the carboxylic acid and induce micelle formation, which is characteristic of the sol phase.[27-29] Subsequently, the system remains in a gel state throughout the pH change.

FmocLG underwent a gel-to-sol transition but did not return to a gel state. The gelators that did not transition to a gel state had an apparent pK_a below the minimum pH reached by the system after the initial peak. The pH did not drop sufficiently to protonate the carboxylic acid and induce network formation.

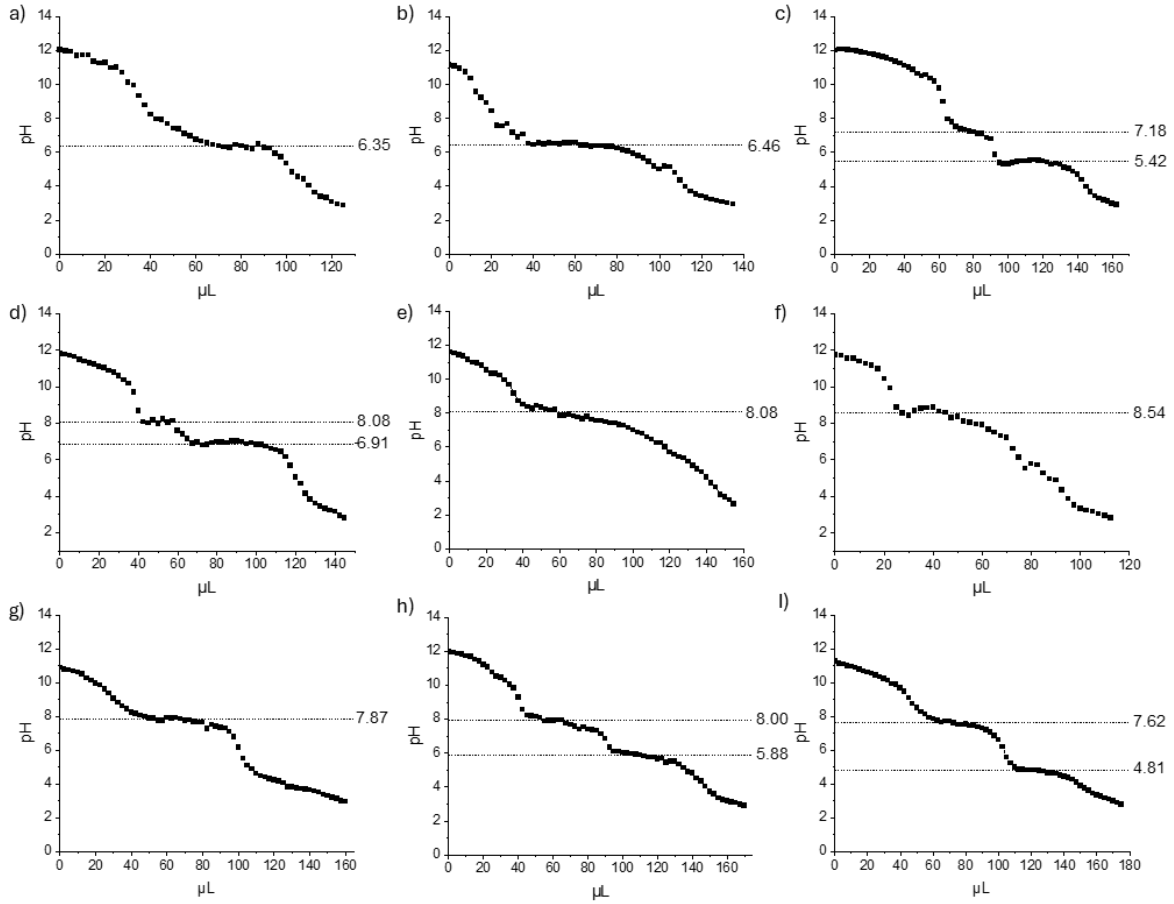

Figure 3.5. pK_a titrations of a) 1ThNapFF, b) 2NapFF, c) 2NapIF, d) 7MeO2NapFV, e) FmocAG, f) FmocFA, g) FmocLG, h) CarbFV, and I) CF_3PhFIF. The apparent pK_a values of each gelator are indicated by a horizontal line.

For those systems in which a complete gel-to-sol-to-gel transition occurred, the transition rates were related to the apparent pK_a of the gelators (Figure 3.5). The gels with the highest pK_a values would be expected to spend the least time in the sol phase, since the pH would drop below their apparent pK_a faster; however, the pH profiles for each gelator are not identical, therefore, the pK_a is not an accurate predictor of transition time. The pH profiles differed because the structures in the gel and sol phases of each gelator differed, altering the interactions between urea and urease across systems. Additionally, urease activity is pH-dependent, following a bell-shaped curve that peaks at approximately pH 7 (Figure 3.6).

Therefore, the reaction proceeds faster as pH approaches the enzyme's optimum pH range.

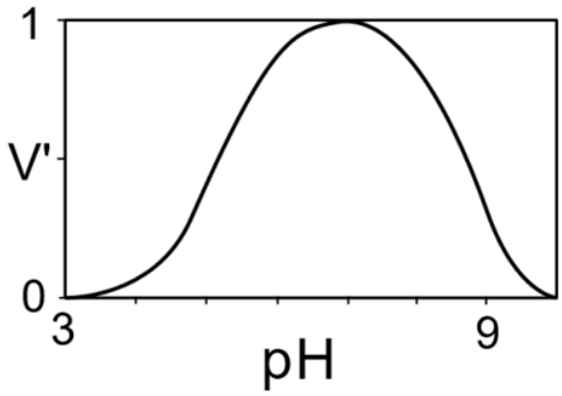

Figure 3.6. pH dependence of the relative enzyme rate v′. The enzyme activity shows a bell-shaped curve, which peaks at approximately pH 7.

Therefore, the gelators can be designed such that they form an H_2O/DMSO solvent switch gel, have a clogP value above 2.10, and an apparent pK_a below 8.1 to show a gel-to-sol-to-gel transition.

To understand the structures underpinning the gel and sol phases, these methyl formate transient systems were probed over the first 20 minutes and over 16 hours using *in situ* small-angle X-ray scattering (SAXS). Static gels refer to H_2O/DMSO solvent-switch gels. Due to time limitations on the beamline, the static gels were initially measured for 2NapFF, FmocFA, CarbFV, and 7MeO2NapFV, and the gelators exhibiting the most pronounced scattering (FmocFA and CarbFV) were selected for the kinetic experiments, along with 1ThNapFF. Also, due to the weak scattering of these 2 mg/mL samples (see Appendix 2.3; Figure A2.3), the gelator concentration was increased to 5 mg/mL for the *in situ* SAXS experiments. This more concentrated system was optimised by increasing the concentrations of urea and urease to 4 M and 0.5 mg/mL, respectively, compared with the previously used 2 M and 0.254 mg/mL. The volumes of urea (4 M), urease (0.5 mg/mL), and methyl formate were kept the same. For the rest of the transient gels in this chapter, a final concentration of 5 mg/mL is used, unless otherwise specified.

The time-sweep data for the gelator systems investigated by SAXS at 5 mg/mL (1ThNapFF, FmocFA, and CarbFV) are shown in Figure 3.7. Because the gels produced were stiffer, the time sweeps had to be performed at 10 rad/s to capture the state change, rather than the 50 rad/s previously used.

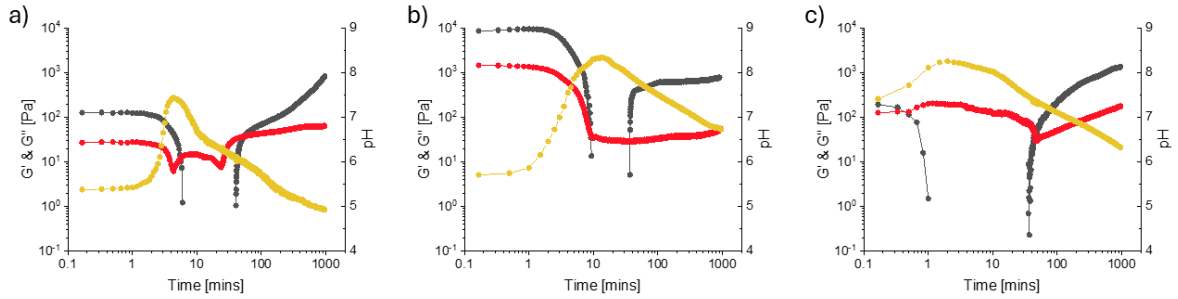

Figure 3.7. Variation of G′ (black), G″ (red), and pH (orange) over time for a) 1ThNapFF, b) FmocFA, c) CarbFV, at a frequency of 10 rad/s over time in the presence of urea-urease reaction and methyl formate, with a final gelator concentration of 5 mg/mL. pH and rheology measurements were performed with two different vials under identical conditions.

For CarbFV, the gel-to-sol-to-gel transitions occurred at times similar to those in the 2 mg/mL system; however, for 1ThNapFF and FmocFA, the timing was altered. For 1ThNapFF, the initial gel-to-sol transition remained at approximately 6 mins, but the secondary transition from sol-to-gel was faster, occurring after 40 mins, compared to the previous 4.5 hours. For FmocFA, both transitions were delayed: from 6 minutes to 9 minutes for the initial gel-to-sol transition, and from 20 minutes to 37 minutes for the secondary sol-to-gel transition. These differences in timing can be attributed to the increased gelator concentration, which influences network density, buffering capacity, and assembly kinetics, which vary between gelator systems.

For 1ThNapFF, the data for the initial gel in the transient system and the static gel both fit well to a cylinder model combined with a power law, matching previously published SAXS data for salt-triggered 1ThNapFF gels.[30] From Figure 3.8, it is not obvious if the structure of 1ThNapFF fibres changes over the first 20 minutes as the transition from gel-to-sol occurs. However, the data modelling shows that the fibres decrease in radius from 26.4 Å to 22.7 Å after 2 minutes, then plateau at around 19.8 Å after 6 minutes. This matches the recorded rheological data, which show the first reduction in mechanical properties at approximately 2 minutes and the absence of a G″ value after 6 minutes.

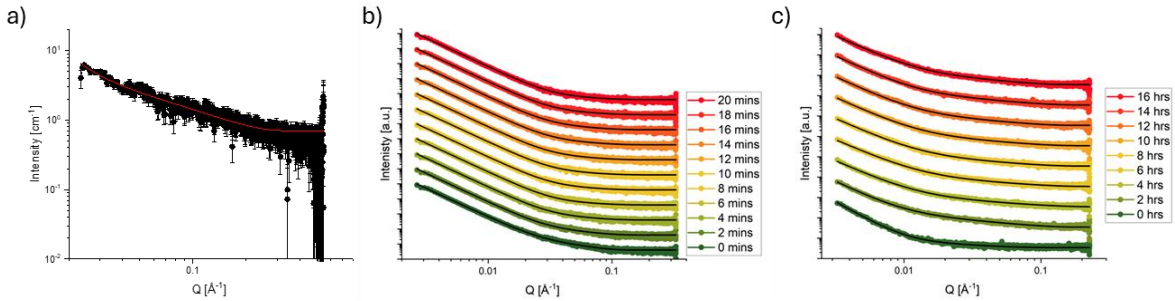

Figure 3.8. SAXS data of 1ThNapFF for the a) static gel, b) *in-situ* methyl formate transient gels over 20 mins, and c) *in-situ* methyl formate transient gels over 16 hours. The overlaid red (a) and black (b,c) lines are the fits to the data (see Appendix 2.3 and 2.4).

The 16-hour *in situ* SAXS experiment also showed a reduction in radius during the gel-to-sol transition (Figure 3.8c). After 2 hours, the radius decreased from 30.8 Å to 14.0 Å, then stabilised between 18 and 21 Å after 8 hours. The second transition from sol-to-gel fixes the network in place, preventing further changes. The variation in radius values at each time point after 8 hours appears random and may reflect differences among individual fibres across the network. This matches the rheological data as G′ and G″ are not an order of magnitude apart, indicating the system is not a true gel until after 10 hours.

For FmocFA, the scattering data for the initial gel in the transient system and the static gel both fit well to an elliptical cylinder model combined with a power law. From Figure 3.9, it is evident that the structure changes over the first 20 minutes as the transition from gel-to-sol occurs. The fibres start as elliptical cylinders combined with a power law, which transition into cylinders combined with a power law during the gel-to-sol transition at approximately 8 mins. This matches the rheological data taken of the system (Figure 3.7). After the gel-to-sol transition, the fibres' radius increases drastically from 42.6 to 70.9 Å by the end of the 20-minute experiment, as the fibres are free to rearrange in the sol phase and seek a more stable configuration.

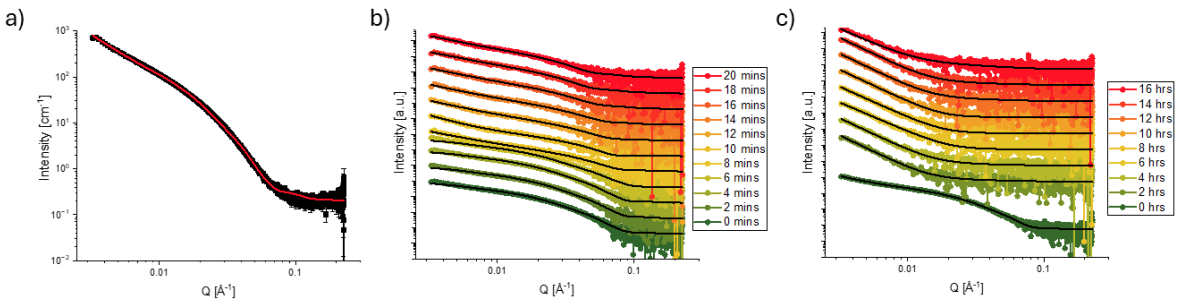

Figure 3.9. SAXS data of FmocFA for the a) static gel, b) *in-situ* methyl formate transient gels over 20 mins, and c) *in-situ* methyl formate transient gels over 16 hours. The overlaid red (a) and black (b,c) lines are the fits to the data (see Appendix 2.3 and 2.4).

During the 16-hour *in situ* SAXS run, the same elliptical cylinder-to-cylinder transition was captured between the initial state and the system after 2 hours. After 2 hours, the rheological data indicate that the second transition from sol to gel has occurred, trapping the fibres in place and preventing any further fibre reorganisation. Thus, the data for the images taken at 2 and 4 hours both fit to cylinders combined with a power law. However, at 6 hours and for all subsequent time points, the system fits a power law. This indicates that the cylindrical fibres might become more entangled, forming a larger network that cannot be captured at this length scale.

In the CarbFV methyl formate transient system, the speed of the first gel-to-sol transition prevented the initial gel from being captured *in situ*. Therefore, the fibre structure is assumed to be the same as that of the static gel for the 1ThNapFF and FmocFA systems. As the data for the static gel of CarbFV fit to elliptical cylinders, the SAXS data imply that during the gel-to-sol transition, the system has transformed into hollow cylinders. During the 20 min SAXS experiment, the hollow cylinders increase in radius from 107 Å to 116 Å and decrease in thickness from 37 Å to 30 Å in the sol phase. Although the values of the radius and thickness differ slightly for the 16-hour SAXS experiment, the same trend is observed. The 16-hour run also indicated that, as with previous gelators, the new fibre size and shape are retained through the gel-to-sol transition.

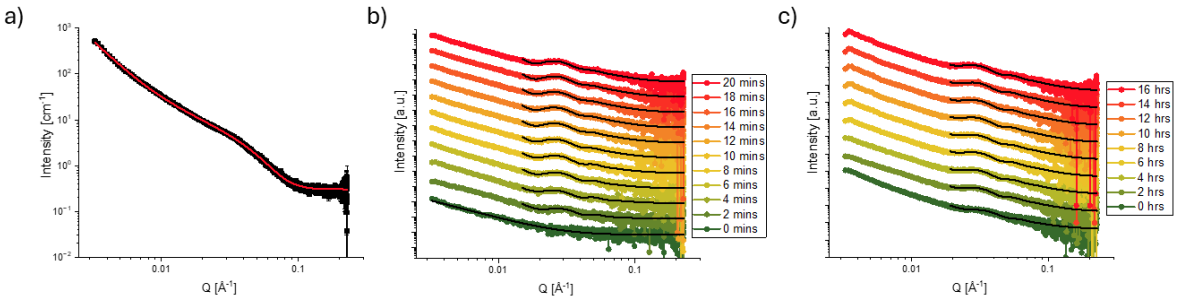

Figure 3.10. SAXS data of CarbFV for the a) static gel, b) *in-situ* methyl formate transient gels over 20 mins, and c) *in-situ* methyl formate transient gels over 16 hours. The overlaid red (a) and black (b,c) lines are the fits to the data (see Appendix 2.3 and 2.4).

For all the gelators discussed above, the SAXS data show that the gel-to-sol transition enables the fibres to organise and gain greater kinetic stability. This more stable network is then trapped by the sol-to-gel transition. For the 1ThNapFF and CarbFV gelator systems, this increases system strength, as shown in Figure 3.7. However, despite the superior kinetic stability of the final gel fibres, the mechanical properties of the FmocFA system do not improve after the gel-to-sol-to-gel transition. This is likely because the resulting network is weaker, despite the individual fibres being more stable. All parameter values for the methyl formate transient SAXS fits are provided in Appendix 2.4.

3.2.2. Control of transient gels *via* formate hydrolysis

The choice of counter-pH trigger plays a critical role in determining the final structural and mechanical properties of the gel. Previously, it has been shown that the ester hydrolysis rate decreases with increasing alkyl chain length because larger alkyl groups introduce steric hindrance around the ester bond and increase hydrophobicity, reducing the accessibility of the carbonyl carbon during hydrolysis.[31] Therefore, the hydrolysis of different alkyl formates could be used to modulate the rate of pH decrease in a transient system and, therefore, control the gelation pathway. For this study, the 1ThNapFF, FmocFA, and CarbFV transient systems discussed previously were replicated, where methyl formate was replaced by 1 molar equivalent of ethyl formate and *n*-propyl formate, which hydrolyse more slowly under identical conditions, providing a more gradual pH reduction compared to methyl formate (Figure 3.11).

By slowing the hydrolysis reaction, the system remains at high pH for a longer period, thereby extending the sol state's lifetime before gelation. Maintaining the sol state for longer allows greater molecular diffusion, redistribution, and reorganisation, favouring thermodynamically stable fibres. In addition to the fibres, this change in kinetics also influences the gel's mechanical properties. This high degree of temporal control allows us to access gels with new properties. Thus, tuning the ester hydrolysis rate provides a powerful and modular strategy to access gels with distinct structural hierarchies and mechanical behaviours from the same molecular building blocks.

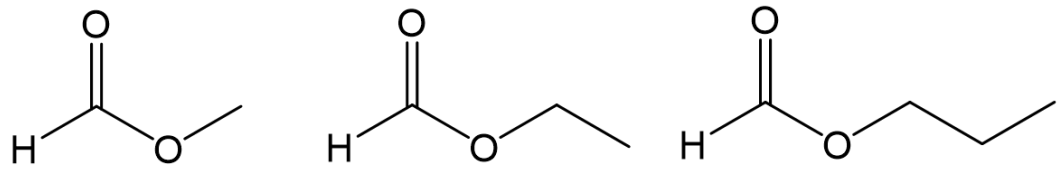

Figure 3.11. Structure of the three formates used in this chapter.

The effect of changing the formate reaction on pH was immediately evident (Figure 3.12). Increasing the alkyl chain length of the formate increases the time the system spends in the sol phase, although the initial increase in pH is slowed. The effect of pH on the rate change is independent of the gelator choice, as all the gelators tested (1ThNapFF, FmocFA, and CarbFV) showed the same trend. The formate systems all reached similar maximum pH values because the pH required to initiate formate hydrolysis is the same; rather, the time to reach this pH is delayed, and the curves follow a similar general profile.

The pH of the CarbFV system is more basic in the first few measurements than that of the other systems due to the speed at which the pH probe was transferred from the storage solution (pH ≈ 7) to the gel. The pH probe takes time to reach an accurate reading, and because the CarbFV system transitions very quickly into the sol state, this first point is more likely to be higher than the other systems. Images of the 1ThNapFF, FmocFA, and CarbFV transient gels with methyl formate, ethyl formate, and *n*-propyl formate are provided in Appendix 2.5.

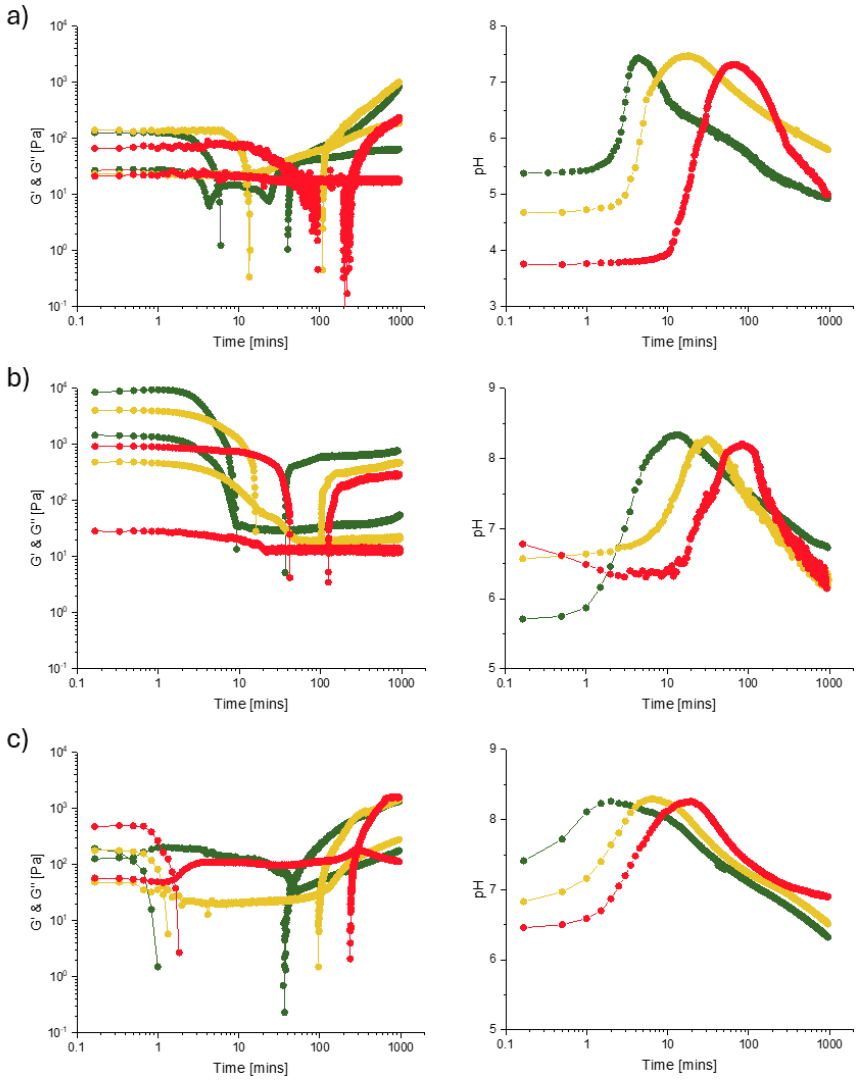

Figure 3.12. Variation of G′, G″, and pH over time for a) 1ThNapFF, b) FmocFA, and c) CarbFV, at a frequency of 10 rad/s in the presence of urea–urease reaction with methyl formate (green), ethyl formate (orange), and *n*-propyl formate (red) with a final gelator concentration of 5 mg/mL. pH and rheology measurements were performed with two different vials under identical conditions.

For the FmocFA systems tested, the gels are less stiff after 16 hours than the initial gel before the transition. However, the rheological values for all three systems continue to increase and have not reached a plateau (Figure 3.12). The same is true for pH; because these systems are pH-dependent, it would be inaccurate to draw a conclusion at this time point, as the gels are clearly still evolving.

For the CabFV and 1ThNapFF systems, the final gels are stiffer than the initial gel, regardless of the formate used. However, unlike the FmocFA gels, the mechanical properties of the CarbFV systems seem to be independent of the rate of pH

change. Each formate system forms a gel with mechanical properties similar to those of the other systems and higher than the initial gel after 16 hours, whereas only the *n*-propyl system appears to have plateaued after 16 hours.

The rheological data make it evident that all three gelator systems are still increasing and have not plateaued; therefore, the ageing of these systems was further investigated in Section 3.2.3.

These alternative hydrolysis systems were also measured using *in situ* SAXS to characterise the underlying network and fibres in the gel and sol phases (Figure 3.13). The systems were measured over 16 hours due to limited beamtime and slower transitions than those of methyl formate.

For 1ThNapFF, the data for the initial gel in the ethyl formate and *n*-propyl systems fit well to an elliptical cylinder model combined with a power law, unlike the previously methyl formate and static gel data. Again, from Figure 3.13, it is not clear whether the structure of 1ThNapFF fibres changes during the gel-to-sol-to-gel transitions; however, the data modelling shows a slight increase in radius for the ethyl formate system and a larger increase for the *n*-propyl formate system. The *n*-propyl formate system also showed a decrease in the cylinder's axis ratio and an increase in the power-law exponent, supporting the conclusion that the network becomes more entangled after the gel-to-sol-to-gel transition, as observed for the FmocFA methyl formate systems.

The increase in radius seen in the methyl formate systems was also observed in the FmocFA ethyl formate systems, but not for the *n*-propyl formate system, where the radius decreased. Although the radius did not increase for *n*-propyl formate, the same fibre shape transitions as the methyl formate system were observed for the *n*-propyl formate system, from cylinders with a power-law to elliptical cylinders with a power-law and finally to just a power law. The ethyl formate systems retained the same shape as the initial gel and showed only the increase in radius mentioned above.

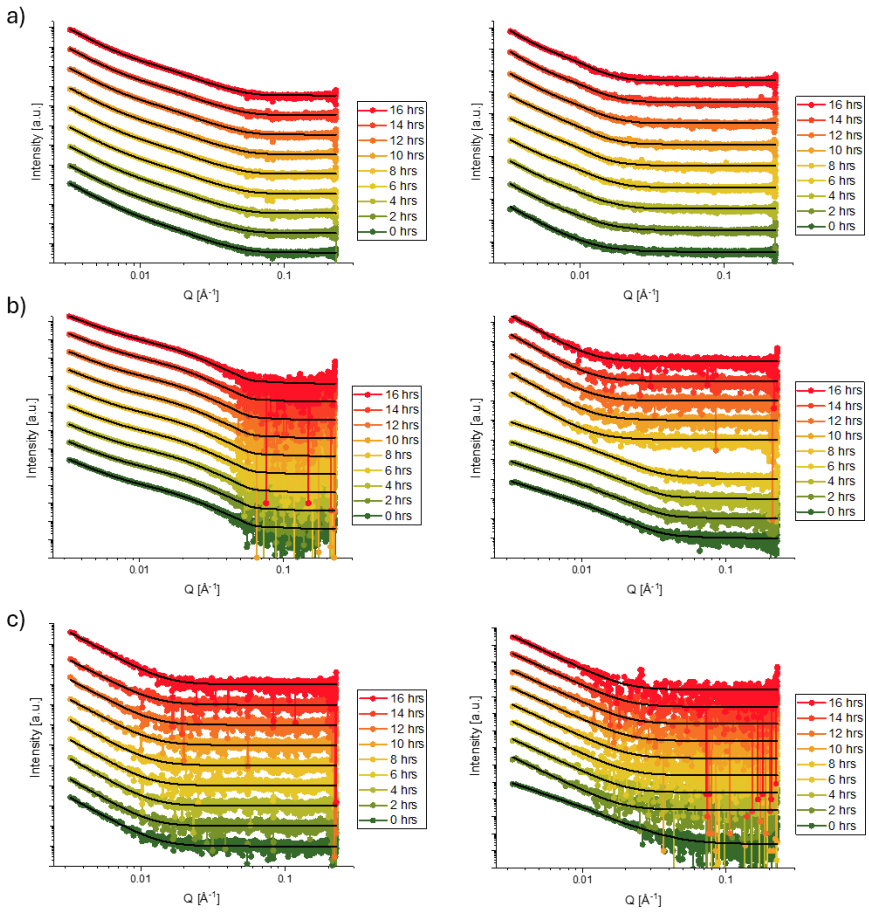

Figure 3.13. SAXS data for a) 1ThNapFF, b) FmocFA, and c) CarbFV transient systems with ethyl formate (left) and *n*-propyl (right) over 16 hours. The black lines are the fits to the data (see Appendix 2.6 and 2.7).

For CarbFV, the initial gel of the ethyl formate system could not be captured *in situ* due to the speed of the transition, and so it is assumed to be the same as the initial gel. This system showed a transition from elliptical cylinders with a power-law to just a power-law. For the propyl formate CarbFV system, the initial gel could be measured and fit to cylinders with a power-law, which then fit to a power-law for all subsequent measurements. For both of these CarbFV systems, no hollow cylinder fibres were measured; however, since the power law indicates that the fibres become more entangled and form a larger network that cannot be observed at this length scale, the network could still contain the hollow cylinders as seen in the methyl formate system, but the scattering is overwhelmed by the larger network.

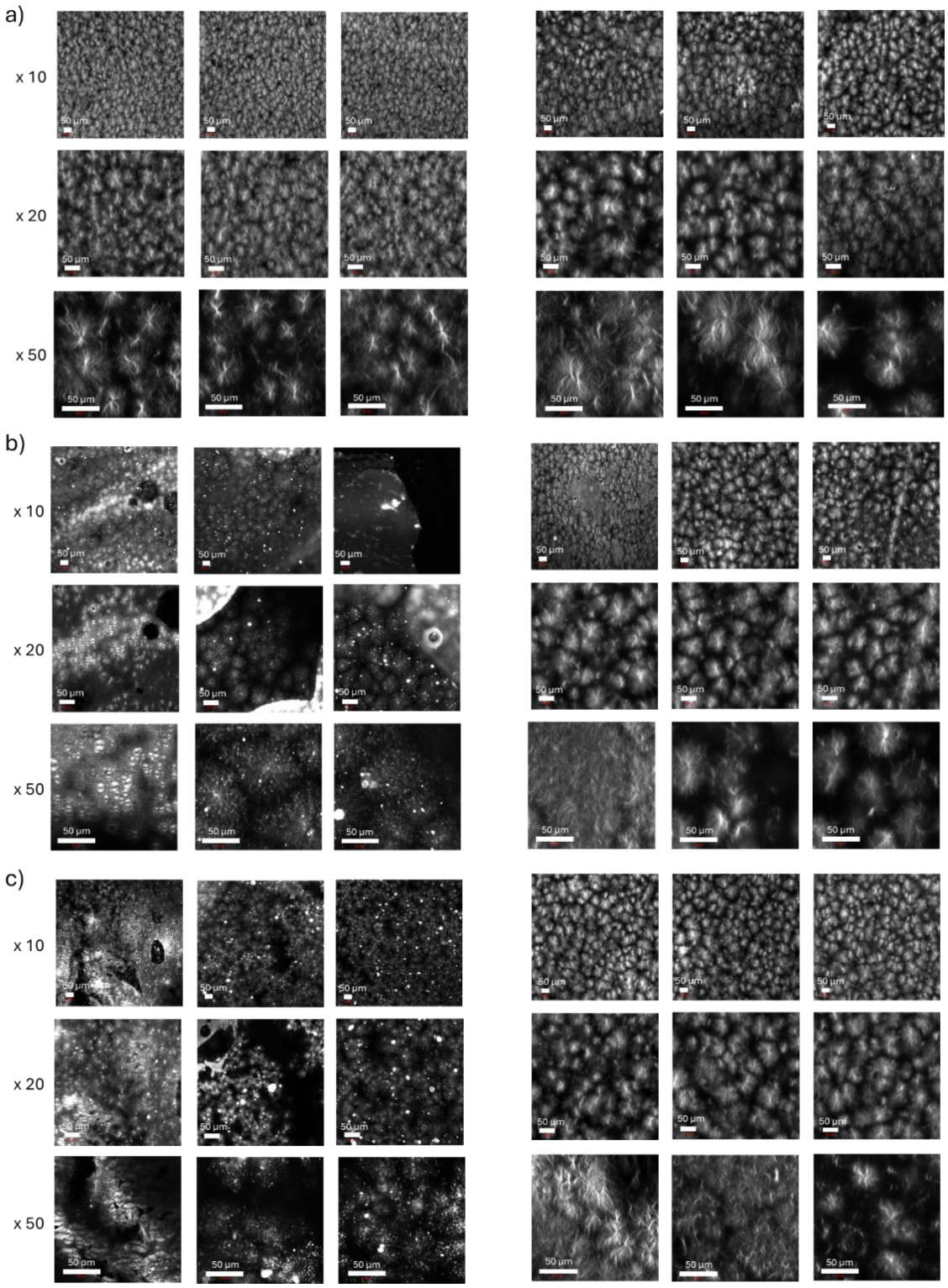

Figure 3.14. Confocal images of the regular (left), a) FmocFA methyl formate transient gels, b) FmocFA ethyl formate transient gels, and c) FmocFA propyl formate transient gels and the systems with no urea (right), imaged 1 day after gelation was triggered. For the systems without urea, no change in state occurred; therefore, these are analogues of the initial gels before the transitions. Scale bars (white) represent 50 µm.

To further understand the morphology of the systems before and after the transition, images of the FmocFA systems were obtained using a confocal microscope 1 day after gelation was triggered (Figure 3.14). FmocFA was chosen because clear images with visible fibres can be obtained with the confocal microscope. Images of the systems without urea were also taken as analogues of the systems before the transitions.

From Figure 3.14, it is evident that the addition of formates reduces the size of spherulites in the network after the transition. These images show that large spherulites form prior to the transition, similar to those found in the DMSO/H_2O solvent-switch gels (Figure 3.15). Although the addition of urease and formate reduces the network's interconnectivity, with spherulites forming farther apart in those gels than in the DMSO/H2O gels.

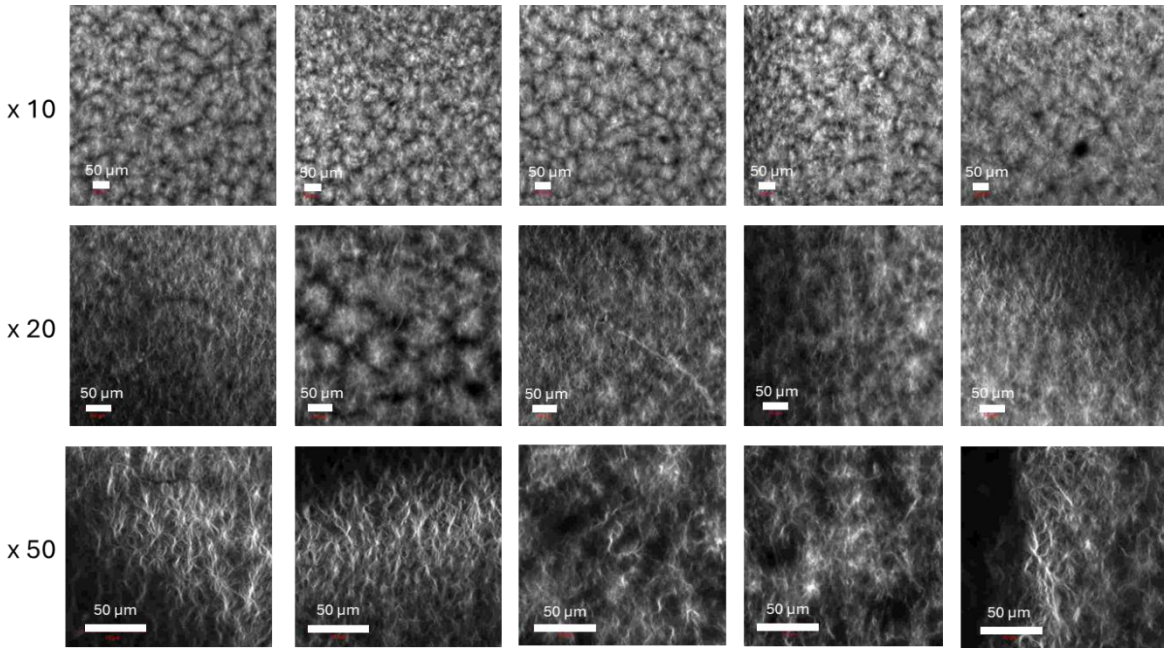

Figure 3.15. Confocal images of FmocFA DMSO/H2O gels, imaged 1 day after gelation was triggered. Scale bars (white) represent 50 µm.

The ethyl formate gels also produce much smaller bubbles of CO_2 from the urea and urease reaction. For the methyl formate and *n*-propyl formate gels, the bubbles are large enough to be seen by eye (Appendix 2.5); for ethyl formate, however, the bubbles are visible under the confocal microscope, obscuring the images.

These systems are not limited to DMSO; they can also be formed in other solvents such as ethanol, as demonstrated with FmocFA (Figure 3.16). Gel-to-sol-to-gel transitions were observed in an ethanol/H_2O (20/80 v/v) system with urease and urea for both methyl formate and ethyl formate. The *n*-propyl formate system was also tested; however, only a sol-to-gel transition occurred.

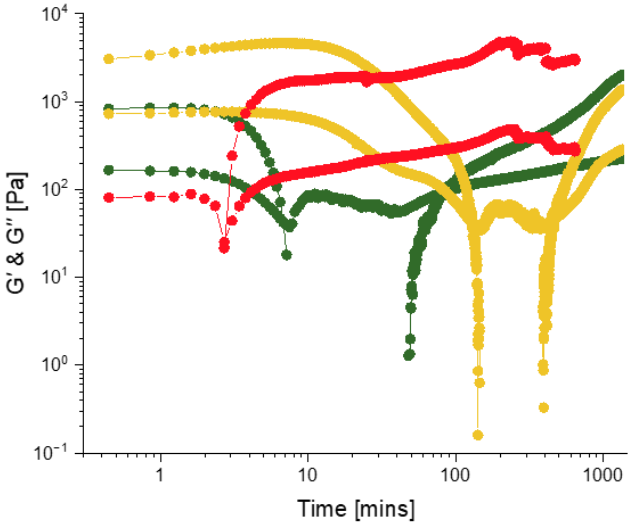

Figure 3.16. Variation of G′, G″, and pH over time for FmocFA at a frequency of 10 rad/s in the presence of urea–urease reaction with methyl formate (green), ethyl formate (orange), and *n*-propyl formate (red) with a final gelator concentration of 5 mg/mL in ethanol.

Again, the transient system altered the mechanical properties of the final gel; however, unlike in the DMSO systems, the methyl formate pH trigger increased the stiffness of the final gel. Although the ethyl formate system exhibited a weaker final gel after 16 hours, as observed in the previous systems, the rate of change of its mechanical properties suggests that it may eventually reach higher G′ and G″ values than the initial gel.

3.2.3. Ageing of transient gels

As mentioned previously, after 16 hours, the systems continue to evolve. In literature, the properties of the "final gel" are often reported based on data collected 24 hours after gelation is triggered, when the system's pH has reached a plateau.[23,24] Accordingly, the rheological properties of all the formate systems were measured after 1 day, 3 days, 1 week, 2 weeks, and 4 weeks to examine ageing, once the pH had plateaued (Figure 3.17). This plateau does not necessarily

mean the system has stopped evolving, and so it is necessary to determine whether the system fully stabilises or ceases to evolve at some point.

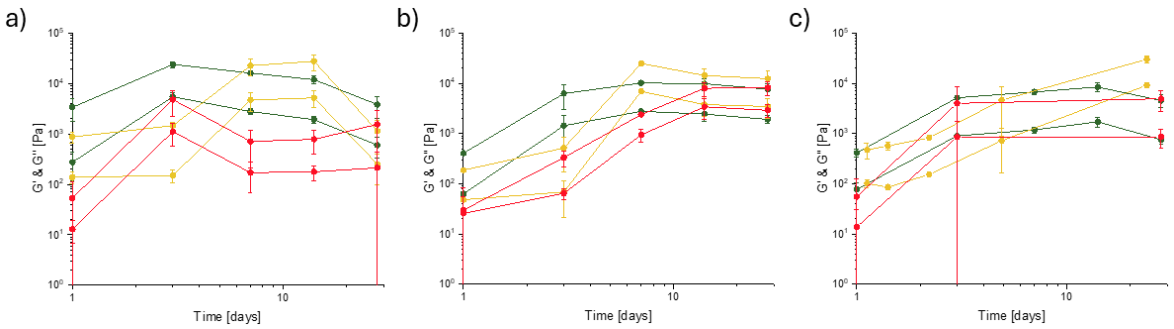

Figure 3.17. Evolution of G′ and G″ over a period of 28 days for a) 1ThNapFF, b) FmocFA, and c) CarbFV in the presence of urea–urease reaction with methyl formate (green), ethyl formate (orange), and *n*-propyl formate (red). Values of G′ and G″ were taken at a strain of 0.5 % from strain sweeps, which were performed over 0.01 % to 1000 % strain at a frequency of 10 rad/s. Strain sweeps were performed in triplicate, and the standard deviations of G′ and G″ were taken from these measurements.

It is evident that, broadly, the systems do not stop evolving for at least 1 week after gelation is triggered. All systems produced stiffer gels after 4 weeks; however, changes in these properties were unpredictable and varied even with the same gelators or formates. Frequency sweeps indicated that, after 2 weeks, the *n*-propyl formate system and, after 4 weeks, the ethyl formate and *n*-propyl formate systems were no longer true gels. All CarbFV systems also underwent gradual syneresis after 3 days, with no further shrinkage after 7 days. Beyond this point, the mechanical properties stabilised (Appendix 2.8). Strain and frequency sweeps of the 1ThNapFF, FmocFA, and CarbFV transient gels after 1 day, 3 days, 1 week, 2 weeks and 4 weeks, with methyl formate, ethyl formate, and *n*-propyl formate are provided in Appendix 2.8.

For practical applications of these materials, it is essential that their properties be observed over extended periods. These results indicate that testing limited to 24 hours, as currently published for these types of transient systems, is insufficient to evaluate long-term stability and performance.

3.2.4. Temperature control of transient systems

In addition to pH modulation, temperature has been shown to be an important parameter in influencing supramolecular forces and the properties of the resulting gel state.[4,7] pH change is not the only factor affecting the properties of the final gel. These systems can be further manipulated by varying the system's temperature during the gel-to-sol-to-gel transition. Methyl formate transient systems containing 1ThNapFF, FmocFA, and CarbFV were investigated by maintaining the systems at temperatures ranging from 10–35 °C (Figure 3.18).

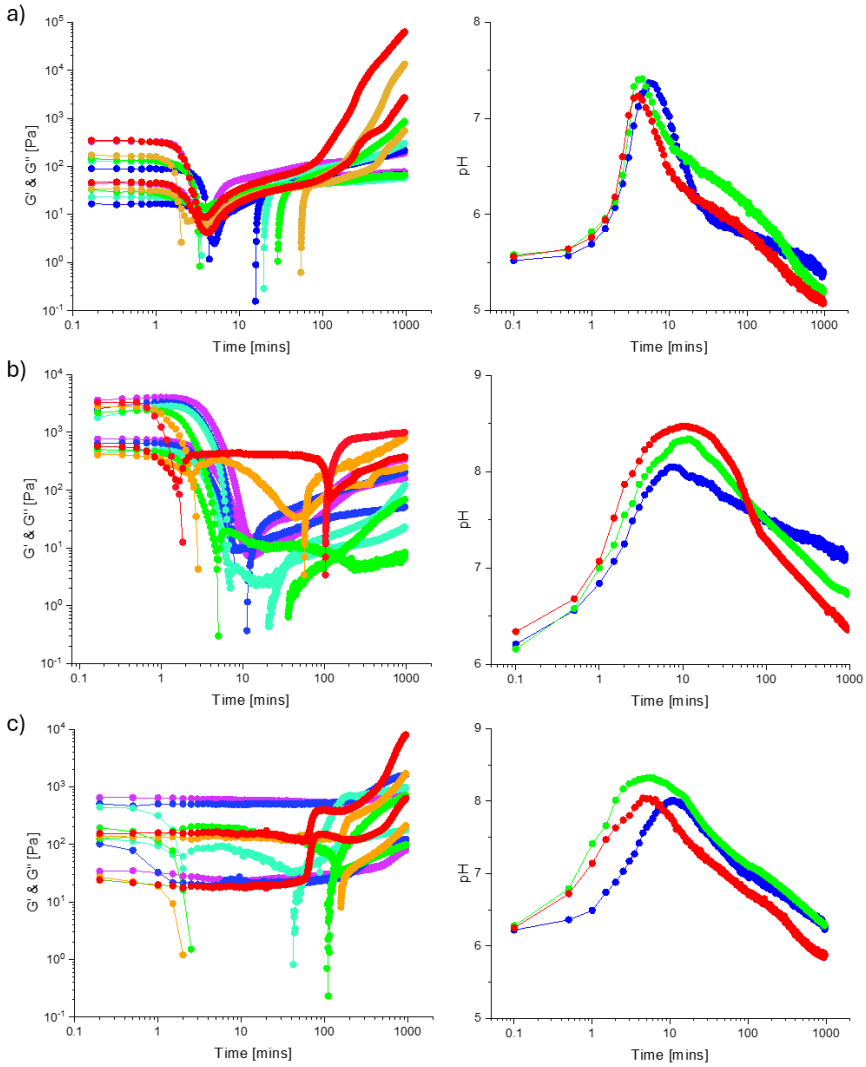

Figure 3.18. Variation of G′, G ″ and pH with time at 10 rad/s for a) 1ThNapFF, b) FmocFA, and c) CarbFV in the presence of urea/urease/methyl formate at 10 °C (purple), 15 °C (blue), 20 °C (teal), 25 °C (green), 30 °C (orange), and 35 °C (red) with a final gelator concentration of 5 mg/mL. pH and rheology measurements were performed in two different vials under identical conditions.

The temperature dramatically alters the kinetics of the urea/urease reaction and methyl formate hydrolysis, allowing the gel-to-sol-to-gel transition to be accurately controlled. As the temperature increases, the gel strength increases because the time spent in the sol phase is longer. For 1ThNapFF, transitions were observed between 15 °C and 30 °C, and for CarbFV between 20 °C and 30 °C. However, the overall temperature control range is 10 °C to 35 °C for 1ThNapFF and 15 °C to 35 °C for CarbFV. Although no gel–to–sol–to–gel transitions occur at the temperature extremes, temperature nevertheless influences the final gel properties. Transitions do not occur at these extremes because the pH peak remains below the pK_a of the gelators; CarbFV had a different range, as this gelator has the highest pK_a. Consequently, the temperature range over which transitions are observed can be predicted from the pK_a of each gelator.

For FmocFA, the system had a temperature control range of 10 -35 °C, with gel-to-sol-to-gel transitions observed between 15 °C and 35 °C. However, because the T_{gel} of the FmocFA system is 31.7 °C, the transition at 35 °C is not solely driven by pH changes but may also reflect thermal destabilisation of the gel network. The pH profile at 35 °C still shows that the pH peak remains above the pK_a of FmocFA, indicating that the transition arises from a combination of pH and temperature effects.

The rheological properties were measured after 1 day, 3 days, 7 days, 14 days, and 28 days for the methyl formate systems at 15 °C, 25 °C, and 35 °C (Figure 3.19). After 28 days, syneresis was observed in CarbFV systems, and gels at all three temperatures show similar mechanical properties. The primary difference between the systems lies in the rate at which mechanical properties increase. This behaviour is likely due to the pH plateau occurring more rapidly at higher temperatures. Increased temperature accelerates methyl formate hydrolysis, causing the system to stabilise sooner once the methyl formate reaction stops. Strain and frequency sweeps for the 1ThNapFF, FmocFA, and CarbFV transient systems with methyl formate at 15 °C, 25 °C, and 35 °C after 1 day, 3 days, 1 week, 2 weeks, and 4 weeks are provided in Appendix 2.9.

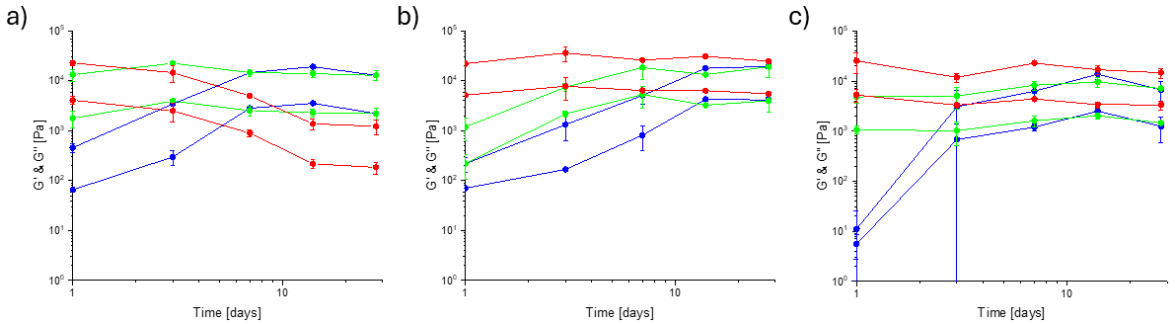

Figure 3.19. Evolution of G′ and G″ over a period of 28 days for a) 1ThNapFF, b) FmocFA, and c) CarbFV at 15 °C (blue), 25 °C (green), and 35 °C (red). Values of G′ and G″ were taken at a strain of 0.501 % from strain sweeps, which were performed over 0.01 % to 1000 % strain at a frequency of 10 rad/s. Strain sweeps were performed in triplicate, and the standard deviations of G′ and G″ were taken from these measurements.

3.3. Conclusions

This chapter has demonstrated that a variety of gelator molecules can be successfully applied to the urea/urease and formate system, resulting in the formation of a transient gel with tuneable properties, to achieve desired material characteristics. By varying the formate hydrolysis reaction, the timing of state transitions was modulated, enabling precise control over the duration the system remains in the sol state. The potential for such systems to remain in the sol state for prolonged periods offers valuable opportunities for applications such as 3D printing and the holding and casting of hydrogels.

In addition, the transient systems were controlled *via* the system's temperature, providing an additional control mechanism. However, temperature variation introduces additional complexity, as it not only influences transition dynamics but also dictates the pathway the system follows, whether a gel-to-sol-to-gel or a gel-to-gel-to-gel transition is observed.

Despite the promising control mechanisms presented, it is commonly assumed that the effects of these modifications are predictable, but these data demonstrate that this is not always the case. The extended duration that transient systems spent in the sol state revealed nuances in individual gelators' responses to changes in reaction conditions. This unpredictability suggests that further studies are

required to refine the control mechanisms and better understand how varying parameters influence the system's behaviour.

The critical role of ageing in the behaviour of transient gel systems was also highlighted. The results show that the systems continue to evolve over several days after formation, indicating that ageing plays a significant role in shaping the final properties of the gels. This behaviour is likely not limited to the systems studied in this research, and the ageing process must be carefully considered when introducing transient gels into any practical application.

Overall, this research demonstrates the feasibility and potential of transient gels as dynamic materials with tuneable properties, leveraging the urea/urease and formate systems.

3.4. Experimental

3.4.1. Materials

The gelators were synthesised by Prof. Dave Adams and Dr Alex Loch as described previously.[32–35] Methyl formate (anhydrous, 99%) and urease (U4002-100KU, Jack Beans, 100,000 units/g solid) were purchased from Sigma-Aldrich. *n*-propyl formate (97%) was purchased from Thermo Scientific. Dimethyl sulfoxide (>= 99%) was purchased from Fischer Scientific. Urea (ultrapure 99%) and ethyl formate (97%) were purchased from Alfa Aesar. Sodium hydroxide and hydrochloric acid were purchased from Honeywell. Deionised water was employed in all experiments.

3.4.2. Preparation of solutions

To prepare the gelator stock solutions, the gelator was dissolved in DMSO and shaken to obtain a concentration of 10 mg/mL or 25 mg/mL, as required. To prepare the stock solutions of urea (2 M) and urease (0.253 mg/mL and 0.5 mg/mL), the solid urea or enzyme powder was weighed, dissolved in a known volume of H_2O, and shaken to obtain the required concentrations.

3.4.3. Preparation of hydrogels

DMSO/H_2O hydrogels were prepared by transferring 1.6 mL of H_2O into 0.4 mL of the gelator solution (10 mg/mL or 25 mg/mL) in DMSO. The final concentration of the gelator was therefore either 2 mg/mL or 5 mg/mL in a 20/80 DMSO/H_2O solution.

To induce the 2 mg/mL gel-to-sol-to-gel transitions, the gels were prepared in the presence of urea (2 M) and either methyl formate, ethyl formate, or *n*-propyl formate; the water was replaced with the urease stock solution (0.254 mg/mL). In a 7 mL sterilin vial, 10 µL of urea and 0.4 mL of the gelator solution were combined. The formate was added to this mixture: 100 µL for methyl formate, 133 µL for ethyl formate, and 158 µL for *n*-propyl formate. 1.59 mL of urease was then transferred into this solution. If not specified, then the system was left undisturbed for 16 hours.

To induce the 5 mg/mL gel-to-sol-to-gel transitions, the gels were prepared in the presence of urea (4 M) and either methyl formate, ethyl formate, or *n*-propyl formate; water was replaced with the urease (0.5 mg/mL) stock solution. In a 7 mL sterilin vial, 10 µL of urea and 0.4 mL of the gelator solution were combined. The formate was added to this mixture: 100 µL for methyl formate, 133 µL for ethyl formate, and 158 µL for *n*-propyl formate. 1.59 mL of urease was then transferred into this solution. If not specified, then the system was left undisturbed for 16 hours.

3.4.4. Rheological measurements

Rheological experiments were carried out on an Anton Paar Physica MCR 301 rheometer. The measurements were taken with a cup-and-vane geometry (ST10-4V-8.8/97.5 - SN42404) at a measuring distance of 2.1 mm. Unless otherwise specified, measurements were taken at 25°C. Strain sweeps were performed over 0.01% to 1000% strain at a frequency of 10 rad/s. Frequency sweeps were performed at 0.5% strain, increasing the frequency from 1 rad/s to 100 rad/s. Time sweeps were performed at a strain of 0.5% and a frequency of 50 rad/s for 16 hours for the transient systems, with a final concentration of 2 mg/mL. Time sweeps were performed at a strain of 0.5% and a frequency of 10 rad/s for 16

hours for the transient systems, with a final concentration of 5 mg/mL. All gel-to-sol-to-gel samples were prepared immediately before the time-sweep measurement.

T_{gel} values were measured using a heat-cool cycle. Gels were made in small aluminium cups 1 day before the measurements. Measurements were taken using an aluminium cup and vane geometry (ST10-4V-8.8/97.5 - SN42404) at a strain of 0.5% and a frequency of 50 rad/s. The temperature was set to 25 °C and increased by 2 °C every minute up to 90 °C, then decreased by 2 °C every minute until 25 °C.

3.4.5. pH measurements

pH measurements were performed using a HANNA FC200 pH probe with a 6 mm × 10 mm conical tip. Unless specified, the measurements were taken at 25°C. The pH values were accurate to ±0.1. To monitor pH changes in the gelator systems containing urea, urease, and methyl formate, the gel was prepared as above, immediately before use, and monitored for 16 hours. The temperature was controlled using a circulating water bath.

The pK_a values of the gelator systems were determined by titration via the addition of 2.5 µL aliquots of 0.1 M HCl solution to the DMSO/H_2O hydrogels with 1 molar equivalence of 0.1 M NaOH at 25°C. The system was stirred between recording the pH values and during HCl addition. The DMSO/H_2O hydrogels with 1 molar equivalence of 0.1 M NaOH were left to equilibrate overnight before the titration.

3.4.6. Confocal microscopy

For imaging, nile blue A dye (0.1 wt% aqueous solution, 2 µL per mL of gel) was incorporated into gels to allow for observation by confocal fluorescence microscopy using a Zeiss LSM 710 confocal microscope fitted with Zeiss N-Achroplan 10×, LD Plan- NEUFLUAR 20× (0.4 Korr Ph 2), and LD EC Epiplan NEUFLUAR 50× (0.55 DIC) objectives. Gels were formed within a 25 mL syringe with the top removed. The gels were left for 16 hours before being placed onto a glass microscope slide and imaged (Figure 3.20)

Figure 3.20. FmocFA gels for confocal microscopy. Gels were formed within a 25 mL syringe with the top removed and placed on a glass microscope slide for imaging.

3.4.7. Small-angle X-ray scattering

Transient gel SAXS measurements were performed using the X-ray beam of the I22 beamline (Diamond Light Source, Oxfordshire, UK) during experiment SM32866 and the X-ray beam of the BM26 DUBBLE beamline (ESRF, Grenoble, France) during SC5410. The experiments were performed at a fixed energy of 12.4 keV and a camera length of 7.721 m at Diamond Light Source, resulting in a Q range of 0.0027–0.329 $Å^{-1}$. The experiments were performed at a fixed energy of 12 keV and a camera length of 5.41m at the BM26 DUBBLE beamline, resulting in a Q range of 0.0036–0.129 $Å^{-1}$. The solutions were prepared in vials as described in the previous sections and loaded in glass capillaries using a 1 mL syringe with a 21G needle. The raw data were processed using the Dawn Science software (version 2.27).[36] As part of the processing, the backgrounds were subtracted from the raw 2D SAXS data and a full azimuthal integration was performed to reduce the data to an I vs q plot. The plots were then fitted to structural models using SasView 5.0.5.[37] To calculate the X-ray scattering length densities (SLDs) for all samples, the NIST neutron activation and scattering calculator (https://www.ncnr.nist.gov/resources/activation/) was used, assuming a density of 1.55 g/cm^3 for the gelators.[38]

3.5. References

1 F. della Sala, S. Neri, S. Maiti, J. L.-Y. Chen and L. J. Prins, *Curr. Opin. Biotechnol.*, 2017, **46**, 27–33.

2 J. Boekhoven, W. E. Hendriksen, G. J. M. Koper, R. Eelkema and J. H. van Esch, *Science*, 2015, **349**, 1075–1079.

3 S. Panja, K. Boháčová, B. Dietrich and D. J. Adams, *Nanoscale*, 2020, **12**, 12840–12848.

4 S. Xian and M. J. Webber, *J. Mater. Chem. B*, 2020, **8**, 9197–9211.

5 S. Panja and D. J. Adams, *Chem. Soc. Rev.*, 2021, **50**, 5165–5200.

6 P. Innocenzi, *The Sol to Gel Transition*, Springer International Publishing, 1st edn., 2016, pp. 1-6.

7 A. D. Drozdov, *Int. J. Eng. Sci.*, 2018, **128**, 79–100.

8 S. Dhiman, K. Jalani and S. J. George, *ACS Appl. Mater. Interfaces*, 2020, **12**, 5259–5264.

9 S. Bianco, L. Wimberger, Y. Ben-Tal, G. T. Williams, A. J. Smith, J. E. Beves and D. J. Adams, *Chem. Eur. J.*, 2024, **30**, e202400544.

10 D. Zhang, B. Ren, Y. Zhang, L. Xu, Q. Huang, Y. He, X. Li, J. Wu, J. Yang, Q. Chen, Y. Chang and J. Zheng, *J. Mater. Chem. B*, 2020, **8**, 3171–3191.

11 S. Panja, C. Patterson and D. J. Adams, *Macromol. Rapid Commun.*, 2019, **40**, 1900251.

12 M. J. Webber, J. B. Matson, V. K. Tamboli and S. I. Stupp, *Biomaterials*, 2012, **33**, 6823–6832.

13 P. Zhang, A. G. Cheetham, Y. Lin and H. Cui, *ACS Nano*, 2013, **7**, 5965–5977.

14 S. Panja, A. M. Fuentes-Caparrós, E. R. Cross, L. Cavalcanti and D. J. Adams, *Chem. Mater.*, 2020, **32**, 5264–5271.

15 N. Singh, B. Lainer, G. J. M. Formon, S. De Piccoli and T. M. Hermans, *J. Am. Chem. Soc.*, 2020, **142**, 4083–4087.

16 O. E. Philippova, D. Hourdet, R. Audebert and A. R. Khokhlov, *Macromolecules*, 1997, **30**, 8278–8285.

17 W. Gao, J. M. Chan and O. C. Farokhzad, *Mol. Pharm.*, 2010, **7**, 1913–1920.

18 S. Dai, P. Ravi and K. C. Tam, *Soft Matter*, 2008, **4**, 435.

19 S. Zhou, S. Matsumoto, H. Tian, H. Yamane, A. Ojida, S. Kiyonaka and I. Hamachi, *Chem. Eur. J.*, 2005, **11**, 1130–1136.

20 Y. Huang and S. Gui, *RSC Adv.*, 2018, **8**, 6978–6987.

21 C. Tao, J. Wang, S. Qin, Y. Lv, Y. Long, H. Zhu and Z. Jiang, *J. Mater. Chem.*, 2012, **22**, 24856.

22 S. Panja and D. J. Adams, *Giant*, 2021, **5**, 100041.

23 S. Bianco, S. Panja and D. J. Adams, *Gels*, 2022, **8**, 132.

24 A. Pape, M. Bastings, R. Kieltyka, H. Wyss, I. Voets, E. Meijer and P. Dankers, *Int. J. Mol. Sci.*, 2014, **15**, 1096–1111.

25 http://www.molinspiration.com.

26 K. A. Houton, K. L. Morris, L. Chen, M. Schmidtmann, J. T. A. Jones, L. C. Serpell, G. O. Lloyd and D. J. Adams, *Langmuir*, 2012, **28**, 9797–9806.

27 E. R. Draper, H. Su, C. Brasnett, R. J. Poole, S. Rogers, H. Cui, A. Seddon and D. J. Adams, *Angew. Chem. Int. Ed.*, 2017, **56**, 10467–10470.

28 R. R. Sonani, S. Bianco, B. Dietrich, J. Doutch, E. R. Draper, D. J. Adams and E. H. Egelman, *Cell Rep. Phys. Sci.*, 2024, **5**, 101812.

29 K. McAulay, B. Dietrich, H. Su, M. T. Scott, S. Rogers, Y. K. Al-Hilaly, H. Cui, L. C. Serpell, A. M. Seddon, E. R. Draper and D. J. Adams, *Chem. Sci.*, 2019, **10**, 7801–7806.

30 R. Huang, D. McDowall, H. Ng, L. Thomson, Y. K. Al-Hilaly, J. Doutch, S. Burholt, L. C. Serpell, R. J. Poole and D. J. Adams, *Chem. Commun.*, 2022, **58**, 10388–10391.

31 H. M. Humphreys and L. P. Hammett, *J. Am. Chem. Soc.*, 1956, **78**, 521–524.

32 L. Chen, K. Morris, A. Laybourn, D. Elias, M. R. Hicks, A. Rodger, L. Serpell and D. J. Adams, *Langmuir*, 2010, **26**, 5232–5242.

33 D. J. Adams, L. M. Mullen, M. Berta, L. Chen and W. J. Frith, *Soft Matter*, 2010, **6**, 1971.

34 J. K. Gupta, D. J. Adams and N. G. Berry, *Chem. Sci.*, 2016, **7**, 4713–4719.

35 E. L. Bowley, S. Bianco, F. H. Stewart, C. M. Wallace, R. E. Ginesi, A. S. Loch, M. Rosenthal, A. J. Smith and D. J. Adams, *ChemSystemsChem*, 2024, **7**, e202400073.

36 J. Filik, A. W. Ashton, P. C. Y. Chang, P. A. Chater, S. J. Day, M. Drakopoulos, M. W. Gerring, M. L. Hart, O. V. Magdysyuk, S. Michalik, A. Smith, C. C. Tang, N. J. Terrill, M. T. Wharmby and H. Wilhelm, *J. Appl. Crystallogr.*, 2017, **50**, 959–966.

37 http://www.sasview.org/ .

38 https://www.ncnr.nist.gov/resources/activation/.

Chapter 4 – Temporal control of lipid phase transitions

This chapter is adapted from the following publications:

"Soft Materials with Time-Programmed Changes in Physical Properties through Lyotropic Phase Transitions Induced by pH-Changing Reactions"

ACS Appl. Mater. Interfaces, 2024, 16(15), 19585–19593.

E. Bowley, W. Liu, D.J. Adams, and A.M. Squires.

E.L. Bowley performed the viscosity and pH experiments. W. Liu (University of Bath) aided the collection and processing of SAXS data.

4.1. Introduction

Amphiphilic molecules, such as lipids, are known for their ability to self-assemble in aqueous environments, forming soft nanomaterials called lyotropic liquid-crystalline phases.[1] These phases can adopt a variety of geometries depending on environmental conditions, leading to dramatic changes in physical properties, including viscosity, optical transparency, and the diffusion and release of soluble molecules.[2-5] Lyotropic phases represent thermodynamic equilibrium states, which can respond dynamically to changes in their surroundings, enabling reversible transitions between different structures.[6]

Lipid-based systems, particularly lipid nanoparticles, have been extensively studied for their potential as in vivo smart drug-delivery carriers, with numerous studies demonstrating their feasibility in biomedical applications.[7,8] A key feature of these systems is their pH responsiveness, in which lipid nanoparticles undergo morphological changes in response to pH fluctuations. Where the pH responsiveness is due to the inclusion of an ionizable headgroup, for example, a fatty acid. This chapter focuses on 1-monoolein (MO), a lipid molecule which is biocompatible, readily available, and widely used in the pharmaceutical and food industry.[9]

In this chapter, three lipid phases are observed (Figure 4.1). An inverse H_{II} phase, which consists of two-dimensional arrays of parallel cylindrical water channels, each surrounded by lipid monolayers.[10,11] And two inverse lipid cubic phases (*Im3m*, *Pn3m*), which are three-dimensional nanostructured materials formed by type II lipids.[12,13] These phases are arranged into a bilayer adopting a unique triply periodic minimal surface, which has zero mean curvature and is periodic and continuous along the three spatial axes.[14] Cubic phases are optically transparent, non-birefringent, and have much higher viscosity and diffusion than the opaque, birefringent H_{II} phase.[11]

MO has previously shown reversible pH-induced phase transitions. Xu *et al.* reported a MO-based nanoparticle system that reversibly transitions from an inverse hexagonal phase (H_{II}) to a micellar cubic phase as the pH of the surrounding

buffer increases from 4 to 7.[15] Similarly, Aota-Nakano *et al*. investigated a ternary system of monoolein/oleic acid/pH buffer and observed phase transitions between primitive cubic (*Im3m*) and double diamond cubic (*Pn3m*) phases, *Pn3m*–*Im3m* and H_{II}–*Im3m*, as the pH increased from 3 to 7, depending on the molar fraction of oleic acid.[16] These studies have largely focused on pH-induced lyotropic phase transitions to trigger the release of pharmaceutical compounds in biomedical applications, exploiting changes in diffusivity within the aqueous channels.

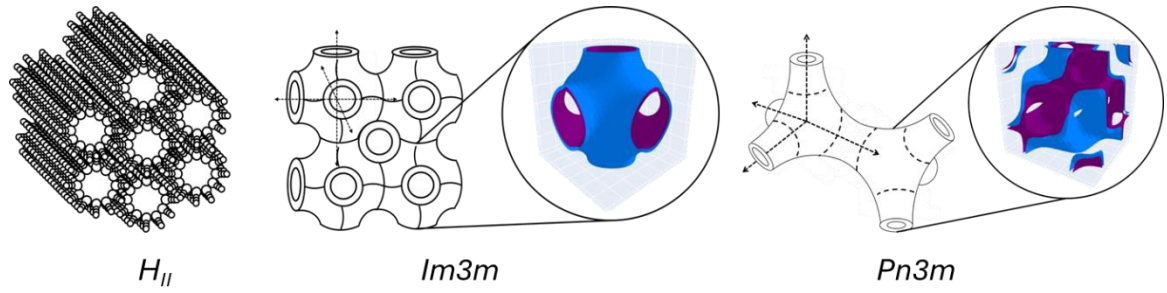

Figure 4.1. Phases observed for monoolein systems: hexagonal (H_{II}), primitive cubic (*Im3m*), and double diamond cubic (*Pn3m*).

Although pH-induced transitions in lipid systems are well studied, the broader range of physical properties that can be altered, and the corresponding applications enabled by these changes, remain relatively underexplored. Notably, the H_{II}-cubic phase transition, which results in a change in appearance from opaque to transparent, could have significant applications in smart materials, such as smart glass.[13,17] Moreover, most existing research has focused on systems that respond to external environmental triggers, but a broader range of applications could be realised if phase transitions were instead triggered over time, with the material's properties evolving dynamically in a controlled, programmable manner.

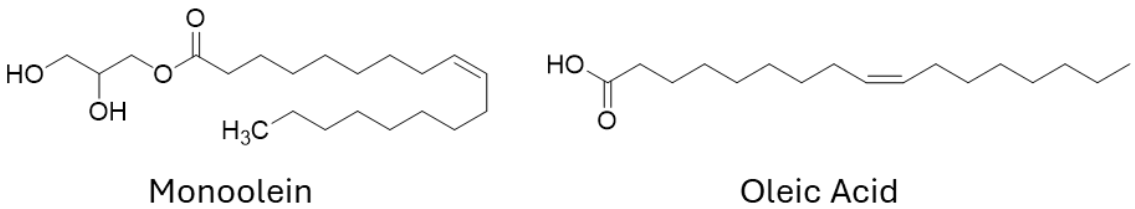

Figure 4.2. Chemical structure of monoolein and oleic acid.

This chapter expands on this concept by presenting pre-programmed temporal control over lipid self-assembly. This is achieved by coupling a monoolein/oleic acid system (Figure 4.2) with the transient pH triggers described in Chapter 3,

offering new insights into the dynamic behaviour of lipid-based materials and their potential applications in responsive, time-controlled systems.

4.1. Results and Discussion

4.2.1. Monoolein phase behaviour

The phase behaviour of the monoolein and 10% oleic acid/monoolein (wt %) systems was determined by Wanli Lu (University of Bath), who showed that MO in an excess-water environment was insensitive to pH changes and adopted a *Pn3m* symmetry between pH 3 and 10. Therefore, to obtain pH-triggered changes, 10% oleic acid was added to the monoolein (10% OA/MO), which displays varying phase behaviours. The system forms an H_{II} at pH 4, a *Pn3m* at pH 10, and a mixed H_{II}-*Pn3m* phase at pH 7 (Figure 4.3).

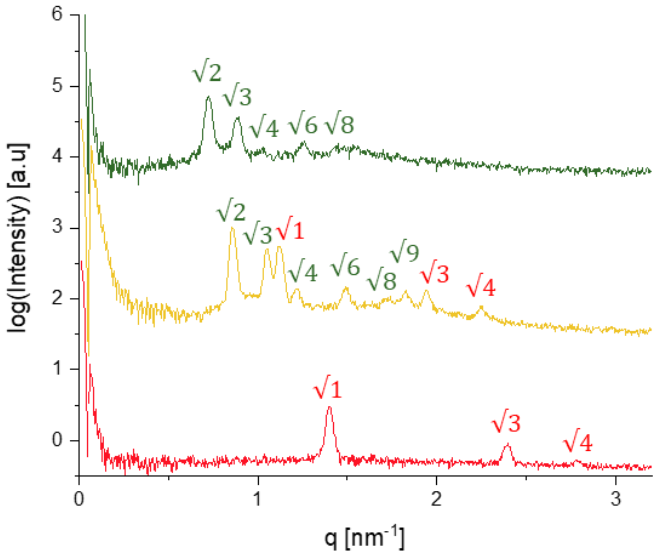

Figure 4.3. a) SAXS of 10% OA/MO soaked in different pH buffers: pH 4 (red), pH 7 (orange), and pH 10 (green) at 25 ˚C. 10% OA/MO cubic phases adopt *Pn3m* symmetry and are indexed as √2, √3, √4, √6, √8, √9. 10% OA/MO hexagonal H_{II} phases are indexed as √1, √3, √4.

The phase change observed with pH is due to the addition of oleic acid. When the pH is lower than the pK_a of oleic acid (pK_a = 5), the carboxyl headgroup is protonated, neutralising the negative charge.[18] The reduction in hydration and repulsion between headgroups decreases the effective area of the hydrophilic headgroups, thereby increasing the curvature of the lipid/water interface and producing the H_{II} phase observed at pH 4. When the pH is higher than the pK_a the

headgroup area of lipids at the interface increases and the acid headgroup becomes negatively charged, producing a flatter interface of the cubic phases. Therefore, the 10% OA/MO system adopts mixed *Pn3m*/H_{II} phase at neutral pH and *Pn3m* at high pH. The peak positions shift toward smaller angles as the surrounding pH increases, indicating that the lattice cell dimension of the crystalline structure increases due to stronger repulsion and reduced interfacial curvature.

The phase behaviour observed here differs from that reported by Aota-Nakano *et al*. However, these slight differences in adopted phases can be attributed to the different impurities present in different sources of monoolein and oleic acid.[16]

4.2.2. *Pn3m-to-HII* phase transition

To trigger a *Pn3m*-to-H_{II} phase transition, the lipid system was combined with the methyl formate hydrolysis reaction (Figure 4.4). An initial *Pn3m* phase was formed by soaking the 10% OA/MO coating in a pH 10 buffer. The buffer solution was replaced with a 5% (v/v) methyl formate solution at pH 10. The methyl formate was added to the buffer solution immediately before replacing the coating solutions. *In situ* flow-through SAXS was used to monitor the phase behaviour over 16 hours.

As shown in Figure 4.4, the 10% OA/MO system initially adopted a *Pn3m* cubic phase in the methyl formate solution. The peak positions gradually shifted to higher q values, suggesting that the lattice cell dimensions were decreasing. After 260 minutes, a new peak was observed at 1.3 nm^{-1}, and after 300 minutes, a new set of peaks was observed at 1.2, 2.1, and 2.4 nm^{-1}. The intensity of these new peaks continued to increase, while their width decreased over time, suggesting either an increase in crystallite size or a decrease in sample heterogeneity. After 600 minutes, the *Pn3m* peaks had disappeared. The H_{II} peaks first appeared at approximately pH 4, and the *Pn3m* peaks fully disappeared at approximately pH 3.

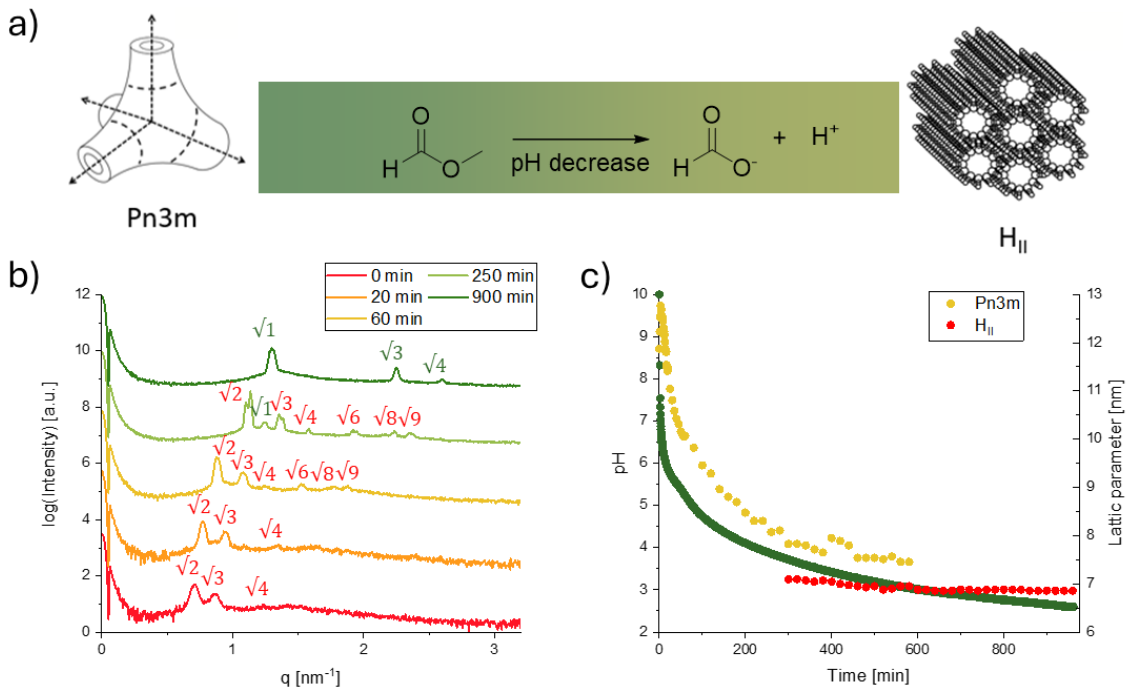

Figure 4.4 a) Schematic illustrating the phase transition of 10% OA/MO from *Pn3m* to H_{II} induced by a methyl formate hydrolysis reaction. b) *in-situ* flow-through SAXS of 10% OA/MO in methyl formate pH 10 buffer solution over 900 minutes. c) pH and lattice parameter over time of 10%OA/MO mesophase during the methyl formate hydrolysis reaction.

The phase transition pH values differ slightly from those observed with the pH buffers alone, in which the sample adopted the H_{II} phase at pH 4. However, this discrepancy may reflect out-of-equilibrium kinetic processes due to hindered diffusion of methyl formate or a delay in the charge being evenly distributed throughout the material. Also, pH was not measured in the SAXS capillary but in a separate beaker containing the solution after flow-through.

4.2.3. H_{II}-to-*Im3m* phase transition

To trigger an H_{II}-to-*Im3m* phase transition, the lipid system was combined with the urea/urease reaction (Figure 4.5). An initial H_{II} phase was formed by soaking the 10% OA/MO system in a pH 4 buffer. The buffer solution was replaced with a urea/urease solution at pH 4. The urea was added to a urease buffer solution immediately before replacing the coating solutions. *In situ* flow-through SAXS was used to monitor the phase behaviour over 60 minutes.

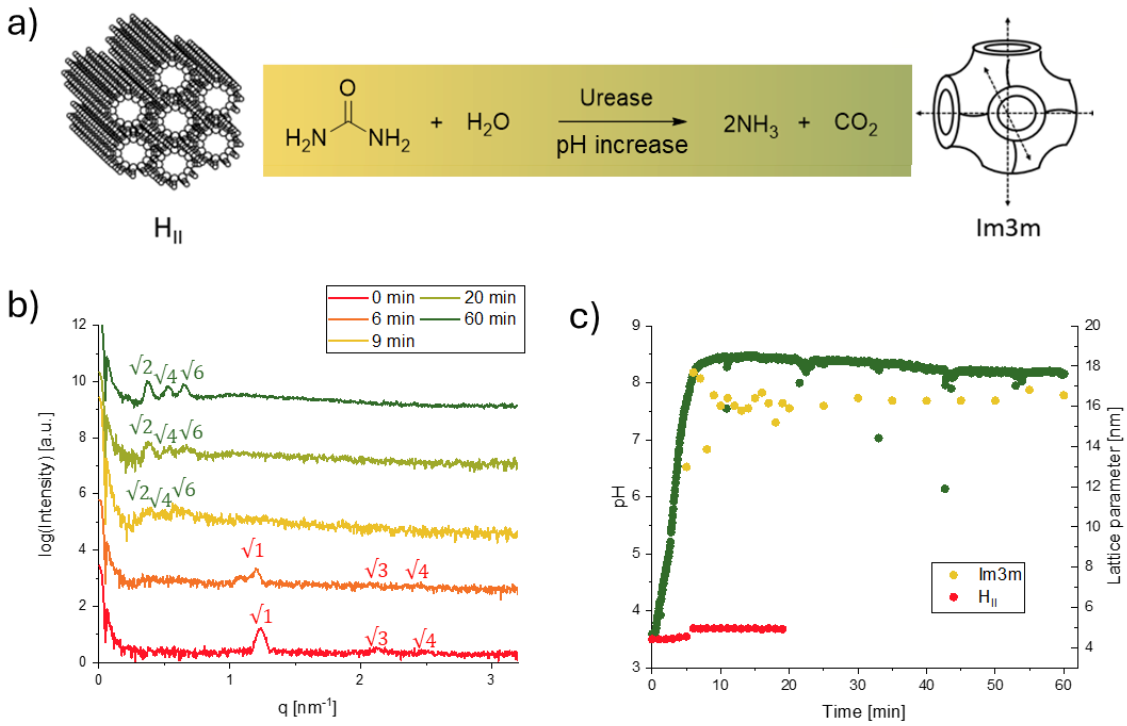

Figure 4.5. a) Schematic illustrating the Phase transition of 10% OA/MO from H_{II} to *In3m* induced by a urea-urease reaction. b) *in-situ* flow-through SAXS of 10% OA/MO in urea-urease pH 4 buffer solution over 60 minutes. c) pH and lattice parameter over time of 10%OA/MO mesophase during the urea-urease reaction.

As shown in Figure 4.5, the 10% OA/MO system initially adopted an H_{II} phase in the urea/urease solution. 5 minutes after replacing the buffer solution, the H_{II} phase peak intensity decreased, and a new peak was observed at 0.35 nm^{-1}. At 20 minutes, all H_{II} peaks disappeared, and more peaks indicating the *Im3m* phase appeared at 0.55 and 0.7 nm^{-1}. As with the methyl formate system, the new peaks increased in intensity over time as more of the material was transformed to *Im3m*. The *I3m3m* peaks first appeared at approximately pH 8, and the H_{II} peaks fully disappeared at approximately pH 8.5.

Notably, the 10% OA/MO system forms the *Im3m* cubic phase rather than the *Pn3m* cubic phase. The adoption of a different cubic symmetry phase may be due to a pathway-dependent trapped state. The *Im3m* and *Pn3m* phases are predicted to be similar in energy under excess water conditions, so there would be little driving force for their interconversion.[19] Alternatively, the *Im3m* phase could be induced by an interaction with one of the species involved in the pH transformation.

As with the methyl formate-induced transition, the phase change occurs at slightly different pH values compared to the buffer solutions: at pH 7, the system remained in the H_{II} phase, whereas in the pH 7 buffer alone, the system was a mixed phase. This is likely due to delayed kinetic processes or to experimental factors in the pH measurement, as mentioned previously.

4.2.4. *H_{II}-to-Im3m-to-H_{II}* phase transition

Finally, both triggers were combined to produce a controlled phase transition from H_{II} to *Im3m* and back to H_{II}. As with the transient gels, the urea/urease reaction is initially dominant, so the pH initially increases to around 8. As urea is consumed, methyl formate hydrolysis becomes dominant, and the pH is reduced to 6.8. *In situ* flow-through SAXS was used to monitor the phase behaviour of the 10% OA/MO system in the presence of both triggers (Figure 4.6).

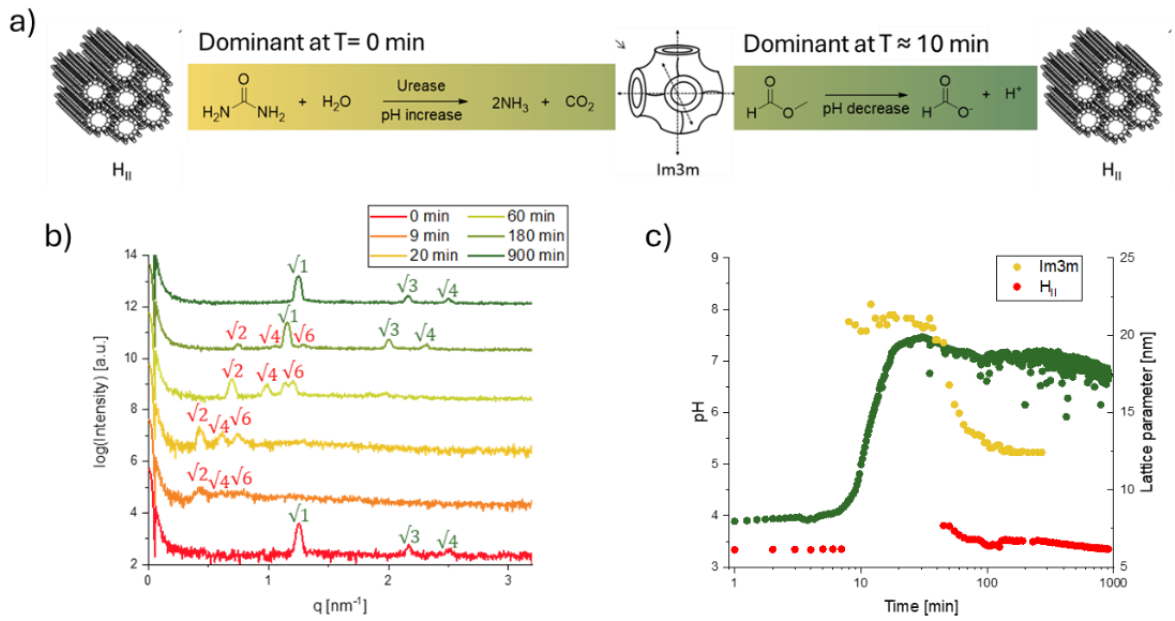

Figure 4.6. a) Schematic illustrating the 10% OA/MO *Im3m*-to-*HII* transition induced by the combined urea–urease and methyl formate reactions. b) *in-situ* flow-through SAXS of 10% OA/MO in methyl formate, urea, and urease solution at pH 4 over 900 minutes. c) pH and lattice parameter over time of 10% OA/MO mesophase during the combined urea–urease and methyl formate reactions.

As with the urea/urease-induced transition, an initial H_{II} phase was formed by soaking the 10% OA/MO system in a pH 4 buffer. This buffer was then replaced

with the urea/urease/methyl formate solution at pH 4, with urea and methyl formate added immediately before replacing the coating solution.

The 10% OA/MO system adopted the H_{II} phase during the first 10 min after injection of the solution. As the pH increases, the *Im3m* peaks start to form at 9 min. This transition from H_{II} to *Im3m* did not proceed *via* coexisting phases, unlike the urea/urease-induced transition. Probably due to the pH change being more rapid, meaning the coexisting phases were missed. As expected, the cubic phase showed the same *Im3m* symmetry as in the previous urea/urease experiment. After 2 hours, the *Im3m* cubic peaks increased in intensity and shifted to higher q values.

The second transition began after 2 hours as the H_{II} peaks reappeared and the *Im3m* peaks stopped shifting. The system remained in a mixed H_{II}-*Im3m* phase for approximately 160 minutes. Once the *Im3m* peaks have disappeared, the remaining H_{II} peaks shift to higher q values as the system becomes more structured and monophasic.

The phase transitions of the 10% OA/MO system depend on the rates of methyl formate hydrolysis and urea/urease reactions. Therefore, as shown in gel transient systems, the rate of pH change can be tuned by varying the concentrations of urea, urease, and methyl formate to control the timing of phase transitions.[20]

4.2.1. Macroscopic properties

In addition to SAXS, the different 10% OA/MO phases can be distinguished by their macroscopic properties. As with the flow-through SAXS, a 10% OA/MO sample was prepared and submerged in a solution containing urea/urease, and methyl formate at pH 4. The system's viscosity was monitored using 1-point viscosity measurements, obtained by removing small samples (Figure 4.7). Initially, the sample in its hexagonal phase was relatively nonviscous, but as the pH increased, the viscosity increased as the cubic phase formed. Then, as the pH decreases, the viscosity drops back to close to its original value. This is consistent with the SAXS data and current research, which suggests that the two phases should have different viscosities.[11]

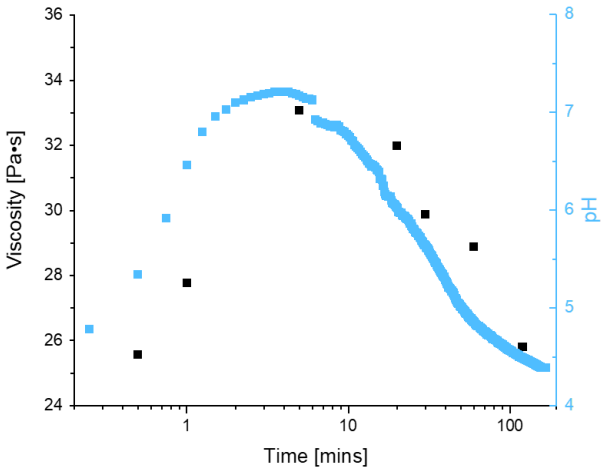

Figure 4.7. Viscosity (black) and pH (blue) over time for the 10% OA/MO system with methyl formate, urea, and urease. pH and rheology measurements were performed with two different samples under identical conditions.

In addition, the two phases have distinct turbidites, as shown in Figure 4.8. These changes in turbidity and viscosity agree with the expected results from flow-through SAXS experiments. At low pH when the lipid adopts the hexagonal phase the system is opaque and at high pH when the lipid adopts the cubic phase the system is transparent. These changes are due to the system becoming more isotropic as the cubic phase predominated.

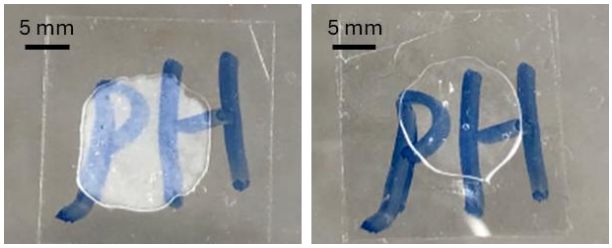

Figure 4.8. Turbidity of 10% OA/MO sample with the hexagonal phase at pH 4 (left) and cubic at pH 10 (right).

4.3. Conclusions

This chapter has demonstrated that pH triggers employed for transient gel systems can be applied to other pH-responsive systems to achieve temporal control. A 10% oleic acid monoolein system, combined with urea, urease, and methyl formate, was used as a new pathway for phase transitions. H_{II}-to-*Im3m*, *Pn3m*-to-H_{II}, and H_{II}-to-*Im3m-to-*H_{II} transitions were successfully demonstrated. Finally, the effect of phase on the macroscopic properties of the MO/OA system was shown. This

system holds significant promise for developing materials with precisely controlled macroscopic properties that can respond to environmental stimuli, opening numerous possibilities for material design.

4.4. Experimental

4.4.1. Materials

Methyl formate (anhydrous, 99%), and urease (U4002-100KU, Jack Beans, 100,000 units/g solid), sodium phosphate monobasic, and sodium phosphate dibasic were purchased from Sigma-Aldrich. Urea (ultrapure 99%) was purchased from Alfa Aesar. Monoolein was purchased from Croda (Cithrol GMOHP-SO-LK, purity >96%). Sodium hydroxide and hydrochloric acid were purchased from Honeywell. Deionised water was employed in all experiments.

4.4.2. Preparation of 10% OA/MO (w/w) matrix

Monoolein was heated and sonicated at 60 °C in a water bath for 20 min to allow the transformation from solid to liquid.[2] After this, 94 mg (approximately 100 µL) of monoolein was pipetted and mixed with 119 µL of ethanol to form a 50/50 monoolein/ethanol (w/w) mixture. This mixture was vortexed for 5 min to homogenise the sample. The procedure above was repeated for oleic acid (OA) to produce a 50/50 oleic acid/ethanol (w/w) mixture. All samples were left to equilibrate to room temperature before use. To prepare 10% OA/MO (w/w), 20 µL of 50% OA/EtOH was added to 200 µL of 50% MO/EtOH, and the mixture was vortexed for 5 min. This lipid ethanol mixture was dried in a fume hood for 48 h to allow for solvent evaporation. The Eppendorf tube containing the sample was weighed before and after evaporation to determine the solvent loss.

4.4.3. Viscosity measurements

Viscosity experiments were carried out on an Anton Paar Physica MCR 302 rheometer at room temperature. A 25 mm cone plate geometry (CP25, cone angle 1°) was used at a measuring distance of 0.047 mm. Viscosity sweeps were performed at a shear rate of $1 \times 10\ s^{-1}$. The 10% OA/MO sample was kept in a water bath at 25 °C in between measurements. For 1-point viscosity measurements, 100 µL of the 10% OA/MO sample was pipetted onto the plate, and 1 mL of the pH

reaction solution was added to fully cover the sample. A viscosity sweep was run for 2 min at each time point, and the first data point was taken as the sample's viscosity.

4.4.4. pH measurements

pH measurements were performed using a HANNA FC200 pH probe with a 6 mm × 10 mm conical tip. The pH values were accurate to ±0.1. To monitor pH changes in the lipid system with urea, urease, and methyl formate, excess solution flowed through the SAXS system and was collected, and pH was measured throughout the SAXS measurements.

4.4.5. Small-angle X-ray scattering

SAXS measurements were performed using a Cu Kα radiation source (λ =1.54 Å) on an AntonPaar SAXSpoint 2.0 instrument. The experiments were performed at a camera length of 0.561 m, resulting in a range of 0.0052–4.3327 nm^{-1}. 2D scattering patterns were acquired on a Dectris Eiger detector, and a full azimuthal integration was performed to reduce the data to an I vs q plot using Anton Paar SAXSAnalysis software. The collection capillary consisted of 2 pieces of 1 m polytetrafluoroethylene (PTFE) tubing (Diba, 0.8 mmID, 1.6 mm OD) that were attached to both sides of a capillary that had been previously coated with OA/MO. The capillary was mounted onto the Anon Paar Multi-Capillary Heated-Cool Sampler. The tubing was fed out of the SAXS chamber; one end was placed into a 100 mL beaker containing a pH probe, while the other end was connected to a 10 mL syringe.

The 10% OA/MO sample was heated at 70 °C on a hot plate for 10 min, after which 40 µL of the sample was pipetted and injected into a capillary flow cell made by Wanli Lu (Great Bay University), where the X-ray beam passes through a 1 mm diameter quartz tube (wall thickness approximately 10 µm). Excess lipids were drained off, followed by gentle purging under N_2 for 30 s to form a coating. The mass of the lipid coating was obtained by weighing the capillary before and after. The thickness of the lipid layer could be estimated by assuming that it adopted a uniform cylindrical shape. The SAXS sample holder is not temperature-controlled,

and the SAXS chamber temperature ranged from 25 to 27 °C. Hence, for all experiments, the temperature was in this range.

For the urea/urease flow-through SAXS measurements, 3.2 mL of urease (0.254 mg/mL) was added to 0.8 mL of water adjusted to pH 4. This solution was then adjusted to < pH 4. Directly before the measurement, 20 µL of urea (2 M) was added, and the resulting solution was used immediately. For the methyl formate flow-through SAXS measurements, 200 µL of methyl formate was added to 3.8 mL of water adjusted to pH 10 to give a 5% (v/v) methyl formate solution, which was then used immediately. For the combined trigger solution (urea/urease and methyl formate), 3.18 mL of urease (0.254 mg/mL) was added to 0.8 mL of water, which had been adjusted to pH 4. This solution was then adjusted to < pH 4. Directly before the measurement, 200 µL of methyl formate and 20 µL of urea (2 M) were added, and the resulting solution was used immediately.

Phase transformation induced by pH changes was monitored at three stages: before, during, and after the reactions. Before the experiment began, 6 mL of buffer solution was dispensed into the capillary to hydrate the lipid coating. The pH of the buffer solution matched the starting pH of the hydrolysis reaction solutions. Five SAXS measurements, each with an exposure time of 60 s, were collected consecutively to assess whether the system was equilibrated. Before loading the reaction solution, the buffer solution inside the capillary was removed by injecting an empty 10 mL syringe. Approximately 4 mL of pH reaction solution was dispensed into the capillary immediately after it was emptied. The phase behaviour of OA/MO soaked in the reaction solution was continuously monitored by SAXS, with 1 min per frame over 20 min. After this, the exposure time was increased to 5 min per frame for the next 40 min. Based on previous data, the pH change rate was expected to peak within the first 20 min, after which it would gradually decrease.[20] Therefore, a longer exposure time was used after 20 min to improve the signal-to-noise ratio. For the samples loaded with methyl formate solutions, the capillary was monitored for an additional 15 hours at 20 min per frame, due to the slow hydrolysis kinetics.

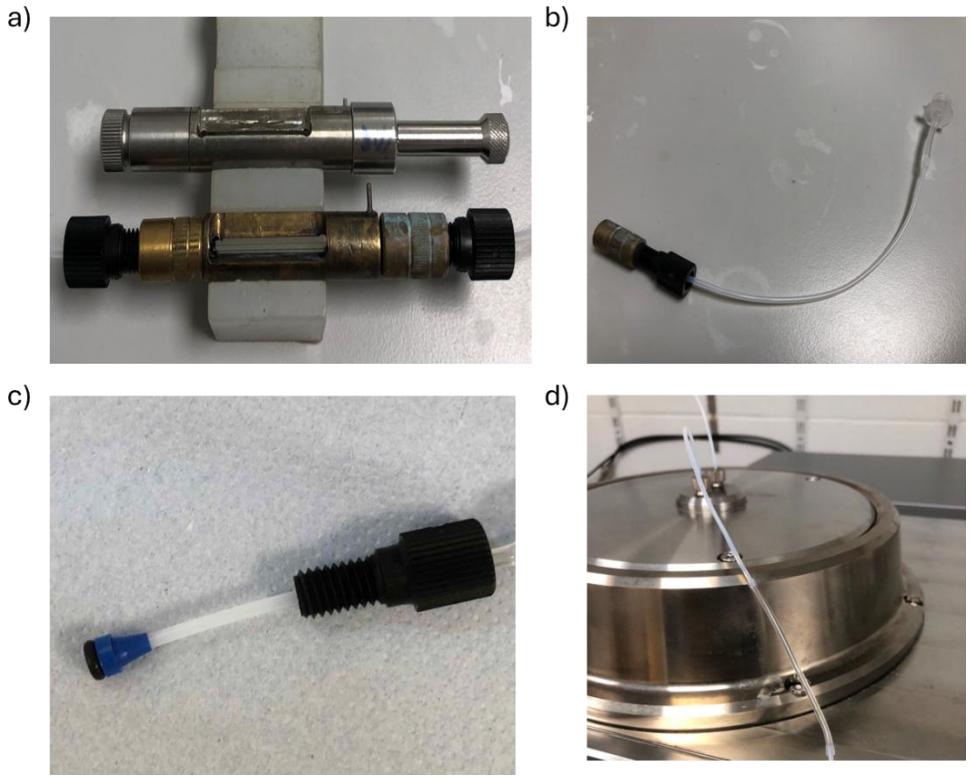

Figure 4.9. a) Anton Paar quartz capillary with metal disk seals (top) and in-house metal case for a borosilicate capillary (ø=0.7mm, thickness=0.1mm) with open-ended disk seals (bottom), b) Metal disk seal to PTFE tubing connector for flow-through experiments, c) Flow-through tubing connector consisting of PTFE tubing with a ETFE ferrule (1/16" OD), the corresponding end fitting threaded through and an O-ring (ID=1 mm) attached to the capillary end, d) PTFE tubing fed into the SAXS chamber for flow-through experiments.

4.5. References

1 S. Ghosh, A. Ray and N. Pramanik, *Biophys. Chem.*, 2020, **265**, 106429.

2 H. Qiu and M. Caffrey, *Biomaterials*, 2000, **21**, 223–234.

3 R. Mezzenga, C. Meyer, C. Servais, A. I. Romoscanu, L. Sagalowicz and R. C. Hayward, *Langmuir*, 2005, **21**, 3322–3333.

4 G. Pelzl and A. Hauser, *Ph. Transit.*, 1991, **37**, 33–62.

5 Y. Huang and S. Gui, *RSC Adv.*, 2018, **8**, 6978–6987.

6 S. Peng, Q. Guo, T. C. Hughes and P. G. Hartley, *Langmuir*, 2014, **30**, 866–872.

7 R. Jnaidi, A. J. Almeida and L. M. Gonçalves, *Pharmaceutics*, 2020, **12**, 860.

8 W. Cui, J. Li and G. Decher, *Adv. Mater.*, 2016, **28**, 1302–1311.

9 S. Mele, S. Murgia, F. Caboi and M. Monduzzi, *Langmuir*, 2004, **20**, 5241–5246.

10 G. C. Salata, I. D. Malagó and L. B. Lopes, *AAPS PharmSciTech*, 2022, **23**, 260.

11 W. Sun, J. J. Vallooran and R. Mezzenga, *Langmuir*, 2015, **31**, 4558–4565.

12 R. Negrini, A. Sánchez-Ferrer and R. Mezzenga, *Langmuir*, 2014, **30**, 4280–4288.

13 C. V. Kulkarni, W. Wachter, G. Iglesias-Salto, S. Engelskirchen and S. Ahualli, *Phys. Chem. Chem. Phys.*, 2011, **13**, 3004–3021.

14 L. Han and S. Che, *Adv. Mater.*, 2018, **20**, 1705708.

15 Z. Xu, J. M. Seddon, P. A. Beales, M. Rappolt and A. I. I. Tyler, *J. Am. Chem. Soc.*, 2021, **143**, 16556–16565.

16 Y. Aota-Nakano, S. J. Li and M. Yamazaki, Biochim. Biophys. Acta Biomembr., 1999, **1461**, 96–102.

17 C.-C. Li, H.-Y. Tseng, C.-W. Chen, C.-T. Wang, H.-C. Jau, Y.-C. Wu, W.-H. Hsu and T.-H. Lin, *ACS Appl. Energy Mater.*, 2020, **3**, 7601–7609.

18 H. Träuble, M. Teubner, P. Woolley and H. Eibl, *Biophys. Chem.*, 1976, **4**, 319–342.

19 G. C. Shearman, O. Ces, R. H. Templer and J. M. Seddon, *J. Phys. Condens. Matter*, 2006, **18**, S1105–S1124.

20 S. Panja, C. Patterson and D. J. Adams, *Macromol. Rapid Commun.*, 2019, **40**, 1900251.

Chapter 5 – Electrofabrication and electropolymerisation of carbazole-protected amino acids

5.1. Introduction

As discussed in Chapter 1, dipeptide LMWGs are ideal candidates for producing easily synthesised, biocompatible, and tuneable gels for a variety of applications.[1,2] Hydrogels formed from these gelators offer distinct advantages over polymer-based hydrogels, due to the presence of non-covalent interactions.[1,2] External stimuli readily perturb the supramolecular networks in hydrogels; therefore, these materials often exhibit reversible, dynamic behaviour.[3] They can be gelled electrochemically via various strategies.[4–6] Compared with naturally derived polymeric gels such as chitosan, these gelators yield materials with greater chemical homogeneity and reproducibility, particularly when synthesised electrochemically.[4]

Thordarson *et al*. introduced the first carbazole-protected dipeptide and tripeptide.[7] From these molecules, polycarbazole can be synthesised via anodic oxidation of carbazole in organic solvents, yielding a well-known redox polymer recognised for its exceptional electrochemical and optical properties.[8–11] Fmoc-protected peptides can also be polymerised into polyfluorenes in organic solvents.[12,13] However, some Fmoc LMWGs have been reported to be cytotoxic in vitro, and the molecules are easily cleaved under basic conditions.[14,15] Although Fmoc LMWGs have been studied more extensively, the carbazole moiety is an attractive analogue to avoid these issues.

In 2015, Kubiak *et al*. showed the first electropolymerisation of a Carb-Ala gel.[16] They developed a method to deposit polymer films onto electrode surfaces by first growing Carb-Ala hydrogels via an electrochemically generated pH gradient.[16] To form the hydrogels, an indirect electrochemical approach was used to produce benzoquinone from hydroquinone, which generates protons at the electro-solution interface, leading to a localised drop in pH. This localised drop below the apparent pK_a of the gelator causes gel growth on the electrode surface.[17,18] After polymerisation via cyclic voltammetry, the hydrogel collapsed into an electrochromic polycarbazole film, which exhibited a morphology distinct from that produced from Carb-Ala in acetonitrile (Figure 5.1). The work demonstrated

how Carb-Ala hydrogels can be used as templates to create polymers with distinctive morphologies [16]

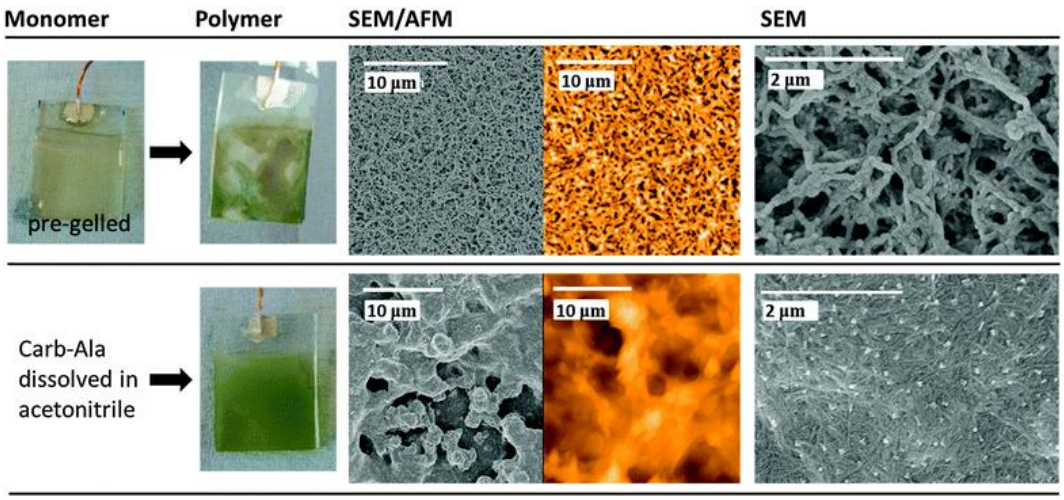

Figure 5.1. A comparison of the structures of large area polymer films grown on FTO glass electrodes by Kubiak et al. The top row shows the structure of the polymer formed during electropolymerisation of the hydrogel. The bottom row shows films obtained from the direct electropolymerisation of Carb-Ala dissolved in acetonitrile. The AFM and SEM images highlight the significant differences in the microstructures of polymer grown via the gel phase. Image reproduced from *Chem. Commun.*, 2015, 51, 10427-10430 with permission from the Royal Society of Chemistry.

The morphology of conjugated polymers, such as poly(carbazoles) and poly(fluorenes), plays a crucial role in determining their bulk physical properties, making the control of morphology essential for various applications.[19,20] These polymers, which show significant promise in areas such as sensors, light-emitting diodes, and solar cells, are valued for their high quantum efficiencies, thermal stabilities, and tuneable photoluminescence.[11,21-23] As surface morphology is key to many applications, there is growing interest in developing polymers with controlled, unique structures.[19,20]

Recent studies have increasingly combined SAXS and SANS with electrochemical techniques to gain deeper insights into the behaviour and performance of materials in electrochemical systems.[24-27] While these techniques have primarily been applied to battery evaluation, they have also been used for electrochemical assembly.[28-32] Randle *et al.* used SANS in an *in situ* electrochemical experiment to

investigate how materials aggregate during electrochemical processes, thereby providing a more comprehensive understanding of the dynamics.[30] Neves et al. examined the fractal behaviour of polyaniline (PANI) composites using SAXS, alongside electrochemical measurements, to explore the structure-property relationships of these materials, which are relevant to applications in sensors, batteries, and capacitors.[33] Using SAXS, they probed the nanostructure of PANI composites, revealing key details about the size, shape, and distribution of pores and aggregates that influence their electrochemical performance.[33]

Recently, numerous *in situ* electrochemical small-angle X-ray scattering (EC-SAXS) experiments have been reported.[34] For example, Loew et al. studied the structural changes of redox enzymes under different electrochemical conditions.[35] By combining SAXS with electrochemical measurements, the study revealed how structural features, such as the size, shape, and aggregation state of the enzymes, changed dynamically during electron transfer. EC-SAXS enabled a deeper understanding of the redox mechanism under study.[35]

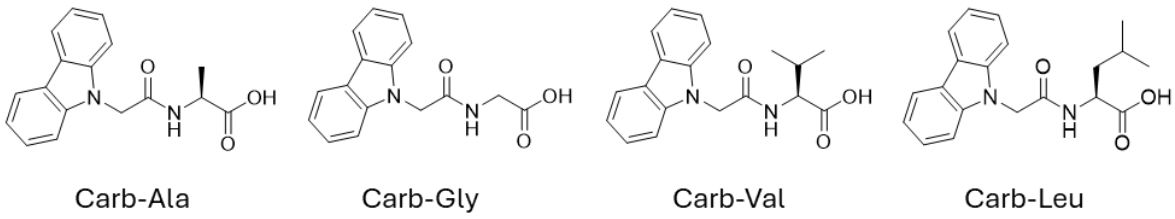

Figure 5.2. Structure of the LMWGs examined in this chapter and the acronyms used.

Building on the success of *in situ* EC-SAXS in studying redox enzymes, a similar approach is applied to investigate the self-assembled structures of electrofabricated carbazole-based hydrogels and their evolution during electropolymerisation. In this chapter, the work of Kubiak *et al.* is extended by replicating their electrochemical gelation with three additional LMWGs: Carb-Gly, Carb-Val, and Carb-Leu (Figure 5.2). Electropolymerisation was then attempted on all hydrogels to obtain the corresponding electrochromic polymers. This process was closely monitored using in situ SAXS to explore the 1D structures of the hydrogels produced and how these structures change during electropolymerisation. This technique provided insights into the structural changes that occur during hydrogel polymerisation, as well as how the design of

the gelator affects the polymerisation success. By understanding how the structure of these materials evolves, we can better design and fabricate polymers with tailored properties.

5.2. Results and discussion

5.2.1. Electrogelation and electropolymerisation

Following the work of Kubiak et al., who previously demonstrated the electropolymerisation of Carb-Ala, carbazole-protected amino acid hydrogels were formed via electrochemical oxidation of hydroquinone (HQ). As previously noted, the following gelators were used: Carb-Gly, Carb-Val, and Carb-Leu, with Carb-Ala as the control (Figure 5.2).

A three-electrode setup was used, consisting of a working electrode (FTO glass slide, 12 x 15 mm), a reference electrode (aq. Ag/AgCl, 3 M), and a counter electrode (platinum wire). A gelator solution (7 mL, 5 mg/mL) containing HQ (5 mg/mL) and NaOH (0.1 M) were added into the container, and a galvanostatic current of 0.7 mA/cm^2 was applied to the working electrode for 300 seconds. To prevent premature oxidation of HQ, the gelator solutions were adjusted from pH 11 to pH 7 prior to gelation, since oxidation is accelerated at high pH.

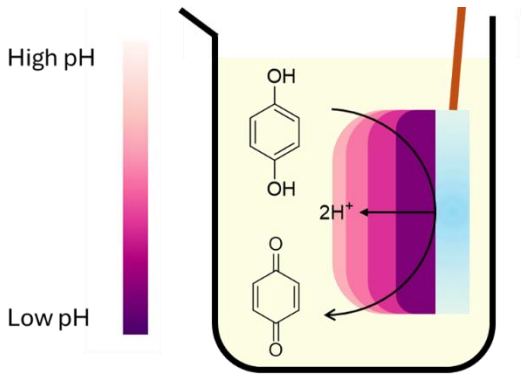

Figure 5.3. Schematic representation of electrochemical gelation. To trigger gelation, a constant current is applied to the electrode surface, electrochemically oxidising hydroquinone to benzoquinone, which generates protons at the electrode-solution interface. As a result, the pH at the electrode surface decreases, leading to gel formation.

The gels form due to a pH gradient, with a low pH at the FTO glass slide surface and a higher pH (pH 7) in the bulk solution (Figure 5.3). In all cases, gelation

occurs via the formation of a 3D network of fibres arising from pH-driven self-assembly of functionalised amino acids.[36] Hydrogels with pH values in the range of 3-4 were formed on the FTO glass surface for all gelators (Figure 5.4).

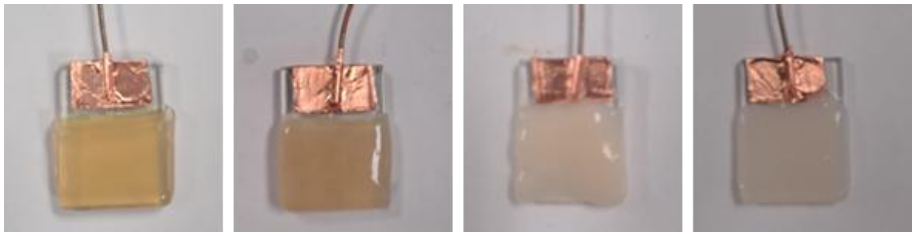

Figure 5.4. Images of the electrofabricated gels in the following order: Carb-Ala, Carb-Gly, Carb-Val, and Carb-Leu (left to right).

To investigate the effect of changing the carbazole gelator on the properties of the resulting gels, strain and frequency data were collected (Figure 5.5). Due to the shape and thickness of the gels, a cup-and-vane geometry could not be employed; therefore, a 12.5 mm parallel-plate geometry was used directly on the gel, which was left on the FTO glass slide. This configuration also prevents artefacts from disturbing the sample. When this type of geometry is used, the hydrogel surface makes the most significant contribution to the average distribution of bulk material properties relative to the rest of the material.[37] However, because the hydrogels on the electrode surface are thin (< 2 mm), this geometry is sufficient for this project and results in a less pronounced effect.

For all of the carbazole-based hydrogels, the G′ and G″ moduli are of approximately the same order of magnitude. Gel stiffness decreases in the order Carb-Ala > Carb-Gly > Carb-Val > Carb-Leu, correlating with increasing side-chain size. This trend suggests that smaller, less sterically hindered side chains promote more efficient molecular packing and alignment within the self-assembled fibres, leading to increased fibre rigidity and higher bulk modulus. In contrast, bulkier side chains likely disrupt packing, producing softer networks with reduced mechanical strength. Strain sweep measurements indicated a narrow LVR and comparable network fragility across the series. Despite differences in absolute stiffness, the similar G′/G″ ratios and behaviour imply that the underlying network structures are mechanically analogous. Consequently, variations in gel strength are unlikely to affect electropolymerisation, suggesting that differences in

electrochemical behaviour are primarily attributable to molecular or electronic effects rather than to macroscopic mechanical constraints.

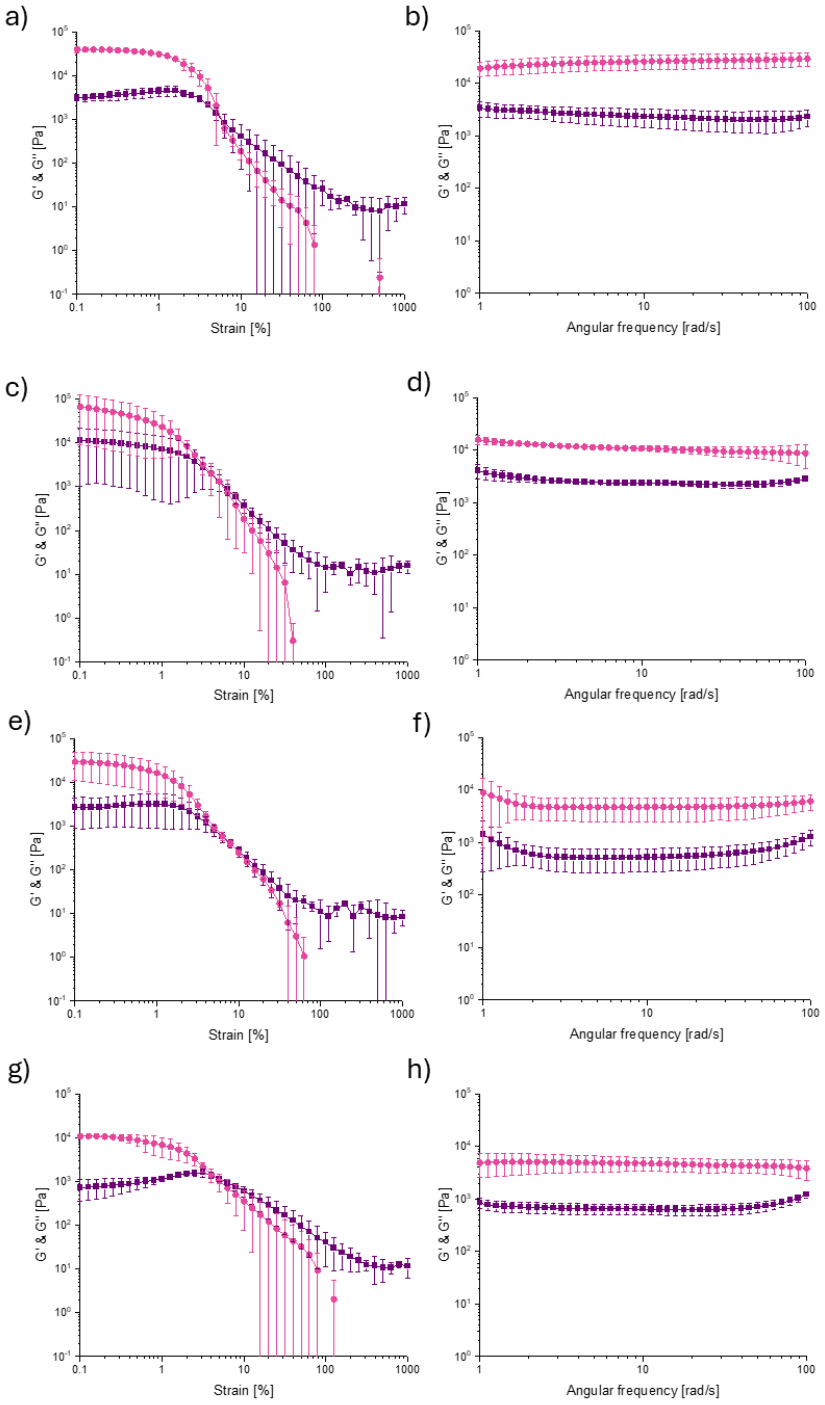

Figure 5.5. Strain and Frequency sweeps, immediately after gelation, for a-b) Carb-Ala, c-d) Carb-Gly, e-f) Carb-Val, and g-h) Carb-Leu.

These hydrogels were subsequently electropolymerised (Figure 5.6). The FTO glass slide on which the hydrogel was attached was removed from the gelator solution,

along with the other electrodes. The glass chamber was rinsed with deionised water to remove any free monomer, and the electrode setup was returned to the container. Perchloric acid (7 mL, 0.1 M) was added. CVs were then repeatedly cycled between 0 and 1.1 V at a scan rate of 40 mV/s for 100 scans. All carbazole derivatives exhibited some degree of electropolymerisation.

Figure 5.6. Images of the electropolymerised samples formed from the gels in the following order: Carb-Ala, Carb-Gly, Carb-Val, and Carb-Leu (left to right).

Two types of behaviour were observed, as depicted in Figure 5.7. The first behaviour was observed in Carb-Ala and Carb-Gly. During polymerisation, the hydrogels collapse into dense polymer films on the electrode for Carb-Ala and Carb-Gly. For the second behaviour observed for Carb-Leu and Carb-Val, there is no collapse onto the surface. The gel layer is maintained, but green polymerisation is observed at the FTO slide surface. In all cases, the polymers produced were electrochromic, cycling between green (oxidation) and colourless (reduction) during CV cycles.

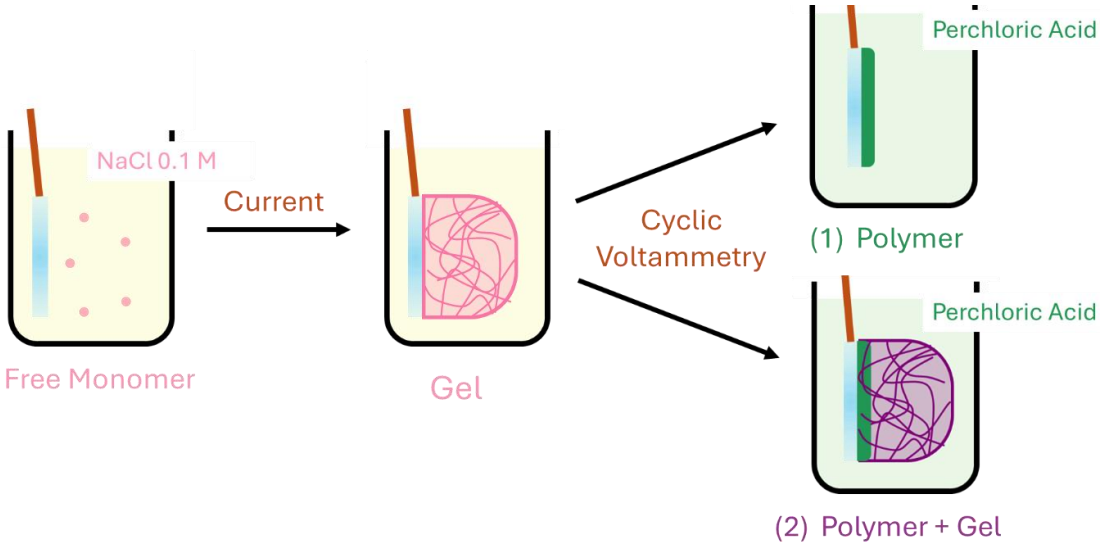

Figure 5.7. Schematic depicting the changes during gelation and polymerisation processes for top (1) Carb-Ala and Carb-Gly, and bottom (2) Carb-Val and Carb-Leu.

Due to the limited solubility of the polycarbazole films, GPC could not be used for characterisation. As a result, only oligomerisation and potential polymerisation could be confirmed. When left overnight, the polymers and gels turned brown due to the reduction of hydroquinone remaining in the gel, and the gel layer for Carb-Val and Carb-Leu dried out as expected.

5.2.2. EC-SAXS Cell

SAXS served as our primary characterisation method for understanding the organisation and nanoscale morphology of carbazole-based gels and polymers. To investigate the self-assembled structures and formation processes of carbazole hydrogels and polymers, an *in situ* EC-SAXS experiment was conducted using a specifically designed EC-SAXS cell (Figure 5.8). This cell was 3D-printed using PLA filament on an Original Prusa i3 MK3S+ printer by Bart Dietrich (University of Glasgow), based on a design developed by Joshua White (University of Southampton) and Sam Richardson (University of Reading).[38]

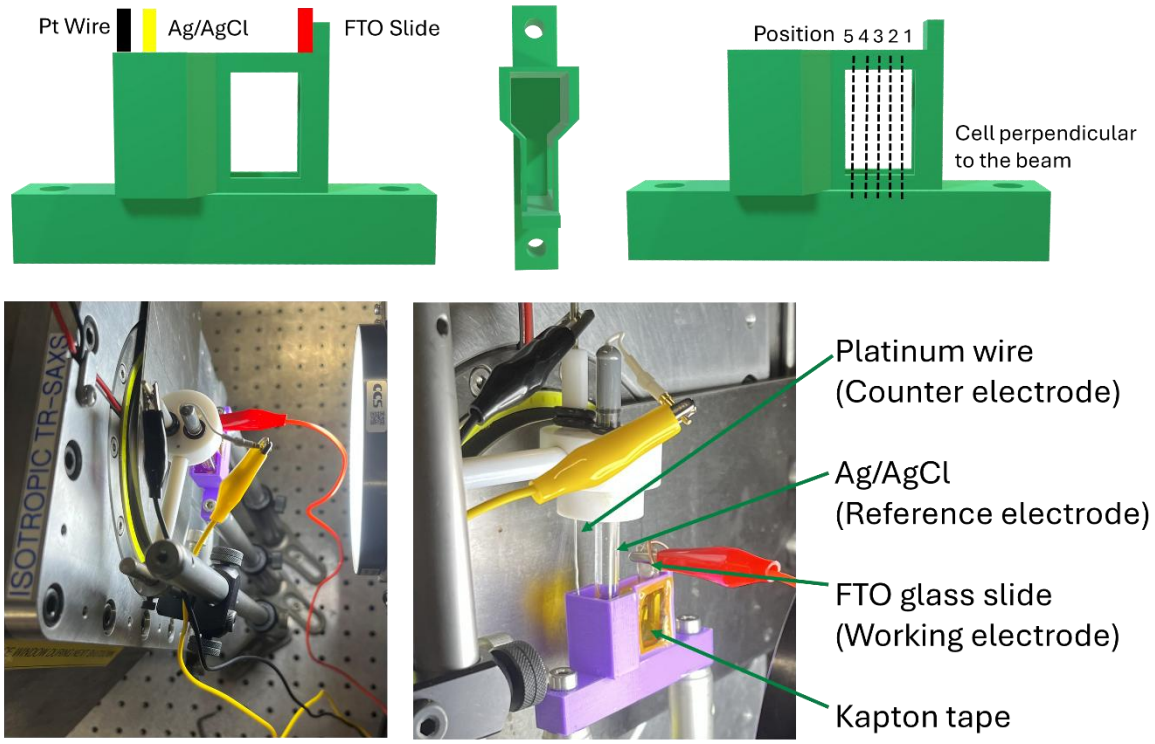

Figure 4.8. Custom EC-SAXS cell used in the *in-situ* SAXS experiment (top), Images of the EC-SAXS set-up at I22 beamline, Diamond Light Source (bottom).

The cell was designed to accommodate the three-electrode configuration and gel growth described previously, with the counter and reference electrodes positioned adjacent to each other. The distance between the working electrode and the counter/reference electrodes was maintained at approximately 2.5 cm, while the separation between the reference and counter electrodes was approximately 1.0 cm. These distances were chosen to closely match those used in laboratory experiments, while keeping the sample width through which the X-ray beam passed relatively small to minimise scattering noise and ensuring that the electrodes did not touch.

During SAXS data acquisition, the EC-SAXS cell was mounted on a metal stage and aligned perpendicular to the X-ray beam. Inside the cell, the same three-electrode system previously mentioned was set up, as illustrated in Figure 5.8. The FTO glass slides were cut into thirds to fit into the cell. The windows on the cell were made of Kapton tape and sealed with epoxy resin to prevent solution leakage. Kapton was selected for its low X-ray scattering properties, which enabled the removal of minor contributions during background subtraction. The electrochemical experiments were carried out by connecting the electrode setup to a potentiostat, which was operated remotely via a computer linked to an external monitor outside the experimental hutch. All these experiments were performed with the help of Alex Loch and Dipankar Ghosh (University of Glasgow), and Adam Squires and Wanli Liu (University of Bath).

5.2.3. In-situ SAXS of electrogelation

To monitor hydrogel growth using SAXS, gels were grown in the custom EC-SAXS cell described above, and the gelator/HQ solutions were prepared as previously described in section 5.2.1. 1.5 mL of the gelator/HQ solution was pipetted into the Echem cell containing the three-electrode setup, filling the cell. A constant current density of 0.1 mA/cm^2 was applied to the FTO glass slide for 300 s. A smaller current density was used to slow down the rate of gelation. Hydrogel formation was observed for all tested gelators: Carb-Ala, Carb-Gly, Carb-Val, and Carb-Leu.

The FTO glass was secured perpendicular to the incoming beam, and SAXS measurements were acquired at 5 positions from the electrode surface to determine whether the nanostructures changed as the hydrogel grew (Figure 5.9). Position 1 was closest to the FTO glass surface, and position 5 was the farthest, with each position spaced 0.2 mm apart. Care was taken for position 1 to avoid beam flaring due to proximity to the FTO surface. Therefore, the beam was manually adjusted to be as close as possible to the glass surface using the beamline camera.

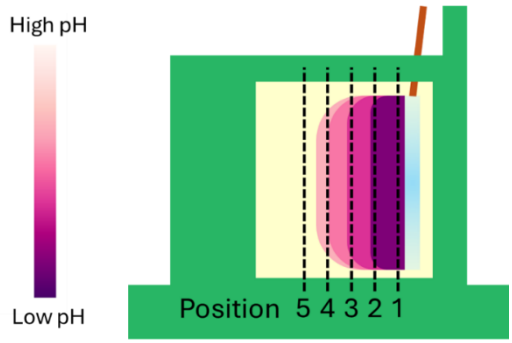

Figure 5.9. Schematic of the sample in the beam showing the positions of the X-ray beam used to probe the samples.

To collect SAXS data, an acquisition script was run concurrently with the electrochemical experiment. An initial scan was performed before the current application to ensure the absence of scattering artefacts (flares) from the FTO glass and to identify any pre-existing nanostructures in the gelator/HQ solutions. Subsequent scans were acquired at 30-second intervals over the 300-second experiment, yielding 12 scans per hydrogel.

To assess potential structural changes during gelation, detailed SAXS analysis was performed at two positions for each gelator: position 1, closest to the electrode surface, and position 3, a representative point in the bulk gel. For the 12 scans at positions 1 and 3, multiple models were fitted to the data to identify the best model for each point. All SAXS data were fitted using five structural models: power law, sphere + power law, cylinder, cylinder + power law, and elliptical cylinder + power law. Model performance was evaluated based on χ^2 values and qualitative fit to the curve. Once the best model was selected, it was then applied to fit the data at positions 2, 4, and 5. All data and fits not discussed in this chapter are provided in Appendix 3.

For these systems, the absolute length is beyond the resolution of this fit.[39] Therefore, for all systems, the length was fixed at an arbitrarily large value of 1000 Å and was not allowed to refine alongside the other parameters from this point onward.

SAXS measurements were collected for the *in situ* electrofabrication of Carb-Ala hydrogel. Hydrogel growth was monitored at all 5 positions by overlaying SAXS scans acquired at each position during gelation (Figures 5.10. a-e). A corresponding heatmap was generated to visualise the intensity of scattered X-rays at q = 0.01 nm^{-1} during gel growth (Figure 5.10f). The scattering intensity range was adjusted to best highlight the gel growth.

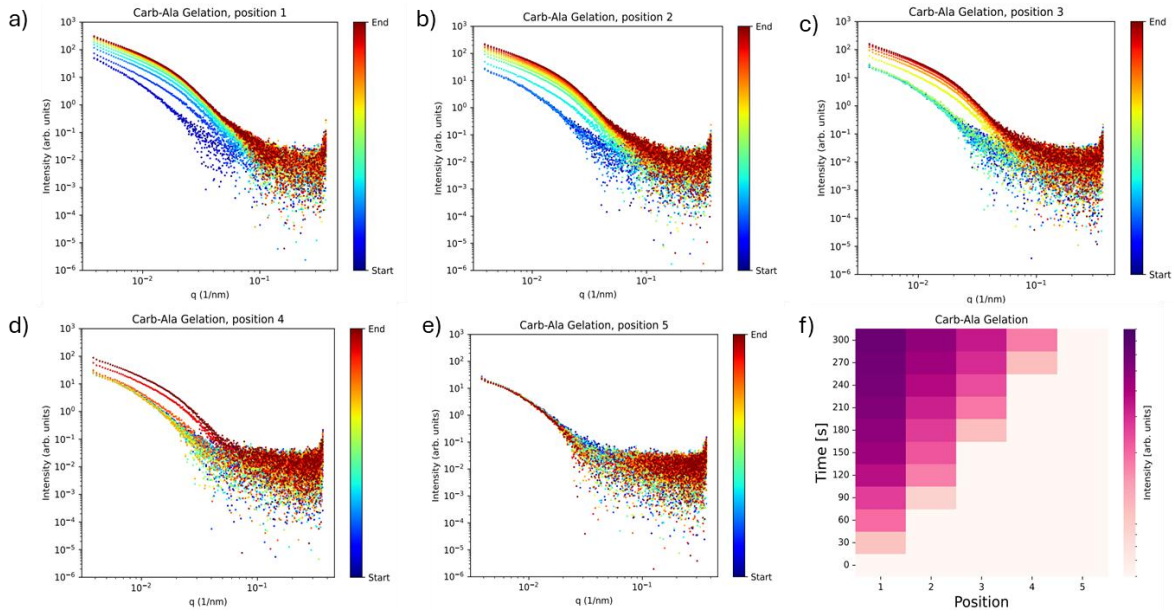

Figure 5.10. (a-e) SAXS plots for positions 1–5 showing Carb-Ala hydrogel formation over 5 mins, with scan colour progressing from blue to red. f) Heatmap of scattering intensity at q = 0.01 nm^{-1} compiled from plots 5.10.a–e. The heatmap scale was set to a minimum intensity of 5 and a maximum of 80.

Both the scatter plots and the heatmap clearly indicate hydrogel formation. The increase in scattering intensity at each position indicates a rising concentration of self-assembled nanostructures, consistent with uniform hydrogel growth. The intensity first increased at position 1 and then progressively increased at positions 2–4, confirming directional growth from the electrode outward. At position 5, the scattering intensity remained low because the hydrogel did not reach that position.

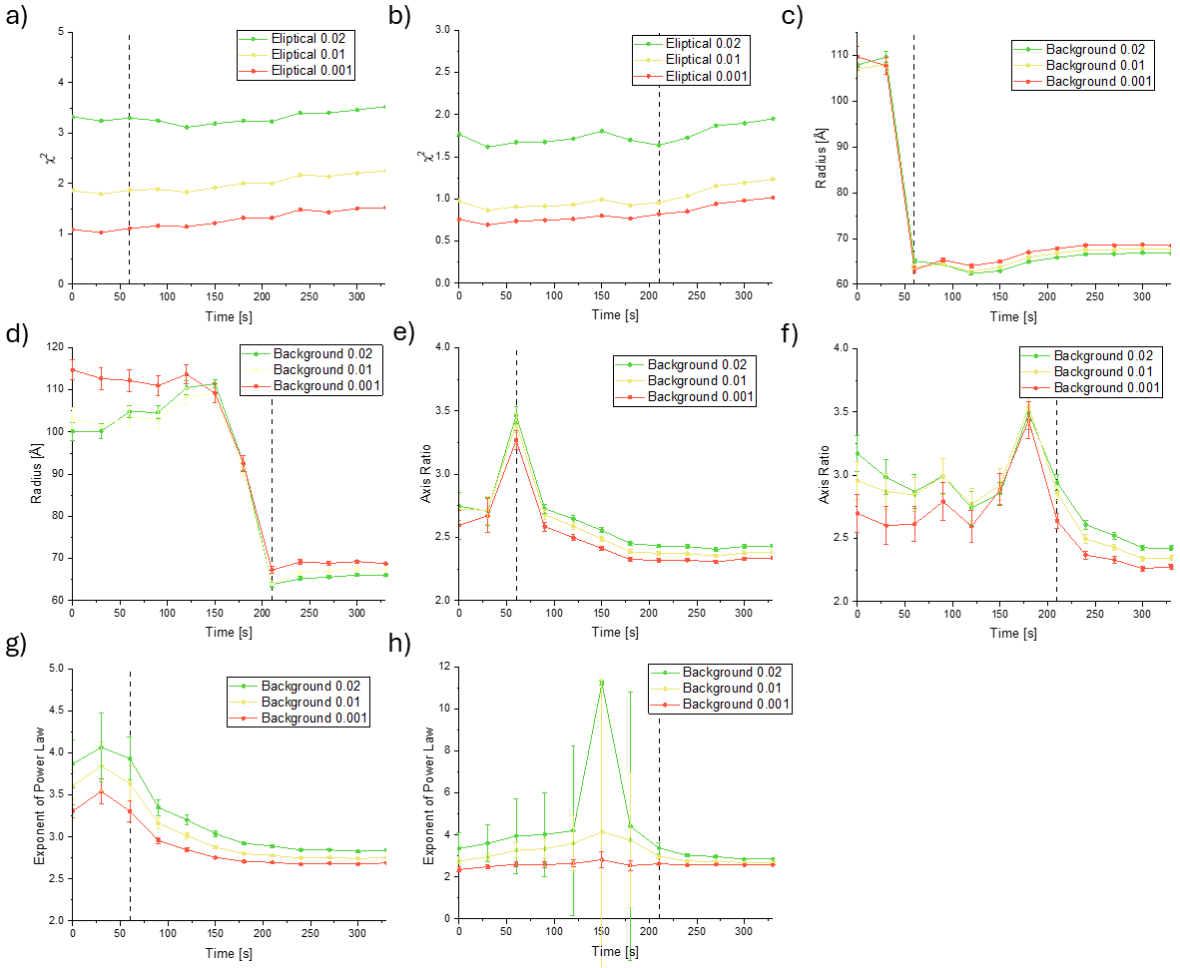

Figure 5.11. Effect of background value on (a) χ^2 for position 1, (b) χ^2 for position 3, c) radius for position 1, d) radius for position 3, e) axis ratio for position 1, f) axis ratio for position 3, g) power-law exponent for position 1, h) power-law exponent for position 3 the dashed line indicates the onset of gel formation. Error bars were derived from the parameter uncertainties calculated during fitting in SasView.

The background was fixed at 0.01 cm^{-1} and was not allowed to vary during the fitting process. To assess the impact of the chosen background value, additional fits were performed for Carb-Ala using background values of 0.001 and 0.2 at positions 1 and 3. The resulting values for χ^2, radius, axis ratio, and power at each position are shown in Figure 5.11. Changing the background did not alter the fitting model; the elliptical cylinder with a power law still fit best, and the values of radius, axis ratio, and power were only minimally affected. Notably, the overall trends observed after gel formation began remained consistent, supporting the conclusion that gel growth was uniform.

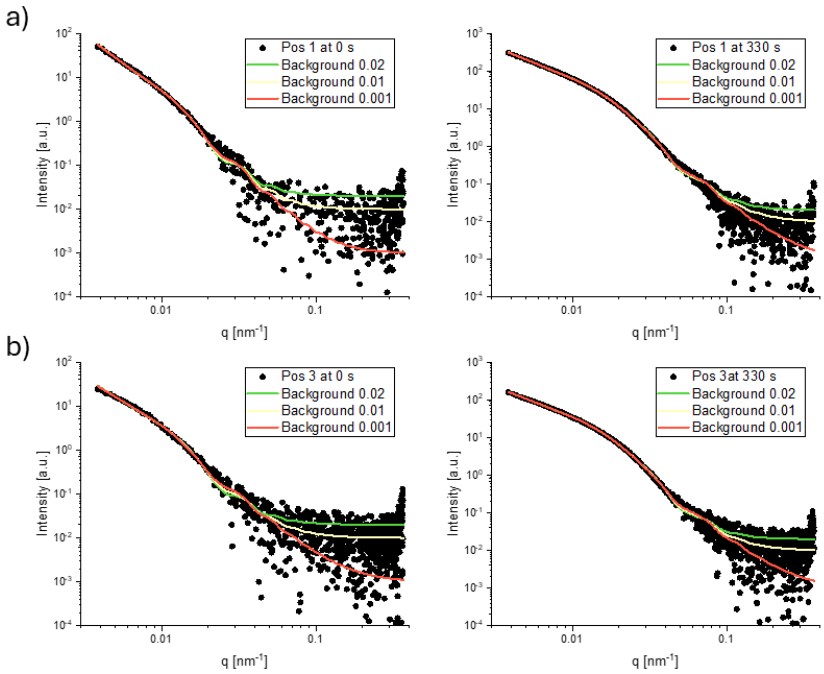

Figure 5.12. SAXS plots at 0 s (left) and 330 s (right) at (a) position 1 and (b) position 3 with elliptical model fits with different fixed background values.

A background value of 0.01 cm^{-1} was selected because it provided the best visual agreement with the SAXS curves, despite yielding slightly higher χ^2 values than the 0.001 cm^{-1} background (Figure 5.12). This background was selected for all gel modelling from this point onward unless otherwise stated.

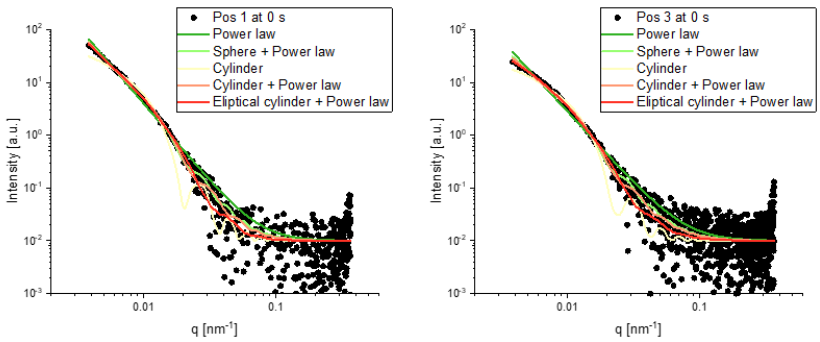

Figure 5.13. Initial SAXS 1D I vs Q plots and fits using different models at positions 1 (left) and 3 (right).

Initial SAXS scans taken prior to the application of current could be fitted to a cylinder with a power-law model (Figure 5.13). Protected amino acids form various micellar nanostructures when dissolved in aqueous conditions, particularly at pH values below 10.5.[40] The cylinder with a power-law model had a relatively low A-scale value compared with those at later time points, suggesting weaker self-

assembled structures in solution compared to in the gel. This contrasts with the stronger, more defined nanostructures observed after gelation onset, which is consistent with hydrogel formation.

The evolution of χ^2 over time for each model is presented in Figure 5.14a. Initially low χ^2 values for all models in early scans reflect overfitting due to the absence of well-defined structures. As gelation progressed, χ^2 increased sharply for the incorrect models after 60 s for position 1 and after 210 s for position 3, indicating the time points at which structures formed, i.e., when the gel reached those positions. After the onset of hydrogel formation, only the elliptical cylinder with a power-law model accurately captured the SAXS curve (Figure 5.14b). Reflecting the presence of hydrogel fibres growing from the electrode and laterally associating into structures with elliptical cross-sections.

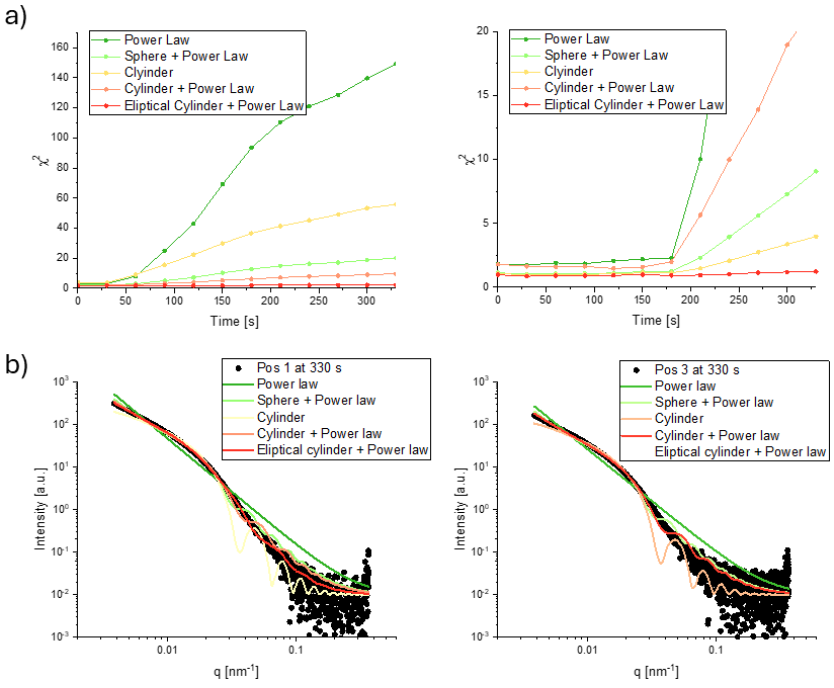

Figure 5.14. a) Evolution of χ^2 over time for all tested models at positions 1 (left) and 3 (right), b) Final SAXS 1D I vs Q plots and fits using different models at positions 1 (left) and 3 (right). Error bars were derived from the parameter uncertainties calculated during fitting in SasView.

At position 1, the radius of the elliptical cylinder increased slightly over time, then stabilised at approximately 68 Å after 210 seconds, likely due to ongoing pH reduction during the experiment, which continued to influence fibre structure. Similarly, the axis ratio decreased over time, then stabilised at approximately 2.4

at 150, and the power-law exponent decreased and stabilised at approximately 2.8 at the same time point, again due to the ongoing pH reduction (Figure 5.11).

For position 3, the radius of the elliptical cylinder increased slightly over time, as with position 1; however, it did not appear to have stabilised by the end of the measurement. The final value radius is 67 Å, comparable to that observed at position 1. Both the axis ratio and the power-law exponent exhibited trends similar to those at position 1, stabilising at approximately 2.4 and 2.7, respectively (Figure 5.11).

The models and fitting values being consistent across positions indicated that the fibres have a consistent shape and size throughout the entire gel sample. All fitting data for Carb-Ala at all positions are provided in the Appendix (Figure A3.1, Table A3.1-Table A3.9).

As with Carb-Ala, SAXS of Carb-Gly was collected and tracked using colour-coded overlays and a heatmap (Figure 5.15). The scattering intensity values are higher for Carb-Gly than for Carb-Ala because a new FTO glass slide was used for each experiment, and the slides were not precisely the same width; the slide for Carb-Gly was likely wider, resulting in a larger gel and, consequently, a higher intensity.

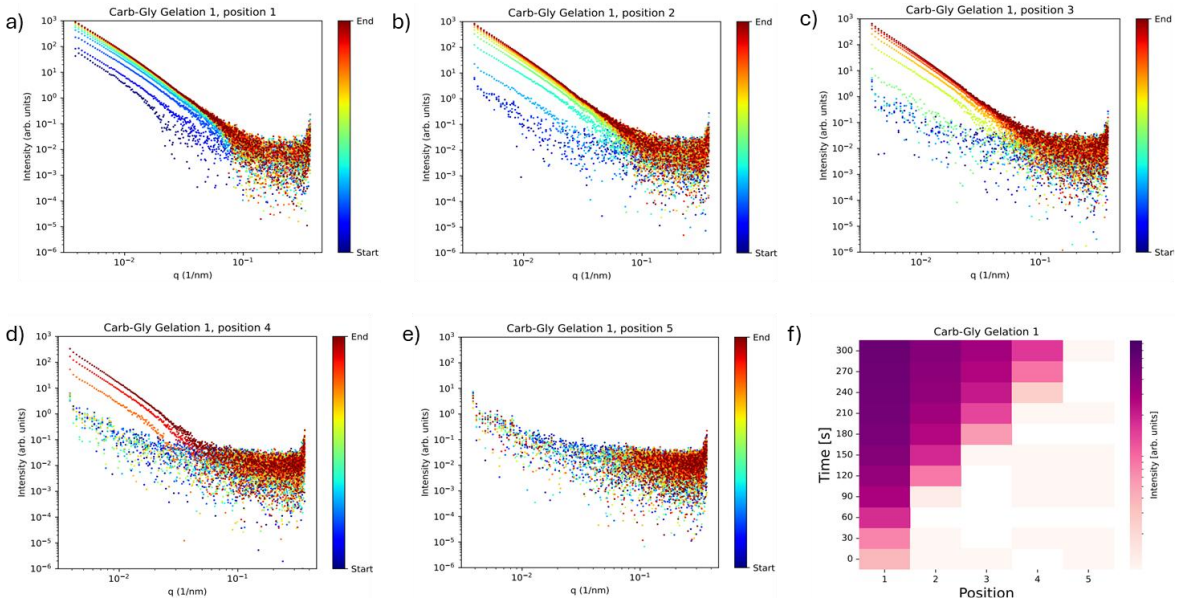

Figure 5.15. (a-e) SAXS plots for positions 1–5 showing Carb-Gly hydrogel formation over 5 mins, with scan colour progressing from blue to red. f) Heatmap of scattering intensity at q = 0.01 nm^{-1} compiled from plots 5.15a-e. The heatmap scale was set to a minimum intensity of 1 and a maximum intensity of 85.

From both the scatter plots and the heatmap, hydrogel formation is again evident. The white boxes observed in the heatmap correspond to negative scattering intensity values, which arise when the sample scattering is comparable to the subtracted background. The increase in scattering intensity at each position indicates a rising concentration of self-assembled nanostructures, consistent with uniform hydrogel growth. Notably, the intensity at position 1 rises earlier than at Carb-Ala, likely because the X-ray beam is positioned closer to the FTO glass surface. Like with Carb-Ala, Carb-Gly had the same directional growth, and no gel was observed at position 5 by the end of the experiment.

SAXS scans of the pre-gel solution reasonably fit to a cylinder model for positions 2-5, but fit to a cylinder with a power law for position 1 (Figure 5.16). However, the fitted radius values were relatively large, varied significantly across positions and time points (ranging from 60 to 370 Å), and were accompanied by substantial errors for individual parameters. The power-law fits also yielded low χ^2 values. The current data cannot distinguish between certain models, but indicates that the fit is not just a power law, suggesting that weakly self-assembled structures are present in the solution before the onset of gelation, and that these structures are most likely cylindrical in nature. However, the specific parameter values derived from these early fits should not be considered accurate, due to the very low scattering intensity, broad variation across the dataset, and significant associated fitting errors. This variability and uncertainty in fitting parameters do not persist once gelation begins, and scattering becomes stronger and more consistent.

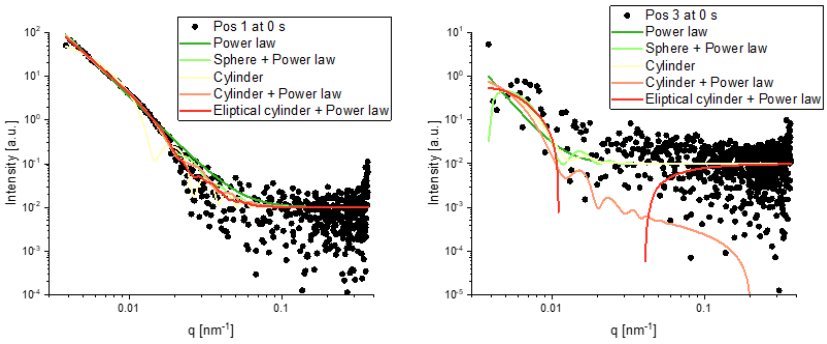

Figure 5.16. Initial SAXS 1D I vs Q plots and fits using different models at positions 1 (left) and 3 (right).

The evolution of χ^2 over time for each model is presented in Figure 5.17a. Initially low χ^2 values across all models in early scans reflect overfitting due to the power-law included in each model. As gelation progressed, χ^2 increased sharply for the incorrect models after 30 s for position 1 and after 180 s for position 3, the time points at which structures form. Models that could not be fitted successfully because parameter or scale values yielded negative results were excluded from the χ^2 analysis.

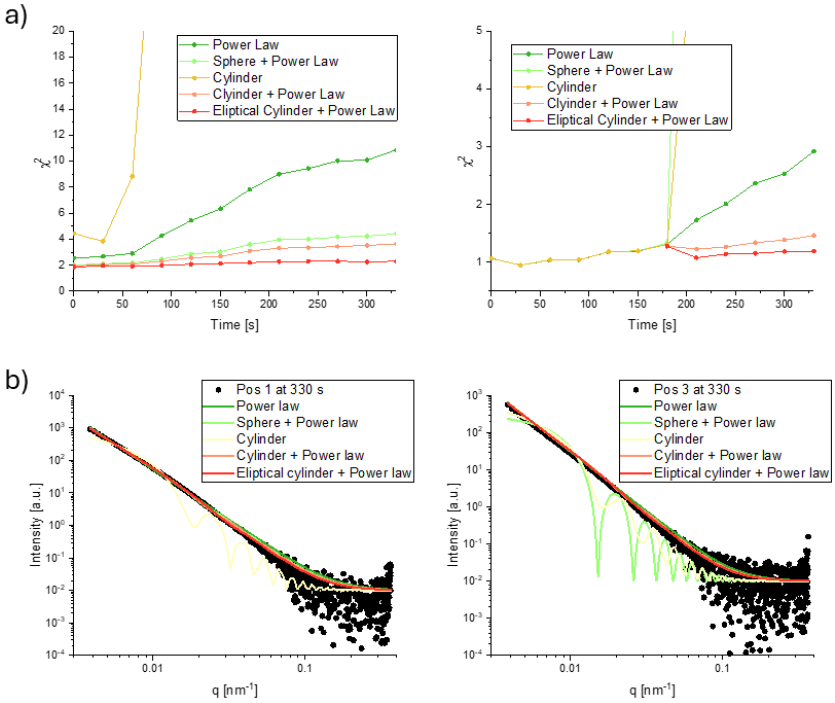

Figure 5.17. a) Evolution of χ^2 over time for all tested models at positions 1 (left) and 3 (right), a) Final SAXS 1D I vs Q plots and fits using different models at positions 1 (left) and 3 (right).

As the hydrogel formed, the data were best described by a cylinder model combined with a power law, unlike Carb-Ala, which had an elliptical cross-section; the laterally associated fibres in Carb-Gly have a cylindrical cross-section. Several models provided good fits with low χ^2 values for position 1, whereas at position 3, only the cylinder with a power-law and the elliptical cylinder provided good fits (Figure 5.17b). Therefore, the cylinder with the power-law model was selected for all positions due to its satisfactory fit at both positions and the fewer fitting parameters than the elliptical cylinder with the power-law model.

The cylinder radius increased slightly over time, then stabilised at approximately 152 Å after 210 s. The power-law exponent initially decreased, then stabilised at approximately 3.1 from 120 seconds onward (Figure 5.18). Again, these structural changes are likely due to ongoing pH reduction during the experiment, which continued to influence fibre structure.

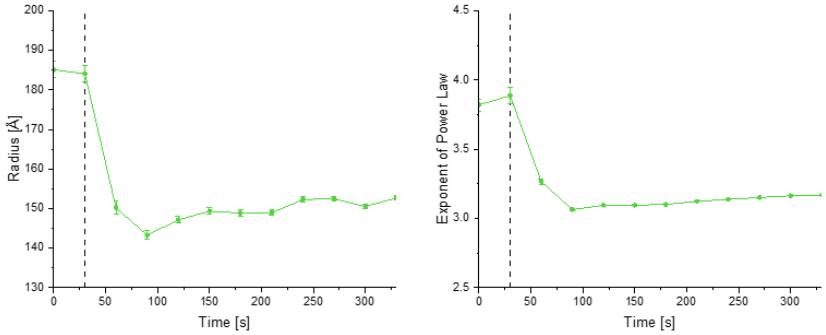

Figure 5.18. Change in radius (left) and power-law exponent (right) over time for position 1; the dashed line indicates the onset of gelation. Error bars were derived from the parameter uncertainties calculated during fitting in SasView.

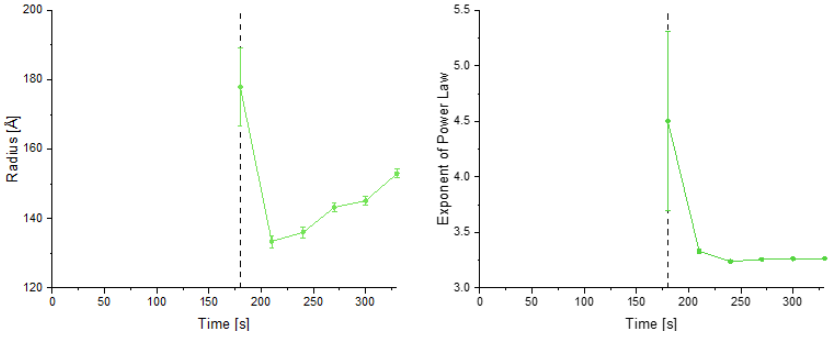

Figure 5.19. Change in radius (left) and power-law exponent (right) over time for position 3; the dashed line indicates the onset of gelation. Before the dashed line, the model could not be fitted because parameter or scale values yielded negative results. Error bars were derived from the parameter uncertainties calculated during fitting in SasView.

As observed at position 1, the cylinder radius increased over time; however, at position 3, the increase was greater and did not appear to have stabilised by the end of the experiment, yet remained comparable to the radius at position 1. In contrast, the power-law exponent values at position 3 did not follow the same trend as those at position 1. They initially decreased, then stabilised at a slightly larger value of ≈ 3.3 (Figure 5.19). Despite the differences in trend, the

corresponding B-scale values (scale values for the power-law part of the model) were lower than at position 1, suggesting only a slight structural variation between the two positions. The fits show that the fibres have a consistent shape and size throughout the entire sample. The fits for Carb-Gly at all positions are provided in the Appendix (Figure A3.2, Table A3.10-Table A3.18).

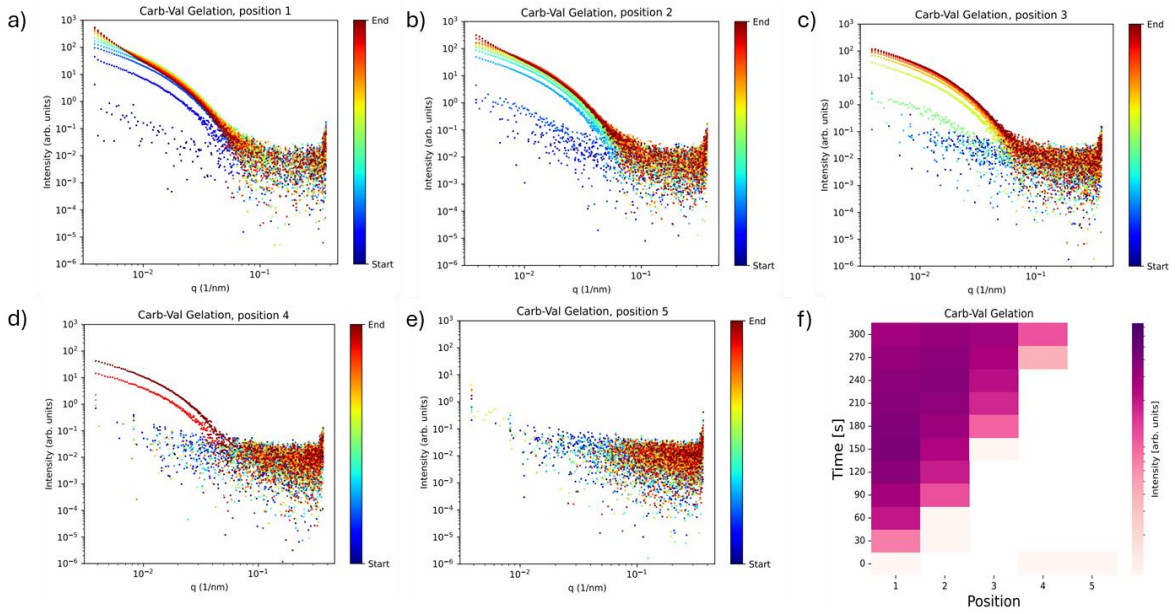

Figure 5.20. (a-e) SAXS plots for positions 1–5 showing Carb-Val hydrogel formation over 5 mins, with scan colour progressing from blue to red. f) Heatmap of scattering intensity at q = 0.01 nm^{-1} compiled from plots 5.20a-e. The heatmap scale was set to a minimum intensity of 1 and a maximum intensity of 75.

SAXS data for Carb-Val was collected and tracked using colour-coded overlays and a heatmap (Figure 5.20). Uniform directional hydrogel growth is evident from both the scatter plots and the heatmap. The reduction in intensity observed in the heatmap toward the end of the experiment at positions 1 and 2 is due to changes in the scattering shape rather than an actual loss of intensity or gel.

The scattering of the pre-gel solution of Carb-Val was too weak for any model to fit the data adequately, with many yielding negative parameters or scale values, except for a power-law fit with all parameters fixed (Figure 5.21). This indicates the absence of nanostructures in the solution before gel formation. This behaviour contrasts with that of the previously discussed gelators and is likely due to the larger valine side chain. The steric bulk may prevent structures from forming at high pH.

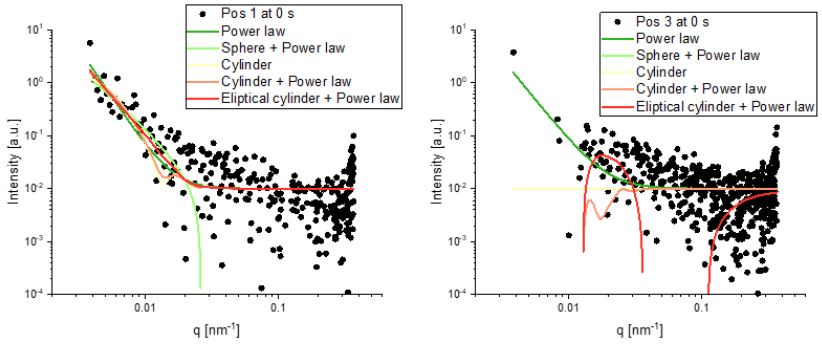

Figure 5.21. Initial SAXS 1D I vs Q plots and fits using different models at positions 1 (left) and 3 (right).

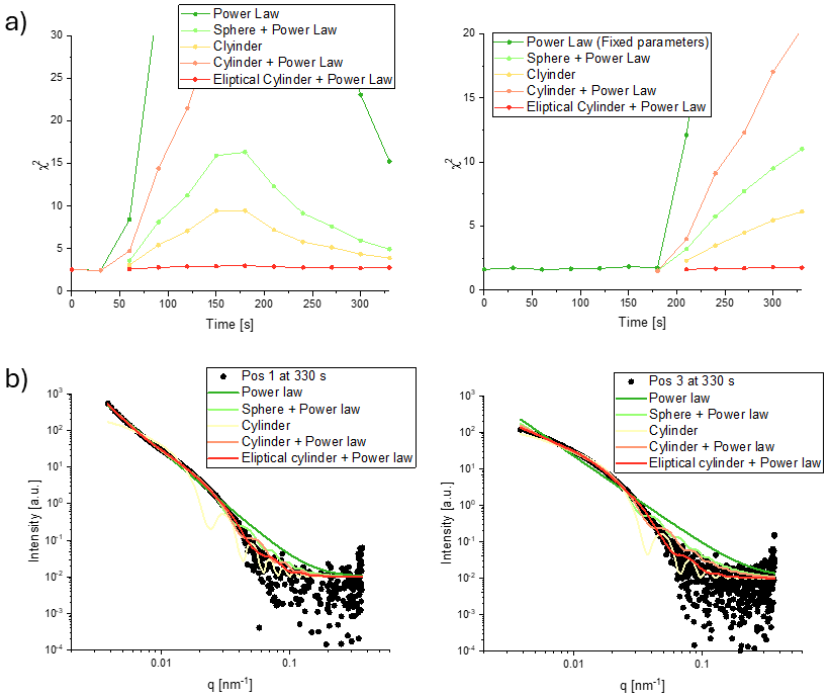

Figure 5.22. a) Final SAXS 1D I vs Q plots and fits using different models at positions 1 (left) and 3 (right), b) Evolution of χ^2 over time for all tested models at positions 1 (left) and 3 (right).

The evolution of χ^2 over time for each model is presented in Figure 5.22a. As discussed above, initially, only a power-law model with all parameters fixed provided a fit without negative parameter/scale values. Once gel formation begins, after 60 s for position 1 and after 210 s for position 3, χ^2 increases sharply for the incorrect models, clearly indicating the time points at which structural changes occur. Models that could not be successfully fitted because parameter values or scales yielded negative results were excluded from the χ^2 analysis. As

the hydrogel formed, the SAXS data were best described by an elliptical cylinder model combined with a power law, as observed for Carb-Ala (Figure 5.22b).

Unlike previous gelators, the radius of the elliptical cylinders remains consistent throughout the experiment, at approximately 64 Å. Although the axis ratio and the power law exponent do not stabilise by the end of the experiment. The axis ratio decreases from 2.9 to 2.5, while the power law exponent initially decreases, reaching a minimum of 3.3, before increasing to 4.0. (Figure 5.23). Suggesting that the ongoing pH reduction has a greater impact on the shape and distribution of the fibres than on their size for Carb-Val, in contrast to the previous gels, which reached a stable configuration more quickly.

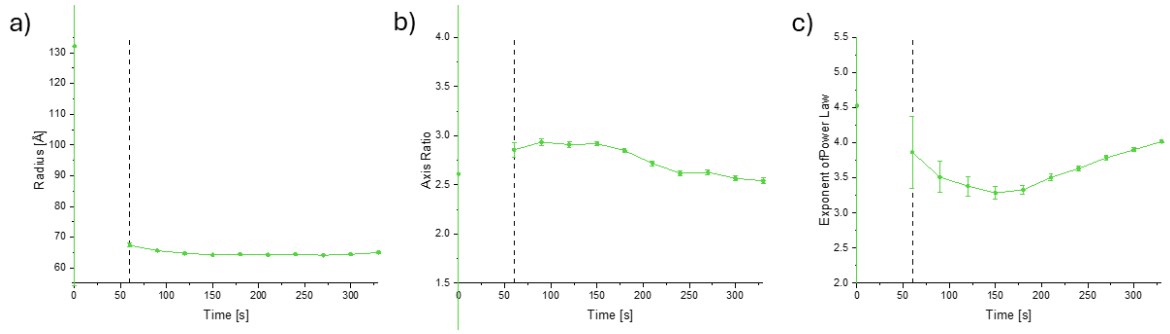

Figure 5.23. Change in (a) radius, (b) axis ratio, and (c) power-law exponent over time for position 1, the dashed line indicates the onset of gel formation. Before the dashed line, the model could not be fitted because parameter or scale values yielded negative results. Error bars were derived from the parameter uncertainties calculated during fitting in SasView.

As observed at position 1, the radius remains relatively constant throughout the experiment, at approximately 60 Å. However, the axis ratio was also constant at 2.9. The slightly smaller radius at position 3 may contribute to this greater stability in the axis ratio. The power-law exponent initially decreases, as observed at position 1, but the experiment was terminated before any increase could be observed (Figure 5.24). These fits suggest that the fibres are less uniform in shape and size across different positions within the gel than for Carb-Ala and Carb-Gly. This variability may be due to steric hindrance from the bulkier valine group, meaning that more time is required for Carb-Val to reach its most favourable configuration. The fits for Carb-Val at all positions are provided in the Appendix (Figure A3.3, Table A3.19-Table A3.22).

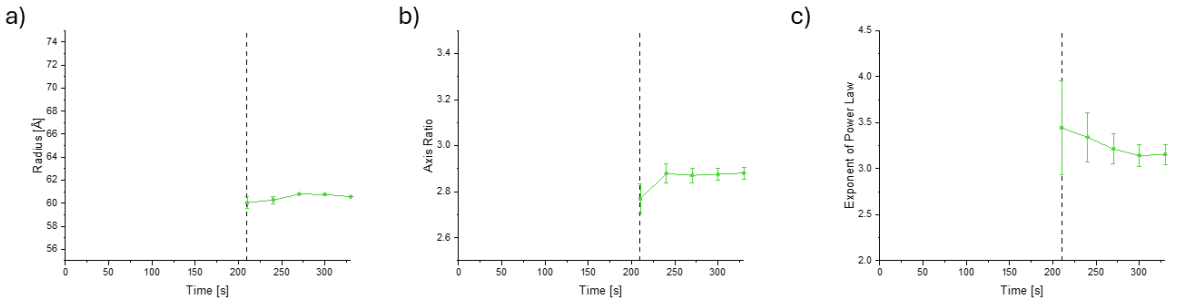

Figure 5.24. Change in (a) radius, (b) axis ratio, and (c) power-law exponent time for position 3, the dashed line indicates the onset of gel formation. Before the dashed line, the model could not be fitted because parameter or scale values yielded negative results. Error bars were derived from the parameter uncertainties calculated during fitting in SasView.

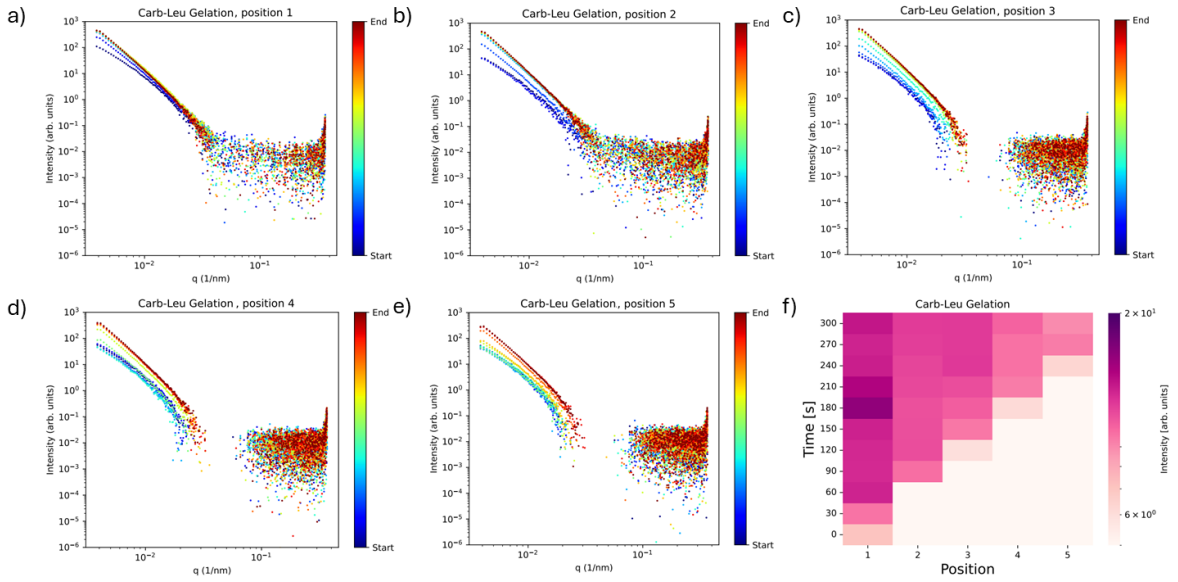

Figure 5.25. (a-e) SAXS plots for positions 1–5 showing Carb-Val hydrogel formation over 5 mins, with scan colour progressing from blue to red. f) Heatmap of scattering intensity at q = 0.01 nm^{-1} compiled from plots 5.25a-e. The heatmap scale was set to a minimum intensity of 5 and a maximum intensity of 20.

SAXS was collected for Carb-Leu and tracked using colour-coded overlays and a heatmap (Figure 5.25). Hydrogel formation is less apparent in the scatter plots and heatmaps compared to the previous three gelators. Although scattering intensity still increases, the increase is notably smaller, and the data at high q is noisy. The maximum intensity of the scatter plot was set to 20, rather than the previously used 75, 80, or 85, to enable any changes. Additionally, no noticeable

change in shape is observed in the scatter plots during gelation, and the intensity at position 5 increases.

During background subtraction, many datasets exhibited regions with missing data points, making it challenging to fit appropriate models; this is evident in Figures 5.25a-e. To address this, different scaling factors (1.0, 0.95, 0.90, 0.85) were applied to the background before subtraction to obtain complete datasets (Figure 5.26). A scaling factor of 0.9 was chosen because it was the highest scaling factor that produced adequate datasets without significant gaps across all positions and time points. Because of the reduced background subtraction from this scaling, the previously used background value of 0.01 was no longer appropriate. Instead, a background value of 0.025 was selected, as it provided good visual agreement with the data. As demonstrated in the Carb-Ala analysis, the choice of background does not affect the overall trends in the parameters and only minimally affects the value.

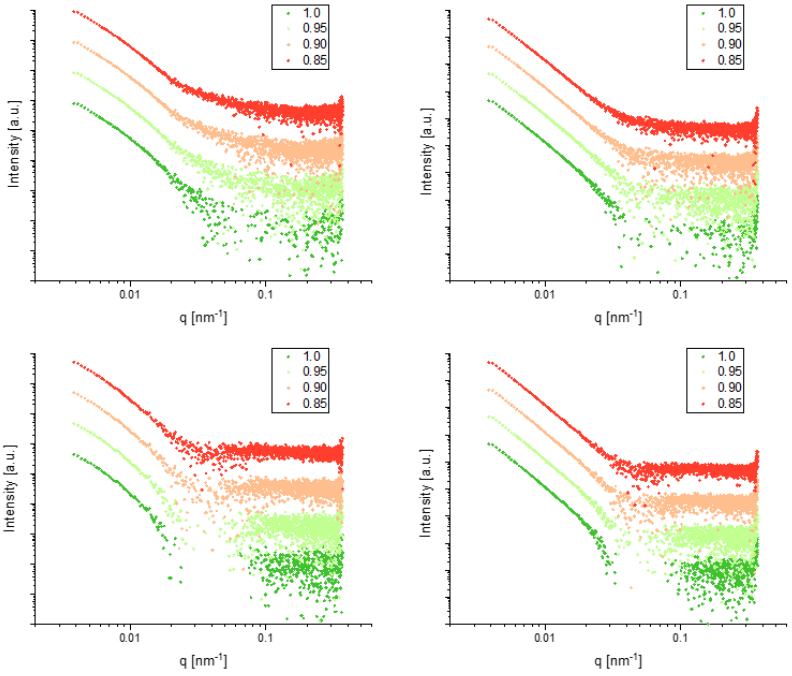

Figure 5.26. SAXS 1D I vs Q plots showing different background scaling applied to the initial (left) and final (right) scans at positions 1 (top) and 3 (bottom).

From the SAXS data, it is difficult to determine when gel formation begins, as there is no apparent increase in χ^2 for incorrect models or a change in fibre shape (a change of model), as seen previously. Of all the models tested, only the cylinder model yielded a high χ^2 value, although the χ^2 values will already be slightly

reduced by the scaled background subtraction, resulting in smaller error bars. By eye, the power law does not quite capture the shape of the curve, but the sphere with a power law, cylinder with a power law, and elliptical cylinder with a power law models all provide reasonable fits (Figure 5.27a-b). As with Carb-Gly, the cylinder with a power model was chosen because it has the fewest parameters and yields reasonable parameter values.

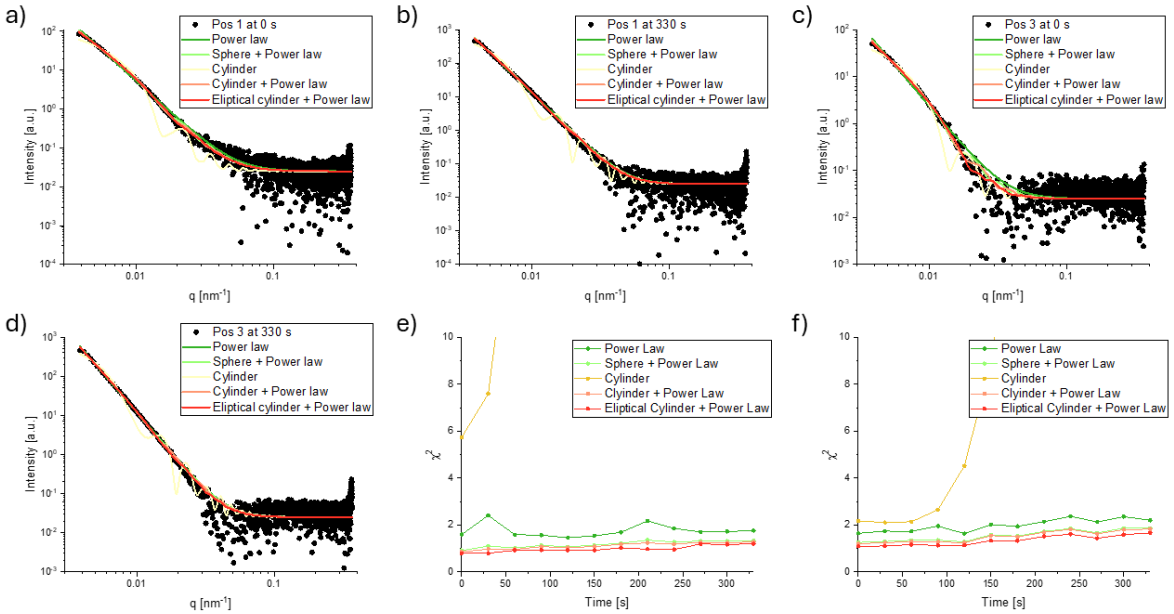

Figure 5.27. SAXS 1D I vs Q plots and fits using different models at position 1, a) after 0 s, b) after 330 s, and position 3, c) after 0 s, d) after 330 s. Evolution of χ^2 over time for all tested models at positions 1 (e) and 3 (f).

The radius of the cylinders appears to increase as the gel grows (from 207 Å to 261 Å); however, the increase is nonlinear and shows considerable variation. The radius is also considerably larger than seen for any of the previous gelators. Unlike with earlier gelators, the onset of gel formation was not immediately apparent. Therefore, it was determined using both the heatmap (Figure 5.25f) and changes in fitting parameters (Figure 5.28). The power-law exponent indicates a clear onset, with a pronounced increase after which the values stabilise at approximately 3.9.

For position 3 again, the cylinder radius appears to increase as the gel forms, with a minimum of 215 Å observed before the onset of gelation, rising to 284 Å by the end of the experiment. Despite this overall increase, the trend does not align precisely with the onset of gelation. The heatmap indicates that gel formation

begins after 150 s, whereas the radius changes is after 90 s (Figure 5.29). As with position 1, the radius trend is nonlinear and exhibits significant variation. In contrast, the trend in the power-law exponent aligns with the heatmap data, suggesting that gel formation begins after 150 s. After this point, the power law exponent remains relatively stable at around 4.0. The fits for Carb-Leu at all positions are provided in the Appendix (Figure A3.4, Table A3.23-Table A3.27).

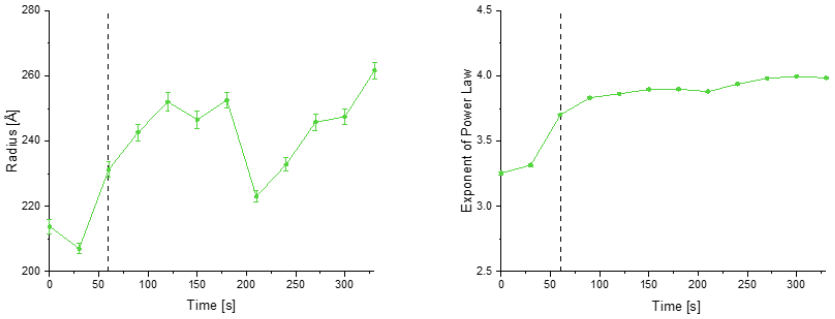

Figure 5.28. Change in radius (left) and power-law exponent (right) over time for position 1; the dashed line indicates the onset of gelation. Error bars were derived from the parameter uncertainties calculated during fitting in SasView.

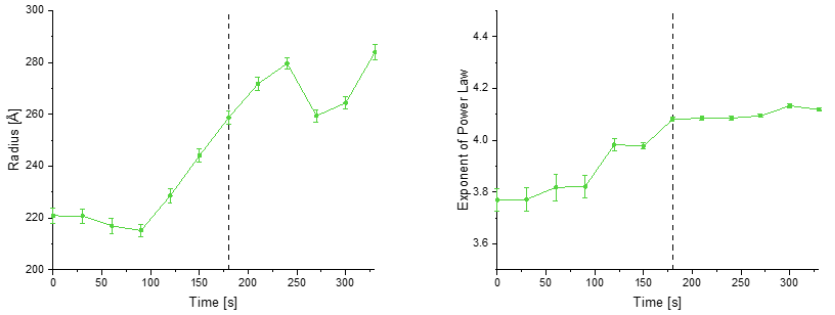

Figure 5.29. Change in radius (left) and power-law exponent (right) over time for position 1; the dashed line indicates the onset of gelation. Error bars were derived from the parameter uncertainties calculated during fitting in SasView.

In summary, hydrogel formation initiated at the electrode surface and progressed outward for all gelators, although the resulting structures varied between gelators. Carb-Ala and Carb-Val gels fit an elliptical cylinder model with a power law, whereas Carb-Gly and Carb-Leu fit a cylinder with a power law model. Carb-Ala showed the most coherent and consistent SAXS trends, with fits indicating the formation of well-defined, uniform fibres and minimal variation across the sample. Carb-Gly exhibited cylindrical structures, though the data were more variable. The power-law exponent differed slightly between positions, suggesting

minor heterogeneity in fibre packing or interaction strength within the gel. Carb-Val showed no structural features in the pre-gel scans, indicating no self-assembled structures in solution. After gelation, the network continued to evolve and never appeared to stabilise, likely due to steric hindrance from the bulky valine side chain, which restricted the formation of a stable fibre network. Carb-Leu showed the least apparent structural change and the weakest scattering intensity, despite eventual gel formation. The radius values were significantly larger than those observed for the other gelators, and trends were highly variable. This suggests a less ordered and more diffuse fibre network, possibly due to the even bulkier leucine side chain. The chronopotentiometry plots from the *in situ* SAXS electrogelation experiments are provided in Appendix 3 (Figure A3.5).

5.2.4. *In-situ* SAXS of electropolymerisation

Once data collection for the electrofabrication of the carbazole hydrogels was complete, the gelator/hydroquinone solution was carefully removed from the EC-SAXS cell using a pipette, minimising disturbance to the hydrogel. 1.5 mL of perchloric acid (0.1 M) was then added to the cell. 100 successive CV scans were performed between 0 and 1.1 V at a scan rate of 40 mV/s for approximately 1.5 hours to attempt to electropolymerise the samples. For SAXS data, the same acquisition script used in prior experiments was employed throughout. CV scans and SAXS data were collected simultaneously.

To investigate potential structural changes occurring during electropolymerisation, detailed SAXS analysis was conducted at two positions for each gelator: position 1, located closest to the electrode surface where polymer formation was anticipated; and position 3, selected as a representative position where the gel was expected to collapse, as observed during the lab experiments discussed in Section 5.2.1. At each position, 19 scans were selected for detailed analysis. These scans are taken at 5-minute intervals, beginning at 0 min and ending after 90 minutes.

For the 19 scans at both positions 1 and 3, multiple structural models were fitted to the data to identify the most appropriate model for each dataset. The models applied included: power law, sphere + power law, cylinder, cylinder + power law,

and elliptical cylinder + power law. Model performance was assessed using χ^2 values, along with a qualitative assessment of fit quality. The best-fit model for each sample was then applied to data collected at additional positions (positions 2, 4, and 5).

SAXS data were collected for Carb-Ala and monitored at all 5 positions by overlaying SAXS scans acquired at each position during the CVs (Figure 5.30a-e). A corresponding heatmap was generated to visualise the intensity of scattered X-rays at q = 0.01 nm^{-1} during polymerisation (Figure 5.30f). The scattering intensity range was adjusted to best highlight the changes for each polymer.

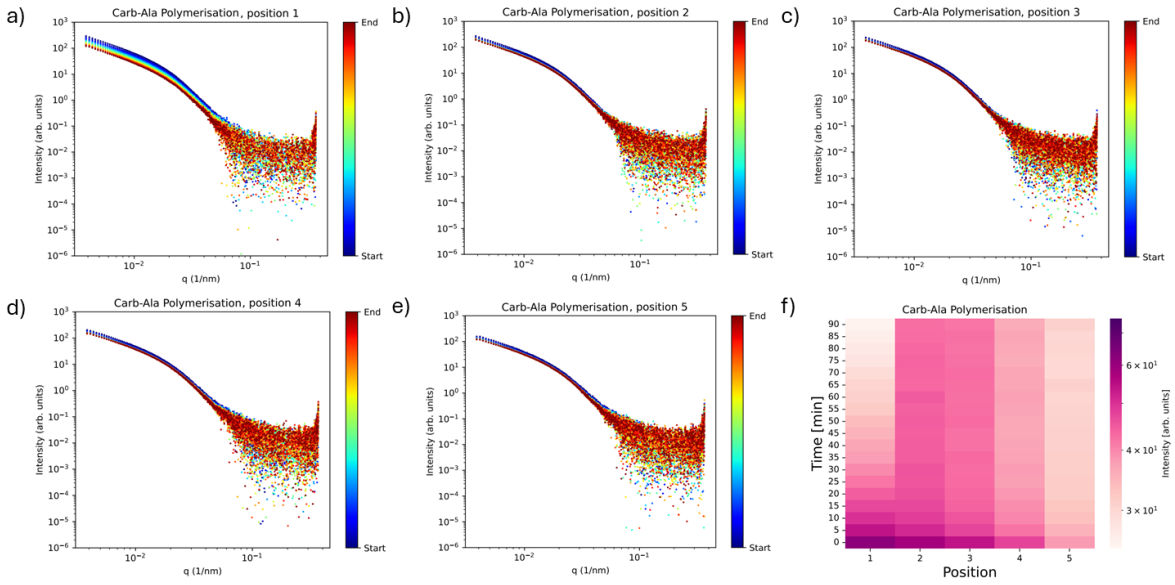

Figure 5.30. (a-e) SAXS plots for positions 1–5 showing Carb-Ala polymerisation over 90 mins, with scan colour progressing from blue to red. f) Heatmap of scattering intensity at q = 0.01 nm^{-1} compiled from plots 5.30a-e. The heatmap scale was set to a minimum intensity of 25 and a maximum intensity of 75.

Despite evidence of polymerisation within the cell, discrepancies exist between the observed macroscopic behaviour and the SAXS data. Notably, the gel exhibited shrinkage and green discolouration, yet the SAXS data indicated minimal changes in the nanostructure. This is unexpected, as the transition from gel to polymer would be expected to induce significant structural changes at this scale. These apparent discrepancies may be attributed to several factors. First, it is possible that the gel detached from the FTO glass slide, as has been observed in previous lab experiments. This detachment would mean that only a small amount of

polymerisation occurred on the glass slide. Additionally, polymerisation appears to be confined to the surface of the FTO glass slide. Given the manual positioning of the SAXS beam, it is likely that the measurement was not sufficiently close to the surface and therefore did not capture the polymerisation site. Minor changes observed at position 1 in the sample are believed to indicate the initiation of polymerisation. Thus, a detailed SAXS analysis was conducted to investigate these early-stage changes.

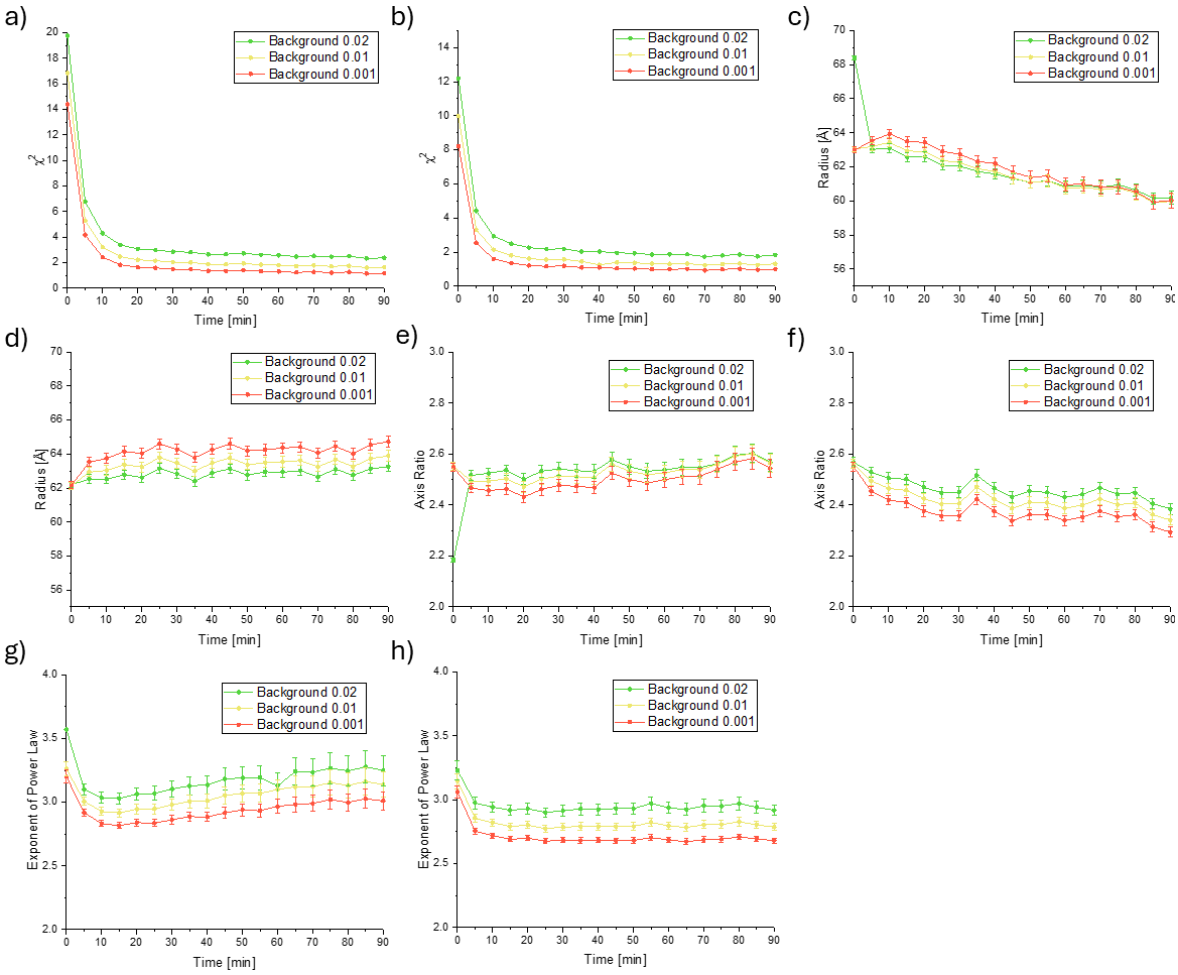

Figure 5.31. Effect of background value on a) χ^2 for position 1, b) χ^2 for position 3, c) radius for position 1, d) radius for position 3, e) axis ratio for position 1, f) axis ratio for position 3, g) exponent of power-law for position 1, h) exponent of power-law for position 3. Error bars were derived from the parameter uncertainties calculated during fitting in SasView.

The background was fixed at 0.01 cm^{-1} and was not allowed to vary during the fitting process. To assess the impact of the chosen background value, additional fits were performed for Carb-Ala using background values of 0.001 and 0.2 at

positions 1 and 3. The resulting values for χ^2, radius, axis ratio, and power at each position are shown in Figure 5.31. Changing the background did not alter the fitting model; the elliptical cylinder with a power law still fit best, and the values of radius, axis ratio, and power were only minimally affected. Notably, the overall trends remained consistent. A background value of 0.01 cm^{-1} was ultimately selected because it provided the best visual agreement with the SAXS curves, despite yielding slightly higher χ^2 values than the 0.001 cm^{-1} background (Figure 5.32). This background was fixed for all polymer modelling from this point onwards unless otherwise stated.

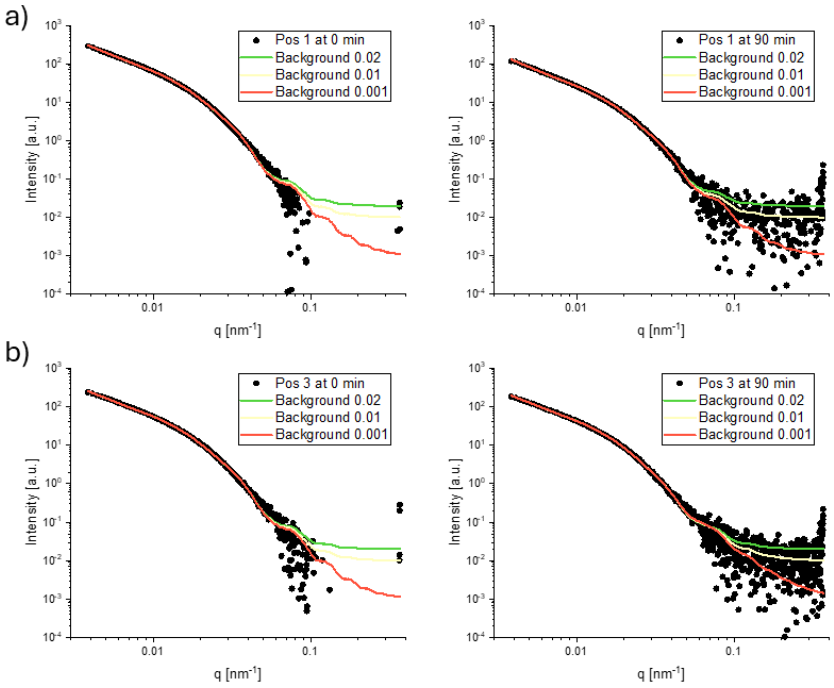

Figure 5.32. SAXS plots at 0 min (left) and 90 min (right) at a) position 1 and b) position 3 with elliptical model fits with different fixed background values.

For some of the initial scans, gaps in the data were observed due to over-subtraction of the background. These samples were processed by removing a perchloric acid (1 M) background, which is more strongly scattering compared to the NaCl (0.1 M) background used for the gel samples (Figure 5.33). The perchloric acid, which had been pipetted into the EC-SAXS cell approximately 10 minutes before the experiment began, had not fully penetrated the gel sample before the experiment started. As a result, the solution within the gel was still primarily, if not entirely, water when the electrochemical experiment was started.

Consequently, subtracting the perchloric acid background resulted in the observed gaps in the data.

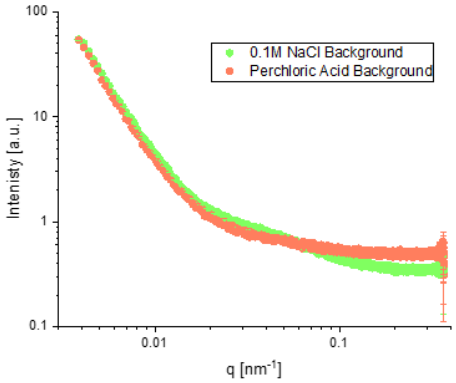

Figure 3.33. SAXS 1D I vs Q plots of the NaCl and perchloric acid backgrounds.

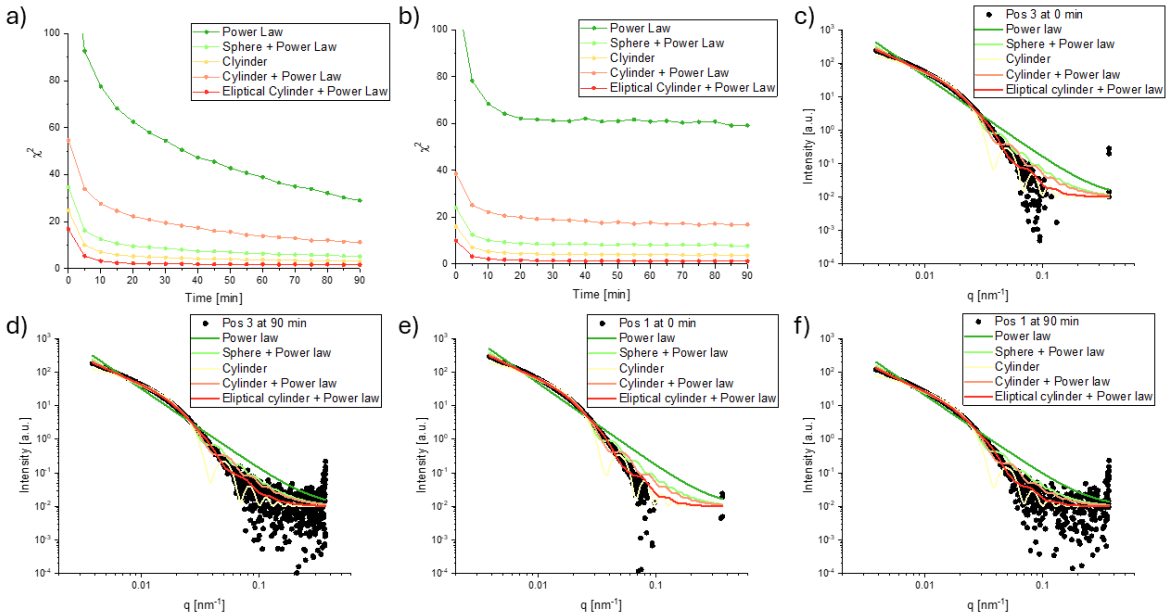

Figure 5.34. Evolution of χ^2 over time for all tested models at a) positions 1 and b) position 3. SAXS 1D I vs Q plots and fits using different models for c) image 1 position 1, d) image 19 position 1, e) image 1 position 3, and f) image 19 position 3.

Because the exact time at which perchloric acid fully permeated the gel is unknown, the perchloric acid background was used for all SAXS scans. However, based on data across all gelators, it appears that structural changes occur only after the perchloric acid has fully penetrated the sample. Therefore, the overall analysis remains valid. This is further supported by the evolution of the χ^2 values

over time (Figures 5.34a-b), in which scans with gaps are identifiable by their large χ^2 values.

For both positions 1 and 3, the model that fit best was an elliptical cylinder with a power-law (Figure 3.34c-f). No changes in shape or model were observed during the electropolymerisation, which we attribute to incomplete polymerisation of the sample. At position 3, no significant changes in any parameter values were observed, indicating that the sample remained unchanged throughout the experiment (Figures 5.31d, 5.31f, 5.31h). However, at position 1, subtle changes in the nanostructure were detected, interpreted as the onset of polymerisation (Figures 5.31c, 5.31e, 5.31g). While the axis ratio and power-law exponent remained constant, the radius of the elliptical cylinders decreased slightly from 63.4 Å to 59.9 Å. The fits for the attempted Carb-Ala electropolymerisation at all positions are provided in the Appendix (Figure A3.6, Table A3.28-Table A3.32).

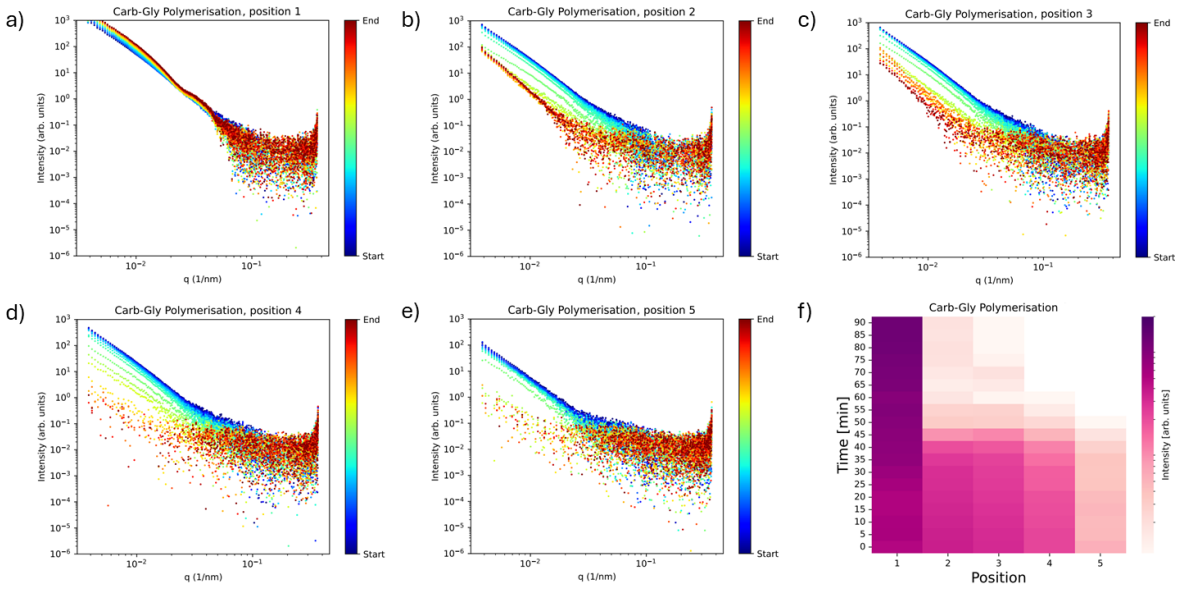

Figure 5.35. (a-e) SAXS plots for positions 1–5 showing Carb-Gly polymerisation over 90 mins, with scan colour progressing from blue to red. f) Heatmap of scattering intensity at q = 0.01 nm^{-1} compiled from plots 5.35a–e. The heatmap scale was set to a minimum intensity of 1 and a maximum intensity of 200.

As with Carb-Ala, SAXS of Carb-Gly was collected and tracked using colour-coded overlays and a heatmap during the consecutive CVs (Figure 5.35). Unlike Carb-Ala, there is a change in the shape of the data at position 1, and the intensity of the scattering at the other positions reduces as the gel collapses. Indicating that the

electropolymerisation was successful, as this matches the observed macroscopic behaviour.

From the heatmap, the collapse of the gel is evident. The decrease in scattering intensity at positions 2, 3, and 4 indicates a reduction in the concentration of self-assembled nanostructures, consistent with hydrogel collapse. Notably, the intensity at position 1 remains constant throughout the experiment, as the fibres change shape but not density.

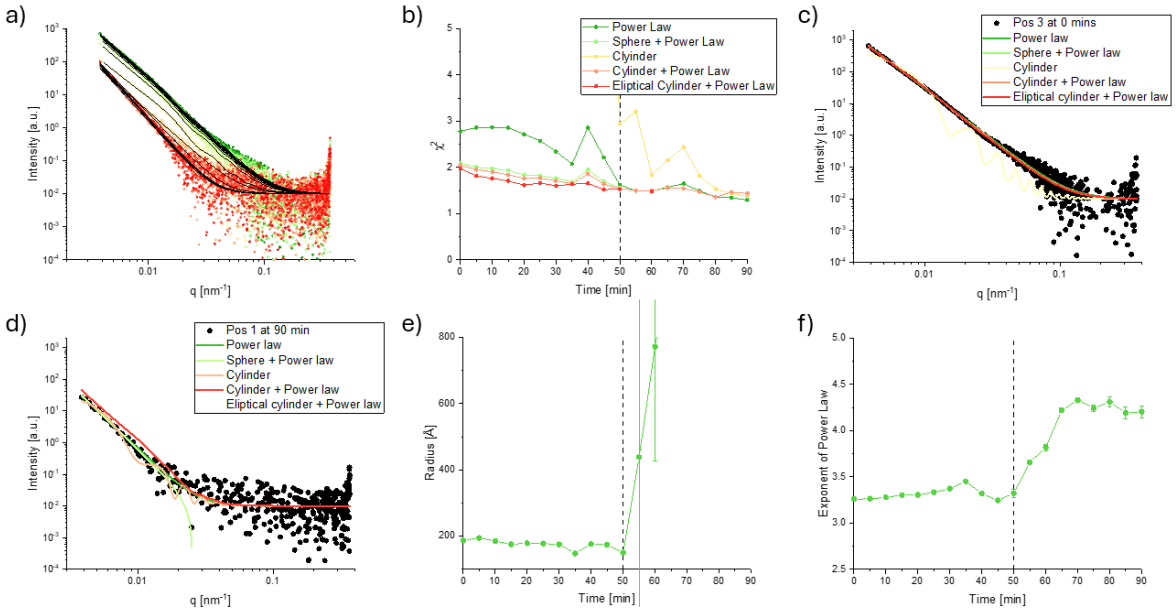

Figure 5.36. a) SAXS plots for position 3 showing the electropolymerisation of Carb-Gly over 90 min, with the scan colour progressing from light green to red; the fits are overlaid in black. b) Evolution of χ^2 over time for all tested models at position 3. c) SAXS 1D I vs Q plots and fits using different models for position 3 d) after 0 min, and e) after 90 min. Change in e) radius and f) exponent of the power law over time for position 3. The dashed line indicates the point at which the models transition from a cylinder with a power-law to only a power-law. Error bars were derived from the parameter uncertainties calculated during fitting in SasView.

At position 3, the data initially best fit a cylinder with a power-law model. However, as seen in Figure 5.36, the intensity of the scattering decreases over time until 55 minutes, at which point the data best fit a power law. This model transition is also observed for positions 2, 4, and 5. This is the gel collapsing at this position; as the intensity decreases, the power-law model represents

scattering from the perchloric acid. This is consistent with the observed macroscopic behaviour of the gel at this position: it is present at the beginning but collapses as a polymer forms, until no sample (gel or polymer) remains at this position.

At position 1, the data could reasonably fit multiple models: sphere, cylinder, and elliptical cylinder, all with a power-law, due to noisy data at high q values. All models visually fit the SAXS curve and had low χ^2 values, although none fully captured the scattering at 0.2 nm^{-1}, including those not discussed here. Therefore, the cylinder with a power-law model was initially chosen because it agreed with the data from the electrogelation run on the same sample and required fewer parameters than the elliptical cylinder with a power-law model. However, as the sample collapsed and polymerised, the model fit best to an elliptical cylinder with a power-law model. This best fit the data curves visually and had the lowest χ^2 values (Figure 5.36a).

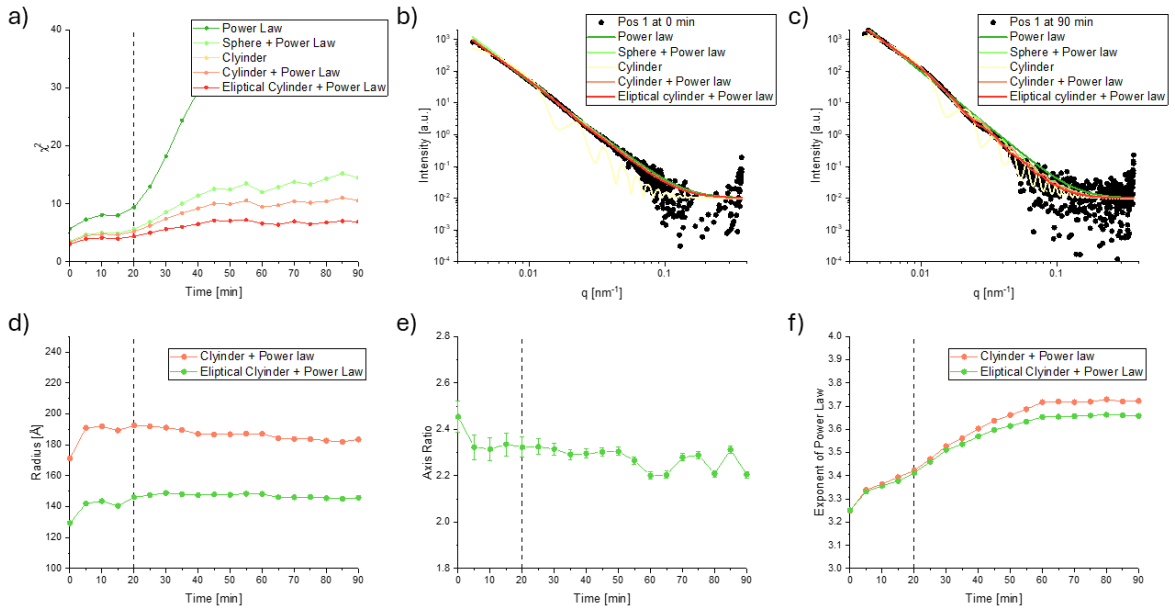

Figure 5.36. a) Evolution of χ^2 over time for all tested models at position 1. SAXS 1D I vs Q plots and fits using different models for b) position 1 after 0 min, c) position 1 after 90 min. Change in d) radius, e) axis ratio, and f) exponent of the power law over time for position 1. The dashed line indicates the point at which the models transition from a cylinder with a power-law to an elliptical cylinder with a power-law. Error bars were derived from the parameter uncertainties calculated during fitting in SasView.

At 20 minutes, the χ^2 values begin to diverge from those of the elliptical cylinder with a power-law model; this is the point at which the model changes. Despite this model change, the trends in the radius and the power-law exponent are the same for both models: the radius slightly decreases over time, and the exponent increases. The axis ratio (only for the elliptical cylinder with a power law model) remains approximately the same value. Therefore, although there is no increase in intensity, the power law increase might suggest that the sample is becoming denser and more entangled as the gel collapses. The change in model suggests that the shape of the fibres has to be altered to allow better confirmation of the molecules and enable them to polymerise, whereas for Carb-Val and Carb-Leu, the bulkier side changes would prevent the same extent of rearrangement; therefore, these gels do not fully collapse/polymerise. The fits for Carb-Gly electropolymerisation at all positions are provided in the Appendix (Figure A3.7, Table A3.33-Table A3.37).

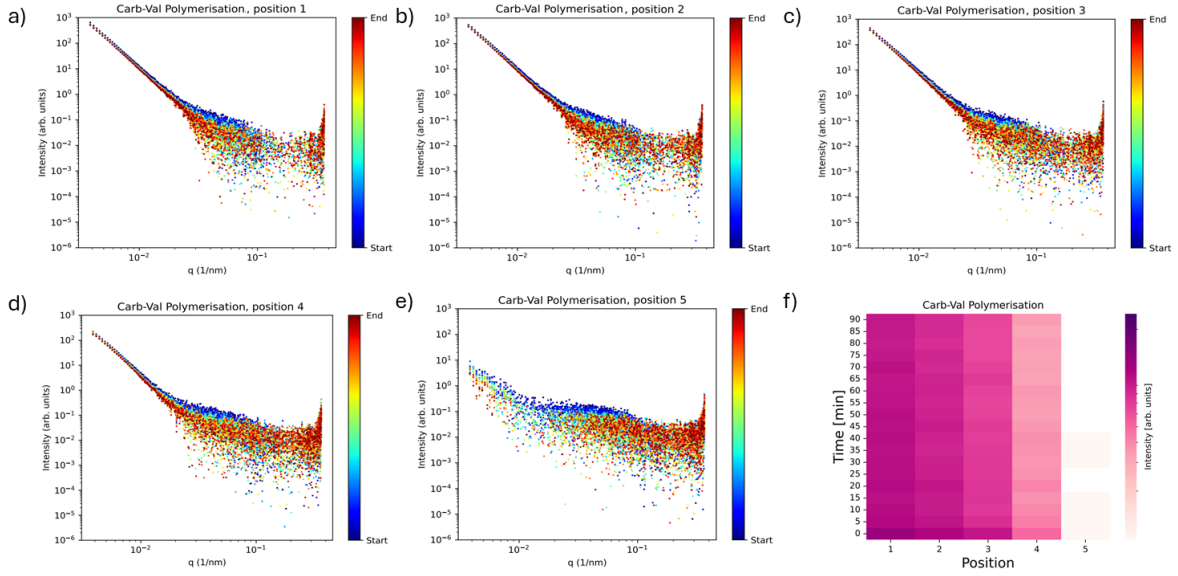

Figure 5.39. (a-e) SAXS plots for positions 1–5 showing Carb-Val polymerisation over 90 mins, with scan colour progressing from blue to red. f) Heatmap of scattering intensity at q = 0.01 nm^{-1} compiled from plots 5.39a–e. The heatmap scale was set to a minimum intensity of 1 and a maximum intensity of 25.

Like with Carb-Ala, Carb-Val did not show a change in intensity at positions 2, 3, and 5, indicating no gel collapse as would be expected for this gelator (Figure 5.39). However, there was also no change in the models or parameters at position 1, meaning that the electropolymerisation was not captured. For this gelator, it

was expected that only partial polymerisation would occur, as this was observed in the lab and in the sample placed in front of the beam, with a green colour appearing on the FTO glass beneath the gel. However, the beam could not be positioned sufficiently close to the edge of the FTO glass to observe any changes without flares obscuring the data. The fits for the attempted Carb-Val electropolymerisation at all positions are provided in the Appendix (Figure A3.8, Table A3.38-Table A3.42).

Finally, Carb-Leu SAXS data were collected during the attempted polymerisation and tracked using colour-coded overlays and a heatmap (Figure 5.42). As with Carb-Ala, the sample appeared to polymerise at the surface of the FTO glass. This gelator also shows the change in SAXS curve at position 1 that Carb-Gly showed; however, if polymerisation is complete is hard to determine, as the gel does not collapse for this gelator, so there is no subsequent reduction in intensity at positions 2, 3, and 4. There is also no change in the model at these positions; the data best fit a power-law model. This indicates that the fibres are beyond the resolution of SAXS, and since the fibres for Carb-Leu started large and the other gelators showed an increase in fibre radius upon the addition of perchloric acid, this is not unrealistic.

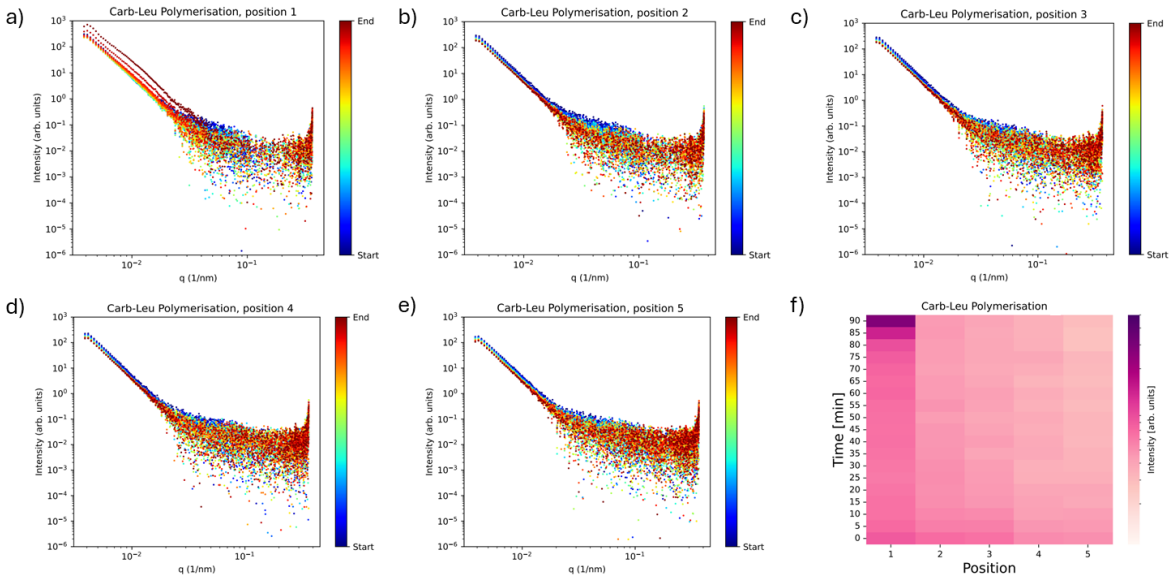

Figure 5.42. (a-e) SAXS plots for positions 1–5 showing Carb-Leu polymerisation over 90 mins, with scan colour progressing from blue to red. f) Heatmap of scattering intensity at q = 0.01 nm^{-1} compiled from plots 5.42a–e. The heatmap scale was set to a minimum intensity of 1 and a maximum intensity of 25.

As mentioned at position 1, the model transitioned from a power-law model to a cylinder with a power-law model after 50 minutes (Figure 5.43a). This is the point at which the χ^2 values of the models start to diverge. As with previous gelators, the χ^2 values for the cylinder with a power-law model and the elliptical cylinder model are very similar, so the cylinder with a power-law model was selected because it had the fewest parameters. Once again, the scattering at 0.2 nm^{-1} was not fully captured by any models tested.

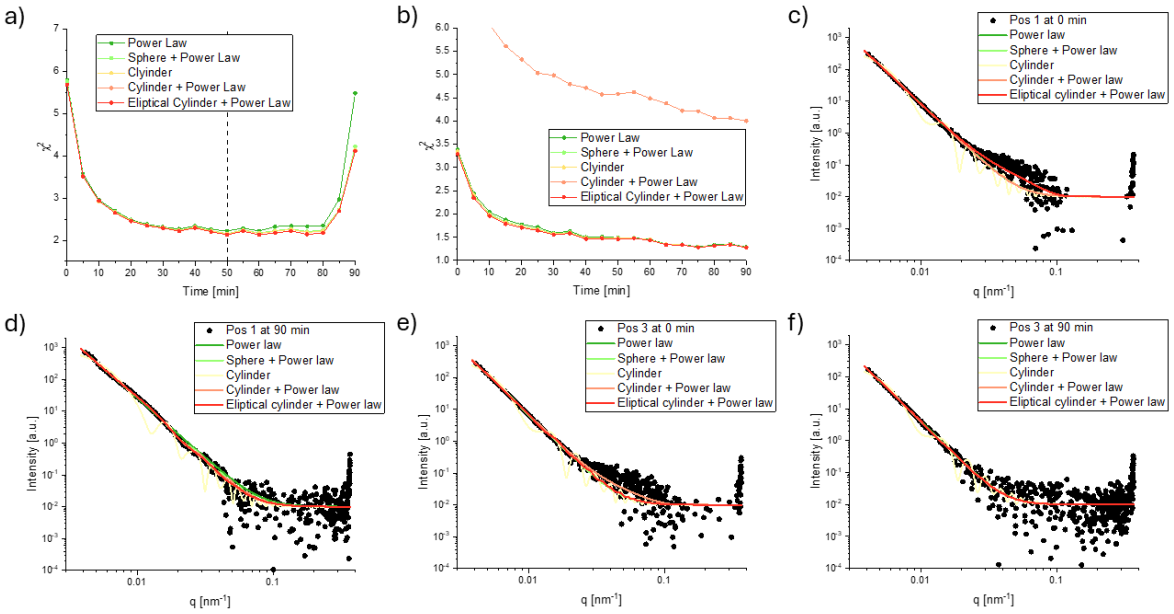

Figure 5.43. Evolution of χ^2 over time for all tested models at e) positions 1 and f) position 3. SAXS 1D I vs Q plots and fits using different models for a) position 1 after 0 min, b) position 1 after 90 min, c) position 3 after 0 min, and d) position 3 after 90 min. Error bars were derived from the parameter uncertainties calculated during fitting in SasView.

Both the cylinder radius and the power exponent decreased from 241 to 177 Å and from 4.05 to 3.94, respectively (Figure 5.44). This contrasts with Carb-Gly, where no change in radius was observed, and the power law exponent increased. This may be because Carb-Gly gel adopts a more favourable conformation and thus requires less rearrangement for polymerisation, whereas Carb-Leu requires more rearrangement because the bulky leucine group obstructs the process. The power law also decreases as the network becomes less dense during fibre rearrangement, whereas for Carb-Gly it increases due to gel collapse. The fits for the attempted

electropolymerisation of Carb-Leu at all positions are provided in the Appendix (Figure A3.9, Table A3.43-Table A3.47).

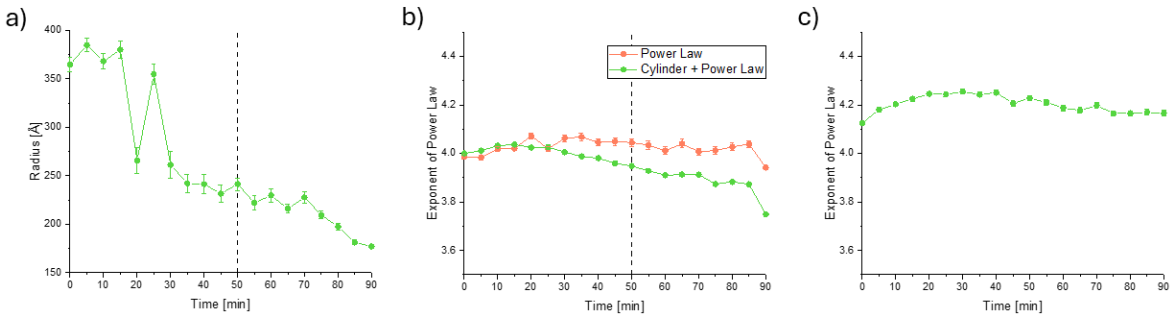

Figure 5.44. Change in a) radius and b) exponent of the power law over time for position 1. c) Change in exponent of the power law for position 3. The dashed line indicates the point at which the models transition from a power-law to a cylinder with a power-law. Error bars were derived from the parameter uncertainties calculated during fitting in SasView.

The SAXS analysis revealed distinct differences in electropolymerisation behaviour among the carbazole gelators, with structural evolution strongly depending on the amino acid side chain. For Carb-Ala and Carb-Val, minimal changes were observed in scattering profiles, model fits, and structural parameters across all positions, indicating little to no polymerisation at the nanoscale because polymer formation was limited to the FTO surface and outside the beam path. Conversely, Carb-Gly showed clear evidence of successful electropolymerisation: changes in model fits, a decrease in scattering intensity away from the electrode, consistent with gel collapse, and subtle structural rearrangements at position 1, suggesting fibre reorganisation during polymer formation. Carb-Leu displayed intermediate behaviour, with changes in model fits and reductions in fibre radius and power-law exponent at the electrode surface, implying structural rearrangement without full gel collapse, possibly due to steric hindrance from the bulky leucine side chain.

The CVs recorded during the *in situ* SAXS electropolymerisation experiments for each gelator are provided in Figure 5.45. The current response was also analysed by plotting current versus time at 0.810 V, taken from the CV scans. At 0.8 V, an oxidation peak was observed, and no reduction peak was detected for any gelator, indicating that the oxidation process is irreversible.

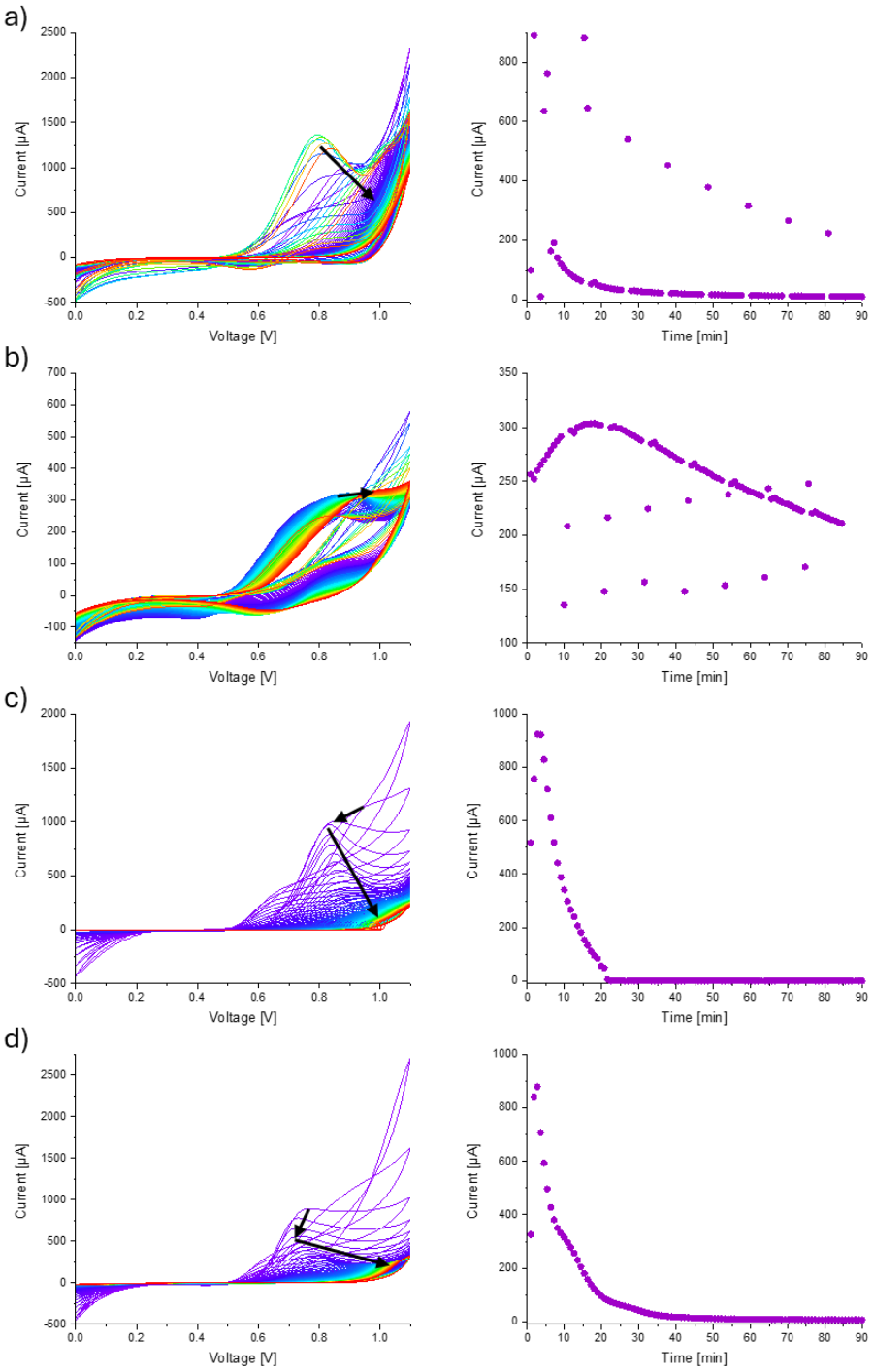

Figure 5.45. CV cycles recorded during the electropolymerisation SAXS experiments of the pre-assembled carbazole-protected hydrogels progressing from purple to red (left) and current values versus time at 0.810 V taken from CV scans (right) for a) Carb-Ala, b) Carb-Gly, c) Carb-Val, and d) Carb-Leu. Arrows included indicate the migration of the oxidation peak.

From Figure 5.45, the carbazole amino acids exhibit very similar CVs within the two observed behaviours. For Carb-Ala and Carb-Gly, an oxidation peak at 0.8V is

observed, with an increase from 0-6 min to 0-20 min for Carb-Gly, followed by a subsequent decrease in the remaining CV cycles. This rise in the current response with increasing CV cycles indicates greater deposition of the conductive polymer on the FTO glass surface, while the subsequent decrease in current suggests the electrode surface has become fully covered with the polymer film, reducing the current because the polymer is less conductive than the FTO slide.[41,42] The current response is also higher and lasts longer for Carb-Gly than for Carb-Ala, which might explain why Carb-Ala was only partially polymerised. The applied current was insufficient to generate the species required for complete polymerisation.

For Carb-Val and Carb-Leu, the increase in the oxidation peak at 0.8 V is significantly larger, reaching 924 μA and 879 μA, respectively, and occurs much more rapidly than in the previously studied carbazoles, after approximately 4 minutes. The peak then decreases to near zero after 20 minutes for Carb-Val and after 40 minutes for Carb-Leu. Again, because the current response is larger and remains higher for longer with Carb-Leu than with Carb-Val, Carb-Val was not polymerised to the same extent. The greater decrease in current response for these polymers suggests that the polymers produced may be less conductive than the Carb-Ala and Carb-Gly polymers. Consequently, polymerisation can only occur at the surface of the FTO slide before the polymer prevents the current from reaching a high enough level to induce further polymerisation, which is why not all the material is polymerised and no gel collapse occurs.

5.3. Conclusion

In conclusion, this chapter has demonstrated that carbazole-protected amino acid LMWGs can be effectively electrofabricated into hydrogels and, in some cases, electropolymerised into electrochromic materials. Their behaviour is strongly influenced by molecular structure. By extending the work of Kubiak *et al.* to Carb-Gly, Carb-Val, and Carb-Leu, clear links between amino acid side-chain sterics and self-assembly have been established.

Electrogelation occurred for all gelators, and in situ SAXS revealed that, despite similar macroscopic gel formation, the internal nanostructures varied significantly. The electropolymerisation behaviour further emphasised the importance of molecular design, with Carb-Gly providing the clearest evidence of

successful polymerisation. Across all systems, successful polymerisation appears to require sufficient structural flexibility to facilitate fibre reorganisation.

This work demonstrates the power of in situ electrochemical SAXS in resolving the dynamic structural evolution of supramolecular systems. Showing that small molecular modifications in gelator design can cause considerable differences in nanoscale structure and material behaviour. These insights offer valuable principles for developing carbazole-based functional materials, in which controlling fibre morphology and packing is essential to achieving efficient and tunable electrochemical performance.

5.4. Experimental

5.4.1. Materials

The gelators were synthesised by Prof. Dave Adams as previously described, using established methods.[16] Sodium chloride (>99.5%) was purchased from Fisher Scientific. Sodium hydroxide and hydrochloric acid were purchased from Honeywell. Hydroquinone was purchased from Sigma-Aldrich. Deionised water was employed in all the experiments.

5.4.2. Preparation of solutions

All gelator stock solutions were prepared the day before the experiments. To prepare the stock solution of the gelator, the gelator powder was dissolved in deionised water containing NaCl (aq. 0.1 M) and 1 molar equivalent of NaOH (aq. 0.1 M) to achieve a final concentration of 5 mg/mL. The solutions were then left to stir overnight. Immediately before the gelation process, the gelator solutions were adjusted to pH 7 using 0.1 M NaOH (aq) and 0.1 M HCl(aq). 35 mg of hydroquinone was weighed out, and 7 mL of gelator solution was added to achieve a final hydroquinone concentration of 5 mg/mL. The solution was stirred until all solids were dissolved. These solutions were then used to electrofabricate hydrogels.

5.4.3. pH measurements

pH measurements were performed using a HANNA FC200 pH probe with a 6 mm × 10 mm conical tip. The measurements were all taken at room temperature. The pH accuracy was ±0.1. The probe was rinsed with deionised water before each reading. The pH of the gelator solution was adjusted using NaOH (aq. 0.1 M) and HCl (aq. 0.1 M) solution. This process was repeated until a pH of 7 was reached with an accuracy of ±0.1.

5.4.4. Electrochemical gelation

To electrofabricate hydrogels, a three-electrode setup was used with an FTO glass slide working electrode (12 x 15 mm), an aqueous Ag/AgCl (3 M) reference electrode, and a platinum wire counter electrode in a glass beaker. 7 mL of the prepared gelator/hydroquinone solution was added to the beaker, and a current density of 0.7 mA/cm^2 was applied to the working electrode for 300 seconds. For all gelator solutions, gelation was observed on the FTO glass surface.

5.4.5. Electropolymerisation of hydrogels

The hydrogels grown on the FTO glass slide as described previously were removed from the gelator/Hydroquinone solution, and the solution was replaced with 7 mL of perchloric acid (0.1 M). The three-electrode setup was then replaced, as previously described, for electrochemical gelation, with the hydrogel attached to the FTO glass slide. The hydrogels were then electropolymerised by running cyclic voltammetry scans between 0 – 1.1 V at a scan rate of 40 mV/s. The hydrogels were scanned 100 times.

5.4.6. Electrochemical measurements

All cyclic voltammetry (CV) and chronopotentiometry measurements were performed using a Dropsens potentiostat and processed using the PSTrace 5.8 software.

5.4.7. Rheological measurements

Rheological experiments were conducted using an Anton Paar Physica MCR 301 rheometer. Frequency and strain sweeps were performed using a 12.5 mm parallel-plate geometry (PP12.5). The measuring distance was manually lowered until a force of 0.01 N was recorded. Unless specified, the measurements were taken at a constant temperature of 25 °C. Strain sweeps were performed over 0.01 % to 1000 % strain at a frequency of 10 rad/s. Frequency sweeps were performed at 0.5 % strain, increasing the frequency from 1 rad/s to 100 rad/s. As the hydrogel was not removed from the FTO glass after gelation, no damage occurred. The rheometer set up is shown in Figure 5.45.

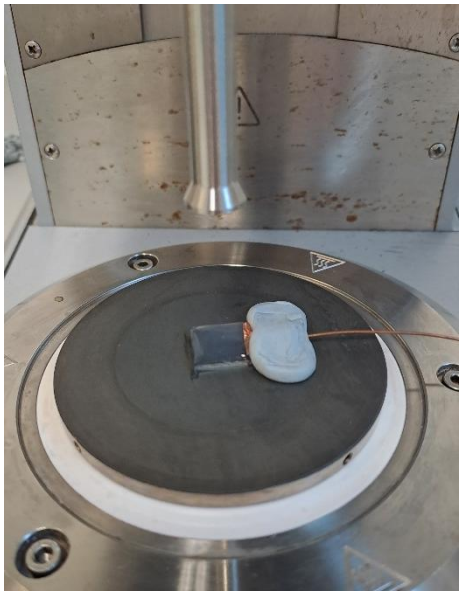

Figure 5.45. Rheometer set up for strain and frequency sweeps.

5.4.8. Small-angle X-ray scattering

Small-angle X-ray scattering (SAXS) measurements were performed using the X-ray beam of the I22 beamline (Diamond Light Source, Oxfordshire, UK), during experiment SM35170-1. The experiments were performed at a fixed energy of 12.4 keV and a camera length of 4.719 m, resulting in a Q range of 0.0038-0.367 $Å^{-1}$. To perform the SAXS measurements. This cell was 3D-printed using PLA filament on an Original Prusa i3 MK3S+ printer by Bart Dietrich (University of Glasgow), based on a design developed by Joshua White (University of Southampton) and Sam Richardson (University of Reading).[38] This EC-SAXS cell was mounted on a

metal stage in front of the I22 beamline. Within the custom cell, the three-electrode setup as previously described was assembled. The working electrode was secured perpendicular to the incoming beam, with a Kapton tape window for the beam to pass through to monitor the gel growth/electropolymerisation away from the FTO glass. To perform the electrochemical experiments, the potentiostat was within the experimental hutch and was connected to a laptop outside the hutch.

For the SAXS measurements, a script was written to program the SAXS beamline to scan at multiple positions across the cell, starting at the FTO glass surface and moving outward. The spacing between SAXS measurement positions was 0.2 mm, and 5 measurements were taken, with position 1 closest to the glass surface. position 1 was assumed to be 0 mm away from the glass surface. It took approximately 30 seconds to scan all 5 positions, and the script was run throughout the electrogelation/electropolymerisation. The electrochemical experiment was started after the 1st round of scans was completed, and the script was stopped after the electrochemical experiment finished. All these experiments were performed with the help of Alex Loch, Dipankar Ghosh (University of Glasgow), Adam Squires, and Wanli Liu (University of Bath).

To grow hydrogels within the Echem cell, the gelator/HQ solutions were made as described above. Immediately before the electrochemical experiment, 1.5 mL of the gelator/HQ solution was pipetted into the Echem cell containing the three-electrode set-up. A current density of 0.1 mA/cm^2 was applied to the FTO glass working electrode for 300 seconds.

To electropolymerise the hydrogels, the gelator/hydroquinone solution was removed from the Echem cell and replaced with 1.5 mL perchloric acid (0.1 M). Care was taken to avoid disturbing the FTO glass slide with the hydrogel attached. The hydrogels were then electropolymerised by running cyclic voltammetry scans between 0 – 1.1 V at a scan rate of 40 mV/s. The hydrogels were scanned 100 times.

To access the raw data collected at Diamond Light Source, the data were processed using Dawn Science software (version 2.27) according to the standard I22 pipeline. As part of the processing, full azimuthal integration was performed

on the raw 2D SAXS data to reduce the data to a 1D I vs Q plot. The files were then exported to .txt files using Dawn Science software.[43] These .txt files could then be loaded into the SasView (version 5.0.6) fitting software.[44] To perform background subtraction, the collected background was manually subtracted from the 1D I-Q plots in SasView.

All SAXS data fitting to structural models was performed using the SasView software. The scattering length density of the gelators was calculated using the National Institute of Standards and Technology Neutron Activation and Scattering Calculator, assuming a density of 1.55 g/cm^3.[45] A scattering length density of 9.469 x 10^{-6} Å^{-2} was used for the solvent (water and NaCl 0.1 M).

References

1 M. Bustamante-Torres, D. Romero-Fierro, B. Arcentales-Vera, K. Palomino, H. Magaña and E. Bucio, *Gels*, 2021, **7**, 182.

2 E. R. Draper and D. J. Adams, *Chem*, 2017, **3**, 390–410.

3 S. S. Babu, V. K. Praveen and A. Ajayaghosh, *Chem. Rev.*, 2014, **114**, 1973–2129.

4 K. Ino, F. Ozawa, N. Dang, K. Hiramoto, S. Hino, R. Akasaka, Y. Nashimoto and H. Shiku, *Adv. Biosyst.*, 2020, **4**, 1900234.

5 R. Fernandes, L.-Q. Wu, T. Chen, H. Yi, G. W. Rubloff, R. Ghodssi, W. E. Bentley and G. F. Payne, *Langmuir*, 2003, **19**, 4058–4062.

6 E. R. Cross, K. McAulay and D. J. Adams, In: Ryadnov, M. (eds) Polypeptide Materials. Methods in Molecular Biology, 2021, pp. 179–188.

7 A. D. Martin, A. B. Robinson and P. Thordarson, *J. Mater. Chem. B*, 2015, **3**, 2277–2280.

8 J. Morin, M. Leclerc, D. Adès and A. Siove, *Macromol. Rapid Commun.*, 2005, **26**, 761–778.

9 D. Witker and J. R. Reynolds, *Macromolecules*, 2005, **38**, 7636–7644.

10 V. Nayana and B. Kandasubramanian, *J. Poly. Res.*, 2020, **27**, 285.

11 F. Bekkar, F. Bettahar, I. Moreno, R. Meghabar, M. Hamadouche, E. Hernáez, J. L. Vilas-Vilela and L. Ruiz-Rubio, *Polymers*, 2020, **12**, 2227.

12 Y. He, W. Guo, M. Pei and G. Zhang, *J. Chem.*, 2012, **30**, 985–991.

13 J. Rault-Berthelot, E. Raoult, J. Tahri-Hassani, H. Le Deit and J. Simonet, *Electrochim. Acta*, 1999, **44**, 3409–3419.

14 D. A. Wellings and E. Atherton, *in Solid-Phase Peptide Synthesis*, Academic Press, 1997, pp. 44–67.

15 W. T. Truong, Y. Su, D. Gloria, F. Braet and P. Thordarson, *Biomater. Sci.*, 2015, **3**, 298–307.

16 P. S. Kubiak, S. Awhida, C. Hotchen, W. Deng, B. Alston, T. O. McDonald, D. J. Adams and P. J. Cameron, *Chem Commun.*, 2015, **51**, 10427–10430.

17 J. Raeburn, B. Alston, J. Kroeger, T. O. McDonald, J. R. Howse, P. J. Cameron and D. J. Adams, *Mater. Horiz.*, 2014, **1**, 241–246.

18 E. K. Johnson, D. J. Adams and P. J. Cameron, *J. Mater. Chem.*, 2011, **21**, 2024–2027.

19 P. Chen, G. Yang, T. Liu, T. Li, M. Wang and W. Huang, *Polym. Int.*, 2006, **55**, 473–490.

20 T.-Y. Chu, S. Alem, S.-W. Tsang, S.-C. Tse, S. Wakim, J. Lu, G. Dennler, D. Waller, R. Gaudiana and Y. Tao, *Appl. Phys. Lett.*, 2011, **98**, 253301.

21 R. C. Advincula, in *Functional Polymer Films*, Wiley, 2011, pp. 379–399.

22 X. Guo, M. Baumgarten and K. Müllen, *Prog. Polym. Sci.*, 2013, **38**, 1832–1908.

23 S. Beaupré, P. T. Boudreault and M. Leclerc, *Adv. Mater.*,2010, **22**, 6-27.

24 V. M. Prabhu and V. Reipa, *J. Phys. Chem. Lett.*, 2012, **3**, 646–650.

25 Z. Nagy, *J. Solid State Electrochem.*, 2011, **15**, 1679–1695.

26 T. Binninger, E. Fabbri, A. Patru, M. Garganourakis, J. Han, D. F. Abbott, O. Sereda, R. Kötz, A. Menzel, M. Nachtegaal and T. J. Schmidt, *J. Electrochem. Soc.*, 2016, **163**, H906–H912.

27 C. R. M. MacDonald and E. R. Draper, *Beilstein J. Org. Chem.*, 2024, **20**, 2608–2634.

28 G. E. Möhl, E. Metwalli and P. Müller-Buschbaum, *ACS Energy Lett.*, 2018, **3**, 1525–1530.

29 S. Risse, E. Härk, B. Kent and M. Ballauff, *ACS Nano*, 2019, **13**, 10233–10241.

30 R. I. Randle, A. M. Fuentes-Caparrós, L. P. Cavalcanti, R. Schweins, D. J. Adams and E. R. Draper, *J. Phys. Chem. C*, 2022, **126**, 13427–13432.

31 M. Povia, J. Sottmann, G. Portale, K. D. Knudsen, S. Margadonna and S. Sartori, *J. Phys. Chem. C*, 2018, **122**, 5917–5923.

32 W. Cheng, M. Zhao, Y. Lai, X. Wang, H. Liu, P. Xiao, G. Mo, B. Liu and Y. Liu, *Exploration*, 2023, **4**, 20230056.

33 S. Neves and C. Polo Fonseca, *Electrochem. commun.*, 2001, **3**, 36–43.

34 M. Bogar, I. Khalakhan, A. Gambitta, Y. Yakovlev and H. Amenitsch, *J. Power Sources*, 2020, **477**, 229030.

35 N. Loew, C. Miura, C. Sawahara, S. Otobe, T. Ogura, Y. Takasaki, H. Watanabe, I. Shitanda and M. Itagaki, *Langmuir*, 2025, **41**, 383–391.

36 L. Chen, K. Morris, A. Laybourn, D. Elias, M. R. Hicks, A. Rodger, L. Serpell and D. J. Adams, *Langmuir*, 2010, **26**, 5232–5242.

37 A. M. Fuentes-Caparrós, Z. Canales-Galarza, M. Barrow, B. Dietrich, J. Läuger, M. Nemeth, E. R. Draper and D. J. Adams, *Biomacromolecules*, 2021, **22**, 1625–1638.

38 S. J. Richardson, M. R. Burton, X. Luo, P. A. Staniec, I. S. Nandhakumar, N. J. Terrill, J. M. Elliott and A. M. Squires, *Nanoscale*, 2017, **9**, 10227–10232.

39 E. R. Draper, B. Dietrich, K. McAulay, C. Brasnett, H. Abdizadeh, I. Patmanidis, S. J. Marrink, H. Su, H. Cui, R. Schweins, A. Seddon and D. J. Adams, *Matter*, 2020, **2**, 764–778.

40 D. McDowall, D. J. Adams and A. M. Seddon, *Soft Matter*, 2022, **18**, 1577–1590.

41 Z. Wei, J. Xu, G. Nie, Y. Du and S. Pu, *J. Electroanal. Chem.*, 2006, **589**, 112–119.

42 F. Scholz, *ChemTexts*, 2015, **1**, 17.

43 J. Filik, A. W. Ashton, P. C. Y. Chang, P. A. Chater, S. J. Day, M. Drakopoulos, M. W. Gerring, M. L. Hart, O. V. Magdysyuk, S. Michalik, A. Smith, C. C. Tang, N. J. Terrill, M. T. Wharmby and H. Wilhelm, *J. Appl. Crystallogr.*, 2017, **50**, 959–966.

44 http://www.sasview.org/ .

45 https://www.ncnr.nist.gov/resources/activation/.

Conclusions

Supramolecular low molecular weight gelators (LMWG) are versatile building blocks capable of accessing unique materials through various strategies. This thesis has demonstrated that these materials can be programmed to exhibit temporal and spatial control, with micro- and macroscopic properties that can be further modulated with high degrees of precision. Highlighting the critical importance of selecting appropriate trigger methods and thoroughly examining the fundamental factors that influence the final gel.

We have demonstrated that cold atmospheric plasma is an effective tool for the gelation of LMWG hydrogels, offering superior spatial and temporal control to form patterned architectures and multilayer structures with defined geometries. Furthermore, we have established that plasma printing can locally modulate material properties. By combining this method with the *in situ* formation of gold nanoparticles, the functional scope and potential applications of plasma-printed hydrogels have been expanded.

Additionally, this work demonstrated that various gelator molecules and materials can be effectively coupled with existing pH triggers, notably with the urea/urease and formate systems. This results in transient gels with tunable lifetimes and mechanical properties. While we showed that temperature and variations in formate hydrolysis can modify the timing of state transitions, the data indicate that these effects are not always linear or predictable.

In the wider literature, it is often generally assumed that the effects of molecular modifications or environmental tweaks are inherently predictable. However, this thesis has shown that this is not the case; small structural or systemic changes result in non-linear, unexpected behaviours. Consequently, a thorough, fundamental understanding of the specific mechanisms and underlying parameters of each trigger method is required to gain true control over these materials.

The unpredictability of these systems and the pronounced importance of ageing effects suggest that further research is needed to refine the transient mechanisms currently discussed in the literature. Although ageing studies are not limited to

transient systems, if we are to use gels for targeted real-world applications, the long-term ageing of these materials demands much more research and a deeper understanding.

We also showed that these transient triggers can be successfully paired with different pH-responsive systems to influence both the nanoscale and macroscale properties of these materials, highlighting that many techniques used by gel chemists could be applied to various other supramolecular materials.

Finally, we showcased *in situ* electrochemical small-angle X-ray scattering (EC-SAXS) in resolving the dynamic structural evolution of supramolecular systems. This illustrates that even minor molecular modifications in gelator design can significantly dictate material behaviour.

Overall, this thesis demonstrates that supramolecular LMWGs can be intentionally designed into highly adaptive, programmable materials when their assembly pathways are understood and precisely controlled. By using external triggers, such as cold atmospheric plasma and electrochemical gradients, or internal chemically driven triggers, such as urea/urease and formate hydrolysis, both spatial patterning and temporal evolution can be finely tuned. This work emphasises that control over these systems depends not on a single factor but on a delicate interplay between trigger selection, environmental conditions, and molecular design.

Furthermore, incorporating functional components, such as *in situ*-generated nanoparticles, and employing advanced characterisation techniques like EC-SAXS highlight how small molecular-scale variations can lead to significant differences in macroscopic behaviour. Collectively, these findings establish that the future development of supramolecular gels depends not only on designing new gelators but also on understanding and controlling the dynamic processes that govern their formation and evolution, ultimately enabling the formation of responsive, functional materials with real-world applicability.

While this thesis establishes robust frameworks for controlling supramolecular assembly, it opens several crucial avenues for future exploration.

A key strength of some of the methods presented is their versatility. Several of these triggers can be easily applied to other classes of supramolecular materials

that are not strictly gels. This was successfully demonstrated within this work using transient lipids, proving that these chemically and physically driven pathways have far-reaching use across the broader soft matter landscape. When new methods are developed, future research should consciously attempt to apply them to as many different material types as possible.

When new triggering methods and chemical systems are being developed, it is vital that a much wider range of gelators is actively studied. New systems should not merely be published alongside a single, optimised example. As explored in Chapter 2, plasma-induced gelation was evaluated using four distinct gelators that formed two different types of micellar assemblies before gelation. Expanding the library of screened gelators in this manner maps out the true operational boundaries and limitations of these gelation triggers, ensuring they can be more effectively tailored, validated, and optimised for diverse applications.

For any future systems targeting real-world applications, ageing effects must be thoroughly investigated and included. In the current literature, long-term stability is frequently overlooked. Without comprehensive ageing data, it cannot be definitively proven that a system is practically useful. Future studies must use long-term rheological testing, for example, to evaluate how mechanical properties, structural integrity, and network homogeneity evolve over extended periods, as any breakdown or premature degradation will severely limit their targeted industrial or biomedical utility.

Ultimately, the future development of supramolecular materials depends not merely on synthesising new gelators but on mastering the dynamic, often unpredictable processes that govern their formation, evolution, and long-term stability.

Appendix 1 - Supplementary data for Chapter 2

1.1. Viscosity

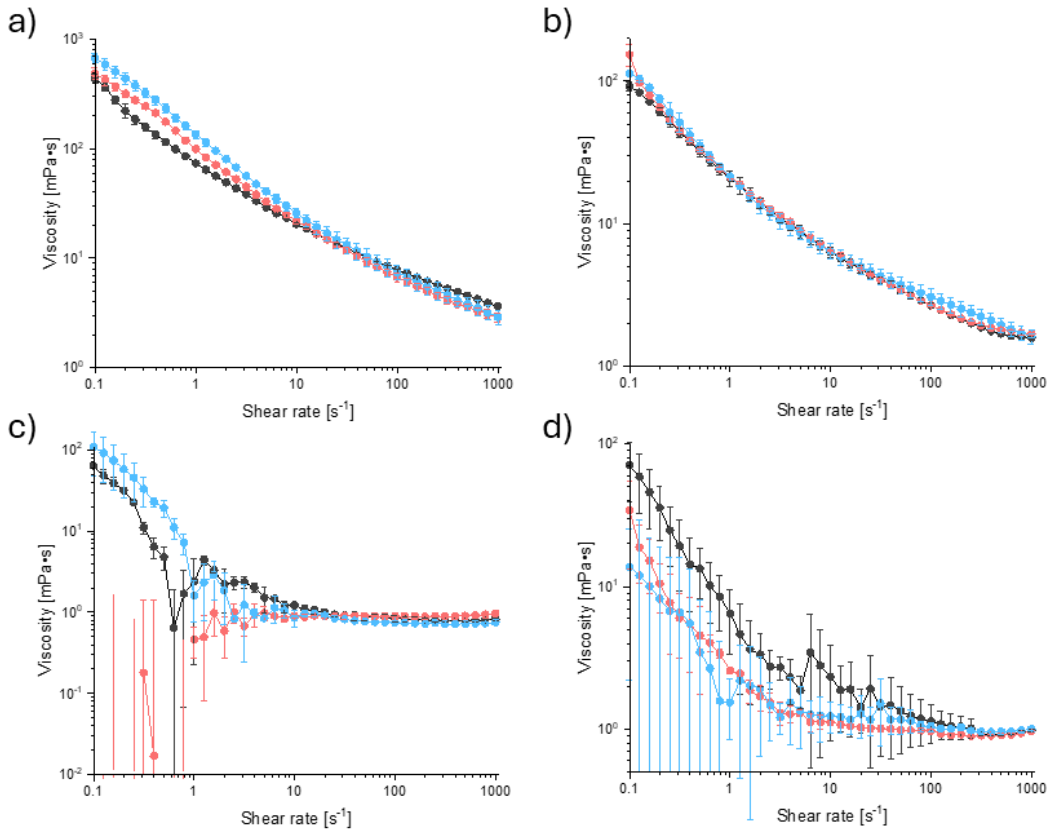

Figure A1.1. Viscosity sweep for a) 2NapFF, b) 2NapFV, c) 6Br2NapAV, and d) 2NapVG solutions at 5 mg/mL with methyl red (red), Nile blue (blue) and with no additive (black) at pH 7.

1.2. pK_a

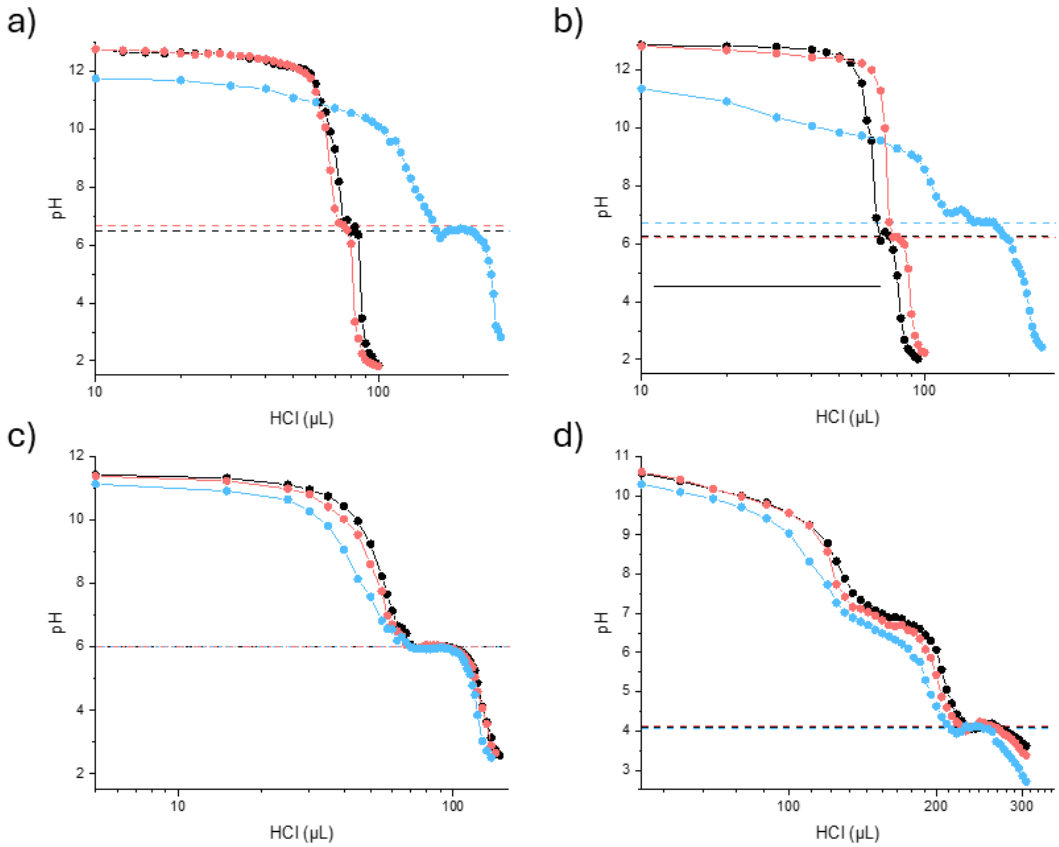

Figure A1.2. Apparent pK_a measurements for a) 2NapFF, b) 2NapFV, c) 6Br2NapAV, and d) 2NapVG at 5 mg/mL with methyl red (red), Nile blue (blue), and with no additive (black).

Table A1.1. Apparent pK_a values of the gelators used for plasma gelation.

Gelator	Dye	pK_a
2NapFF	-	6.47
2NapFF	Methyl red	6.65
2NapFF	Nile blue	6.50
2NapFV	-	6.25
2NapFV	Methyl red	6.19
2NapFV	Nile blue	6.69
6Br2NapAV	-	6.00
6Br2NapAV	Methyl red	6.01
6BrNapAV	Nile blue	6.01
2NapVG	-	4.10
2NapVG	Methyl red	4.13
2NapVG	Nile blue	4.06

1.3. Hue calibration values for Kineticolor analysis

Table A1.2. Calibration values for NaCl (0.1 M) solution in a Petri dish.

	Mean			Standard Deviation		
pH	hue	saturation	value	hue	saturation	value
2.0	-6.93454	82.94677	137.0034	3.737134	3.20454	1.93357
2.5	-11.9579	88.91	136.0617	2.752473	2.917954	1.840914
3.0	-13.4333	89.27435	136.8346	2.055743	2.792125	1.911261
3.5	-10.2756	66.33671	135.2309	2.884255	2.413066	1.956209
4.0	-6.86805	85.40364	136.2004	3.693084	2.850354	2.111206
4.5	29.94966	75.33504	134.3405	3.42981	4.28344	2.263221
5.0	54.98206	71.43536	128.5727	3.288372	3.018506	1.526306
5.5	62.31346	64.48992	126.6235	3.305966	2.996667	1.128526
6.0	61.20413	87.95986	113.7782	3.124245	3.80136	1.632055
6.5	77.36727	57.55614	130.2424	3.878493	5.254626	1.488119
7.0	87.02329	49.431	125.9811	4.319361	3.512563	1.372434
7.5	102.2711	49.48865	125.6668	5.79482	4.495582	1.703801
8.0	133.6186	56.55622	126.2991	4.930915	5.524994	1.923129
8.5	151.1814	68.96113	124.3049	2.722976	4.943554	2.066558
9.0	164.4077	73.08324	120.7037	3.372792	6.157353	2.4654
9.5	192.4253	45.9573	117.4435	8.38899	4.938309	2.2009
10.0	236.521	46.54375	114.82	8.466862	3.792328	2.221119

Table A1.3. Calibration values for NaCl (0.1 M) solution in a cuvette.

	Mean			Standard Deviation		
pH	hue	saturation	value	hue	saturation	value
2.0	-11.7745	176.3195	136.9795	0.945976	2.210024	1.456974
2.5	-11.7378	176.4216	136.9024	0.978885	2.176477	1.430608
3.0	-11.8085	176.149	136.5265	0.958905	2.166132	1.356406
3.5	-8.44584	128.2835	133.2898	1.464751	3.440051	1.85018
4.0	-3.86502	148.7346	133.5631	1.272236	2.698261	1.459951
4.5	32.3184	142.5925	126.9606	1.777658	2.995858	1.887433
5.0	49.00056	131.4371	125.6876	1.326328	2.877523	1.381775
5.5	56.36235	126.6526	120.8875	2.391501	3.275071	1.866611
6.0	46.86125	139.2753	122.6421	1.761336	3.198718	1.621889
6.5	58.7028	128.3708	115.4956	2.012296	3.142259	1.49711
7.0	84.22092	123.3568	110.1622	3.056676	6.198517	2.250575
7.5	90.77058	112.9633	110.0379	2.613783	4.580021	2.13569
8.0	158.4338	161.5295	99.63749	1.832734	6.733245	2.157313
8.5	165.0671	181.1397	97.05736	2.112811	7.924903	2.124468
9.0	179.1939	162.3803	83.2614	2.933078	7.467386	1.617701
9.5	204.0366	141.3763	84.74443	3.50747	6.562668	2.142923
10.0	261.9756	133.0473	97.78428	2.262341	5.474843	2.464527

Table A1.4. Calibration values for 2NapFF (5 mg/mL) solution in a Petri dish.

	Mean			Standard Deviation		
pH	hue	saturation	value	hue	saturation	value
3.35	-16.9166	76.2544	136.7608	3.0849	4.0823	1.8909
4.09	-17.1304	69.1092	131.0435	3.6630	2.9584	1.8741
4.41	-14.6447	66.7506	129.7659	3.2925	3.2971	2.0361
4.93	-10.3373	62.6965	130.3706	3.5685	3.2794	2.0055
5.27	-7.5993	60.3854	130.3485	4.3016	3.0904	1.9386
5.49	2.2376	58.4277	130.3734	5.4511	3.4471	2.4071
5.75	10.3586	59.1243	130.2810	3.7445	3.8234	2.7166
5.94	19.1153	60.3707	128.5134	3.8067	4.2614	2.8801
6.24	44.9413	60.0940	126.1265	4.5064	5.2111	2.9084
6.59	34.4067	59.1878	131.3083	3.8505	3.4206	1.8924
7.05	47.6023	49.5566	130.3430	4.2284	2.9708	1.8349
7.18	65.1379	44.4117	121.7606	5.2111	4.1942	3.5403
7.65	96.9040	35.0742	124.4800	6.5948	3.7993	1.5577
8.02	150.6223	52.5071	127.2410	3.9954	5.4806	2.7454
8.51	157.4782	56.2618	127.2042	3.4303	5.1506	1.7047
8.95	159.7904	51.6031	126.3512	3.8803	5.4737	1.8161
9.46	168.2222	45.8252	122.1222	5.6271	6.0320	2.2555
9.93	176.6207	42.6784	118.0354	6.7824	5.5241	2.1772

Table A1.5. Calibration values for 2NapFF (5 mg/mL) solution in a cuvette.

	Mean			Standard Deviation		
pH	hue	saturation	value	hue	saturation	value
3.6	-11.5797	148.7545	120.5467	2.0213	3.0213	1.7559
4.04	-13.5953	146.3737	121.7132	2.2217	3.4158	1.9783
4.51	-14.3668	144.7240	121.9299	1.9278	3.3346	2.1857
4.74	-14.3903	144.7246	121.9784	2.0566	3.4961	2.3548
5	-13.2216	137.4754	120.6197	2.3500	4.3270	2.6628
5.26	-7.3138	125.6068	122.6312	1.4261	2.8712	2.3891
5.51	-0.9313	115.4801	122.5472	2.3506	3.1579	2.3554
5.76	7.3141	115.1493	122.3507	2.1709	3.8569	2.5199
5.97	15.6337	121.3454	122.3311	2.2524	3.7399	2.5811
6.2	24.0483	121.3417	121.2072	2.2515	3.5747	3.1012
6.51	36.8694	124.7806	119.4097	2.2136	4.7807	3.0429
6.7	43.7749	126.2573	117.0796	2.1087	4.7345	3.4994
6.91	62.5444	110.0309	108.7529	3.0093	6.3456	3.5256
7.05	53.5415	99.3431	104.0927	3.5465	4.0277	2.0489
7.18	68.2982	91.4396	96.3145	3.5434	4.7586	2.5604
7.65	112.0000	76.7863	97.1901	3.9485	4.5609	2.0308
8.02	157.2583	131.5482	98.2950	2.1441	6.2723	2.1900
8.51	162.3479	137.7595	110.3353	1.9795	5.9651	2.4436
8.95	165.8848	130.0075	104.7610	2.6245	5.8219	2.4112
9.46	186.8753	99.9873	96.5139	3.8451	5.8522	2.3221
9.93	202.5608	92.9490	97.4128	4.0296	4.8428	1.8596

1.4. SAXS fitting parameters for nanoparticle plasma gels

Table A1.6. Fitting parameters of the sphere with cylinders and power-law model for 2NapFF 5 mg/mL gel containing 0.1 mM $HAuCl_4 \bullet H_2O$.* indicates parameters that were not permitted to vary during fitting.

Parameter	**Value**
Background*	0.025
A Scale	$1.14 \times 10^{-3} \pm 1.5 \times 10^{-4}$
Radius (Sphere)	26.6 ± 2.0
B Scale	$4.40 \times 10^{-4} \pm 5.9 \times 10^{-5}$
Length*	1000
Kuhn Length	99.97 ± 9.4
Radius (Cylinder)	35.8 ± 8.1
Axis Ratio	1.45 ± 0.4
C Scale	$2.95 \times 10^{-4} \pm 4.9 \times 10^{-5}$
Power Law	2.15 ± 0.03
χ^2	0.21

Table A1.7. Fitting parameters of the sphere with cylinders and power-law model for 2NapFF 5 mg/mL gel containing 0.5 mM $HAuCl_4 \bullet H_2O$.* indicates parameters that were not permitted to vary during fitting.

Parameter	**Value**
Background*	0.025
A Scale	$7.57 \times 10^{-3} \pm 1.1 \times 10^{-4}$
Radius (Sphere)	36.4 ± 0.3
B Scale	$6.40 \times 10^{-3} \pm 4.4 \times 10^{-5}$
Length*	1000
Kuhn Length	63.4 ± 0.5
Radius (Cylinder)	43.3 ± 0.3
Axis Ratio	2.69 ± 0.02
C Scale	$3.19 \times 10^{-4} \pm 1.7 \times 10^{-5}$
Power Law	2.53 ± 0.01
χ^2	0.75

Table A1.8. Fitting parameters of the sphere with cylinders and power-law model for 2NapFF 5 mg/mL gel containing 2.5 mM $HAuCl_4 \bullet H_2O$.* indicates parameters that were not permitted to vary during fitting.

Parameter	**Value**
Background*	0.025
A Scale	$8.75 \times 10^{-3} \pm 3.8 \times 10^{-4}$
Radius (Sphere)	36.2 ± 0.2
B Scale	$0.025 \pm 3.4 \times 10^{-4}$
Length*	1000
Kuhn Length	314.7 ± 2.0
Radius (Cylinder)	19.0 ± 0.07
Axis Ratio	2.62 ± 0.02
C Scale	$4.04 \times 10^{-4} \pm 1.5 \times 10^{-5}$
Power Law	2.70 ± 0.01
χ^2	1.01

Table A1.9. Fitting parameters of the ellipsoid with cylinders and power-law model for 2NapFF 5 mg/mL gel containing 5.0 mM $HAuCl_4 \bullet H_2O$.* indicates parameters that were not permitted to vary during fitting.

Parameter	**Value**
Background*	0.03
A Scale	$9.70 \times 10^{-5} \pm 3.1 \times 10^{-7}$
Radius Polar (Ellipsoid)	28.5 ± 0.1
Radius Equatorial (Ellipsoid)	111.07 ± 0.2
B Scale	$0.033 \pm 1.3 \times 10^{-4}$
Length*	1000
Kuhn Length	558.0 ± 2.5
Radius (Cylinder)	50.1 ± 0.08
Axis Ratio	1.69 ± 0.005
C Scale	$7.10 \times 10^{-4} \pm 1.4 \times 10^{-5}$
Power Law	2.79 ± 0.003
χ^2	3.90

Appendix 2 - Supplementary data for Chapter 3

2.1. Frequency sweeps

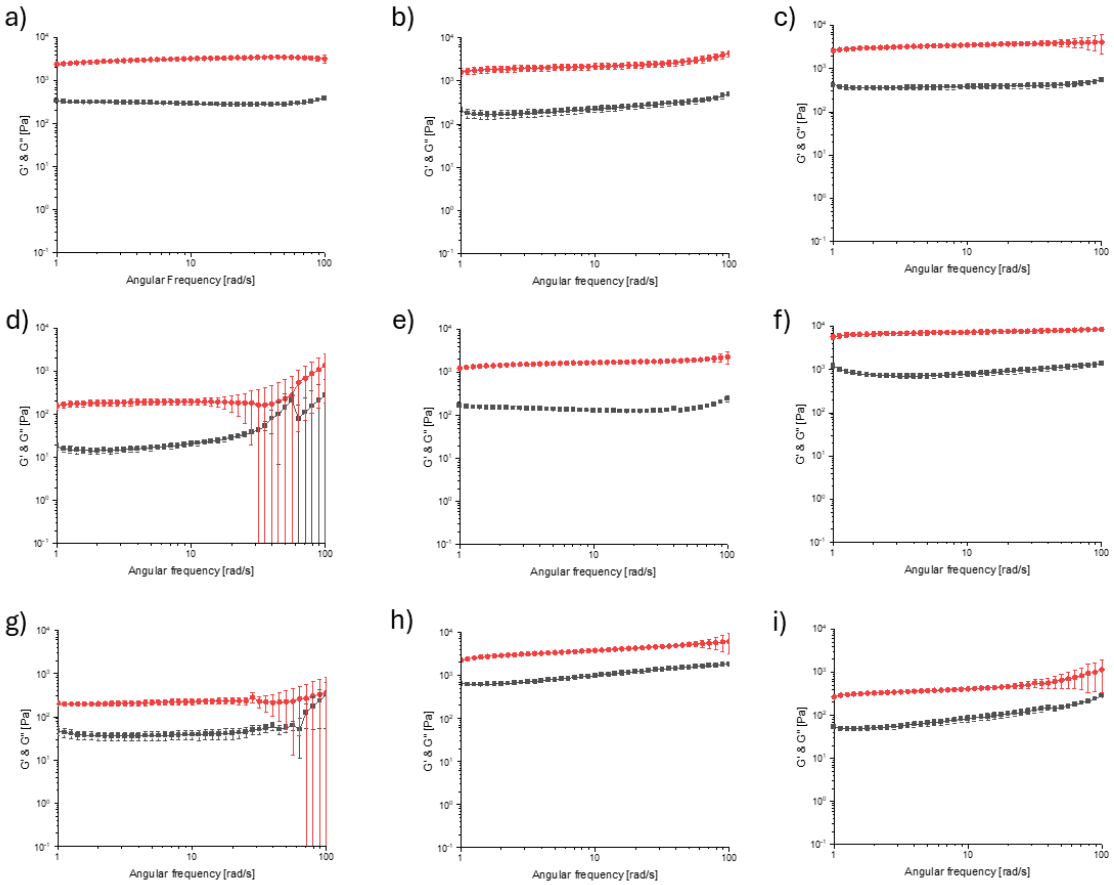

Figure A2.1. Frequency sweeps of a) 1ThNapFF, b) 2NapFF, c) 2NapIF, d) 7MeO2NapFV, e) CarbFV, f) CF_3PhFIF, g) FmocAG, h) FmocFA, and i) FmocLG. The red symbols represent G′, the black symbols G″. Samples were collected in triplicate and averaged. Error bars show the standard deviation between samples.

2.2. Heat-Cool cycles

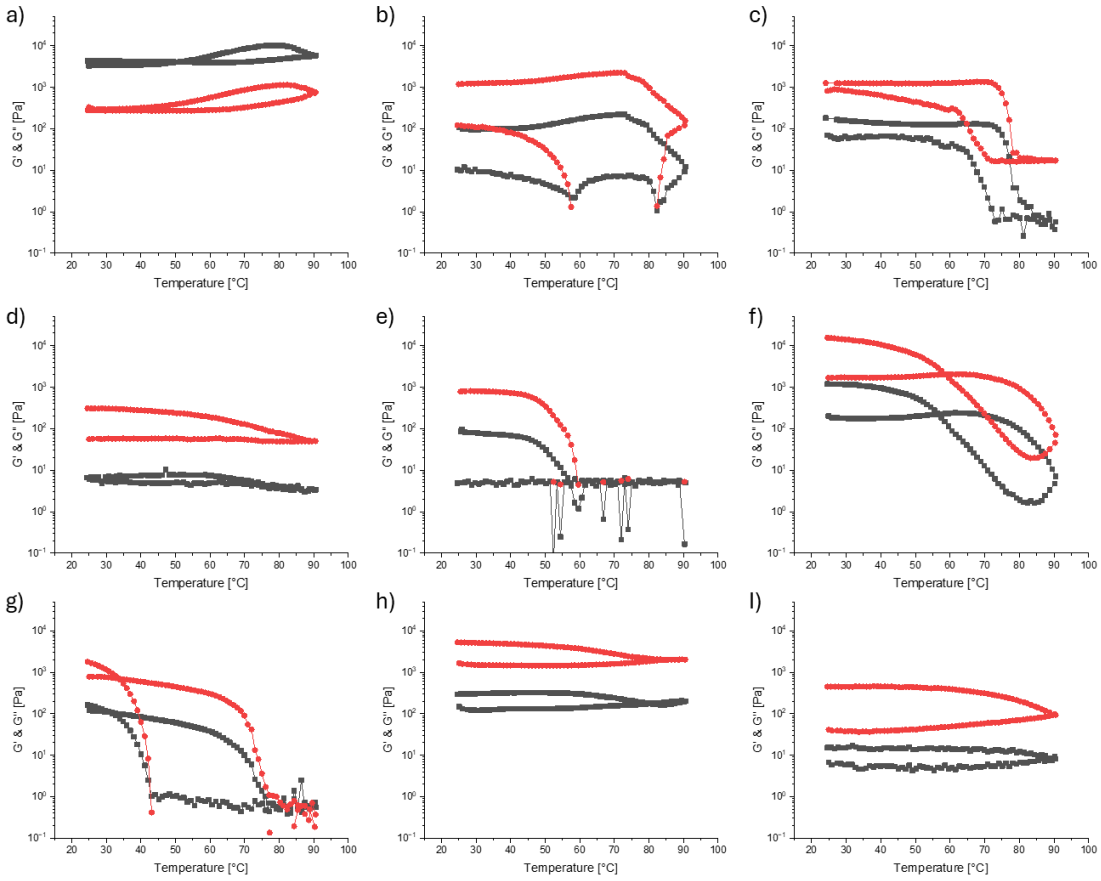

Figure A2.2. Heat/Cool graphs of a) 1ThNapFF, b) 2NapFF, c) 2NapIF, d) 7MeO2NapFV, e) CarbFV, f) CF3PhFIF, g) FmocAG, h) FmocFA, and I) FmocLG. The T_{gel} value was taken as the point at which G′ (red) and G″ (black) were 95 % of their initial value. For 1ThNapFF, the melting point is outside the measured range.

2.3. SAXS data for DMSO-H_2O gels

Table A2.1. Fitting parameters for the cylinder with a power-law model of the 1ThNapFF 5 mg/mL DMSO/H_2O 20/80 gel. Columns annotated with an asterisk * were fixed and not allowed to refine during the fitting process

Parameter	**Value**
Background* (cm^{-1})	0.7
A Scale	0.04 ± 0.002
Radius (Å)	10.6 ± 0.3
Length* (Å)	1000
B Scale	$1.49 \times 10^{-7} \pm 6.0 \times 10^{-7}$
Power Law	4.35 ± 1.08
χ^2	1.73

Table A2.2. Fitting parameters for the elliptical cylinder with a power-law model of the FmocFA 5 mg/mL DMSO/H_2O 20/80 gel. Columns annotated with an asterisk * were fixed and not allowed to refine during the fitting process

Parameter	**Value**
Background* (cm^{-1})	0.2
A Scale	$0.01 \pm 4.4 \times 10^{-5}$
Radius (Å)	47.9 ± 0.1
Axis Ratio	2.89 ± 0.01
Length* (Å)	1000
B Scale	$4.46 \times 10^{-5} \pm 0.30 \times 10^{-5}$
Power Law	2.84 ± 0.012
χ^2	2.49

Table A2.3. Fitting parameters for the elliptical cylinder with a power-law model of the CarbFV 5 mg/mL DMSO/H_2O 20/80 gel. Columns annotated with an asterisk * were fixed and not allowed to refine during the fitting process

Parameter	**Value**
Background* (cm^{-1})	0.3
A Scale	$7.01 \times 10^{-3} \pm 0.04 \times 10^{-3}$
Radius (Å)	26.8 ± 0.2
Axis Ratio	1.93 ± 0.03
Length* (Å)	1000
B Scale	$1.41 \times 10^{-5} \pm 0.06 \times 10^{-5}$
Power Law	3.02 ± 0.01
χ^2	2.03

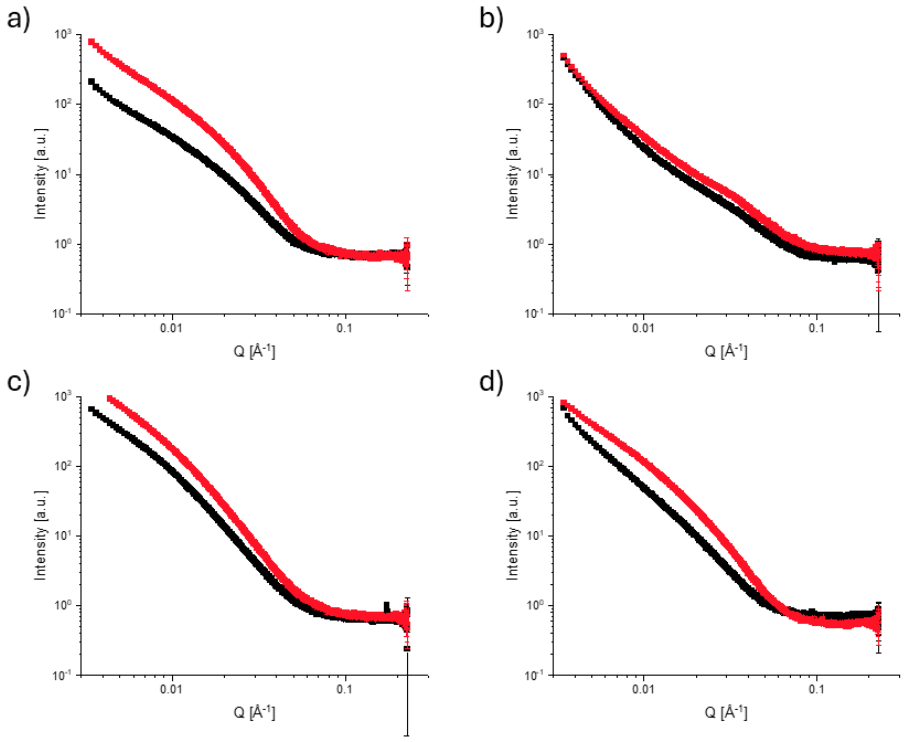

Figure A2.3. SAXS data for a) FmocFA, b) CarbFV, c)7MeO2NapFV, and d) 2NapFF DMSO/H_2O 20/80 gels with a final concentration of 2 mg/mL (black) and 5 mg/mL (red).

2.4. SAXS fitting parameters for methyl formate transient systems

Table A2.4. Fitting parameters for the SAXS data for the 1ThNapFF methyl formate system over the first 20 mins. All data fit a cylinder with a power-law model. The background and length parameters were not included in the table, as they were fixed at 0.04 cm^{-1} and 1000 Å, respectively.

	A Scale	Radius (Å)	B Scale	B Power	χ^2
0 min	$2.35 \times 10^{-4} \pm 0.12 \times 10^{-4}$	26.4 ± 0.9	$1.70 \times 10^{-7} \pm 0.04 \times 10^{-9}$	3.79 ± 0.004	2.28
2 min	$2.03 \times 10^{-4} \pm 0.17 \times 10^{-4}$	22.7 ± 1.2	$1.57 \times 10^{-7} \pm 0.03 \times 10^{-7}$	3.80 ± 0.004	2.38
4 min	$1.68 \times 10^{-4} \pm 0.20 \times 10^{-4}$	21.2 ± 1.6	$1.49 \times 10^{-7} \pm 0.03 \times 10^{-7}$	3.81 ± 0.004	2.43
6 min	$1.48 \times 10^{-4} \pm 0.23 \times 10^{-4}$	19.6 ± 1.9	$1.51 \times 10^{-7} \pm 0.03 \times 10^{-7}$	3.81 ± 0.004	2.34
8 min	$1.60 \times 10^{-4} \pm 0.22 \times 10^{-4}$	19.8 ± 1.7	$1.52 \times 10^{-7} \pm 0.03 \times 10^{-7}$	3.81 ± 0.004	2.15
10 min	$1.60 \times 10^{-4} \pm 0.23 \times 10^{-4}$	19.7 ± 1.7	$1.48 \times 10^{-7} \pm 0.03 \times 10^{-7}$	3.81 ± 0.004	2.45
12 min	$1.84 \times 10^{-4} \pm 0.23 \times 10^{-4}$	19.5 ± 1.5	$1.50 \times 10^{-7} \pm 0.03 \times 10^{-7}$	3.81 ± 0.004	2.43
14 min	$1.85 \times 10^{-4} \pm 0.22 \times 10^{-4}$	19.9 ± 1.5	$1.51 \times 10^{-7} \pm 0.03 \times 10^{-7}$	3.81 ± 0.004	2.23
16 min	$1.87 \times 10^{-4} \pm 0.22 \times 10^{-4}$	20.1 ± 1.5	$1.44 \times 10^{-7} \pm 0.03 \times 10^{-7}$	3.82 ± 0.004	2.39
18 min	$1.86 \times 10^{-4} \pm 0.23 \times 10^{-4}$	19.6 ± 1.5	$1.51 \times 10^{-7} \pm 0.03 \times 10^{-7}$	3.81 ± 0.004	2.52
20 min	$1.70 \times 10^{-4} \pm 0.24 \times 10^{-4}$	19.4 ± 1.7	$1.52 \times 10^{-7} \pm 0.03 \times 10^{-7}$	3.81 ± 0.004	2.27

Table A2.5. Fitting parameters for the SAXS data for the 1ThNapFF methyl formate system overnight. All data fit a cylinder with a power-law model. The background and length parameters were not included in the table, as they were fixed at 0.35 cm^{-1} and 1000 Å, respectively.

	A Scale	Radius (Å)	B Scale	B Power	χ^2
0 hrs	$2.44 \times 10^{-4} \pm 0.08 \times 10^{-4}$	30.8 ± 0.3	$2.06 \times 10^{-8} \pm 0.38 \times 10^{-8}$	3.78 ± 0.034	1.11
2 hrs	$2.10 \times 10^{-4} \pm 0.06 \times 10^{-3}$	18.6 ± 0.3	$3.45 \times 10^{-7} \pm 0.50 \times 10^{-7}$	3.29 ± 0.027	0.92
4 hrs	$3.31 \times 10^{-3} \pm 0.12 \times 10^{-3}$	14.0 ± 0.3	$1.60 \times 10^{-6} \pm 0.18 \times 10^{-6}$	3.03 ± 0.021	1.00
6 hrs	$2.24 \times 10^{-3} \pm 0.08 \times 10^{-3}$	16.5 ± 0.4	$2.36 \times 10^{-6} \pm 0.26 \times 10^{-6}$	2.97 ± 0.020	1.00
8 hrs	$1.87 \times 10^{-3} \pm 0.07 \times 10^{-3}$	18.3 ± 0.4	$2.02 \times 10^{-6} \pm 0.20 \times 10^{-6}$	3.02 ± 0.019	0.95
10 hrs	$1.90 \times 10^{-3} \pm 0.07 \times 10^{-3}$	18.4 ± 0.4	$1.43 \times 10^{-6} \pm 0.14 \times 10^{-6}$	3.10 ± 0.018	0.93
12 hrs	$1.62 \times 10^{-3} \pm 0.05 \times 10^{-3}$	20.3 ± 0.4	$1.15 \times 10^{-6} \pm 0.12 \times 10^{-6}$	3.14 ± 0.019	0.90
14 hrs	$2.04 \times 10^{-3} \pm 0.06 \times 10^{-3}$	18.5 ± 0.4	$8.63 \times 10^{-7} \pm 0.85 \times 10^{-7}$	3.20 ± 0.018	1.10
16 hrs	$1.48 \times 10^{-3} \pm 0.05 \times 10^{-3}$	21.4 ± 0.4	$1.49 \times 10^{-6} \pm 0.15 \times 10^{-6}$	3.10 ± 0.018	1.00

Table A2.6. Fitting parameters for the SAXS data for the FmocFA methyl formate system over the first 20 mins. From 0-6 mins, the data fit an elliptical cylinder model, and from 8-20 mins, the data fit a cylinder with a power-law model. The background and length parameters were not included in the table, as they were fixed at 0.4 cm^{-1} and 1000 Å, respectively.

	A Scale	Radius (Å)	Axis ratio	B Scale	B Power	χ^2
0 min	$2.86 \times 10^{-3} \pm 0.01 \times 10^{-3}$	36.9 ± 0.2	3.14 ± 0.02	-	-	3.61
2 min	$2.85 \times 10^{-3} \pm 0.01 \times 10^{-3}$	37.3 ± 0.2	3.09 ± 0.02	-	-	3.81
4 min	$2.88 \times 10^{-3} \pm 0.10 \times 10^{-3}$	36.2 ± 0.2	3.25 ± 0.02	-	-	3.86
6 min	$1.90 \times 10^{-3} \pm 0.12 \times 10^{-3}$	31.5 ± 0.3	3.65 ± 0.04	-	-	3.66
8 min	$4.69 \times 10^{-4} \pm 0.23 \times 10^{-4}$	42.6 ± 0.7	-	$7.77 \times 10^{-5} \pm 1.99 \times 10^{-5}$	2.07 ± 0.05	0.78
10 min	$3.94 \times 10^{-4} \pm 0.10 \times 10^{-4}$	44.2 ± 0.8	-	$4.57 \times 10^{-7} \pm 2.91 \times 10^{-7}$	2.99 ± 0.12	0.78
12 min	$2.48 \times 10^{-4} \pm 0.18 \times 10^{-4}$	49.0 ± 1.1	-	$3.50 \times 10^{-5} \pm 1.14 \times 10^{-5}$	2.22 ± 0.06	0.76
14 min	$1.98 \times 10^{-4} \pm 0.14 \times 10^{-4}$	54.7 ± 1.4	-	$7.66 \times 10^{-5} \pm 1.56 \times 10^{-5}$	2.09 ± 0.04	0.81
16 min	$1.73 \times 10^{-4} \pm 0.11 \times 10^{-4}$	63.2 ± 1.5	-	$1.02 \times 10^{-4} \pm 0.15 \times 10^{-4}$	2.07 ± 0.03	0.74
18 min	$1.83 \times 10^{-4} \pm 0.09 \times 10^{-4}$	70.2 ± 1.3	-	$1.05 \times 10^{-4} \pm 0.14 \times 10^{-4}$	2.07 ± 0.02	0.77
20 min	$1.85 \times 10^{-4} \pm 0.09 \times 10^{-4}$	70.9 ± 1.3	-	$9.30 \times 10^{-5} \pm 1.22 \times 10^{-5}$	2.11 ± 0.02	0.71

Table A2.7. Fitting parameters for the SAXS data for the FmocFA methyl formate system overnight. At 0 hrs, the data fit an elliptical cylinder with a power-law model from 2-4 hrs, the data fit a cylinder with a power-law model, and from 6-16 hrs, the data fit a power-law model. Columns annotated with an asterisk * were fixed and not allowed to refine during the fitting process. The background parameter is not included in the table, as it was fixed at 0.055 cm^{-1}.

	A Scale	Radius (Å)	Axis ratio	Length* (Å)	B Scale	B Power	χ^2
0 hrs	$3.48 \times 10^{-3} \pm 0.01 \times 10^{-3}$	37.8 ± 0.2	2.61 ± 0.02	1000	$1.13 \times 10^{-7} \pm 0.02 \times 10^{-7}$	3.5 ± 0.0	0.88
2 hrs	$5.74 \times 10^{-5} \pm 4.53 \times 10^{-5}$	21.5 ± 9.9	-	1000	$2.25 \times 10^{-7} \pm 0.68 \times 10^{-7}$	4.11 ± 0.05	0.67
4 hrs	$3.72 \times 10^{-5} \pm 3.20 \times 10^{-5}$	25.3 ± 13.1	-	1000	$4.60 \times 10^{-9} \pm 1.17 \times 10^{-9}$	4.01 ± 0.05	0.71
6 hrs	-	-	-	-	$3.74 \times 10^{-9} \pm 5.60 \times 10^{-9}$	3.64 ± 0.03	1.00
8 hrs	-	-	-	-	$1.26 \times 10^{-8} \pm 2.31 \times 10^{-9}$	3.82 ± 0.03	0.88
10 hrs	-	-	-	-	$5.84 \times 10^{-9} \pm 1.07 \times 10^{-9}$	3.98 ± 0.03	0.74
12 hrs	-	-	-	-	$6.92 \times 10^{-9} \pm 1.28 \times 10^{-9}$	3.94 ± 0.03	0.72
14 hrs	-	-	-	-	$6.44 \times 10^{-9} \pm 1.20 \times 10^{-9}$	3.96 ± 0.03	1.47
16 hrs	-	-	-	-	$2.29 \times 10^{-8} \pm 6.00 \times 10^{-8}$	3.1 ± 0.05	0.89

Table A2.8. Fitting parameters for the SAXS data for the CarbFV methyl formate system over the first 20 mins. At 0 mins, the data fit a power-law model, and from 2-20 mins, the data fit a hollow cylinder with a power-law model. Columns annotated with an asterisk * were fixed and not allowed to refine during the fitting process.

	Background	A Scale	Radius (Å)	Thickness (Å)	Length* (Å)	B Scale	B Power	χ^2
0 min	0.07	-	-	-	-	$1.96 \times 10^{-5} \pm 022 \times 10^{-5}$	2.33 ± 0.02	0.84
2 min	0.08	$2.21 \times 10^{-5} \pm 7.74 \times 10^{-5}$	107.4 ± 7.7	37.6 ± 14.0	1000	$7.12 \times 10^{-5} \pm 4.71 \times 10^{-5}$	2.07 ± 0.16	0.76
4 min	0.08	$3.35 \times 10^{-4} \pm 1.00 \times 10^{-4}$	119.3 ± 5.8	34.5 ± 10.8	1000	$3.22 \times 10^{-4} \pm 1.09 \times 10^{-4}$	1.77 ± 0.08	1.01
6 min	0.08	$8.14 \times 10^{-4} \pm 1.55 \times 10^{-4}$	115.0 ± 3.0	32.6 ± 5.8	1000	$1.22 \times 10^{-4} \pm 0.78 \times 10^{-4}$	2.03 ± 0.15	0.84
8 min	0.08	$1.04 \times 10^{-3} \pm 2.06 \times 10^{-3}$	116.0 ± 2.0	33.1 ± 3.0	1000	$1.85 \times 10^{-4} \pm 0.17 \times 10^{-4}$	1.96 ± 0.16	0.87
10 min	0.08	$1.56 \times 10^{-3} \pm 0.21 \times 10^{-3}$	116.5 ± 1.9	30.7 ± 3.7	1000	$1.37 \times 10^{-4} \pm 1.11 \times 10^{-4}$	1.96 ± 0.19	0.95
12 min	0.08	$1.74 \times 10^{-3} \pm 0.21 \times 10^{-3}$	116.5 ± 1.8	30.8 ± 3.3	1000	$1.67 \times 10^{-4} \pm 1.19 \times 10^{-4}$	1.93 ± 0.16	1.02
14 min	0.08	$2.14 \times 10^{-3} \pm 0.23 \times 10^{-3}$	115.8 ± 1.4	30.2 ± 2.8	1000	$1.00 \times 10^{-4} \pm 1.22 \times 10^{-4}$	1.95 ± 0.28	0.92
16 min	0.08	$2.14 \times 10^{-3} \pm 0.22 \times 10^{-3}$	115.3 ± 1.4	31.0 ± 2.7	1000	$1.21 \times 10^{-4} \pm 1.09 \times 10^{-4}$	1.98 ± 0.20	1.03
18 min	0.08	$2.36 \times 10^{-3} \pm 0.23 \times 10^{-3}$	115.9 ± 1.3	30.1 ± 2.6	1000	$8.47 \times 10^{-5} \pm 11.0 \times 10^{-5}$	1.99 ± 0.29	0.93
20 min	0.08	$2.52 \times 10^{-3} \pm 0.26 \times 10^{-3}$	115.7 ± 1.3	29.5 ± 2.6	1000	$6.81 \times 10^{-5} \pm 13.1 \times 10^{-5}$	1.95 ± 0.43	1.01

Table A2.9. Fitting parameters for the SAXS data for the CarbFV methyl formate system overnight. All data fit a hollow cylinder with a power-law model. The background and length parameters were not included in the table, as they were fixed at 0.04 cm^{-1} and 1000 Å, respectively.

	A Scale	Radius (Å)	Thickness	B Scale	B Power	χ^2
0 hrs	$6.57 \times 10^{-4} \pm 3.66 \times 10^{-4}$	94.9 ± 6.1	23.8 ± 12.0	$2.47 \times 10^{-4} \pm 1.21 \times 10^{-4}$	2.04 ± 0.12	0.70
2 hrs	$1.09 \times 10^{-3} \pm 0.21 \times 10^{-3}$	102.4 ± 2.9	30.4 ± 5.7	$5.90 \times 10^{-4} \pm 1.54 \times 10^{-4}$	1.88 ± 0.06	0.86
4 hrs	$1.15 \times 10^{-3} \pm 0.22 \times 10^{-3}$	103.9 ± 2.8	30.2 ± 5.4	$7.35 \times 10^{-4} \pm 1.74 \times 10^{-4}$	1.83 ± 0.06	0.83
6 hrs	$1.20 \times 10^{-3} \pm 0.18 \times 10^{-3}$	103.1 ± 2.4	31.4 ± 4.7	$7.24 \times 10^{-4} \pm 1.52 \times 10^{-4}$	1.85 ± 0.05	0.83
8 hrs	$1.22 \times 10^{-3} \pm 0.19 \times 10^{-3}$	103.1 ± 2.4	31.2 ± 4.7	$7.00 \times 10^{-4} \pm 1.51 \times 10^{-4}$	1.86 ± 0.05	0.92
10 hrs	$1.29 \times 10^{-3} \pm 0.22 \times 10^{-3}$	105.0 ± 2.5	30.2 ± 4.9	$6.67 \times 10^{-4} \pm 1.58 \times 10^{-4}$	1.88 ± 0.06	0.85
12 hrs	$1.32 \times 10^{-3} \pm 0.19 \times 10^{-3}$	104.1 ± 2.2	31.2 ± 4.4	$6.68 \times 10^{-4} \pm 1.46 \times 10^{-4}$	1.88 ± 0.05	0.91
14 hrs	$1.41 \times 10^{-3} \pm 0.19 \times 10^{-3}$	104.3 ± 2.1	31.1 ± 4.1	$7.00 \times 10^{-4} \pm 1.50 \times 10^{-4}$	1.87 ± 0.05	0.91
16 hrs	$1.38 \times 10^{-3} \pm 0.20 \times 10^{-3}$	104.7 ± 2.2	31.2 ± 4.2	$6.29 \times 10^{-4} \pm 1.39 \times 10^{-4}$	1.91 ± 0.06	0.91

2.5. Images of the transient systems

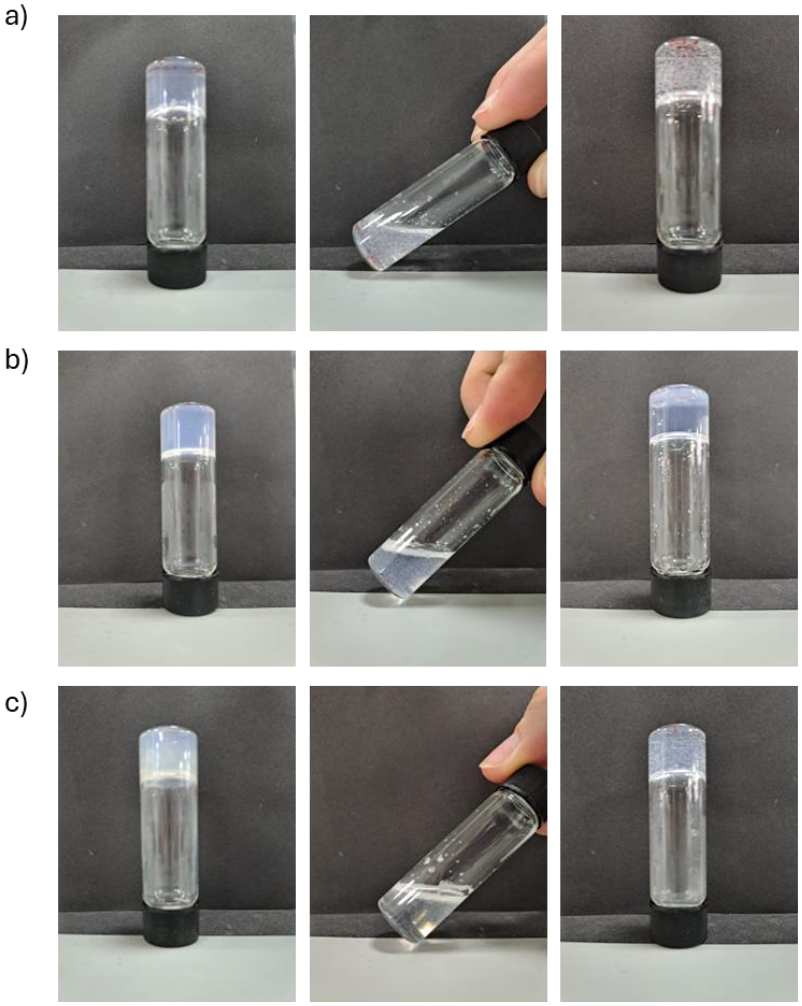

Figure 2.4. Images of the 1ThNapFF transient system approximately 1 minute after initial gel formation (left), the sol phase (middle) 10 minutes after gel formation, and the gel 16 hours after gel formation (right), with a) methyl formate, b) ethyl formate, and c) *n*-propyl formate.

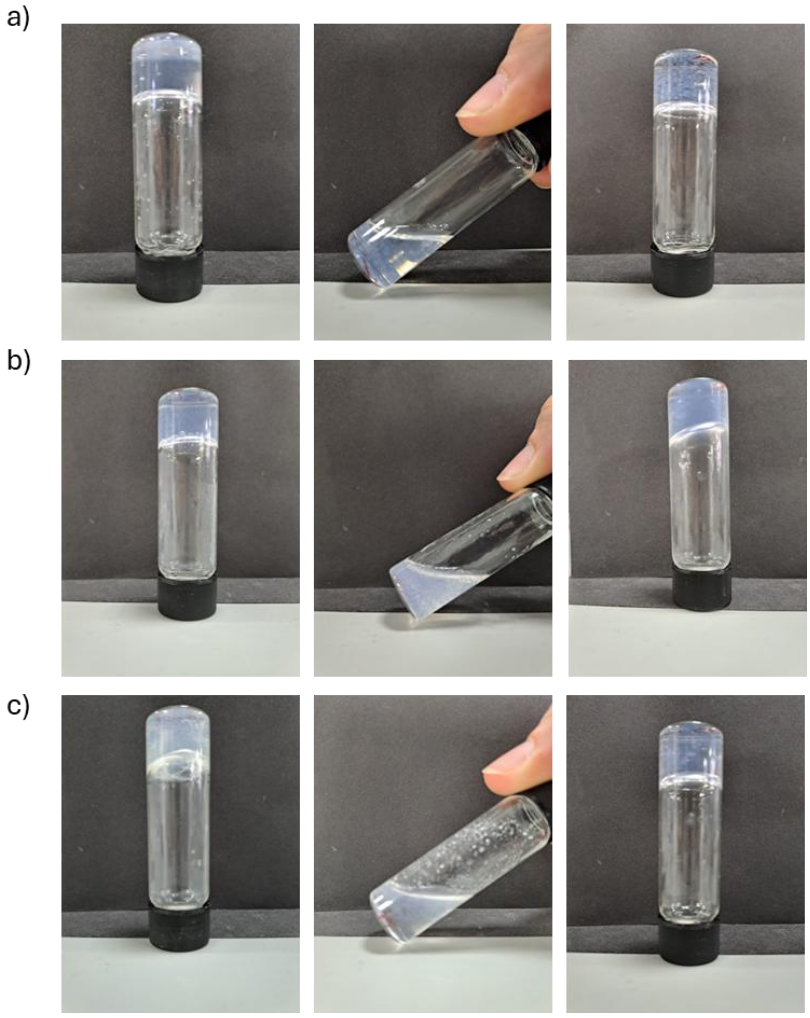

Figure A2.5. Images of the FmocFA transient system approximately 1 minute after initial gel formation (left), the sol phase (middle) 10 minutes after gel formation, and the gel 16 hours after gel formation (right), with a) methyl formate, b) ethyl formate, and c) *n*-propyl formate.

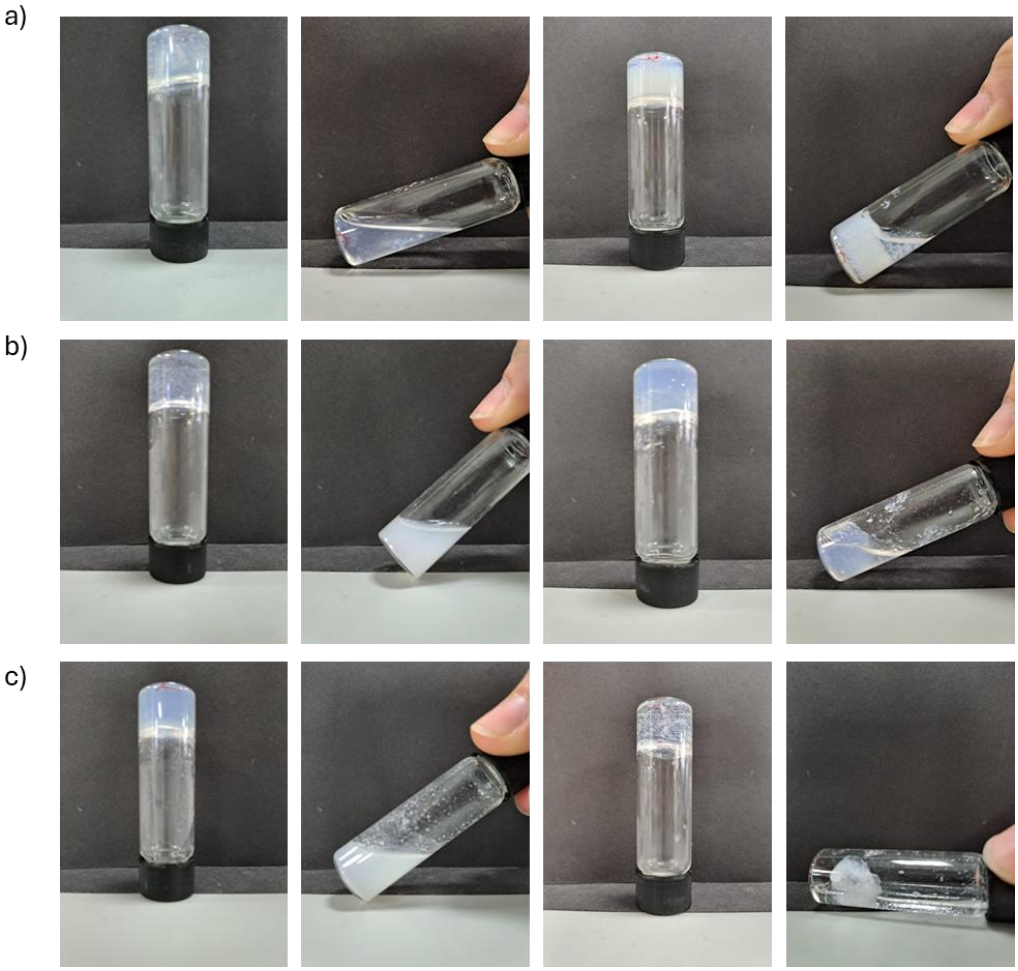

Figure A2.6. Images of the CarbFV transient system approximately 1 minute after initial gel formation, the sol phase 10 minutes after gel formation, the gel 16 hours after gel formation, and the gel after 3 days once syneresis occurred, respectively, with a) methyl formate, b) ethyl formate, and c) *n*-propyl formate.

2.6. SAXS fitting parameters for ethyl formate transient systems

Table A2.10. Fitting parameters for the SAXS data for the 1ThNapFF ethyl formate system. All data fit a cylinder with a power-law model. The background, Axis ratio and length parameters were not included in the table, as they were fixed at 0.35 cm^{-1}, 3.5 and 1000 Å, respectively.

	A Scale	**Radius (Å)**	**B Scale**	**B Power**	χ^2
0 hrs	$1.31 \times 10^{-3} \pm 0.01 \times 10^{-3}$	38.2 ± 0.3	$1.88 \times 10^{-7} \pm 0.09 \times 10^{-7}$	3.92 ± 0.008	2.13
2 hrs	$1.32 \times 10^{-3} \pm 0.01 \times 10^{-3}$	39.7 ± 0.3	$1.48 \times 10^{-7} \pm 0.08 \times 10^{-7}$	3.93 ± 0.010	2.02
4 hrs	$1.38 \times 10^{-3} \pm 0.01 \times 10^{-3}$	39.3 ± 0.3	$1.45 \times 10^{-7} \pm 0.08 \times 10^{-7}$	3.92 ± 0.010	1.71
6 hrs	$1.39 \times 10^{-3} \pm 0.01 \times 10^{-3}$	39.6 ± 0.3	$1.39 \times 10^{-7} \pm 0.08 \times 10^{-7}$	3.92 ± 0.011	1.86
8 hrs	$1.41 \times 10^{-3} \pm 0.01 \times 10^{-3}$	39.9 ± 0.3	$1.25 \times 10^{-7} \pm 0.08 \times 10^{-7}$	3.93 ± 0.011	1.84
10 hrs	$1.44 \times 10^{-3} \pm 0.01 \times 10^{-3}$	39.4 ± 0.3	$1.21 \times 10^{-7} \pm 0.07 \times 10^{-7}$	3.94 ± 0.011	1.93
12 hrs	$1.48 \times 10^{-3} \pm 0.01 \times 10^{-3}$	39.8 ± 0.3	$9.53 \times 10^{-8} \pm 0.59 \times 10^{-8}$	3.98 ± 0.011	1.91
14 hrs	$1.49 \times 10^{-3} \pm 0.01 \times 10^{-3}$	39.9 ± 0.3	$8.34 \times 10^{-8} \pm 0.53 \times 10^{-8}$	4.00 ± 0.011	1.74
16 hrs	$1.51 \times 10^{-3} \pm 0.01 \times 10^{-3}$	41.0 ± 0.3	$6.16 \times 10^{-8} \pm 0.40 \times 10^{-8}$	4.06 ± 0.012	2.12

Table A2.11. Fitting parameters for the SAXS data for the FmocFA ethyl formate system. All data fit an elliptical cylinder with a power-law model. The background and length parameters were not included in the table, as they were fixed at 0.04 cm^{-1} and 1000 Å, respectively.

	A Scale	Radius (Å)	Axis Ratio	B Scale	B Power	χ^2
0 hrs	$8.60 \times 10^{-4} \pm 0.11 \times 10^{-4}$	50.1 ± 0.6	2.5 ± 0.1	$2.56 \times 10^{-7} \pm 0.36 \times 10^{-7}$	3.60 ± 0.02	1.05
2 hrs	$8.52 \times 10^{-4} \pm 0.11 \times 10^{-4}$	51.2 ± 0.6	2.4 ± 0.1	$3.04 \times 10^{-7} \pm 0.45 \times 10^{-7}$	3.60 ± 0.03	1.16
4 hrs	$8.55 \times 10^{-4} \pm 0.11 \times 10^{-4}$	51.3 ± 0.6	2.5 ± 0.1	$2.14 \times 10^{-7} \pm 0.35 \times 10^{-7}$	3.61 ± 0.03	1.25
6 hrs	$8.34 \times 10^{-4} \pm 0.11 \times 10^{-4}$	51.8 ± 0.6	2.4 ± 0.1	$2.48 \times 10^{-7} \pm 0.40 \times 10^{-7}$	3.58 ± 0.03	1.24
8 hrs	$8.44 \times 10^{-4} \pm 0.01 \times 10^{-4}$	51.8 ± 0.6	2.4 ± 0.1	$2.24 \times 10^{-7} \pm 0.36 \times 10^{-7}$	3.60 ± 0.03	1.13
10 hrs	$8.16 \times 10^{-4} \pm 0.01 \times 10^{-4}$	52.8 ± 0.6	2.4 ± 0.1	$2.61 \times 10^{-7} \pm 0.43 \times 10^{-7}$	3.57 ± 0.03	1.13
12 hrs	$8.07 \times 10^{-4} \pm 0.11 \times 10^{-4}$	52.7 ± 0.6	2.5 ± 0.1	$2.57 \times 10^{-7} \pm 0.43 \times 10^{-7}$	3.58 ± 0.03	1.05
14 hrs	$7.52 \times 10^{-4} \pm 0.11 \times 10^{-4}$	54.1 ± 0.7	2.4 ± 0.1	$3.40 \times 10^{-7} \pm 0.55 \times 10^{-7}$	3.52 ± 0.03	1.01
16 hrs	$7.17 \times 10^{-4} \pm 0.12 \times 10^{-4}$	53.3 ± 0.7	2.3 ± 0.1	$5.14 \times 10^{-7} \pm 0.84 \times 10^{-7}$	3.44 ± 0.03	1.07

Table A2.12. Fitting parameters for the SAXS data for the CarbFV ethyl formate system. All data fit a power-law model. The background parameter is not included in the table, as it was fixed at 0.1 cm^{-1}.

	Scale	Power	χ^2
0 hrs	$5.79 \times 10^{-9} \pm 1.73 \times 10^{-9}$	3.87 ± 0.06	0.86
2 hrs	$1.79 \times 10^{-9} \pm 0.75 \times 10^{-9}$	4.04 ± 0.08	0.95
4 hrs	$2.51 \times 10^{-9} \pm 0.97 \times 10^{-9}$	3.99 ± 0.07	0.93
6 hrs	$1.83 \times 10^{-9} \pm 0.84 \times 10^{-9}$	4.02 ± 0.08	0.89
8 hrs	$3.00 \times 10^{-9} \pm 1.31 \times 10^{-9}$	3.93 ± 0.08	0.89
10 hrs	$5.44 \times 10^{-9} \pm 2.21 \times 10^{-9}$	3.82 ± 0.08	0.81
12 hrs	$4.71 \times 10^{-9} \pm 1.98 \times 10^{-9}$	3.84 ± 0.08	0.92
14 hrs	$8.58 \times 10^{-9} \pm 3.52 \times 10^{-9}$	3.72 ± 0.08	0.97
16 hrs	$1.22 \times 10^{-8} \pm 2.40 \times 10^{-9}$	3.81 ± 0.04	0.81

2.7. SAXS fitting parameters for *n*-propyl formate transient systems

Table A2.13. Fitting parameters for the SAXS data for the 1ThNapFF *n*-propyl formate system. All data fit a cylinder with a power-law model. The background and length parameters were not included in the table, as they were fixed at 0.35 cm^{-1} and 1000 Å, respectively.

	A Scale	Radius (Å)	Axis Ratio	B Scale	B Power	χ^2
0 hrs	$2.15 \times 10^{-5} \pm 0.89 \times 10^{-5}$	66.2 ± 17.7	4.3 ± 1.6	$1.02 \times 10^{-8} \pm 1.32 \times 10^{-8}$	3.86 ± 0.22	1.29
2 hrs	$3.66 \times 10^{-5} \pm 1.16 \times 10^{-5}$	79.4 ± 7.7	3.4 ± 0.8	$1.52 \times 10^{-8} \pm 2.12 \times 10^{-8}$	3.81 ± 0.24	1.36
4 hrs	$5.32 \times 10^{-5} \pm 1.17 \times 10^{-5}$	92.6 ± 4.8	3.1 ± 0.4	$1.03 \times 10^{-8} \pm 1.43 \times 10^{-8}$	3.91 ± 0.24	1.23
6 hrs	$5.41 \times 10^{-5} \pm 1.17 \times 10^{-5}$	115.4 ± 5.0	2.5 ± 0.3	$1.66 \times 10^{-8} \pm 2.21 \times 10^{-8}$	3.81 ± 0.23	1.86
8 hrs	$2.95 \times 10^{-5} \pm 0.38 \times 10^{-5}$	186.5 ± 2.3	1.3 ± 0.3	$2.17 \times 10^{-7} \pm 0.61 \times 10^{-8}$	3.37 ± 0.05	1.69
10 hrs	$3.18 \times 10^{-5} \pm 0.65 \times 10^{-5}$	150.2 ± 1.3	1.9 ± 0.3	$9.24 \times 10^{-8} \pm 4.46 \times 10^{-8}$	3.54 ± 0.08	1.47
12 hrs	$5.31 \times 10^{-5} \pm 1.06 \times 10^{-5}$	117.2 ± 4.5	2.4 ± 0.3	$7.03 \times 10^{-9} \pm 8.57 \times 10^{-9}$	4.01 ± 0.21	1.66
14 hrs	$7.01 \times 10^{-5} \pm 0.64 \times 10^{-5}$	121.3 ± 3.6	2.4 ± 0.2	$1.73 \times 10^{-10} \pm 2.47 \times 10^{-10}$	4.66 ± 0.25	1.58
16 hrs	$7.47 \times 10^{-5} \pm 0.60 \times 10^{-5}$	130.2 ± 3.5	2.4 ± 0.2	$5.78 \times 10^{-11} \pm 9.63 \times 10^{-11}$	4.84 ± 0.29	1.93

Table A2.14. Fitting parameters for the SAXS data for the FmocFA *n*-propyl formate system. From 0-6 hrs, the data fit an elliptical cylinder with a power-law model; from 8-10 hrs, the data fit a cylinder with a power-law model; and from 12-16 hrs, the data fit a power-law model. The background parameter is not included in the table, as it was fixed at 0.1 cm^{-1}.

	A Scale	Radius (Å)	Axis Ratio	Length (Å)	B Scale	B Power	χ^2
0 hrs	$1.71 \times 10^{-4} \pm 0.11 \times 10^{-4}$	83.8 ± 2.6	2.9 ± 0.2	1000	$4.06 \times 10^{-6} \pm 0.86 \times 10^{-6}$	2.90 ± 0.04	0.82
2 hrs	$1.93 \times 10^{-4} \pm 0.14 \times 10^{-4}$	77.8 ± 2.2	3.4 ± 0.2	1000	$2.06 \times 10^{-6} \pm 0.67 \times 10^{-6}$	3.01 ± 0.05	0.81
4 hrs	$1.81 \times 10^{-4} \pm 0.13 \times 10^{-4}$	79.7 ± 2.3	3.3 ± 0.2	1000	$2.05 \times 10^{-6} \pm 0.65 \times 10^{-6}$	3.01 ± 0.05	0.86
6 hrs	$1.25 \times 10^{-4} \pm 0.06 \times 10^{-4}$	87.8 ± 2.4	3.2 ± 0.2	1000	$7.84 \times 10^{-6} \pm 0.98 \times 10^{-6}$	2.79 ± 0.02	0.75
8 hrs	$6.86 \times 10^{-6} \pm 7.08 \times 10^{-6}$	48.2 ± 4.8	-	1000	$1.73 \times 10^{-9} \pm 0.74 \times 10^{-9}$	4.10 ± 0.08	0.78
10 hrs	$4.72 \times 10^{-6} \pm 5.76 \times 10^{-6}$	53.0 ± 6.9	-	1000	$2.49 \times 10^{-9} \pm 1.11 \times 10^{-9}$	4.03 ± 0.08	0.76
12 hrs	-	-	-	-	$3.12 \times 10^{-9} \pm 0.93 \times 10^{-9}$	3.97 ± 0.06	0.77
14 hrs	-	-	-	-	$2.50 \times 10^{-9} \pm 0.78 \times 10^{-9}$	4.00 ± 0.06	0.73
16 hrs	-	-	-	-	$2.64 \times 10^{-9} \pm 0.88 \times 10^{-9}$	3.98 ± 0.06	0.75

Table A2.15. Fitting parameters for the SAXS data for the CarbFV *n*-propyl formate system. At 0 hrs, the data fit a cylinder with a power-law model and from 2-16 hrs, the data fit a power-law model. The background parameter is not included in the table, as it was fixed at 0.025 cm^{-1}.

	A Scale	Radius (Å)	Length (Å)	B Scale	B Power	χ^2
0 hrs	$2.29 \times 10^{-5} \pm 0.21 \times 10^{-5}$	208.2 ± 7.4	1000	$2.50 \times 10^{-6} \pm 0.18 \times 10^{-6}$	3.03 ± 0.01	0.84
2 hrs	-	-	-	$3.72 \times 10^{-9} \pm 1.04 \times 10^{-9}$	3.98 ± 0.05	0.93
4 hrs	-	-	-	$7.35 \times 10^{-9} \pm 1.70 \times 10^{-9}$	3.89 ± 0.04	0.88
6 hrs	-	-	-	$8.72 \times 10^{-9} \pm 1.91 \times 10^{-9}$	3.86 ± 0.04	0.98
8 hrs	-	-	-	$8.31 \times 10^{-9} \pm 1.86 \times 10^{-9}$	3.86 ± 0.04	1.12
10 hrs	-	-	-	$1.22 \times 10^{-8} \pm 2.69 \times 10^{-9}$	3.78 ± 0.04	1.18
12 hrs	-	-	-	$1.13 \times 10^{-8} \pm 0.25 \times 10^{-8}$	3.80 ± 0.04	1.76
14 hrs	-	-	-	$9.62 \times 10^{-9} \pm 2.18 \times 10^{-9}$	3.83 ± 0.04	1.35
16 hrs	-	-	-	$5.34 \times 10^{-9} \pm 1.26 \times 10^{-9}$	3.94 ± 0.04	1.71

2.8. Ageing rheology

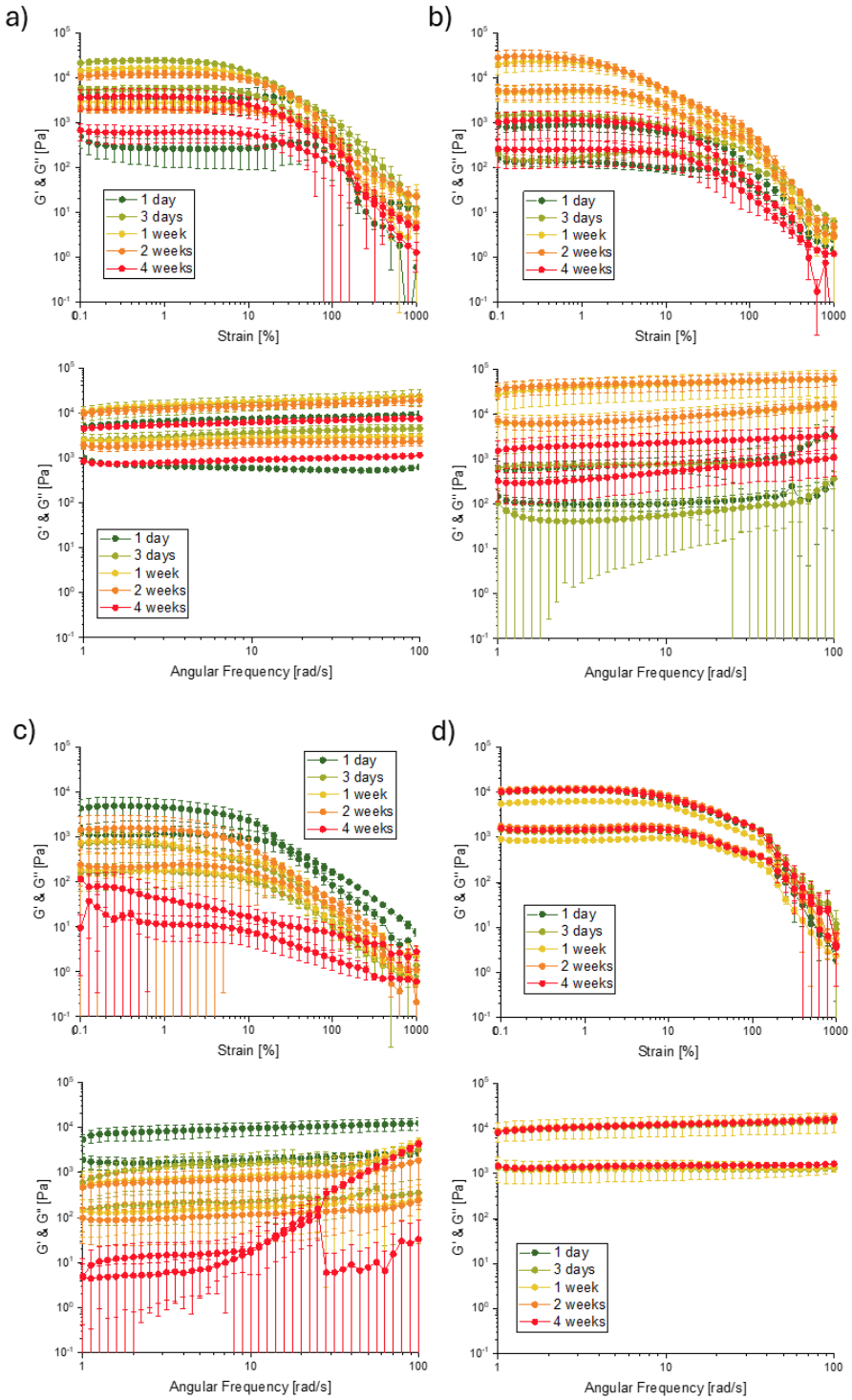

Figure A2.7. Strain (top) and frequency (bottom) sweeps of 1ThNapFF transient systems with a) methyl formate, b) ethyl formate, c) *n*-propyl formate and d) the DMSO/H_2O 1ThNapFF gels measured over 4 weeks. Graphs b) and c) use the same legend as the other graphs; however, the legend has been intentionally omitted in this panel to avoid obscuring the data. Samples were collected in triplicate and averaged. Error bars show the standard deviation between samples.

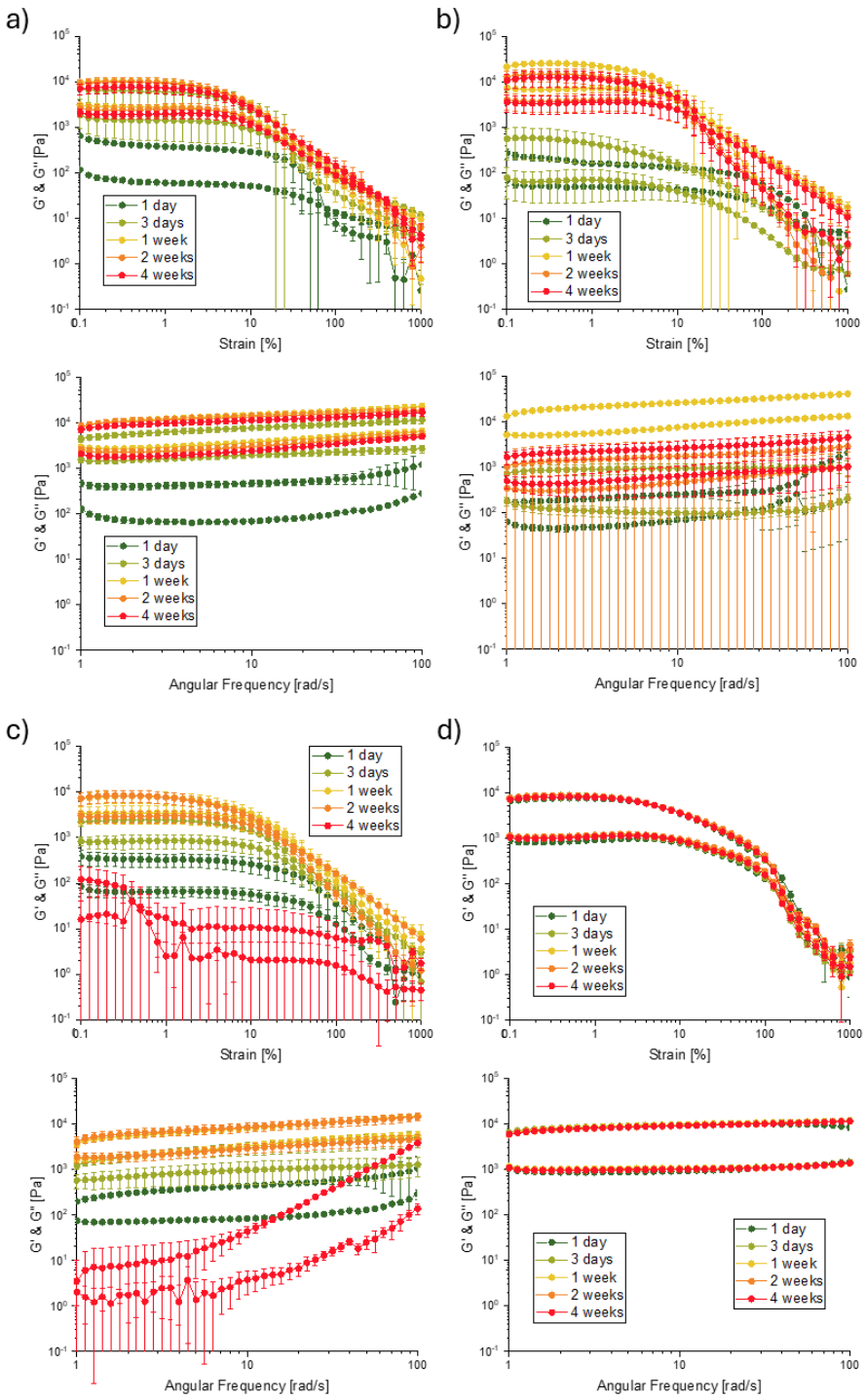

Figure A2.8. Strain (top) and frequency (bottom) sweeps of FmocFA transient systems with a) methyl formate, b) ethyl formate, c) *n*-propyl formate and d) the DMSO/H_2O FmocFA gels measured over 4 weeks. Graphs c) and b) use the same legend as the other graphs; however, the legend has been intentionally omitted in this panel to avoid obscuring the data. Samples were collected in triplicate and averaged. Error bars show the standard deviation between samples.

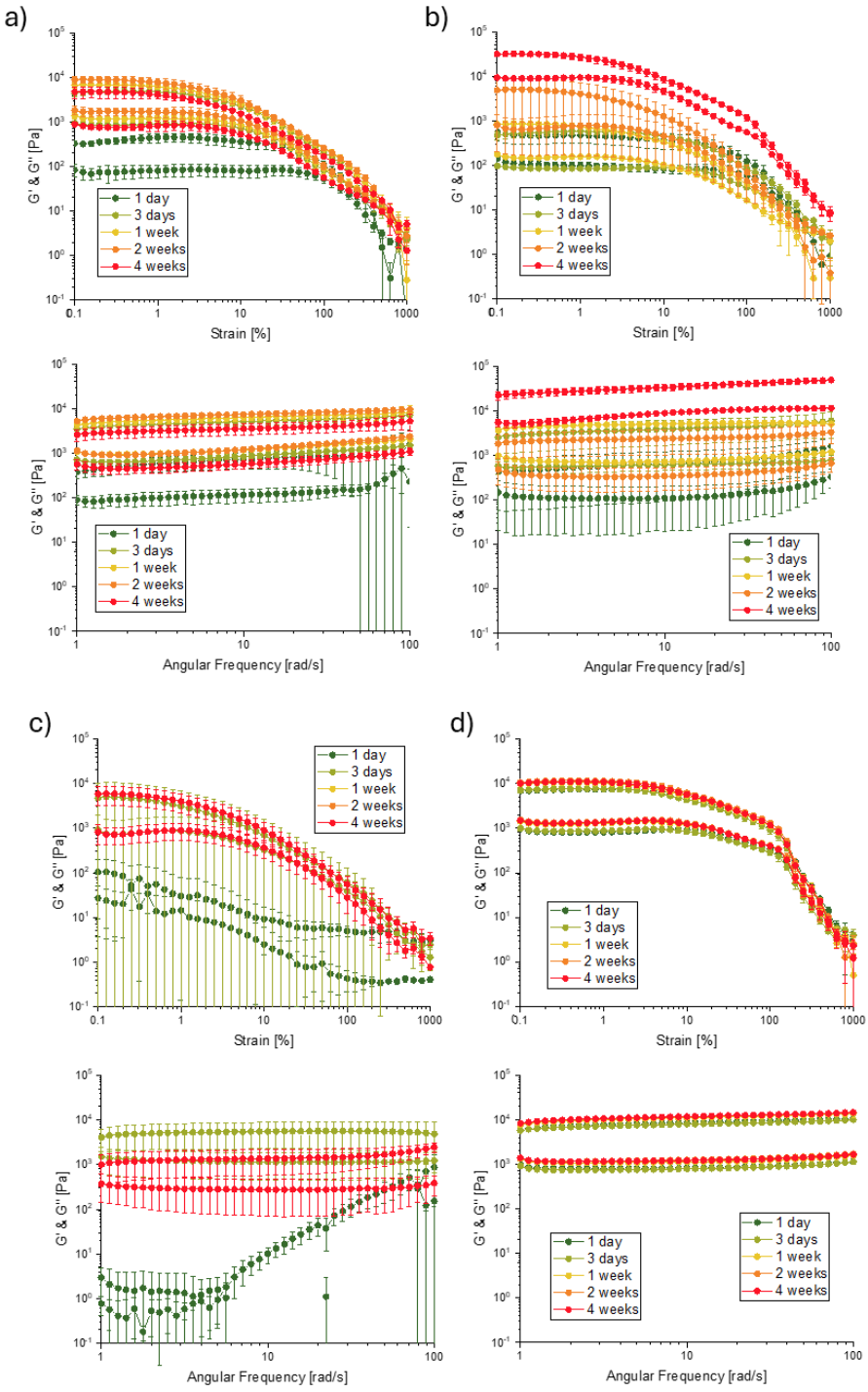

Figure A2.9. Strain (top) and frequency (bottom) sweeps of CarbFV transient systems with a) methyl formate, b) ethyl formate, c) *n*-propyl formate and d) the DMSO/H_2O CarbFV gels measured over 4 weeks. Graphs c) and b) use the same legend as the other graphs; however, the legend has been intentionally omitted in this panel to avoid obscuring the data. Samples were collected in triplicate and averaged. Error bars show the standard deviation between samples.

2.9. Temperature rheology

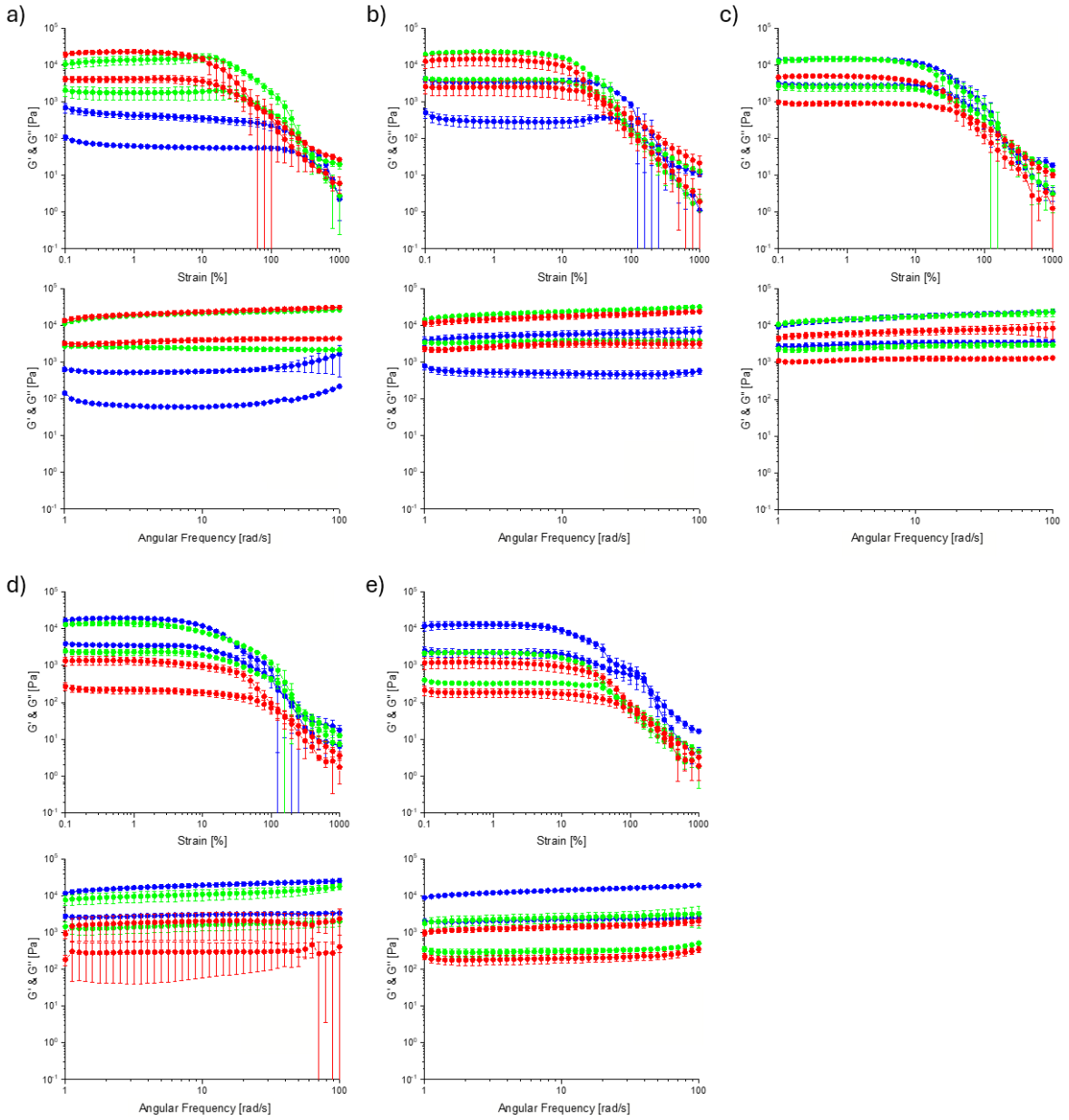

Figure A2.10. Strain (top) and frequency (bottom) sweeps of 1ThNapFF transient systems with methyl formate measured after a) 1 day, b) 3 days, c) 7 days, d) 14 days, and e) 28 days at temperatures of 15 °C (blue), 25 °C (green), and 35 °C (red). Samples were collected in triplicate and averaged. Error bars show the standard deviation between samples.

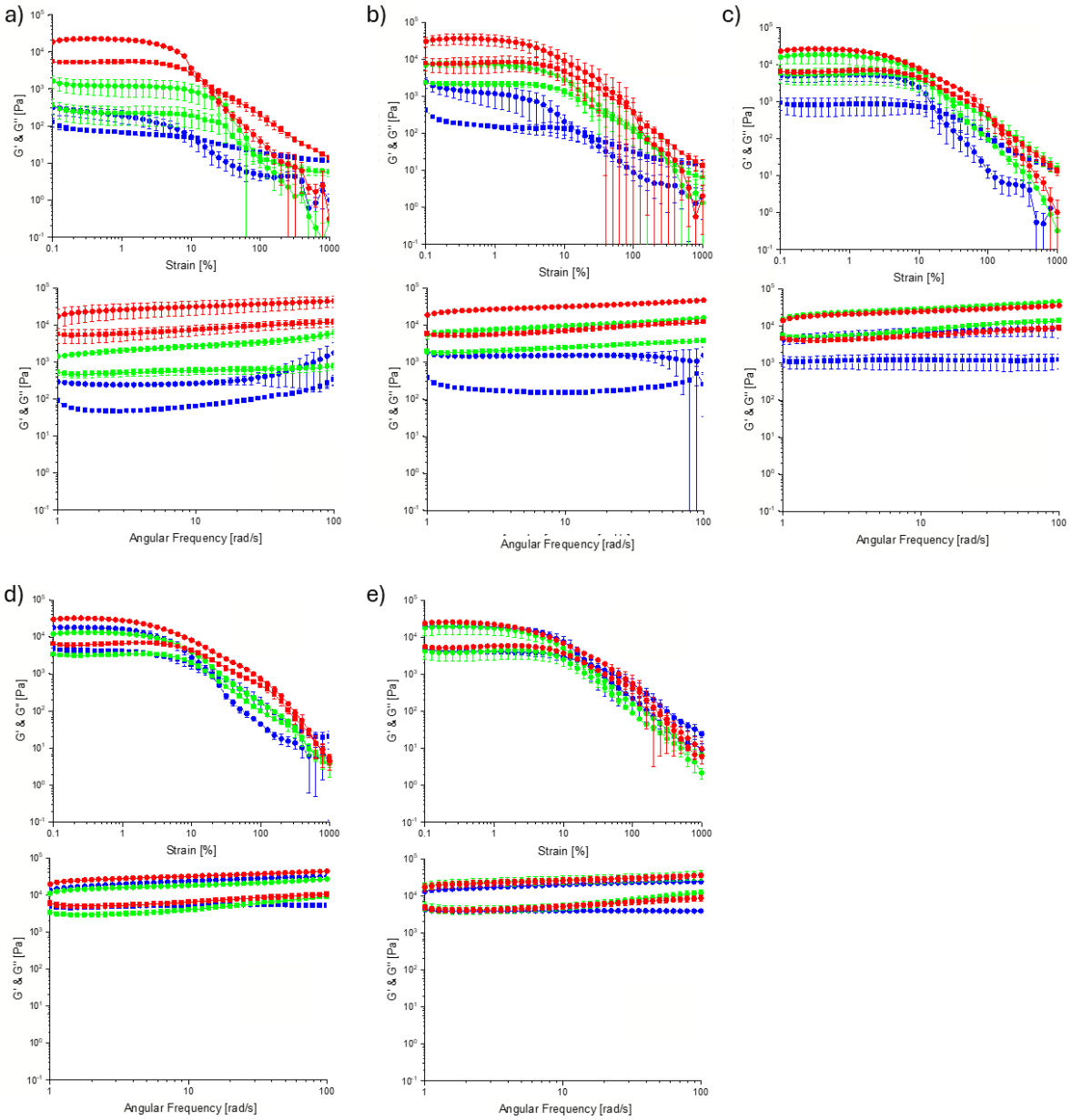

Figure A2.11. Strain (top) and frequency (bottom) sweeps of FmocFA transient systems with methyl formate measured after a) 1 day, b) 3 days, c) 7 days, d) 14 days, and e) 28 days at temperatures of 15 °C (blue), 25 °C (green), and 35 °C (red). Samples were collected in triplicate and averaged. Error bars show the standard deviation between samples.

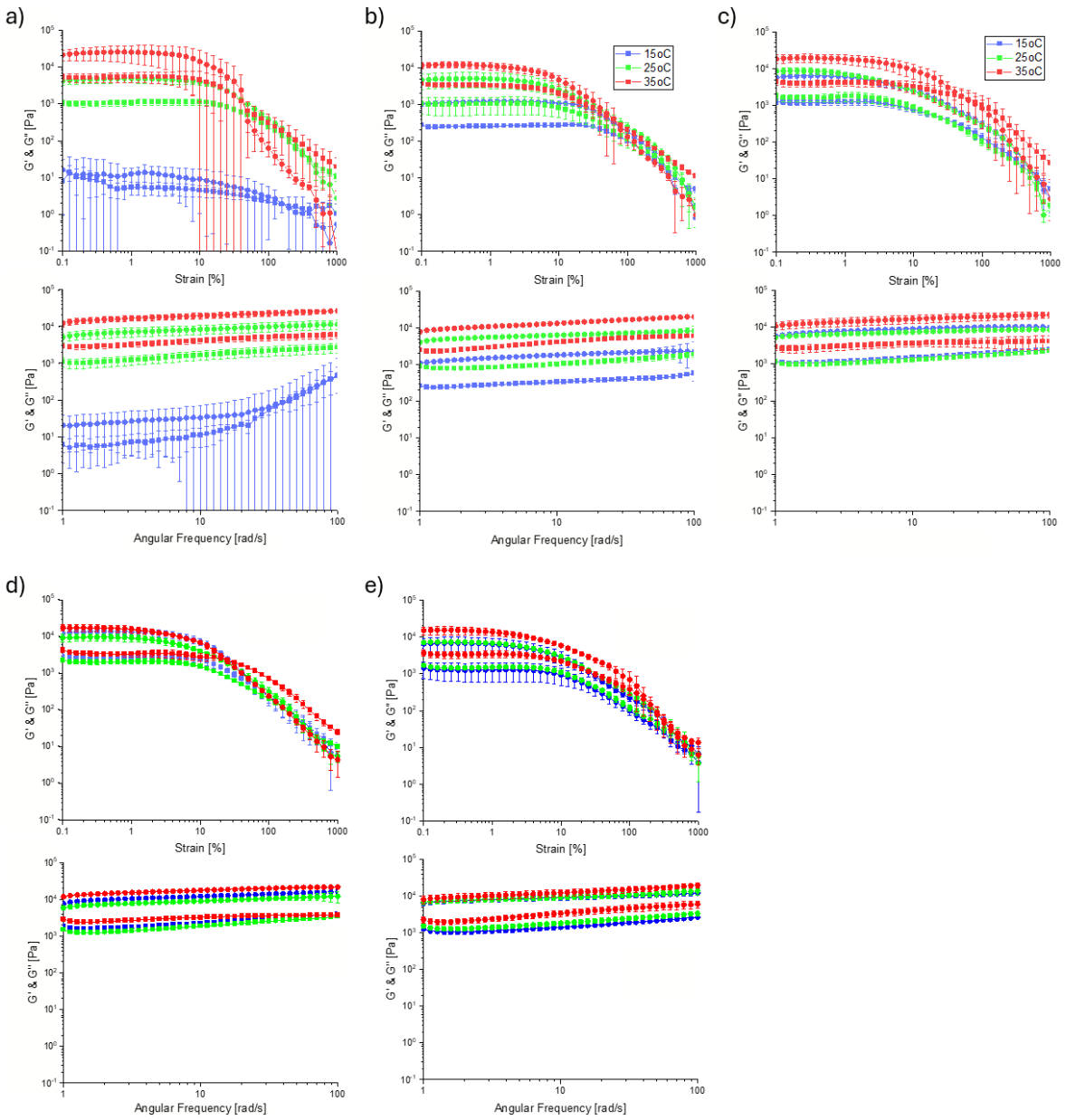

Figure A2.12. Strain (top) and frequency (bottom) sweeps of CarbFV transient systems with methyl formate measured after a) 1 day, b) 3 days, c) 7 days, d) 14 days, and e) 28 days at temperatures of 15 °C (blue), 25 °C (green), and 35 °C (red). Samples were collected in triplicate and averaged. Error bars show the standard deviation between samples.

Appendix 3 - Supplementary data for Chapter 5

3.1. SAXS data for Carb-Ala electrogelation

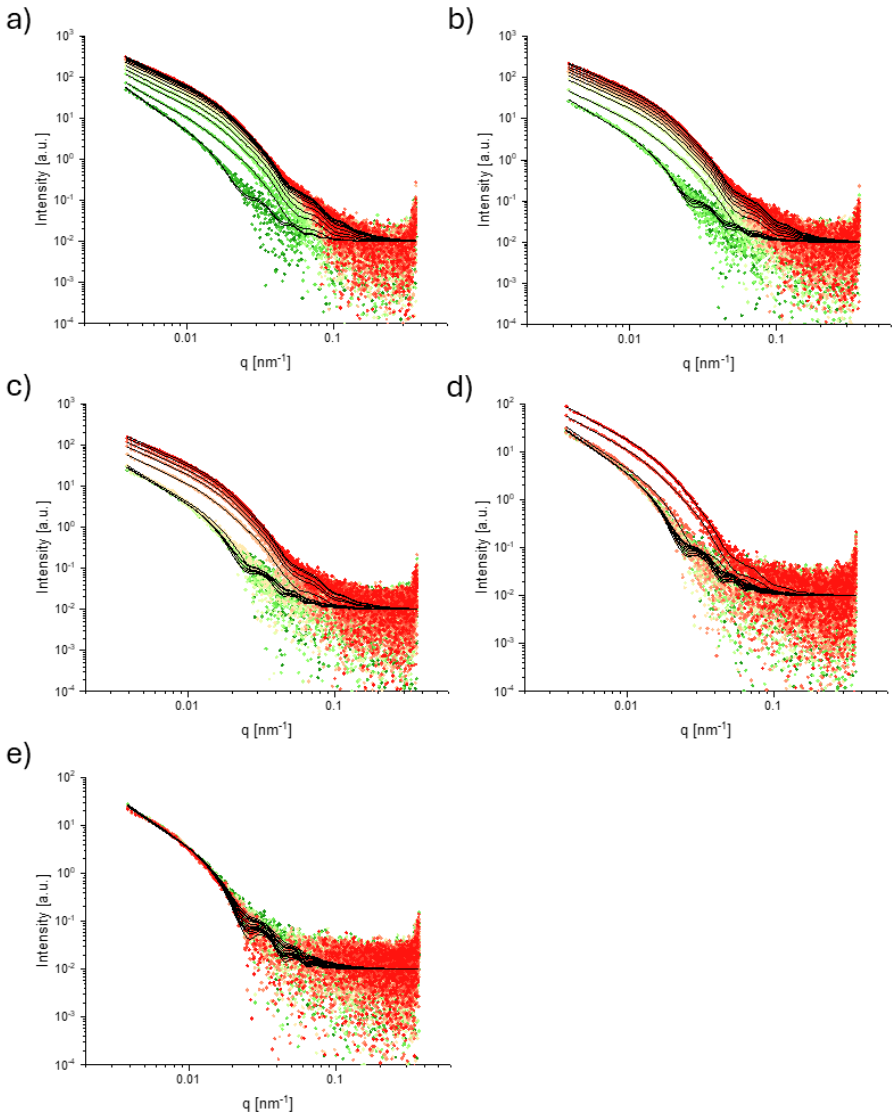

Figure A3.1. SAXS plots for Positions 1–5 (a-e) showing Carb-Ala hydrogel formation over time, with scan colour progressing from light green to red; the fits are overlaid in black.

Table A3.1. Fitting parameters for Carb-Ala SAXS data at Position 1 before the onset of gel formation. The data fit a cylinder with a power-law model. The background and length parameters were not included in the table, as they were fixed at 0.01 cm^{-1} and 1000 Å, respectively.

	A Scale	Radius (Å)	B Scale	B Power	χ^2
Before Current	$1.08 \times 10^{-4} \pm 3.21 \times 10^{-6}$	162.0 ± 1.70	$9.92 \times 10^{-7} \pm 1.47 \times 10^{-7}$	3.17 ± 0.03	2.01
0 s	$1.14 \times 10^{-4} \pm 3.38 \times 10^{-6}$	159.7 ± 1.60	$6.70 \times 10^{-7} \pm 1.19 \times 10^{-7}$	3.23 ± 0.03	1.97

Table A3.2. Fitting parameters for Carb-Ala SAXS data at Position 1 after the onset of gel formation. The data fit an elliptical cylinder with a power-law model. The background and length parameters were not included in the table, as they were fixed at 0.01 cm^{-1} and 1000 Å, respectively.

	A Scale	Radius (Å)	Axis Ratio	B Scale	B Power	χ^2
30 s	$6.46 \times 10^{-4} \pm 1.87 \times 10^{-5}$	63.8 ± 0.47	3.40 ± 0.07	$6.52 \times 10^{-8} \pm 7.56 \times 10^{-8}$	3.64 ± 0.20	1.87
60 s	$1.22 \times 10^{-3} \pm 1.94 \times 10^{-5}$	64.4 ± 0.43	2.68 ± 0.04	$1.47 \times 10^{-6} \pm 5.14 \times 10^{-7}$	3.16 ± 0.06	1.89
90 s	$1.75 \times 10^{-3} \pm 1.87 \times 10^{-5}$	62.9 ± 0.33	2.59 ± 0.03	$4.13 \times 10^{-6} \pm 8.47 \times 10^{-7}$	3.02 ± 0.04	1.83
120 s	$2.32 \times 10^{-3} \pm 1.65 \times 10^{-5}$	63.8 ± 0.27	2.49 ± 0.02	$1.06 \times 10^{-5} \pm 1.25 \times 10^{-6}$	2.88 ± 0.02	1.92
150 s	$2.76 \times 10^{-3} \pm 1.49 \times 10^{-5}$	65.9 ± 0.23	2.39 ± 0.02	$1.92 \times 10^{-5} \pm 1.49 \times 10^{-6}$	2.80 ± 0.01	2.01
180 s	$3.07 \times 10^{-3} \pm 1.45 \times 10^{-5}$	66.8 ± 0.21	2.37 ± 0.01	$2.32 \times 10^{-5} \pm 1.56 \times 10^{-6}$	2.78 ± 0.01	2.00
210 s	$3.26 \times 10^{-3} \pm 1.69 \times 10^{-5}$	67.6 ± 0.20	2.37 ± 0.01	$2.93 \times 10^{-5} \pm 1.69 \times 10^{-6}$	2.75 ± 0.01	2.17
240 s	$3.42 \times 10^{-3} \pm 1.43 \times 10^{-5}$	67.6 ± 0.19	2.35 ± 0.01	$3.07 \times 10^{-5} \pm 1.66 \times 10^{-6}$	2.76 ± 0.01	2.15
270 s	$3.59 \times 10^{-3} \pm 1.41 \times 10^{-5}$	67.8 ± 0.18	2.38 ± 0.01	$3.39 \times 10^{-5} \pm 1.71 \times 10^{-6}$	2.74 ± 0.01	2.21
300 s	$3.76 \times 10^{-3} \pm 1.44 \times 10^{-5}$	67.6 ± 0.18	2.38 ± 0.01	$3.23 \times 10^{-5} \pm 1.65 \times 10^{-6}$	2.76 ± 0.01	2.25

Table A3.3. Fitting parameters for Carb-Ala SAXS data at Position 2 before the onset of gel formation. The data fit a cylinder with a power-law model. The background and length parameters were not included in the table, as they were fixed at 0.01 cm^{-1} and 1000 Å, respectively.

	A Scale	Radius (Å)	B Scale	B Power	χ^2
Before Current	$9.11 \times 10^{-5} \pm 2.80 \times 10^{-6}$	155.8 ± 1.97	$3.75 \times 10^{-6} \pm 6.08 \times 10^{-7}$	2.79 ± 0.03	1.27
0 s	$9.43 \times 10^{-5} \pm 2.83 \times 10^{-6}$	157.1 ± 1.90	$2.58 \times 10^{-6} \pm 4.78 \times 10^{-7}$	2.85 ± 0.04	1.23
30 s	$9.77 \times 10^{-5} \pm 2.96 \times 10^{-6}$	154.4 ± 1.83	$1.77 \times 10^{-6} \pm 3.74 \times 10^{-7}$	2.92 ± 0.04	1.26
60 s	$1.07 \times 10^{-4} \pm 3.15 \times 10^{-6}$	152.2 ± 1.67	$1.03 \times 10^{-6} \pm 2.75 \times 10^{-7}$	3.01 ± 0.05	1.30

Table A3.4. Fitting parameters for Carb-Ala SAXS data at Position 2 after the onset of gel formation. The data fit an elliptical cylinder with a power-law model. The background and length parameters were not included in the table, as they were fixed at 0.01 cm^{-1} and 1000 Å, respectively.

	A Scale	Radius (Å)	Axis Ratio	B Scale	B Power	χ^2
90 s	$5.86 \times 10^{-4} \pm 2.13 \times 10^{-5}$	61.2 ± 0.62	3.39 ± 0.08	$1.82 \times 10^{-7} \pm 3.25 \times 10^{-7}$	3.30 ± 0.31	1.16
120 s	$1.10 \times 10^{-3} \pm 1.54 \times 10^{-5}$	65.3 ± 0.50	2.56 ± 0.04	$3.75 \times 10^{-6} \pm 1.10 \times 10^{-6}$	2.90 ± 0.05	1.20
150 s	$1.44 \times 10^{-3} \pm 1.38 \times 10^{-5}$	65.9 ± 0.39	2.50 ± 0.03	$9.09 \times 10^{-6} \pm 1.54 \times 10^{-6}$	2.79 ± 0.03	1.31
180 s	$1.73 \times 10^{-3} \pm 1.36 \times 10^{-5}$	66.2 ± 0.34	2.42 ± 0.02	$1.33 \times 10^{-5} \pm 1.66 \times 10^{-6}$	2.75 ± 0.02	1.35
210 s	$2.07 \times 10^{-3} \pm 1.34 \times 10^{-5}$	66.0 ± 0.29	2.39 ± 0.02	$2.03 \times 10^{-5} \pm 1.95 \times 10^{-6}$	2.70 ± 0.02	1.38
240 s	$2.43 \times 10^{-3} \pm 1.33 \times 10^{-5}$	66.2 ± 0.25	2.37 ± 0.02	$2.60 \times 10^{-5} \pm 2.09 \times 10^{-6}$	2.67 ± 0.01	1.42
270 s	$2.82 \times 10^{-3} \pm 1.29 \times 10^{-5}$	67.0 ± 0.22	2.32 ± 0.01	$3.37 \times 10^{-5} \pm 2.19 \times 10^{-6}$	2.65 ± 0.01	1.49
300 s	$3.07 \times 10^{-3} \pm 1.32 \times 10^{-5}$	66.8 ± 0.21	2.35 ± 0.01	$3.56 \times 10^{-5} \pm 2.16 \times 10^{-6}$	2.66 ± 0.01	1.56

Table A3.5. Fitting parameters for Carb-Ala SAXS data at Position 3 before the onset of gel formation. The data fit a cylinder with a power-law model. The background and length parameters were not included in the table, as they were fixed at 0.01 cm^{-1} and 1000 Å, respectively.

	A Scale	Radius (Å)	B Scale	B Power	χ^2
Before Current	$8.51 \times 10^{-5} \pm 2.74 \times 10^{-6}$	158.6 ± 2.10	$3.95 \times 10^{-6} \pm 6.16 \times 10^{-7}$	2.78 ± 0.03	1.07
0 s	$8.76 \times 10^{-5} \pm 2.76 \times 10^{-6}$	158.7 ± 2.04	$3.39 \times 10^{-6} \pm 5.65 \times 10^{-7}$	2.80 ± 0.03	0.97
30 s	$9.42 \times 10^{-5} \pm 2.85 \times 10^{-6}$	158.3 ± 1.90	$1.94 \times 10^{-6} \pm 3.96 \times 10^{-7}$	2.90 ± 0.04	1.02
60 s	$9.18 \times 10^{-5} \pm 2.95 \times 10^{-6}$	156.0 ± 1.95	$1.58 \times 10^{-6} \pm 3.41 \times 10^{-7}$	2.95 ± 0.04	1.02
90 s	$1.00 \times 10^{-4} \pm 2.83 \times 10^{-6}$	155.8 ± 1.71	$1.41 \times 10^{-6} \pm 3.48 \times 10^{-7}$	2.93 ± 0.05	1.04
120 s	$1.03 \times 10^{-4} \pm 3.00 \times 10^{-6}$	156.0 ± 1.66	$9.01 \times 10^{-7} \pm 2.56 \times 10^{-7}$	3.02 ± 0.05	1.14
150 s	$1.20 \times 10^{-4} \pm 3.50 \times 10^{-6}$	133.4 ± 1.43	$2.05 \times 10^{-6} \pm 4.35 \times 10^{-7}$	2.92 ± 0.04	1.12

Table A3.6. Fitting parameters for Carb-Ala SAXS data at Position 3 after the onset of gel formation. The data fit an elliptical cylinder with a power-law model. The background and length parameters were not included in the table, as they were fixed at 0.01 cm^{-1} and 1000 Å, respectively.

	A Scale	Radius (Å)	Axis Ratio	B Scale	B Power	χ^2
180 s	$6.86 \times 10^{-4} \pm 1.69 \times 10^{-5}$	64.0 ± 0.73	2.86 ± 0.06	$1.56 \times 10^{-6} \pm 8.69 \times 10^{-7}$	2.99 ± 0.10	0.96
210 s	$1.12 \times 10^{-3} \pm 1.32 \times 10^{-5}$	66.8 ± 0.49	2.49 ± 0.03	$8.92 \times 10^{-6} \pm 1.59 \times 10^{-6}$	2.76 ± 0.03	1.04
240 s	$1.48 \times 10^{-3} \pm 1.32 \times 10^{-5}$	67.0 ± 0.39	2.43 ± 0.03	$1.16 \times 10^{-5} \pm 1.62 \times 10^{-6}$	2.75 ± 0.02	1.15
270 s	$1.84 \times 10^{-3} \pm 1.25 \times 10^{-5}$	67.6 ± 0.32	2.34 ± 0.02	$2.10 \times 10^{-5} \pm 1.92 \times 10^{-6}$	2.69 ± 0.02	1.19
300 s	$2.13 \times 10^{-3} \pm 1.28 \times 10^{-5}$	67.4± 0.28	2.35± 0.02	$2.21 \times 10^{-5} \pm 1.91 \times 10^{-6}$	2.69 ± 0.02	1.24

Table A3.7. Fitting parameters for Carb-Ala SAXS data at Position 4 before the onset of gel formation. The data fit a cylinder with a power-law model. The background and length parameters were not included in the table, as they were fixed at 0.01 cm^{-1} and 1000 Å, respectively.

	A Scale	Radius (Å)	B Scale	B Power	χ^2
Before Current	$9.07 \times 10^{-5} \pm 2.67 \times 10^{-6}$	161.2 ± 1.96	$6.68 \times 10^{-6} \pm 9.41 \times 10^{-7}$	2.67 ± 0.03	0.97
0 s	$8.89 \times 10^{-5} \pm 2.73 \times 10^{-6}$	158.9 ± 2.01	$4.26 \times 10^{-6} \pm 6.83 \times 10^{-7}$	2.75 ± 0.03	0.91
30 s	$8.98 \times 10^{-5} \pm 2.72 \times 10^{-6}$	160.3 ± 1.99	$3.39 \times 10^{-6} \pm 5.77 \times 10^{-7}$	2.80 ± 0.03	0.94
60 s	$9.01 \times 10^{-5} \pm 2.77 \times 10^{-6}$	159.1 ± 1.99	$2.76 \times 10^{-6} \pm 5.08 \times 10^{-7}$	2.83 ± 0.04	0.91
90 s	$9.50 \times 10^{-5} \pm 2.76 \times 10^{-6}$	161.4 ± 1.89	$2.13 \times 10^{-6} \pm 4.35 \times 10^{-7}$	2.87 ± 0.04	0.97
120 s	$1.01 \times 10^{-4} \pm 2.96 \times 10^{-6}$	156.8 ± 1.77	$1.19 \times 10^{-6} \pm 3.07 \times 10^{-7}$	2.97 ± 0.05	0.98
150 s	$9.66 \times 10^{-5} \pm 2.81 \times 10^{-6}$	163.4 ± 1.86	$1.31 \times 10^{-6} \pm 3.03 \times 10^{-7}$	2.96 ± 0.04	1.01
180 s	$1.03 \times 10^{-4} \pm 3.08 \times 10^{-6}$	156.9 ± 1.73	$7.54 \times 10^{-7} \pm 2.28 \times 10^{-7}$	3.05 ± 0.06	0.95
210 s	$1.03 \times 10^{-4} \pm 3.06 \times 10^{-6}$	160.6 ± 1.72	$5.32 \times 10^{-7} \pm 1.83 \times 10^{-7}$	3.11 ± 0.06	0.98
240 s	$1.40 \times 10^{-4} \pm 3.56 \times 10^{-6}$	131.9 ± 1.28	$3.14 \times 10^{-6} \pm 5.73 \times 10^{-7}$	2.85 ± 0.03	1.08

Table A3.8. Fitting parameters for Carb-Ala SAXS data at Position 4 after the onset of gel formation. The data fit an elliptical cylinder with a power-law model. The background and length parameters were not included in the table, as they were fixed at 0.01 cm^{-1} and 1000 Å, respectively.

	A Scale	Radius (Å)	Axis Ratio	B Scale	B Power	χ^2
270 s	$6.90 \times 10^{-4} \pm 1.67 \times 10^{-5}$	64.0 ± 0.73	2.81 ± 0.06	$1.44 \times 10^{-6} \pm 8.58 \times 10^{-7}$	2.99 ± 0.10	0.92
300 s	$1.09 \times 10^{-3} \pm 1.34 \times 10^{-5}$	66.5 ± 0.51	2.45 ± 0.03	$7.56 \times 10^{-6} \pm 1.48 \times 10^{-6}$	2.78 ± 0.03	0.99

Table A3.9. Fitting parameters for Carb-Ala SAXS data at Position 5. The data fit a cylinder with a power-law model. The background and length parameters were not included in the table, as they were fixed at 0.01 cm^{-1} and 1000 Å, respectively.

	A Scale	Radius (Å)	B Scale	B Power	χ^2
Before Current	$8.27 \times 10^{-5} \pm 2.69 \times 10^{-6}$	158.2 ± 2.14	$6.48 \times 10^{-6} \pm 9.42 \times 10^{-7}$	2.67 ± 0.03	0.85
0 s	$8.38 \times 10^{-5} \pm 2.68 \times 10^{-6}$	159.0 ± 2.11	$4.97 \times 10^{-6} \pm 8.00 \times 10^{-7}$	2.71 ± 0.03	0.86
30 s	$8.58 \times 10^{-5} \pm 2.72 \times 10^{-6}$	160.2 ± 2.08	$3.36 \times 10^{-6} \pm 5.82 \times 10^{-7}$	2.79 ± 0.03	0.94
60 s	$8.84 \times 10^{-5} \pm 2.68 \times 10^{-6}$	161.7 ± 2.01	$3.09 \times 10^{-6} \pm 5.87 \times 10^{-7}$	2.79 ± 0.04	0.91
90 s	$9.43 \times 10^{-5} \pm 2.81 \times 10^{-6}$	158.4 ± 1.90	$1.97 \times 10^{-6} \pm 4.44 \times 10^{-7}$	2.87 ± 0.04	0.89
120 s	$9.75 \times 10^{-5} \pm 2.87 \times 10^{-6}$	159.1 ± 1.83	$1.26 \times 10^{-6} \pm 3.35 \times 10^{-7}$	2.94 ± 0.05	0.92
150 s	$9.81 \times 10^{-5} \pm 2.85 \times 10^{-6}$	161.5 ± 1.82	$9.82 \times 10^{-7} \pm 2.84 \times 10^{-7}$	2.98 ± 0.05	0.94
180 s	$1.00 \times 10^{-4} \pm 2.92 \times 10^{-6}$	162.4 ± 1.78	$6.68 \times 10^{-7} \pm 2.25 \times 10^{-7}$	3.05 ± 0.06	0.95
210 s	$1.02 \times 10^{-4} \pm 3.00 \times 10^{-6}$	160.6 ± 1.74	$5.51 \times 10^{-7} \pm 2.07 \times 10^{-7}$	3.07 ± 0.07	0.93
240 s	$1.01 \times 10^{-4} \pm 3.00 \times 10^{-6}$	162.8 ± 1.76	$4.46 \times 10^{-7} \pm 1.73 \times 10^{-7}$	3.12 ± 0.07	0.98
270 s	$1.02 \times 10^{-4} \pm 3.24 \times 10^{-6}$	159.7 ± 1.71	$2.75 \times 10^{-7} \pm 1.23 \times 10^{-7}$	3.22 ± 0.08	0.99
300 s	$1.10 \times 10^{-4} \pm 3.58 \times 10^{-6}$	157.6 ± 1.54	$1.05 \times 10^{-7} \pm 7.22 \times 10^{-8}$	3.37 ± 0.12	0.97

3.2. SAXS data for Carb-Gly electrogelation

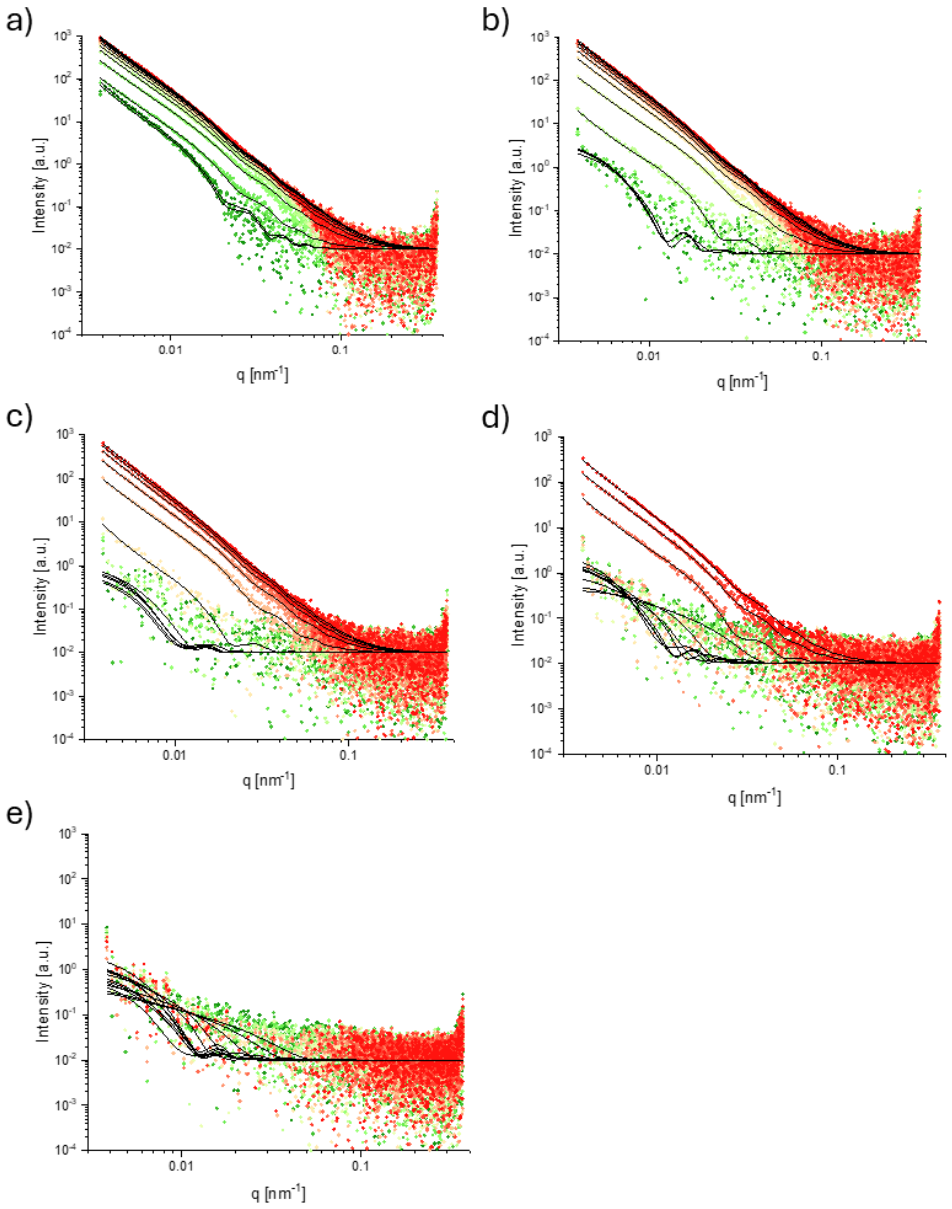

Figure A3.2. SAXS plots for Positions 1–5 (a-e) showing Carb-Gly hydrogel formation over time, with scan colour progressing from light green to red; the fits are overlaid in black.

Table A3.10. Fitting parameters for Carb-Gly SAXS data at Position 1 before the onset of gel formation. The data fit a cylinder with a power-law model. The background and length parameters were not included in the table, as they were fixed at 0.01 cm^{-1} and 1000 Å, respectively.

	A Scale	Radius (Å)	B Scale	B Power	χ^2
Before Current	$8.74 \times 10^{-5} \pm 3.81 \times 10^{-6}$	185.1 ± 2.04	$4.34 \times 10^{-8} \pm 1.03 \times 10^{-8}$	3.82 ± 0.04	1.94

Table A3.11. Fitting parameters for Carb-Gly SAXS data at Position 1 after the onset of gel formation. The data fit a cylinder with a power-law model. The background and length parameters were not included in the table, as they were fixed at 0.01 cm^{-1} and 1000 Å, respectively.

	A Scale	Radius (Å)	B Scale	B Power	χ^2
0 s	$8.62 \times 10^{-5} \pm 3.91 \times 10^{-6}$	184.1 ± 1.99	$2.43 \times 10^{-8} \pm 7.84 \times 10^{-8}$	$3.89 \pm 5.80 \times 10^{-2}$	2.05
30 s	$1.14 \times 10^{-4} \pm 3.96 \times 10^{-6}$	150.1 ± 1.67	$1.24 \times 10^{-6} \pm 1.17 \times 10^{-7}$	$3.27 \pm 1.72 \times 10^{-2}$	2.08
60 s	$2.11x\ 10^{-4} \pm 4.80 \times 10^{-6}$	143.3 ± 1.08	$9.84 \times 10^{-6} \pm 2.79 \times 10^{-7}$	$3.06 \pm 5.30 \times 10^{-3}$	2.32
90 s	$2.90 \times 10^{-4} \pm 4.80 \times 10^{-6}$	147.2 ± 0.90	$1.48 \times 10^{-5} \pm 2.62 \times 10^{-7}$	$3.01 \pm 3.33 \times 10^{-3}$	2.57
120 s	$3.50 \times 10^{-4} \pm 5.07 \times 10^{-6}$	149.4 ± 0.80	$1.87 \times 10^{-5} \pm 2.69 \times 10^{-7}$	$3.10 \pm 2.72 \times 10^{-3}$	2.68
150 s	$4.21 \times 10^{-4} \pm 5.34 \times 10^{-6}$	148.9 ± 0.70	$2.16 \times 10^{-5} \pm 2.72 \times 10^{-7}$	$3.10 \pm 2.39 \times 10^{-3}$	3.09
180 s	$4.79 \times 10^{-4} \pm 5.54 \times 10^{-6}$	149.0 ± 0.63	$2.16 \times 10^{-5} \pm 2.56 \times 10^{-7}$	$3.12 \pm 2.25 \times 10^{-3}$	3.32
210 s	$5.03 \times 10^{-4} \pm 5.59 \times 10^{-6}$	152.3 ± 0.62	$2.15 \times 10^{-5} \pm 2.43 \times 10^{-7}$	$3.14 \pm 2.14 \times 10^{-3}$	3.35
240 s	$5.31 \times 10^{-4} \pm 5.68 \times 10^{-6}$	152.5 ± 0.60	$2.10 \times 10^{-5} \pm 2.32 \times 10^{-7}$	$3.15 \pm 2.10 \times 10^{-3}$	3.44
270 s	$5.41 \times 10^{-4} \pm 5.82 \times 10^{-6}$	150.5 ± 0.59	$2.05 \times 10^{-5} \pm 2.27 \times 10^{-7}$	$3.16 \pm 2.09 \times 10^{-3}$	3.53
300 s	$5.71 \times 10^{-4} \pm 5.83 \times 10^{-6}$	152.7 ± 0.56	$2.04 \times 10^{-5} \pm 2.04 \times 10^{-7}$	$3.17 \pm 2.04 \times 10^{-3}$	3.64

Table A3.12. Fitting parameters for Carb-Gly SAXS data at Position 2 before the onset of gel formation. The data fit a cylinder model. The background and length parameters were not included in the table, as they were fixed at 0.01 cm^{-1} and 1000 Å, respectively.

	Scale	Radius (Å)	χ^2
Before Current	$7.57 \times 10^{-6} \pm 6.84 \times 10^{-7}$	330.8 ± 21.5	1.22
0 s	$7.15 \times 10^{-6} \pm 6.92 \times 10^{-7}$	299.9 ± 21.3	1.27
30 s	$8.11 \times 10^{-6} \pm 6.83 \times 10^{-7}$	328.0 ± 19.9	1.32
60 s	$7.50 \times 10^{-6} \pm 6.82 \times 10^{-7}$	330.2 ± 21.6	1.43

Table A3.13. Fitting parameters for Carb-Gly SAXS data at Position 2 after the onset of gel formation. The data fit a cylinder with a power-law model. The background and length parameters were not included in the table, as they were fixed at 0.01 cm^{-1} and 1000 Å, respectively.

	A Scale	Radius (Å)	B Scale	B Power	χ^2
90 s	$3.87 \times 10^{-5} \pm 4.19 \times 10^{-6}$	145.7 ± 3.71	$6.91 \times 10^{-9} \pm 8.39 \times 10^{-9}$	3.89 ± 0.22	1.39
120 s	$1.31 \times 10^{-4} \pm 5.12 \times 10^{-6}$	118.4 ± 1.42	$3.30 \times 10^{-6} \pm 2.56 \times 10^{-7}$	$3.12 \pm 1.42 \times 10^{-3}$	1.54
150 s	$1.70 \times 10^{-4} \pm 4.79 \times 10^{-6}$	137.8 ± 1.34	$8.04 \times 10^{-6} \pm 2.27 \times 10^{-7}$	$3.14 \pm 5.22 \times 10^{-3}$	1.68
180 s	$2.09 \times 10^{-4} \pm 4.87 \times 10^{-6}$	146.6 ± 1.21	$1.03 \times 10^{-5} \pm 2.00 \times 10^{-7}$	$3.17 \pm 3.64 \times 10^{-3}$	1.73
210 s	$2.49 \times 10^{-4} \pm 5.18 \times 10^{-6}$	146.9 ± 1.07	$1.09 \times 10^{-5} \pm 1.83 \times 10^{-7}$	$3.20 \pm 3.14 \times 10^{-3}$	1.88
240 s	$2.73 \times 10^{-4} \pm 5.28 \times 10^{-6}$	150.4 ± 1.03	$1.15 \times 10^{-5} \pm 1.72 \times 10^{-7}$	$3.22 \pm 2.80 \times 10^{-3}$	1.90
270 s	$3.02 \times 10^{-4} \pm 5.48 \times 10^{-6}$	149.7 ± 0.95	$1.12 \times 10^{-5} \pm 1.61 \times 10^{-7}$	$3.24 \pm 2.68 \times 10^{-3}$	1.96
300 s	$3.17 \times 10^{-4} \pm 5.63 \times 10^{-6}$	149.1 ± 0.92	$1.14 \times 10^{-5} \pm 1.58 \times 10^{-7}$	$3.25 \pm 2.60 \times 10^{-3}$	2.04

Table A3.14. Fitting parameters for Carb-Gly SAXS data at Position 3 before the onset of gel formation. The data fit a cylinder model. The background and length parameters were not included in the table, as they were fixed at 0.01 cm^{-1} and 1000 Å, respectively.

	Scale	Radius (Å)	χ^2
Before Current	$2.28 \times 10^{-6} \pm 6.84 \times 10^{-7}$	309.5 ± 67.9	1.07
0 s	$1.22 \times 10^{-6} \pm 6.79 \times 10^{-7}$	355.1 ± 140.3	0.95
30 s	$1.06x\ 10^{-6} \pm 6.79 \times 10^{-7}$	362.2 ± 162.8	1.04
60 s	$1.59 \times 10^{-6} \pm 6.78 \times 10^{-7}$	346.6 ± 105.3	1.04
90 s	$1.88 \times 10^{-6} \pm 6.80 \times 10^{-7}$	360.7 ± 91.8	1.18
120 s	$1.72 \times 10^{-6} \pm 6.77 \times 10^{-7}$	350.6 ± 98.5	1.20

Table A3.15. Fitting parameters for Carb-Gly SAXS data at Position 3 after the onset of gel formation. The data fit a cylinder with a power-law model. The background and length parameters were not included in the table, as they were fixed at 0.01 cm^{-1} and 1000 Å, respectively.

	A Scale	Radius (Å)	B Scale	B Power	χ^2
150 s	$1.34 \times 10^{-5} \pm 3.56 \times 10^{-6}$	177.9 ± 11.2	$9.64 \times 10^{-11} \pm 4.30 \times 10^{-10}$	4.50 ± 0.81	1.28
180 s	$1.01 \times 10^{-4} \pm 4.72 \times 10^{-6}$	133.4 ± 1.74	$7.93 \times 10^{-7} \pm 1.03 \times 10^{-7}$	$3.33 \pm 2.36 \times 10^{-2}$	1.23
210 s	$1.39 \times 10^{-4} \pm 4.85 \times 10^{-6}$	136.1 ± 1.51	$3.53 \times 10^{-6} \pm 1.53 \times 10^{-7}$	$3.24 \pm 7.97 \times 10^{-3}$	1.27
240 s	$1.73 \times 10^{-4} \pm 4.95 \times 10^{-6}$	143.3 ± 1.36	$5.38 \times 10^{-6} \pm 1.44 \times 10^{-7}$	$3.26 \pm 4.93 \times 10^{-3}$	1.34
270 s	$1.93 \times 10^{-4} \pm 5.16 \times 10^{-6}$	145.2 ± 1.30	$6.77 \times 10^{-6} \pm 1.44 \times 10^{-7}$	$3.26 \pm 3.93 \times 10^{-3}$	1.39
300 s	$2.18 \times 10^{-4} \pm 5.06 \times 10^{-6}$	153.0 ± 1.22	$7.87 \times 10^{-6} \pm 1.38 \times 10^{-7}$	$3.27 \pm 3.27 \times 10^{-3}$	1.46

Table A3.16. Fitting parameters for Carb-Gly SAXS data at Position 4 before the onset of gel formation. The data fit a cylinder model. The background and length parameters were not included in the table, as they were fixed at 0.01 cm^{-1} and 1000 Å, respectively.

	Scale	Radius (Å)	χ^2
Before Current	$1.46 \times 10^{-5} \pm 2.18 \times 10^{-6}$	88.7 ± 9.8	0.91
0 s	$4.39 \times 10^{-6} \pm 6.89 \times 10^{-7}$	369.8 ± 40.6	0.92
30 s	$4.73 \times 10^{-6} \pm 7.23 \times 10^{-7}$	261.5 ± 29.6	0.91
60 s	$6.69 \times 10^{-6} \pm 9.94 \times 10^{-7}$	162.0 ± 18.1	0.90
90 s	$3.53 \times 10^{-6} \pm 6.81 \times 10^{-7}$	329.5 ± 46.0	0.86
120 s	$3.94 \times 10^{-6} \pm 7.80 \times 10^{-7}$	224.5 ± 33.1	0.94
150 s	$3.46 \times 10^{-6} \pm 6.79 \times 10^{-7}$	329.7 ± 46.7	1.02
180 s	$3.67 \times 10^{-6} \pm 6.81 \times 10^{-7}$	330.3 ± 44.2	1.01
210 s	$4.24 \times 10^{-6} \pm 6.82 \times 10^{-7}$	323.1 ± 37.7	1.07

Table A3.17. Fitting parameters for Carb-Gly SAXS data at Position 4 after the onset of gel formation. The data fit a cylinder with a power-law model. The background and length parameters were not included in the table, as they were fixed at 0.01 cm^{-1} and 1000 Å, respectively.

	A Scale	Radius (Å)	B Scale	B Power	χ^2
240 s	$6.59 \times 10^{-5} \pm 4.59 \times 10^{-6}$	137.7 ± 2.27	$4.88 \times 10^{-8} \pm 2.24 \times 10^{-8}$	3.68 ± 0.08	1.04
270 s	$1.18 \times 10^{-4} \pm 4.85 \times 10^{-6}$	135.8 ± 1.58	$1.19 \times 10^{-6} \pm 9.79 \times 10^{-8}$	3.35 ± 0.02	1.05
300 s	$1.48 \times 10^{-4} \pm 4.88 \times 10^{-6}$	142.3 ± 1.46	$2.77 \times 10^{-6} \pm 1.10 \times 10^{-7}$	3.32 ± 0.01	1.16

Table A3.18. Fitting parameters for Carb-Gly SAXS data at Position 5. The data fit a cylinder model. The background and length parameters were not included in the table, as they were fixed at 0.01 cm^{-1} and 1000 Å, respectively.

	Scale	Radius (Å)	χ^2
Before Current	$1.71 \times 10^{-5} \pm 3.77 \times 10^{-6}$	64.1 ± 9.7	0.87
0 s	$9.69 \times 10^{-6} \pm 2.13 \times 10^{-6}$	90.0 ± 14.6	0.83
30 s	$6.06 \times 10^{-6} \pm 1.19 \times 10^{-6}$	135.5 ± 20.0	0.81
60 s	$5.00 \times 10^{-6} \pm 8.34 \times 10^{-7}$	203.3 ± 25.3	0.82
90 s	$3.08 \times 10^{-6} \pm 6.82 \times 10^{-7}$	324.4 ± 51.9	0.85
120 s	$2.95 \times 10^{-6} \pm 6.85 \times 10^{-7}$	312.0 ± 52.9	0.82
150 s	$4.24 \times 10^{-6} \pm 7.38 \times 10^{-7}$	250.3 ± 32.4	0.84
180 s	$1.65 \times 10^{-6} \pm 6.86 \times 10^{-7}$	306.8 ± 93.5	0.92
210 s	$1.90 \times 10^{-6} \pm 6.89 \times 10^{-7}$	298.7 ± 79.3	0.94
240 s	$1.94 \times 10^{-6} \pm 6.82 \times 10^{-7}$	319.7 ± 81.8	1.03
270 s	$1.05 \times 10^{-6} \pm 6.84 \times 10^{-7}$	366.2 ± 166.4	1.04
300 s	$4.39 \times 10^{-6} \pm 6.84 \times 10^{-7}$	329.8 ± 37.1	1.10

3.3. SAXS data for Carb-Val electrogelation

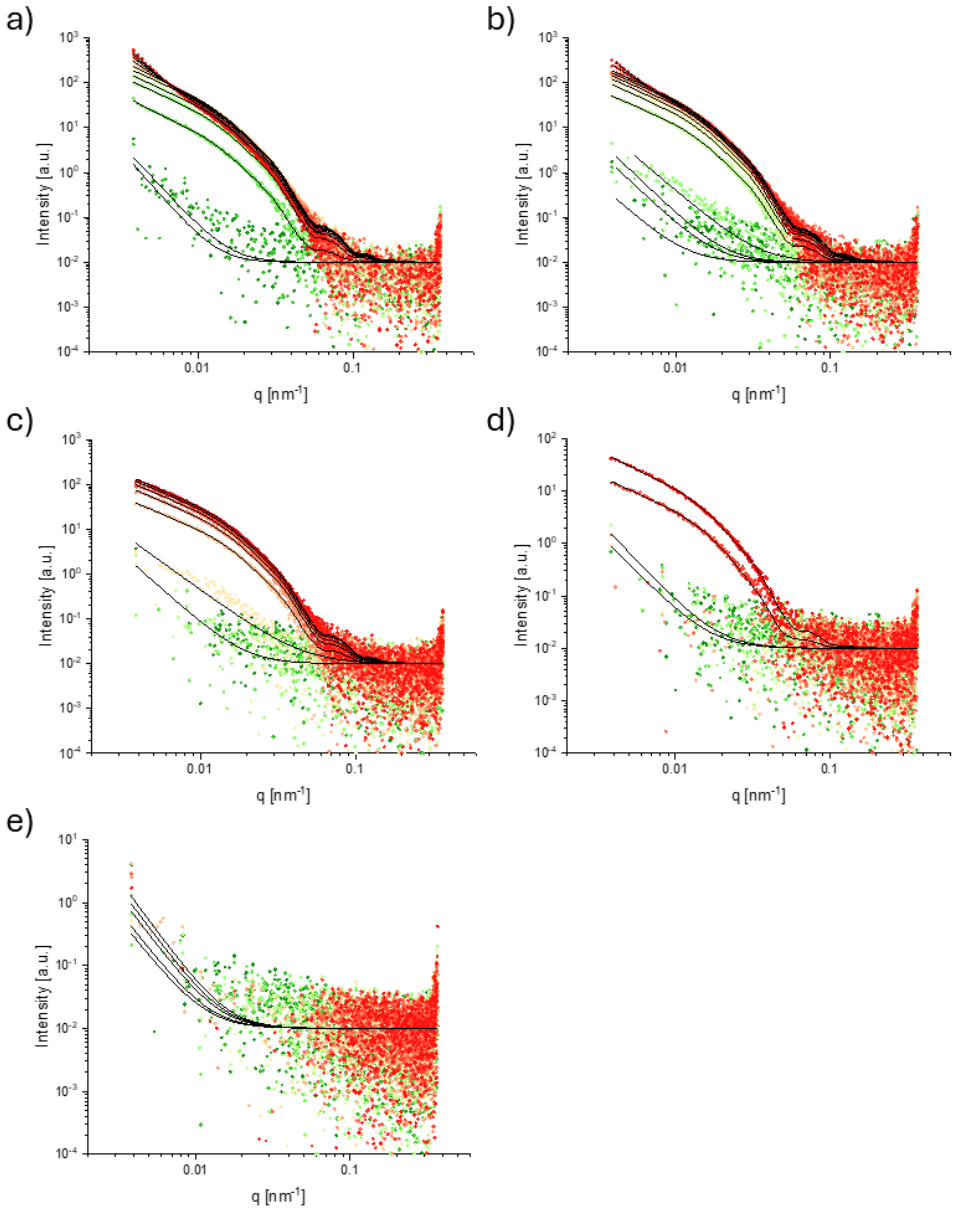

Figure A3.3. SAXS plots for Positions 1–5 (a-e) showing Carb-Val hydrogel formation over time, with scan colour progressing from light green to red; the fits are overlaid in black.

Table A3.19. Fitting parameters for Carb-Val SAXS data at Position 1 after the onset of gel formation. The data fit an elliptical cylinder with a power-law model. The background and length parameters were not included in the table, as they were fixed at 0.01 cm^{-1} and 1000 Å, respectively.

	A Scale	Radius (Å)	Axis Ratio	B Scale	B Power	χ^2
30 s	$4.48 \times 10^{-4} \pm 1.22 \times 10^{-5}$	67.4 ± 0.64	2.86 ± 0.08	$7.06 \times 10^{-9} \pm 2.03 \times 10^{-8}$	3.87 ± 0.51	2.60
60 s	$1.33 \times 10^{-3} \pm 1.97 \times 10^{-5}$	65.6 ± 0.27	2.93 ± 0.04	$1.11 \times 10^{-7} \pm 1.39 \times 10^{-7}$	3.51 ± 0.22	2.81
90 s	$1.84 \times 10^{-3} \pm 2.11 \times 10^{-5}$	64.7 ± 0.23	2.91 ± 0.03	$3.10 \times 10^{-7} \pm 2.44 \times 10^{-7}$	3.38 ± 0.14	2.92
120 s	$2.47 \times 10^{-3} \pm 2.15 \times 10^{-5}$	64.3 ± 0.20	2.92 ± 0.02	$7.02 \times 10^{-7} \pm 3.61 \times 10^{-7}$	3.29 ± 0.09	2.97
150 s	$2.67 \times 10^{-3} \pm 2.21 \times 10^{-5}$	64.4 ± 0.19	2.85 ± 0.02	$8.94 \times 10^{-7} \pm 3.14 \times 10^{-7}$	3.33 ± 0.06	3.02
180 s	$2.41 \times 10^{-3} \pm 2.18 \times 10^{-5}$	64.3 ± 0.18	2.72 ± 0.02	$6.20 \times 10^{-7} \pm 1.57 \times 10^{-7}$	3.51 ± 0.05	2.89
210 s	$2.16 \times 10^{-3} \pm 1.98 \times 10^{-5}$	64.4 ± 0.19	2.62 ± 0.02	$4.37 \times 10^{-7} \pm 8.64 \times 10^{-8}$	3.63 ± 0.04	2.79
240 s	$1.97 \times 10^{-3} \pm 1.72 \times 10^{-5}$	64.1 ± 0.19	2.63 ± 0.02	$2.26 \times 10^{-7} \pm 4.04 \times 10^{-8}$	3.79 ± 0.03	2.81
270 s	$1.67 \times 10^{-3} \pm 1.51 \times 10^{-5}$	64.4 ± 0.22	2.57 ± 0.03	$1.49 \times 10^{-7} \pm 2.25 \times 10^{-8}$	3.90 ± 0.03	2.73
300 s	$1.36 \times 10^{-3} \pm 1.27 \times 10^{-5}$	65.0 ± 0.26	2.54 ± 0.03	$9.15 \times 10^{-8} \pm 1.15 \times 10^{-8}$	4.02 ± 0.02	2.79

Table A3.20. Fitting parameters for Carb-Val SAXS data at Position 2 after the onset of gel formation. The data fit an elliptical cylinder with a power-law model. The background and length parameters were not included in the table, as they were fixed at 0.01 cm^{-1} and 1000 Å, respectively.

	A Scale	Radius (Å)	Axis Ratio	B Scale	B Power	χ^2
90 s	$7.33 \times 10^{-4} \pm 1.61 \times 10^{-5}$	64. 5± 0.41	2.95 ± 0.07	$1.89 \times 10^{-8} \pm 6.44 \times 10^{-8}$	3.65 ± 0.60	1.96
120 s	$1.25 \times 10^{-3} \pm 2.00 \times 10^{-5}$	64.3 ± 0.32	2.91 ± 0.04	$1.77 \times 10^{-7} \pm 2.25 \times 10^{-7}$	3.39 ± 0.22	2.00
150 s	$1.64 \times 10^{-3} \pm 2.03 \times 10^{-5}$	64.3 ± 0.28	2.89 ± 0.03	$4.31 \times 10^{-7} \pm 3.44 \times 10^{-7}$	3.29 ± 0.14	2.16
180 s	$1.98 \times 10^{-3} \pm 2.03 \times 10^{-5}$	63.7 ± 0.25	2.89 ± 0.03	$7.55 \times 10^{-7} \pm 4.54 \times 10^{-7}$	3.21 ± 0.11	2.23
210 s	$2.31 \times 10^{-3} \pm 2.02 \times 10^{-5}$	63.1 ± 0.23	2.87 ± 0.02	$1.23 \times 10^{-6} \pm 5.52 \times 10^{-7}$	3.16 ± 0.08	2.30
240 s	$2.55 \times 10^{-3} \pm 2.12 \times 10^{-5}$	62.1 ± 0.21	2.91 ± 0.02	$1.47 \times 10^{-6} \pm 5.56 \times 10^{-7}$	3.17 ± 0.07	2.24
270 s	$2.25 \times 10^{-3} \pm 2.26 \times 10^{-5}$	61.5 ± 0.25	2.80 ± 0.02	$1.31 \times 10^{-6} \pm 3.06 \times 10^{-7}$	3.34 ± 0.04	2.26
300 s	$1.86 \times 10^{-3} \pm 1.97 \times 10^{-5}$	61.8 ± 0.23	2.58 ± 0.03	$7.12 \times 10^{-7} \pm 1.25 \times 10^{-7}$	3.54 ± 0.03	2.26

Table A3.21. Fitting parameters for Carb-Val SAXS data at Position 3 after the onset of gel formation. The data fit an elliptical cylinder with a power-law model. The background and length parameters were not included in the table, as they were fixed at 0.01 cm^{-1} and 1000 Å, respectively.

	A Scale	Radius (Å)	Axis Ratio	B Scale	B Power	χ^2
180 s	$6.61 \times 10^{-4} \pm 1.69 \times 10^{-5}$	60.1 ± 0.54	2.77 ± 0.06	$5.30 \times 10^{-8} \pm 1.53 \times 10^{-7}$	3.44 ± 0.51	1.62
210 s	$1.21 \times 10^{-3} \pm 2.04 \times 10^{-5}$	60.3 ± 0.34	2.88 ± 0.04	$1.83 \times 10^{-7} \pm 2.77 \times 10^{-7}$	3.34 ± 0.27	1.68
240 s	$1.57 \times 10^{-3} \pm 2.09 \times 10^{-5}$	60.8 ± 0.30	2.87 ± 0.03	$5.02 \times 10^{-7} \pm 4.62 \times 10^{-7}$	3.21 ± 0.16	1.72
270 s	$1.87 \times 10^{-3} \pm 2.07 \times 10^{-5}$	60.8 ± 0.27	2.88 ± 0.03	$8.76 \times 10^{-7} \pm 5.96 \times 10^{-7}$	3.14 ± 0.12	1.79
300 s	$2.08 \times 10^{-3} \pm 2.11 \times 10^{-5}$	60.6 ± 0.25	2.88 ± 0.03	$9.73 \times 10^{-7} \pm 5.82 \times 10^{-7}$	3.15 ± 0.11	1.76

Table A3.22. Fitting parameters for Carb-Val SAXS data at Position 4 after the onset of gel formation. The data fit an elliptical cylinder with a power-law model. The background and length parameters were not included in the table, as they were fixed at 0.01 cm^{-1} and 1000 Å, respectively.

	A Scale	Radius (Å)	Axis Ratio	B Scale	B Power	χ^2
270 s	$2.84 \times 10^{-4} \pm 1.08 \times 10^{-5}$	64.0 ± 1.16	2.45 ± 0.11	$4.31 \times 10^{-9} \pm 3.98 \times 10^{-8}$	3.67 ± 1.66	1.39
300 s	$7.65 \times 10^{-4} \pm 1.72 \times 10^{-5}$	61.4 ± 0.48	2.75 ± 0.06	$5.23 \times 10^{-8} \pm 1.50 \times 10^{-7}$	3.46 ± 0.51	1.44

3.4. SAXS data for Carb-Leu electrogelation

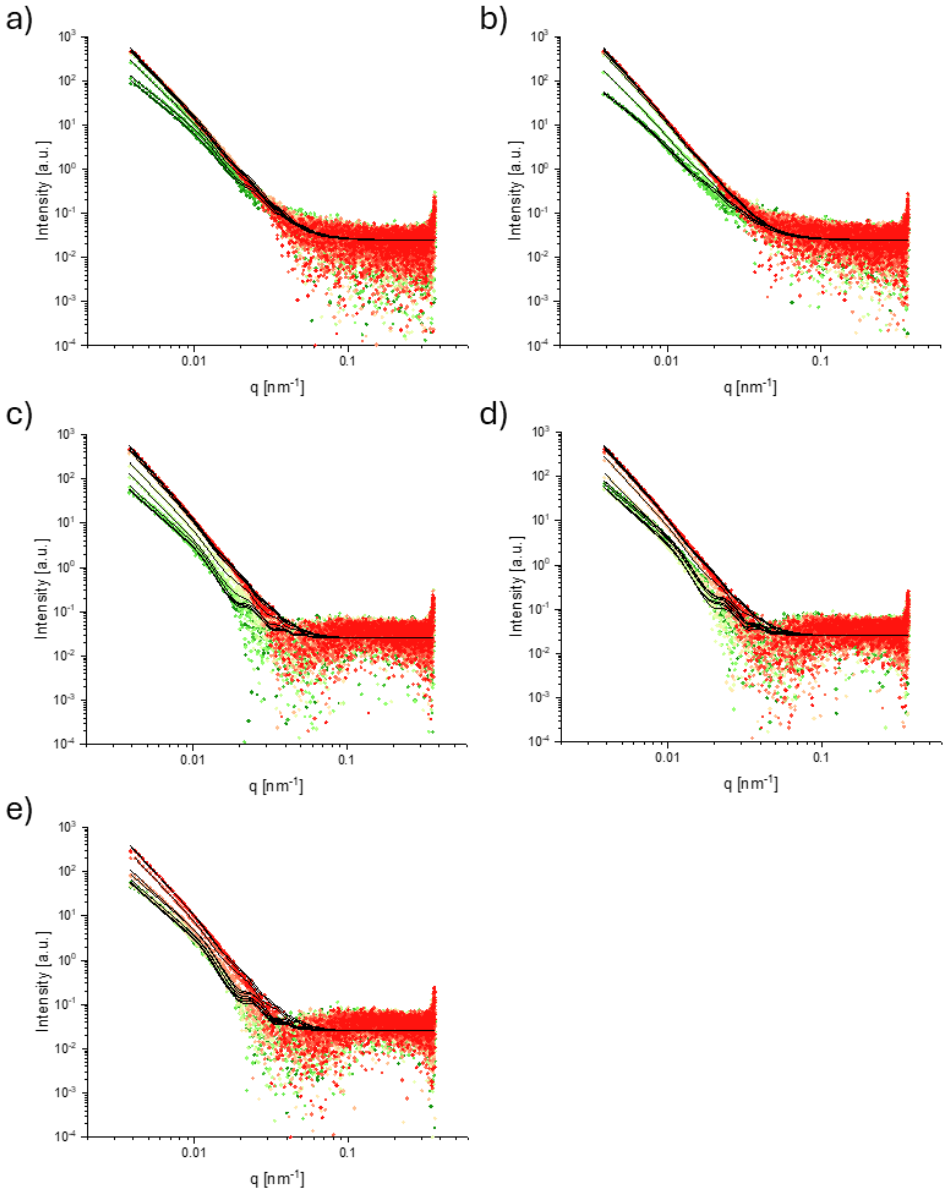

Figure A3.4. SAXS plots for Positions 1–5 (a-e) showing Carb-Leu hydrogel formation over time, with scan colour progressing from light green to red; the fits are overlaid in black.

Table A3.23. Fitting parameters for Carb-Leu SAXS data at Position 1. The data fit a cylinder with a power-law model. The background and length parameters were not included in the table, as they were fixed at 0.025 cm^{-1} and 1000 Å, respectively.

	A Scale	Radius (Å)	B Scale	B Power	χ^2
Before Current	7.91×10^{-5} $\pm 2.47 \times 10^{-6}$	213.8 ± 2.28	1.21×10^{-6} $\pm 7.51 \times 10^{-8}$	3.25 ± 0.012	0.86
0 s	1.17×10^{-4} $\pm 2.62 \times 10^{-6}$	207.1 ± 1.59	1.08×10^{-6} $\pm 6.17 \times 10^{-8}$	3.32 ± 0.011	0.98
30 s	9.07×10^{-5} $\pm 3.10 \times 10^{-6}$	231.3 ± 2.32	3.20×10^{-7} $\pm 1.28 \times 10^{-8}$	3.70 $\pm 7.34 \times 10^{-3}$	0.97
60 s	9.10×10^{-5} $\pm 3.48 \times 10^{-6}$	242.7 ± 2.54	2.39×10^{-7} $\pm 7.56 \times 10^{-9}$	3.83 $\pm 5.78 \times 10^{-3}$	1.08
90 s	8.52×10^{-5} $\pm 3.54 \times 10^{-6}$	252.1 ± 2.78	2.10×10^{-7} $\pm 6.43 \times 10^{-9}$	3.86 $\pm 5.62 \times 10^{-3}$	1.04
120 s	8.99×10^{-5} $\pm 3.57 \times 10^{-6}$	246.6 ± 2.60	1.79×10^{-7} $\pm 5.75 \times 10^{-9}$	3.90 $\pm 5.75 \times 10^{-3}$	1.08
150 s	9.55×10^{-5} $\pm 3.63 \times 10^{-6}$	252.6 ± 2.51	1.84×10^{-7} $\pm 5.60 \times 10^{-9}$	3.90 $\pm 5.55 \times 10^{-3}$	1.18
180 s	1.36×10^{-4} $\pm 3.56 \times 10^{-6}$	223.0 ± 1.72	2.23×10^{-7} $\pm 7.14 \times 10^{-9}$	3.88 $\pm 5.82 \times 10^{-3}$	1.24
210 s	1.11×10^{-4} $\pm 3.70 \times 10^{-6}$	232.8 ± 2.06	1.60×10^{-7} $\pm 5.34 \times 10^{-9}$	3.94 $\pm 6.03 \times 10^{-3}$	1.19
240 s	9.09×10^{-5} $\pm 3.69 \times 10^{-6}$	245.8 ± 2.57	1.25×10^{-7} $\pm 4.16 \times 10^{-9}$	3.98 $\pm 6.01 \times 10^{-3}$	1.26
270 s	9.44×10^{-5} $\pm 3.71x 10^{-6}$	247.5 ± 2.49	1.17×10^{-7} $\pm 3.87 \times 10^{-9}$	4.00 $\pm 6.00 \times 10^{-3}$	1.25
300 s	9.69×10^{-5} $\pm 3.77 \times 10^{-6}$	261.7 ± 2.54	1.27×10^{-7} $\pm 3.82 \times 10^{-9}$	3.98 $\pm 5.47 \times 10^{-3}$	1.28

Table A3.24. Fitting parameters for Carb-Leu SAXS data at Position 2. The data fit a cylinder with a power-law model. The background and length parameters were not included in the table, as they were fixed at 0.025 cm^{-1} and 1000 Å, respectively.

	A Scale	Radius (Å)	B Scale	B Power	χ^2
Before Current	$3.83 \times 10^{-5} \pm 2.67 \times 10^{-6}$	276.6 ± 4.54	$2.39 \times 10^{-6} \pm 2.22 \times 10^{-7}$	3.00± 0.022	0.91
0 s	$3.81 \times 10^{-5} \pm 2.48 \times 10^{-6}$	259.1 ± 4.62	$1.71 \times 10^{-6} \pm 1.41 \times 10^{-7}$	3.08± 0.019	0.90
30 s	$3.11 \times 10^{-5} \pm 2.60 \times 10^{-6}$	278.5 ± 5.94	$1.17 \times 10^{-6} \pm 1.11 \times 10^{-7}$	3.14± 0.021	0.92
60 s	$3.45 \times 10^{-5} \pm 3.02 \times 10^{-6}$	293.0 ± 6.23	$2.36 \times 10^{-7} \pm 1.15 \times 10^{-8}$	$3.66 \pm 9.58 \times 10^{-3}$	0.90
90 s	$5.60 \times 10^{-5} \pm 3.55 \times 10^{-6}$	279.5 ± 4.31	$1.31 \times 10^{-7} \pm 4.21 \times 10^{-9}$	$3.93 \pm 5.92 \times 10^{-3}$	0.99
120 s	$6.86 \times 10^{-5} \pm 3.84 \times 10^{-6}$	290.5 ± 3.72	$1.43 \times 10^{-7} \pm 4.03 \times 10^{-9}$	$3.94 \pm 5.24 \times 10^{-3}$	1.08
150 s	$7.05 \times 10^{-5} \pm 4.00 \times 10^{-6}$	302.4 ± 3.71	$1.21 \times 10^{-7} \pm 3.32 \times 10^{-9}$	$3.97 \pm 5.14 \times 10^{-3}$	1.19
180 s	$6.52 \times 10^{-5} \pm 3.96 \times 10^{-6}$	296.6 ± 3.98	$1.03 \times 10^{-7} \pm 2.92 \times 10^{-9}$	$4.01 \pm 5.26 \times 10^{-3}$	1.09
210 s	$6.50 \times 10^{-5} \pm 4.00 \times 10^{-6}$	297.5 ± 4.02	$9.96 \times 10^{-8} \pm 2.77 \times 10^{-9}$	$4.02 \pm 5.15 \times 10^{-3}$	1.06
240 s	$6.49 \times 10^{-5} \pm 4.08 \times 10^{-6}$	301.7 ± 4.07	$9.67 \times 10^{-8} \pm 2.64 \times 10^{-9}$	$4.03 \pm 5.06 \times 10^{-3}$	1.09
270 s	$7.26 \times 10^{-5} \pm 4.22 \times 10^{-6}$	309.9 ± 3.71	$8.73 \times 10^{-8} \pm 2.34 \times 10^{-9}$	$4.05 \pm 4.98 \times 10^{-3}$	1.05
300 s	$7.03 \times 10^{-5} \pm 4.13 \times 10^{-6}$	302.5 ± 3.78	$8.57 \times 10^{-8} \pm 2.34 \times 10^{-9}$	$4.06 \pm 5.03 \times 10^{-3}$	1.17

Table A3.25. Fitting parameters for Carb-Leu SAXS data at Position 3. The data fit a cylinder with a power-law model. The background and length parameters were not included in the table, as they were fixed at 0.025 cm^{-1} and 1000 Å, respectively.

	A Scale	Radius (Å)	B Scale	B Power	χ^2
Before Current	$5.76 \times 10^{-5} \pm 2.60 \times 10^{-6}$	220.9 ± 2.89	$3.70 \times 10^{-8} \pm 9.10 \times 10^{-9}$	3.77 ± 0.044	1.21
0 s	$6.08 \times 10^{-5} \pm 2.61 \times 10^{-6}$	220.8 ± 2.74	$3.48 \times 10^{-8} \pm 9.05 \times 10^{-9}$	3.77 ± 0.046	1.25
30 s	$5.68 \times 10^{-5} \pm 2.69 \times 10^{-6}$	216.9 ± 2.87	$2.68 \times 10^{-8} \pm 7.70 \times 10^{-9}$	3.82 ± 0.052	1.30
60 s	$7.34 \times 10^{-5} \pm 2.77 \times 10^{-6}$	215.2 ± 2.26	$3.36 \times 10^{-8} \pm 7.79 \times 10^{-9}$	3.82 ± 0.042	1.29
90 s	$6.26 \times 10^{-5} \pm 2.96 \times 10^{-6}$	228.6 ± 2.83	$2.80 \times 10^{-8} \pm 3.89 \times 10^{-9}$	3.98 ± 0.025	1.25
120 s	$7.61 \times 10^{-5} \pm 3.09 \times 10^{-6}$	244.1 ± 2.63	$5.42 \times 10^{-8} \pm 3.81 \times 10^{-9}$	3.98 ± 0.013	1.55
150 s	$8.67 \times 10^{-5} \pm 3.55 \times 10^{-6}$	258.7 ± 2.62	$5.78 \times 10^{-8} \pm 2.48 \times 10^{-9}$	$4.08 \pm 7.73 \times 10^{-3}$	1.50
180 s	$9.14 \times 10^{-5} \pm 3.69 \times 10^{-6}$	271.7 ± 2.63	$6.16 \times 10^{-8} \pm 2.33 \times 10^{-9}$	$4.09 \pm 6.82 \times 10^{-3}$	1.69
210 s	$1.06 \times 10^{-4} \pm 3.84 \times 10^{-6}$	279.6 ± 2.36	$6.67 \times 10^{-8} \pm 2.28 \times 10^{-9}$	$4.09 \pm 6.18 \times 10^{-3}$	1.82
240 s	$9.89 \times 10^{-5} \pm 3.78 \times 10^{-6}$	259.4 ± 2.41	$6.78 \times 10^{-8} \pm 2.44 \times 10^{-9}$	$4.09 \pm 6.48 \times 10^{-3}$	1.63
270 s	$1.05 \times 10^{-4} \pm 3.84 \times 10^{-6}$	264.4 ± 2.30	$5.59 \times 10^{-8} \pm 2.04 \times 10^{-9}$	$4.13 \pm 6.54 \times 10^{-3}$	1.80
300 s	$8.99 \times 10^{-5} \pm 3.96 \times 10^{-6}$	284.0 ± 2.84	$6.13 \times 10^{-8} \pm 1.98 \times 10^{-9}$	$4.12 \pm 5.82 \times 10^{-3}$	1.83

Table A3.26. Fitting parameters for Carb-Leu SAXS data at Position 4. The data fit a cylinder with a power-law model. The background and length parameters were not included in the table, as they were fixed at 0.025 cm^{-1} and 1000 Å, respectively.

	A Scale	Radius (Å)	B Scale	B Power	χ^2
Before Current	$8.99 \times 10^{-5} \pm 2.68 \times 10^{-6}$	212.5 ± 1.89	$7.67 \times 10^{-8} \pm 1.33 \times 10^{-8}$	3.69 ± 0.031	1.48
0 s	$7.25 \times 10^{-5} \pm 2.62 \times 10^{-6}$	216.5 ± 2.32	$6.20 \times 10^{-8} \pm 1.20 \times 10^{-8}$	3.71 ± 0.035	1.38
30 s	$7.91 \times 10^{-5} \pm 2.64 \times 10^{-6}$	215.7 ± 2.16	$7.62 \times 10^{-8} \pm 1.27 \times 10^{-8}$	3.70 ± 0.030	1.49
60 s	$6.28 \times 10^{-5} \pm 2.58 \times 10^{-6}$	225.2 ± 2.67	$3.20 \times 10^{-8} \pm 8.26 \times 10^{-9}$	3.79 ± 0.046	1.49
90 s	$5.72 \times 10^{-5} \pm 2.65 \times 10^{-6}$	222.4 ± 2.90	$2.62 \times 10^{-8} \pm 7.33 \times 10^{-9}$	3.82 ± 0.050	1.41
120 s	$5.71 \times 10^{-5} \pm 3.04 \times 10^{-6}$	211.8 ± 2.73	$9.73 \times 10^{-9} \pm 3.76 \times 10^{-9}$	4.01 ± 0.069	1.48
150 s	$5.64 \times 10^{-5} \pm 2.95 \times 10^{-6}$	230.4 ± 3.11	$2.24 \times 10^{-8} \pm 3.46 \times 10^{-9}$	4.01 ± 0.028	1.48
180 s	$6.76 \times 10^{-5} \pm 3.27 \times 10^{-6}$	243.0 ± 2.99	$3.92 \times 10^{-8} \pm 2.66 \times 10^{-9}$	4.07 ± 0.012	1.68
210 s	$8.85 \times 10^{-5} \pm 3.51 \times 10^{-6}$	250.0 ± 2.51	$6.64 \times 10^{-8} \pm 2.97 \times 10^{-9}$	$4.05 \pm 8.05 \times 10^{-3}$	1.90
240 s	$8.75 \times 10^{-5} \pm 3.72 \times 10^{-6}$	288.5 ± 2.81	$5.62 \times 10^{-8} \pm 2.10 \times 10^{-9}$	$4.09 \pm 6.77 \times 10^{-3}$	1.79
270 s	$8.73 \times 10^{-5} \pm 3.73 \times 10^{-6}$	279.1 ± 2.79	$5.31 \times 10^{-8} \pm 2.03 \times 10^{-9}$	$4.11 \pm 6.89 \times 10^{-3}$	2.10
300 s	$9.81 \times 10^{-5} \pm 3.81 \times 10^{-6}$	282.5 ± 2.53	$5.59 \times 10^{-8} \pm 2.00 \times 10^{-9}$	$4.11 \pm 6.48 \times 10^{-3}$	1.95

Table A3.27. Fitting parameters for Carb-Leu SAXS data at Position 5. The data fit a cylinder with a power-law model. The background and length parameters were not included in the table, as they were fixed at 0.025 cm^{-1} and 1000 Å, respectively.

	A Scale	Radius (Å)	B Scale	B Power	χ^2
Before Current	$5.95 \times 10^{-5} \pm 2.58 \times 10^{-6}$	218.2 ± 2.77	$4.02 \times 10^{-8} \pm 1.05 \times 10^{-8}$	3.74 ± 0.047	1.50
0 s	$7.01 \times 10^{-5} \pm 2.69 \times 10^{-6}$	213.6 ± 2.37	$4.75 \times 10^{-8} \pm 1.04 \times 10^{-8}$	3.75 ± 0.040	1.51
30 s	$6.23 \times 10^{-5} \pm 2.65 \times 10^{-6}$	223.7 ± 2.67	$2.35 \times 10^{-8} \pm 6.82 \times 10^{-9}$	3.84 ± 0.052	1.48
60 s	$5.92 \times 10^{-5} \pm 2.66 \times 10^{-6}$	219.6 ± 2.80	$3.18 \times 10^{-8} \pm 8.31 \times 10^{-9}$	3.80 ± 0.047	1.55
90 s	$6.07 \times 10^{-5} \pm 2.96 \times 10^{-6}$	206.9 ± 2.58	$1.62 \times 10^{-8} \pm 5.73 \times 10^{-9}$	3.91 ± 0.063	1.54
120 s	$7.88 \times 10^{-5} \pm 2.84 \times 10^{-6}$	209.8 ± 2.07	$3.05 \times 10^{-8} \pm 7.99 \times 10^{-9}$	3.82 ± 0.047	1.65
150 s	$6.90 \times 10^{-5} \pm 2.88 \times 10^{-6}$	214.2 ± 2.34	$1.63 \times 10^{-8} \pm 5.52 \times 10^{-9}$	3.91 ± 0.061	1.62
180 s	$1.01 \times 10^{-4} \pm 2.89 \times 10^{-6}$	211.8 ± 1.68	$4.15 \times 10^{-8} \pm 8.12 \times 10^{-9}$	3.82 ± 0.035	1.78
210 s	$8.96 \times 10^{-5} \pm 2.99 \times 10^{-6}$	213.5± 1.91	$3.81 \times 10^{-8} \pm 6.25 \times 10^{-9}$	3.89 ± 0.029	1.64
240 s	$7.83 \times 10^{-5} \pm 3.16 \times 10^{-6}$	248.0 ± 2.64	$5.68 \times 10^{-8} \pm 3.64 \times 10^{-9}$	3.99 ± 0.012	1.90
270 s	$1.06 \times 10^{-4} \pm 3.45 \times 10^{-6}$	234.2 ± 1.96	$6.97 \times 10^{-8} \pm 3.66 \times 10^{-9}$	$4.01 \pm 9.44 \times 10^{-3}$	2.29
300 s	$9.74 \times 10^{-5} \pm 3.48 \times 10^{-6}$	268.0 ± 2.37	$6.84 \times 10^{-8} \pm 2.93 \times 10^{-9}$	$4.03 \pm 7.76 \times 10^{-3}$	2.24

3.5. Chronopotentiometry

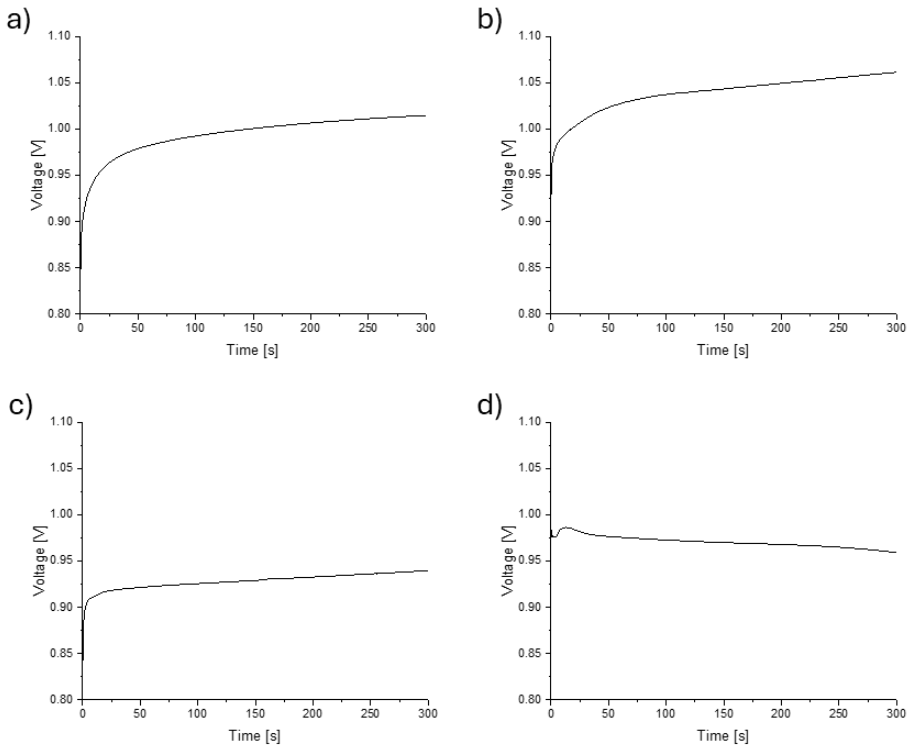

Figure A3.5. Chronopotentiometry measurements of electrogelation of a) Carb-Ala, b) Carb-Gly, c) Carb-Val, and d) Carb-Leu during in situ SAXS experiment.

3.6. SAXS data for Carb-Ala electropolymerisation

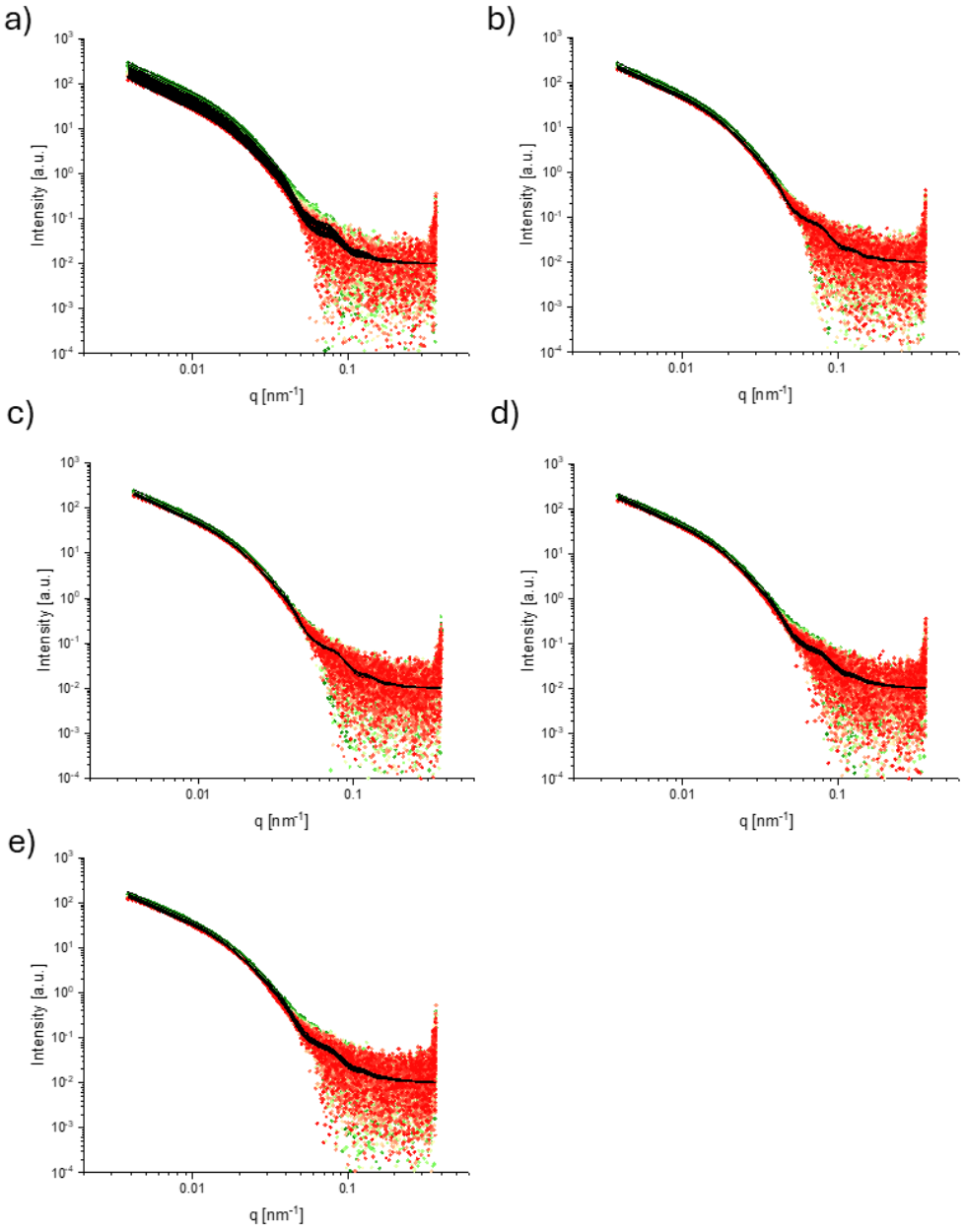

Figure A3.6. SAXS plots for Positions 1–5 (a-e) showing the attempted electropolymerisation of Carb-Ala over 90 min, with scan colour progressing from light green to red; the fits are overlaid in black.

Table A3.28. Fitting parameters for Carb-Ala SAXS data at Position 1. The data fit an elliptical cylinder with a power-law model. The background and length parameters are not included, as they were fixed at 0.01 cm^{-1} and 1000 Å, respectively.

	A Scale	Radius (Å)	Axis Ratio	B Scale	B Power	χ^2
0 min	$4.47 \times 10^{-3} \pm 2.94 \times 10^{-5}$	63.0 ± 0.17	2.55 ± 0.02	$1.61 \times 10^{-6} \pm 5.27 \times 10^{-7}$	3.26 ± 0.06	16.8
5 min	$3.71 \times 10^{-3} \pm 2.63 \times 10^{-5}$	63.2 ± 0.23	2.49 ± 0.02	$6.40 \times 10^{-6} \pm 1.24 \times 10^{-6}$	3.01 ± 0.03	5.28
10 min	$3.41 \times 10^{-3} \pm 2.49 \times 10^{-5}$	63.4 ± 0.25	2.49 ± 0.02	$8.97 \times 10^{-6} \pm 1.58 \times 10^{-6}$	2.93 ± 0.03	3.22
15 min	$3.22 \times 10^{-3} \pm 2.52 \times 10^{-5}$	62.9 ± 0.27	2.50 ± 0.02	$9.02 \times 10^{-6} \pm 1.66 \times 10^{-6}$	2.92 ± 0.03	2.48
20 min	$3.04 \times 10^{-3} \pm 2.57 \times 10^{-5}$	62.9 ± 0.29	2.47 ± 0.02	$7.38 \times 10^{-6} \pm 1.52 \times 10^{-6}$	2.95 ± 0.04	2.22
25 min	$2.92 \times 10^{-3} \pm 2.62 \times 10^{-5}$	62.4 ± 0.30	2.50 ± 0.02	$6.87 \times 10^{-6} \pm 1.54 \times 10^{-6}$	2.95 ± 0.04	2.15
30 min	$2.81 \times 10^{-3} \pm 2.69 \times 10^{-5}$	62.2 ± 0.31	2.51 ± 0.02	$5.42 \times 10^{-6} \pm 1.40 \times 10^{-6}$	2.98 ± 0.05	2.03
35 min	$2.70 \times 10^{-3} \pm 2.77 \times 10^{-5}$	61.9 ± 0.32	2.51 ± 0.02	$4.57 \times 10^{-6} \pm 1.30 \times 10^{-6}$	3.01 ± 0.05	2.02
40 min	$2.58 \times 10^{-3} \pm 2.76 \times 10^{-5}$	61.7 ± 0.33	2.51 ± 0.03	$4.41 \times 10^{-6} \pm 1.29 \times 10^{-6}$	3.01 ± 0.05	1.87
45 min	$2.53 \times 10^{-3} \pm 2.88 \times 10^{-5}$	61.3 ± 0.33	2.56 ± 0.03	$3.05 \times 10^{-6} \pm 1.14 \times 10^{-6}$	3.05 ± 0.07	1.87
50 min	$2.42 \times 10^{-3} \pm 2.89 \times 10^{-5}$	61.1 ± 0.34	2.53 ± 0.03	$2.85 \times 10^{-6} \pm 1.08 \times 10^{-6}$	3.07 ± 0.07	1.93
55 min	$2.34 \times 10^{-3} \pm 2.88 \times 10^{-5}$	61.2 ± 0.35	2.52 ± 0.03	$2.67 \times 10^{-6} \pm 1.08 \times 10^{-6}$	3.07 ± 0.07	1.84
60 min	$2.28 \times 10^{-3} \pm 2.93 \times 10^{-5}$	60.8 ± 0.35	2.53 ± 0.03	$2.21 \times 10^{-6} \pm 9.73 \times 10^{-7}$	3.10 ± 0.08	1.80
65 min	$2.21 \times 10^{-3} \pm 2.96 \times 10^{-5}$	60.8 ± 0.36	2.54 ± 0.03	$1.94 \times 10^{-6} \pm 9.11 \times 10^{-7}$	3.12 ± 0.08	1.73
70 min	$2.13 \times 10^{-3} \pm 2.95 \times 10^{-5}$	60.7 ± 0.37	2.54 ± 0.03	$1.87 \times 10^{-6} \pm 9.01 \times 10^{-7}$	3.12 ± 0.09	1.77
75 min	$2.09 \times 10^{-3} \pm 2.98 \times 10^{-5}$	60.8 ± 0.37	2.56 ± 0.03	$1.43 \times 10^{-6} \pm 8.06 \times 10^{-7}$	3.15 ± 0.10	1.71

80 min	$2.01 \times 10^{-3} \pm 2.97 \times 10^{-5}$	60.5 ± 0.38	2.59 ± 0.03	$1.61 \times 10^{-6} \pm 8.72 \times 10^{-7}$	3.13 ± 0.10	1.75
85 min	$1.98 \times 10^{-3} \pm 3.03 \times 10^{-5}$	59.9 ± 0.38	2.60 ± 0.04	$1.33 \times 10^{-6} \pm 7.88 \times 10^{-7}$	3.16 ± 0.11	1.61
90 min	$1.90 \times 10^{-3} \pm 2.97 \times 10^{-5}$	60.0 ± 0.40	2.57 ± 0.04	$1.55 \times 10^{-6} \pm 8.48 \times 10^{-7}$	3.14 ± 0.10	1.64

Table A3.29. Fitting parameters for Carb-Ala SAXS data at Position 2. The data fit an elliptical cylinder with a power-law model. The background and length parameters are not included, as they were fixed at 0.01 cm^{-1} and 1000 Å, respectively.

	A Scale	Radius (Å)	Axis Ratio	B Scale	B Power	χ^2
0 min	$4.24 \times 10^{-3} \pm 2.93 \times 10^{-5}$	62.6 ± 0.18	2.55 ± 0.02	$1.73 \times 10^{-6} \pm 6.01 \times 10^{-7}$	3.23 ± 0.06	13.21
5 min	$3.35 \times 10^{-3} \pm 2.50 \times 10^{-5}$	63.1 ± 0.24	2.49 ± 0.02	$7.92 \times 10^{-6} \pm 1.52 \times 10^{-6}$	2.94 ± 0.03	4.18
10 min	$3.30 \times 10^{-3} \pm 2.33 \times 10^{-5}$	63.7 ± 0.26	2.44 ± 0.03	$1.21 \times 10^{-5} \pm 1.88 \times 10^{-6}$	2.86 ± 0.03	2.64
15 min	$3.18 \times 10^{-3} \pm 2.25 \times 10^{-5}$	63.7 ± 0.28	2.45 ± 0.02	$1.61 \times 10^{-5} \pm 2.24 \times 10^{-6}$	2.80 ± 0.02	2.00
20 min	$3.15 \times 10^{-3} \pm 2.31 \times 10^{-5}$	63.5 ± 0.28	2.43 ± 0.02	$1.36 \times 10^{-5} \pm 2.07 \times 10^{-6}$	2.83 ± 0.03	1.85
25 min	$3.12 \times 10^{-3} \pm 2.26 \times 10^{-5}$	63.8 ± 0.28	2.42 ± 0.02	$1.51 \times 10^{-5} \pm 2.22 \times 10^{-6}$	2.81 ± 0.03	1.82
30 min	$3.11 \times 10^{-3} \pm 2.30 \times 10^{-5}$	63.6 ± 0.28	2.42 ± 0.02	$1.39 \times 10^{-5} \pm 2.14 \times 10^{-6}$	2.82 ± 0.03	1.67
35 min	$3.06 \times 10^{-3} \pm 2.25 \times 10^{-5}$	64.2 ± 0.29	2.38 ± 0.02	$1.50 \times 10^{-5} \pm 2.18 \times 10^{-6}$	2.81 ± 0.03	1.62
40 min	$3.11 \times 10^{-3} \pm 2.33 \times 10^{-5}$	63.3 ± 0.28	2.43 ± 0.02	$1.27 \times 10^{-5} \pm 2.13 \times 10^{-6}$	2.83 ± 0.03	1.63
45 min	$3.05 \times 10^{-3} \pm 2.27 \times 10^{-5}$	63.9 ± 0.29	2.38 ± 0.02	$1.43 \times 10^{-5} \pm 2.17 \times 10^{-6}$	2.82 ± 0.03	1.54
50 min	$3.07 \times 10^{-3} \pm 2.28 \times 10^{-5}$	63.8 ± 0.29	2.38 ± 0.02	$1.29 \times 10^{-5} \pm 2.11 \times 10^{-6}$	2.83 ± 0.03	1.63
55 min	$3.05 \times 10^{-3} \pm 2.30 \times 10^{-5}$	64.0 ± 0.29	2.36 ± 0.02	$1.24 \times 10^{-5} \pm 2.06 \times 10^{-6}$	2.83 ± 0.03	1.55

60 min	$3.05 \times 10^{-3} \pm 2.30 \times 10^{-5}$	64.0 ± 0.29	2.36 ± 0.02	$1.24 \times 10^{-5} \pm 2.06 \times 10^{-6}$	2.83 ± 0.03	1.55
65 min	$3.08 \times 10^{-3} \pm 2.39 \times 10^{-5}$	63.6 ± 0.29	2.39 ± 0.02	$9.76 \times 10^{-6} \pm 1.87 \times 10^{-6}$	2.87 ± 0.03	1.52
70 min	$3.00 \times 10^{-3} \pm 2.22 \times 10^{-5}$	64.1 ± 0.30	2.36 ± 0.02	$1.46 \times 10^{-5} \pm 2.24 \times 10^{-6}$	2.80 ± 0.03	1.55
75 min	$3.03 \times 10^{-3} \pm 2.32 \times 10^{-5}$	63.9 ± 0.29	2.38 ± 0.02	$1.14 \times 10^{-5} \pm 2.03 \times 10^{-6}$	2.84 ± 0.03	1.46
80 min	$3.00 \times 10^{-3} \pm 2.30 \times 10^{-5}$	63.8 ± 0.30	2.38 ± 0.02	$1.17 \times 10^{-5} \pm 2.08 \times 10^{-6}$	2.83 ± 0.03	1.43
85 min	$3.01 \times 10^{-3} \pm 2.34 \times 10^{-5}$	63.5 ± 0.30	2.39 ± 0.02	$1.01 \times 10^{-5} \pm 1.96 \times 10^{-6}$	2.86 ± 0.03	1.44
90 min	$2.99 \times 10^{-3} \pm 2.39 \times 10^{-5}$	63.4 ± 0.31	2.40 ± 0.02	$9.61 \times 10^{-6} \pm 1.91 \times 10^{-6}$	2.87 ± 0.04	1.41

Table A3.30. Fitting parameters for Carb-Ala SAXS data at Position 3. The data fit an elliptical cylinder with a power-law model. The background and length parameters are not included, as they were fixed at 0.01 cm^{-1} and 1000 Å, respectively.

	A Scale	Radius (Å)	Axis Ratio	B Scale	B Power	χ^2
0 min	$3.96 \times 10^{-3} \pm 2.86 \times 10^{-5}$	62.1 ± 0.20	2.56 ± 0.02	$2.35 \times 10^{-6} \pm 7.97 \times 10^{-7}$	3.15 ± 0.06	9.98
5 min	$3.34 \times 10^{-3} \pm 2.35 \times 10^{-5}$	62.9 ± 0.26	2.49 ± 0.02	$1.11 \times 10^{-5} \pm 1.93 \times 10^{-6}$	2.86 ± 0.03	3.33
10 min	$3.14 \times 10^{-3} \pm 2.30 \times 10^{-5}$	63.0 ± 0.28	2.47 ± 0.02	$1.36 \times 10^{-5} \pm 2.15 \times 10^{-6}$	2.82 ± 0.03	2.14
15 min	$3.05 \times 10^{-3} \pm 2.24 \times 10^{-5}$	63.4 ± 0.29	2.46 ± 0.02	$1.53 \times 10^{-5} \pm 2.33 \times 10^{-6}$	2.79 ± 0.03	2.81
20 min	$3.00 \times 10^{-3} \pm 2.27 \times 10^{-5}$	63.2 ± 0.29	2.43 ± 0.02	$1.49 \times 10^{-5} \pm 2.28 \times 10^{-6}$	2.80 ± 0.03	1.61
25 min	$2.97 \times 10^{-3} \pm 2.19 \times 10^{-5}$	63.8 ± 0.30	2.40 ± 0.02	$1.67 \times 10^{-5} \pm 2.43 \times 10^{-6}$	2.77 ± 0.03	1.56
30 min	$2.97 \times 10^{-3} \pm 2.24 \times 10^{-5}$	63.5 ± 0.30	2.41 ± 0.02	$1.56 \times 10^{-5} \pm 2.37 \times 10^{-6}$	2.79 ± 0.03	1.57
35 min	$2.99 \times 10^{-3} \pm 2.28 \times 10^{-5}$	63.0 ± 0.29	2.47 ± 0.02	$1.41 \times 10^{-5} \pm 2.37 \times 10^{-6}$	2.79 ± 0.03	1.45

40 min	$2.98 \times 10^{-3} \pm 2.23 \times 10^{-5}$	63.5 ± 0.29	2.42 ± 0.02	$1.43 \times 10^{-5} \pm 2.34 \times 10^{-6}$	2.79 ± 0.03	1.45
45 min	$2.96 \times 10^{-3} \pm 2.23 \times 10^{-5}$	63.8 ± 0.30	2.39 ± 0.02	$1.43 \times 10^{-5} \pm 2.35 \times 10^{-6}$	2.79 ± 0.03	1.39
50 min	$2.96 \times 10^{-3} \pm 2.25 \times 10^{-5}$	63.4 ± 0.30	2.41 ± 0.02	$1.42 \times 10^{-5} \pm 2.34 \times 10^{-6}$	2.79 ± 0.03	1.37
55 min	$2.99 \times 10^{-3} \pm 2.31 \times 10^{-5}$	63.5 ± 0.30	2.41 ± 0.02	$1.14 \times 10^{-5} \pm 2.15 \times 10^{-6}$	2.82 ± 0.03	1.31
60 min	$2.94 \times 10^{-3} \pm 2.24 \times 10^{-5}$	63.5 ± 0.30	2.39 ± 0.02	$1.39 \times 10^{-5} \pm 2.31 \times 10^{-6}$	2.80 ± 0.03	1.31
65 min	$2.96 \times 10^{-3} \pm 2.22 \times 10^{-5}$	63.6 ± 0.30	2.40 ± 0.02	$1.41 \times 10^{-5} \pm 2.39 \times 10^{-6}$	2.78 ± 0.03	1.33
70 min	$2.96 \times 10^{-3} \pm 2.29 \times 10^{-5}$	63.3 ± 0.30	2.42 ± 0.02	$1.28 \times 10^{-5} \pm 2.27 \times 10^{-6}$	2.80 ± 0.03	1.22
75 min	$2.95 \times 10^{-3} \pm 2.27 \times 10^{-5}$	63.7 ± 0.30	2.40 ± 0.02	$1.23 \times 10^{-5} \pm 2.25 \times 10^{-6}$	2.81 ± 0.03	1.29
80 min	$2.96 \times 10^{-3} \pm 2.32 \times 10^{-5}$	63.3 ± 0.30	2.41 ± 0.02	$1.12 \times 10^{-5} \pm 2.13 \times 10^{-6}$	2.83 ± 0.03	1.32
85 min	$2.91 \times 10^{-3} \pm 2.26 \times 10^{-5}$	63.7 ± 0.31	2.36 ± 0.02	$1.34 \times 10^{-5} \pm 2.26 \times 10^{-6}$	2.80 ± 0.03	1.25
90 min	$2.88 \times 10^{-3} \pm 2.21 \times 10^{-5}$	63.9 ± 0.31	2.3 4 ± 0.02	$1.49 \times 10^{-5} \pm 2.36 \times 10^{-6}$	2.79 ± 0.03	1.31

Table A3.31. Fitting parameters for Carb-Ala SAXS data at Position 4. The data fit an elliptical cylinder with a power-law model. The background and length parameters are not included, as they were fixed at 0.01 cm^{-1} and 1000 Å, respectively.

	A Scale	Radius (Å)	Axis Ratio	B Scale	B Power	χ^2
0 min	$3.35 \times 10^{-3} \pm 2.27 \times 10^{-5}$	60.6 ± 0.25	2.61 ± 0.02	$1.87 \times 10^{-6} \pm 2.56 \times 10^{-6}$	2.76 ± 0.02	7.06
5 min	$2.88 \times 10^{-3} \pm 2.17 \times 10^{-5}$	61.5 ± 0.30	2.53 ± 0.02	$2.67 \times 10^{-5} \pm 3.13 \times 10^{-6}$	2.69 ± 0.02	3.33
10 min	$2.73 \times 10^{-3} \pm 2.07 \times 10^{-5}$	62.0 ± 0.31	2.52 ± 0.02	$3.24 \times 10^{-5} \pm 3.55 \times 10^{-6}$	2.64 ± 0.01	2.33
15 min	$2.67 \times 10^{-3} \pm 2.09 \times 10^{-5}$	62.0 ± 0.32	2.50 ± 0.02	$3.02 \times 10^{-5} \pm 3.50 \times 10^{-6}$	2.65 ± 0.02	1.93

20 min	$2.64 \times 10^{-3} \pm 2.07 \times 10^{-5}$	62.1 ± 0.32	2.52 ± 0.02	$2.85 \times 10^{-5} \pm 3.50 \times 10^{-6}$	2.65 ± 0.03	1.86
25 min	$2.62 \times 10^{-3} \pm 2.14 \times 10^{-5}$	61.8 ± 0.33	2.52 ± 0.02	$2.54 \times 10^{-5} \pm 3.34 \times 10^{-6}$	2.67 ± 0.02	1.65
30 min	$2.61 \times 10^{-3} \pm 2.19 \times 10^{-5}$	61.9 ± 0.24	2.48 ± 0.02	$2.06 \times 10^{-5} \pm 2.98 \times 10^{-6}$	2.71 ± 0.03	1.62
35 min	$262 \times 10^{-3} \pm 2.13 \times 10^{-5}$	62.2 ± 0.33	2.47 ± 0.02	$2.25 \times 10^{-5} \pm 3.20 \times 10^{-6}$	2.69 ± 0.03	1.46
40 min	$2.59 \times 10^{-3} \pm 2.10 \times 10^{-5}$	62.4 ± 0.33	2.44 ± 0.02	$2.28 \times 10^{-5} \pm 3.21 \times 10^{-6}$	2.68 ± 0.03	1.49
45 min	$2.60 \times 10^{-3} \pm 2.22 \times 10^{-5}$	61.8 ± 0.33	2.48 ± 0.02	$1.90 \times 10^{-5} \pm 2.99 \times 10^{-6}$	2.72 ± 0.03	1.44
50 min	$2.60 \times 10^{-3} \pm 2.14 \times 10^{-5}$	62.6 ± 0.33	2.43 ± 0.02	$1.84 \times 10^{-5} \pm 2.94 \times 10^{-6}$	2.71 ± 0.03	1.42
55 min	$2.60 \times 10^{-3} \pm 2.16 \times 10^{-5}$	62.5 ± 0.33	2.43 ± 0.02	$1.85 \times 10^{-5} \pm 2.97 \times 10^{-6}$	2.71 ± 0.03	1.42
60 min	$2.59 \times 10^{-3} \pm 2.12 \times 10^{-5}$	63.0 ± 0.34	2.40 ± 0.02	$1.85 \times 10^{-5} \pm 2.94 \times 10^{-6}$	2.71 ± 0.03	1.41
65 min	$2.58 \times 10^{-3} \pm 2.19 \times 10^{-5}$	62.4 ± 0.34	2.43 ± 0.02	$1.71 \times 10^{-5} \pm 3.84 \times 10^{-6}$	2.73 ± 0.03	1.30
70 min	$2.59 \times 10^{-3} \pm 2.24 \times 10^{-5}$	62.2 ± 0.34	2.44 ± 0.02	$1.54 \times 10^{-5} \pm 2.71 \times 10^{-6}$	2.74 ± 0.03	1.36
75 min	$2.60 \times 10^{-3} \pm 2.21 \times 10^{-5}$	62.5 ± 0.34	2.44 ± 0.02	$1.48 \times 10^{-5} \pm 2.72 \times 10^{-6}$	2.74 ± 0.03	1.29
80 min	$2.60 \times 10^{-3} \pm 2.28 \times 10^{-5}$	62.3 ± 0.34	2.46 ± 0.02	$1.26 \times 10^{-5} \pm 2.52 \times 10^{-6}$	2.77 ± 0.04	1.28
85 min	$2.58 \times 10^{-3} \pm 2.24 \times 10^{-5}$	62.3 ± 0.34	2.46 ± 0.02	$1.47 \times 10^{-5} \pm 2.72 \times 10^{-6}$	2.74 ± 0.03	1.25
90 min	$2.56 \times 10^{-3} \pm 2.18 \times 10^{-5}$	62.8 ± 0.34	2.42 ± 0.02	$1.59 \times 10^{-5} \pm 2.79 \times 10^{-6}$	2.73 ± 0.03	1.27

Table A3.32. Fitting parameters for Carb-Ala SAXS data at Position 5. The data fit an elliptical cylinder with a power-law model. The background and length parameters are not included, as they were fixed at 0.01 cm^{-1} and 1000 Å, respectively.

	A Scale	Radius (Å)	Axis Ratio	B Scale	B Power	χ^2
0 min	$2.80 \times 10^{-3} \pm 2.34 \times 10^{-5}$	60.0 ± 0.30	2.67 ± 0.02	$1.41 \times 10^{-6} \pm 2.58 \times 10^{-6}$	2.77 ± 0.03	5.76
5 min	$2.43 \times 10^{-3} \pm 2.09 \times 10^{-5}$	61.0 ± 0.34	2.64 ± 0.03	$2.75 \times 10^{-5} \pm 3.74 \times 10^{-6}$	2.63 ± 2.44	2.60
10 min	$2.31 \times 10^{-3} \pm 2.05 \times 10^{-5}$	61.7 ± 0.36	2.58 ± 0.03	$2.63 \times 10^{-5} \pm 3.68 \times 10^{-6}$	2.63 ± 0.03	1.98
15 min	$2.19 \times 10^{-3} \pm 1.95 \times 10^{-5}$	62.8 ± 0.38	2.46 ± 0.03	$3.19 \times 10^{-5} \pm 3.92 \times 10^{-6}$	2.60 ± 0.02	1.75
20 min	$2.21 \times 10^{-3} \pm 2.07 \times 10^{-5}$	61.9 ± 0.38	2.52 ± 0.03	$2.19 \times 10^{-5} \pm 3.44 \times 10^{-6}$	2.66 ± 0.03	1.60
25 min	$2.17 \times 10^{-3} \pm 1.99 \times 10^{-5}$	62.8 ± 0.39	2.45 ± 0.03	$2.44 \times 10^{-5} \pm 3.60 \times 10^{-6}$	2.64 ± 0.03	1.50
30 min	$2.20 \times 10^{-3} \pm 2.10 \times 10^{-5}$	62.2 ± 0.38	2.46 ± 0.03	$1.78 \times 10^{-5} \pm 3.15 \times 10^{-6}$	2.69 ± 0.03	1.39
35 min	$2.18 \times 10^{-3} \pm 2.04 \times 10^{-5}$	62.6 ± 0.39	2.46 ± 0.03	$2.01 \times 10^{-5} \pm 3.40 \times 10^{-6}$	2.66 ± 0.03	1.37
40 min	$2.18 \times 10^{-3} \pm 2.09 \times 10^{-5}$	62.6 ± 0.39	2.43 ± 0.03	$1.72 \times 10^{-5} \pm 3.12 \times 10^{-6}$	2.69 ± 0.03	1.38
45 min	$2.19 \times 10^{-3} \pm 2.14 \times 10^{-5}$	62.3 ± 0.39	2.44 ± 0.03	$1.52 \times 10^{-5} \pm 3.04 \times 10^{-6}$	2.70 ± 0.04	1.36
50 min	$2.15 \times 10^{-3} \pm 2.02 \times 10^{-5}$	63.1 ± 0.39	2.37 ± 0.03	$1.80 \times 10^{-5} \pm 3.18 \times 10^{-6}$	2.68 ± 0.03	1.33
55 min	$2.18 \times 10^{-3} \pm 2.14 \times 10^{-5}$	62.4 ± 0.39	2.43 ± 0.03	$1.43 \times 10^{-5} \pm 2.97 \times 10^{-6}$	2.71 ± 0.04	1.22
60 min	$2.19 \times 10^{-3} \pm 2.15 \times 10^{-5}$	62.6 ± 0.39	2.45 ± 0.03	$1.21 \times 10^{-5} \pm 2.75 \times 10^{-6}$	2.74 ± 0.04	1.24
65 min	$2.18 \times 10^{-3} \pm 2.18 \times 10^{-5}$	62.5 ± 0.39	2.43 ± 0.03	$1.23 \times 10^{-5} \pm 2.77 \times 10^{-6}$	2.74 ± 0.04	1.16
70 min	$2.16 \times 10^{-3} \pm 2.13 \times 10^{-5}$	62.9 ± 0.40	2.38 ± 0.03	$1.29 \times 10^{-5} \pm 2.77 \times 10^{-6}$	2.73 ± 0.04	1.24
75 min	$2.14 \times 10^{-3} \pm 2.07 \times 10^{-5}$	63.3 ± 0.40	2.37 ± 0.03	$1.44 \times 10^{-5} \pm 2.92 \times 10^{-6}$	2.71 ± 0.04	1.19

80 min	$2.17 \times 10^{-3} \pm 2.15 \times 10^{-5}$	62.8 ± 0.39	2.41 ± 0.03	$1.21 \times 10^{-5} \pm 2.76 \times 10^{-6}$	2.73 ± 0.04	1.19
85 min	$2.17 \times 10^{-3} \pm 2.18 \times 10^{-5}$	62.6 ± 0.39	2.42 ± 0.03	$1.14 \times 10^{-5} \pm 2.69 \times 10^{-6}$	2.74 ± 0.04	1.12
90 min	$2.17 \times 10^{-3} \pm 2.23 \times 10^{-5}$	62.7 ± 0.40	2.40 ± 0.03	$9.61 \times 10^{-6} \pm 2.47 \times 10^{-6}$	2.78 ± 0.05	1.14

3.7. SAXS data for Carb-Gly electropolymerisation

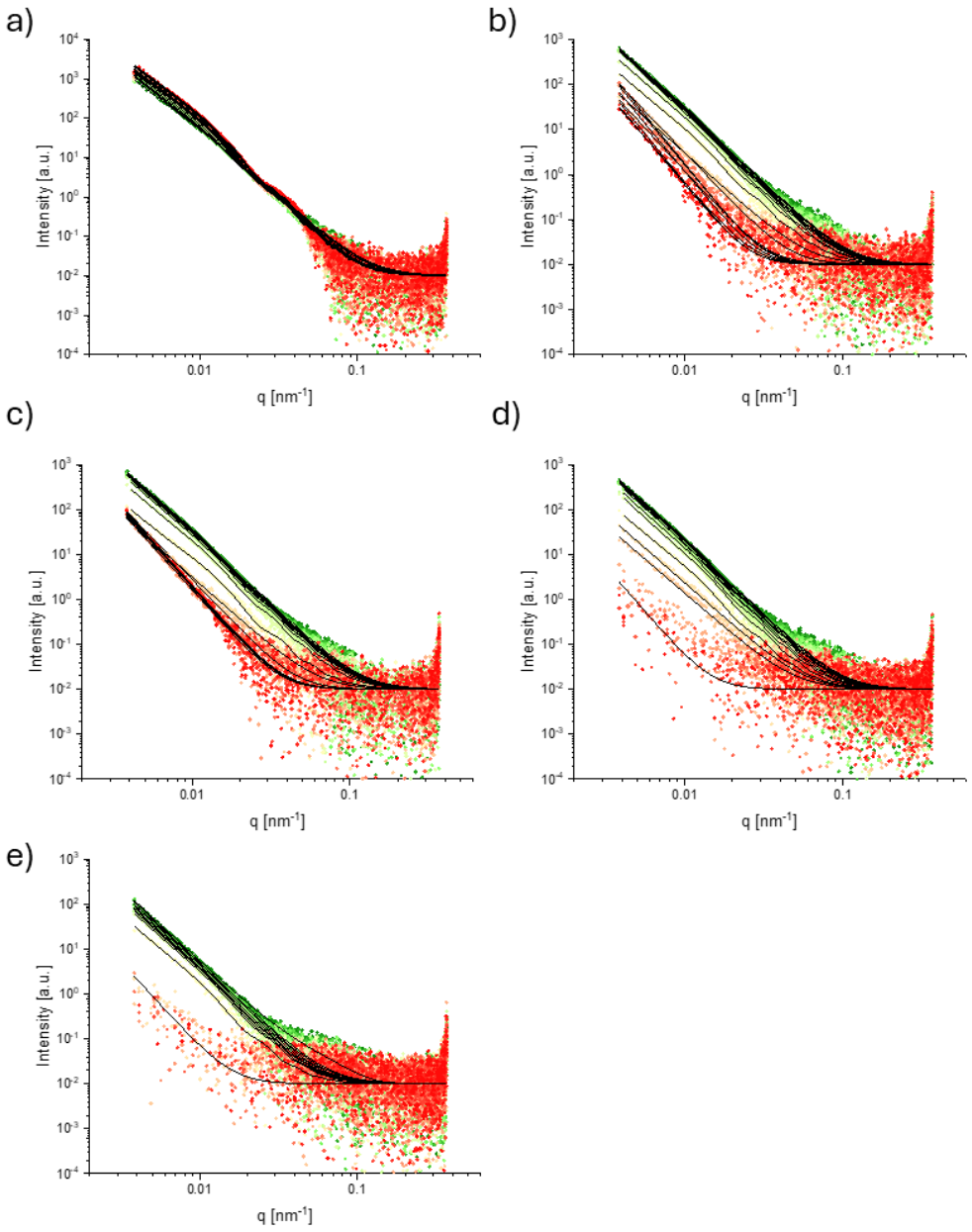

Figure A3.7. SAXS plots for Positions 1–5 (a-e) showing the electropolymerisation of Carb-Gly over 90 min, with scan colour progressing from light green to red; the fits are overlaid in black.

Table A3.33. Fitting parameters for Carb-Gly SAXS data at Position 1. The data fit an elliptical cylinder with a power-law model. From 0-15 mins, the data fit a cylinder model, and from 20-90 mins, the data fit an elliptical cylinder with a power-law model. The background and length parameters are not included, as they were fixed at 0.01 cm^{-1} and 1000 Å, respectively.

	A Scale	Radius (Å)	Axis Ratio	B Scale	B Power	χ^2
0 min	$3.85 \times 10^{-4} \pm 6.77 \times 10^{-6}$	171.1 ± 1.06	-	$1.30 \times 10^{-5} \pm 1.84 \times 10^{-7}$	$3.25 \pm 2.69 \times 10^{-3}$	3.36
5 min	$4.44 \times 10^{-4} \pm 7.03 \times 10^{-6}$	191.0 ± 1.00	-	$1.00 \times 10^{-5} \pm 1.26 \times 10^{-7}$	$3.33 \pm 2.41 \times 10^{-3}$	4.49
10 min	$4.78 \times 10^{-4} \pm 7.03 \times 10^{-6}$	191.9 ± 0.93	-	$8.61 \times 10^{-6} \pm 1.13 \times 10^{-7}$	$3.36 \pm 2.51 \times 10^{-3}$	4.79
15 min	$4.66 \times 10^{-4} \pm 6.86 \times 10^{-6}$	189.3 ± 0.92	-	$7.32 \times 10^{-6} \pm 1.03 \times 10^{-7}$	$3.38 \pm 2.67 \times 10^{-3}$	4.68
20 min	$8.64 \times 10^{-4} \pm 1.57 \times 10^{-5}$	146.2 ± 0.99	2.32 ± 0.04	$5.21 \times 10^{-6} \pm 1.16 \times 10^{-7}$	$3.42 \pm 4.47 \times 10^{-3}$	4.40
25 min	$1.13 \times 10^{-3} \pm 1.61 \times 10^{-5}$	147.5 ± 0.78	2.32 ± 0.03	$4.24 \times 10^{-6} \pm 9.63 \times 10^{-8}$	$3.47 \pm 4.48 \times 10^{-3}$	5.03
30 min	$1.49 \times 10^{-3} \pm 1.68 \times 10^{-5}$	148.9 ± 0.61	2.31 ± 0.03	$3.36 \times 10^{-6} \pm 7.92 \times 10^{-8}$	$3.53 \pm 4.57 \times 10^{-3}$	5.64
35 min	$1.87 \times 10^{-3} \pm 1.72 \times 10^{-5}$	148.2 ± 0.50	2.29 ± 0.02	$2.90 \times 10^{-6} \pm 7.16 \times 10^{-8}$	$3.56 \pm 4.70 \times 10^{-3}$	6.03
40 min	$2.12 \times 10^{-3} \pm 1.75 \times 10^{-5}$	147.4 ± 0.45	2.30 ± 0.02	$2.26 \times 10^{-6} \pm 6.23 \times 10^{-8}$	$3.60 \pm 5.16 \times 10^{-3}$	6.55
45 min	$2.32 \times 10^{-3} \pm 1.79 \times 10^{-5}$	147.9 ± 0.42	2.30 ± 0.02	$1.92 \times 10^{-6} \pm 5.55 \times 10^{-8}$	$3.64 \pm 5.36 \times 10^{-3}$	7.13
50 min	$2.40 \times 10^{-3} \pm 1.81 \times 10^{-5}$	147.7 ± 0.40	2.30 ± 0.02	$1.78 \times 10^{-6} \pm 5.11 \times 10^{-8}$	$3.66 \pm 5.32 \times 10^{-3}$	7.10
55 min	$2.54 \times 10^{-3} \pm 1.83 \times 10^{-5}$	148.4 ± 0.39	2.27 ± 0.02	$1.66 \times 10^{-6} \pm 5.17 \times 10^{-8}$	$3.69 \pm 5.17 \times 10^{-3}$	7.24
60 min	$2.31 \times 10^{-3} \pm 1.78 \times 10^{-5}$	148.1 ± 0.41	2.20 ± 0.02	$1.42 \times 10^{-6} \pm 4.20 \times 10^{-8}$	$3.72 \pm 5.37 \times 10^{-3}$	6.62
65 min	$2.72 \times 10^{-3} \pm 1.87 \times 10^{-5}$	146.1 ± 0.36	2.20 ± 0.02	$1.60 \times 10^{-6} \pm 4.38 \times 10^{-8}$	$3.72 \pm 4.96 \times 10^{-3}$	6.43
70 min	$2.90 \times 10^{-3} \pm 1.96 \times 10^{-5}$	146.1 ± 0.35	2.28 ± 0.02	$1.63 \times 10^{-6} \pm 4.48 \times 10^{-8}$	$3.72 \pm 4.99 \times 10^{-3}$	6.99

75 min	$3.08 \times 10^{-3} \pm 1.99 \times 10^{-5}$	146.3 ± 0.34	2.29 ± 0.02	$1.67 \times 10^{-6} \pm 4.48 \times 10^{-8}$	$3.72 \pm 4.89 \times 10^{-3}$	6.51
80 min	$3.20 \times 10^{-3} \pm 1.99 \times 10^{-5}$	145.6 ± 0.33	2.21 ± 0.01	$1.67 \times 10^{-6} \pm 4.44 \times 10^{-8}$	$3.73 \pm 4.81 \times 10^{-3}$	6.79
85 min	$3.37 \times 10^{-3} \pm 2.06 \times 10^{-5}$	145.2 ± 0.32	2.31 ± 0.01	$1.74 \times 10^{-6} \pm 4.60 \times 10^{-8}$	$3.72 \pm 4.81 \times 10^{-3}$	7.05
90 min	$3.30 \times 10^{-3} \pm 2.01 \times 10^{-5}$	145.8 ± 0.31	2.21 ± 0.01	$1.75 \times 10^{-6} \pm 4.56 \times 10^{-8}$	$3.72 \pm 4.72 \times 10^{-3}$	6.89

Table A3.34. Fitting parameters for Carb-Gly SAXS data at Position 2. From 0-50 min, the data fit a cylinder model, and from 55-90 min, the data fit a power-law model. The background and length parameters are not included, as they were fixed at 0.01 cm^{-1} and 1000 Å, respectively.

	A Scale	Radius (Å)	B Scale	B Power	χ^2
0 min	$2.36 \times 10^{-4} \pm 5.88 \times 10^{-6}$	187.7 ± 1.63	$1.23 \times 10^{-5} \pm 1.78 \times 10^{-7}$	$3.22 \pm 3.08 \times 10^{-3}$	2.47
5 min	$2.40 \times 10^{-4} \pm 5.92 \times 10^{-6}$	179.3 ± 1.55	$9.62 \times 10^{-6} \pm 1.68 \times 10^{-7}$	$3.24 \pm 3.34 \times 10^{-3}$	2.26
10 min	$2.64 \times 10^{-4} \pm 5.90 \times 10^{-6}$	177.2 ± 1.39	$8.72 \times 10^{-6} \pm 1.61 \times 10^{-7}$	$3.25 \pm 3.51 \times 10^{-3}$	2.25
15 min	$2.67 \times 10^{-4} \pm 5.85 \times 10^{-6}$	176.4 ± 1.36	$8.05 \times 10^{-6} \pm 1.56 \times 10^{-7}$	$3.26 \pm 3.66 \times 10^{-3}$	2.14
20 min	$2.64 \times 10^{-4} \pm 5.89 \times 10^{-6}$	173.3 ± 1.35	$7.40 \times 10^{-6} \pm 1.54 \times 10^{-7}$	$3.27 \pm 3.91 \times 10^{-3}$	2.10
25 min	$2.67 \times 10^{-4} \pm 5.98 \times 10^{-5}$	166.1 ± 1.30	$6.66 \times 10^{-6} \pm 1.52 \times 10^{-7}$	$3.28 \pm 4.27 \times 10^{-3}$	2.42
30 min	$2.54 \times 10^{-4} \pm 5.86 \times 10^{-6}$	168.1 ± 1.36	$6.55 \times 10^{-6} \pm 1.53 \times 10^{-7}$	$3.28 \pm 4.39 \times 10^{-3}$	2.09
35 min	$2.60 \times 10^{-4} \pm 5.81 \times 10^{-6}$	164.6 ± 1.28	$5.45 \times 10^{-6} \pm 1.48 \times 10^{-7}$	$3.29 \pm 5.06 \times 10^{-3}$	2.07
40 min	$2.30 \times 10^{-4} \pm 5.34 \times 10^{-6}$	164.4 ± 1.28	$4.66 \times 10^{-6} \pm 1.65 \times 10^{-7}$	$3.25 \pm 6.62 \times 10^{-3}$	2.07
45 min	$1.46 \times 10^{-4} \pm 5.19 \times 10^{-6}$	145.9 ± 1.75	$2.58 \times 10^{-6} \pm 2.47 \times 10^{-7}$	$3.15 \pm 1.76 \times 10^{-2}$	1.87
50 min	$5.38 \times 10^{-5} \pm 6.52 \times 10^{-6}$	124.6 ± 3.79	$3.70 \times 10^{-7} \pm 1.09 \times 10^{-7}$	$3.39 \pm 5.39 \times 10^{-2}$	1.81

55 min	-	-	$1.29 \times 10^{-7} \pm 1.08 \times 10^{-8}$	$3.66 \pm 1.63 \times 10^{-2}$	1.78
60 min	-	-	$3.81 \times 10^{-8} \pm 5.00 \times 10^{-9}$	$3.82 \pm 2.53 \times 10^{-2}$	1.78
65 min	-	-	$2.48 \times 10^{-8} \pm 3.31 \times 10^{-9}$	$3.91 \pm 2.53 \times 10^{-2}$	1.74
70 min	-	-	$2.83 \times 10^{-8} \pm 3.37 \times 10^{-9}$	$3.91 \pm 2.29 \times 10^{-2}$	1.70
75 min	-	-	$3.96 \times 10^{-8} \pm 4.62 \times 10^{-9}$	$3.84 \pm 2.26 \times 10^{-2}$	1.72
80 min	-	-	$3.92 \times 10^{-8} \pm 4.43 \times 10^{-9}$	$3.85 \pm 2.18 \times 10^{-2}$	1.66
85 min	-	-	$3.23 \times 10^{-8} \pm 3.54 \times 10^{-9}$	$3.90 \pm 2.11 \times 10^{-2}$	1.77
90 min	-	-	$2.40 \times 10^{-8} \pm 2.62 \times 10^{-9}$	$3.96 \pm 2.10 \times 10^{-2}$	1.75

Table A3.35. Fitting parameters for Carb-Gly SAXS data at Position 3. From 0-50 min, the data fit a cylinder model, and from 55-90 min, the data fit a power-law model. The background and length parameters are not included, as they were fixed at 0.01 cm^{-1} and 1000 Å, respectively.

	A Scale	Radius (Å)	B Scale	B Power	χ^2
0 min	$1.82 \times 10^{-4} \pm 5.69 \times 10^{-6}$	187.2 ± 2.03	$8.29 \times 10^{-6} \pm 1.49 \times 10^{-7}$	$3.26 \pm 3.45 \times 10^{-3}$	2.05
5 min	$2.00 \times 10^{-4} \pm 5.60 \times 10^{-6}$	194.7 ± 1.85	$7.78 \times 10^{-6} \pm 1.41 \times 10^{-7}$	$3.26 \pm 3.50 \times 10^{-3}$	1.95
10 min	$2.06 \times 10^{-4} \pm 5.62 \times 10^{-6}$	185.6 ± 1.76	$6.98 \times 10^{-6} \pm 1.38 \times 10^{-7}$	$3.28 \pm 3.76 \times 10^{-3}$	1.91
15 min	$2.12 \times 10^{-4} \pm 5.70 \times 10^{-6}$	175.4 ± 1.64	$5.87 \times 10^{-6} \pm 1.32 \times 10^{-7}$	$3.30 \pm 4.21 \times 10^{-3}$	1.84
20 min	$2.02 \times 10^{-4} \pm 5.60 \times 10^{-6}$	178.8 ± 1.72	$5.56 \times 10^{-6} \pm 1.27 \times 10^{-7}$	$3.31 \pm 4.30 \times 10^{-3}$	1.77
25 min	$1.84 \times 10^{-4} \pm 5.58 \times 10^{-6}$	177.6 ± 1.85	$4.72 \times 10^{-6} \pm 1.14 \times 10^{-7}$	$3.33 \pm 4.51 \times 10^{-3}$	1.77
30 min	$1.65 \times 10^{-4} \pm 5.68 \times 10^{-6}$	175.1 ± 2.03	$3.82 \times 10^{-6} \pm 9.94 \times 10^{-8}$	$3.37 \pm 4.84 \times 10^{-3}$	1.71

35 min	$1.56 \times 10^{-4} \pm 6.88 \times 10^{-6}$	148.0 ± 1.93	$2.49 \times 10^{-6} \pm 9.09 \times 10^{-8}$	$3.45 \pm 6.70 \times 10^{-3}$	1.65
40 min	$1.83 \times 10^{-4} \pm 5.06 \times 10^{-6}$	176.4 ± 1.69	$3.16 \times 10^{-6} \pm 1.13 \times 10^{-7}$	$3.32 \pm 6.68 \times 10^{-3}$	1.86
45 min	$1.19 \times 10^{-4} \pm 4.39 \times 10^{-6}$	175.3 ± 2.31	$2.34 \times 10^{-6} \pm 1.40 \times 10^{-7}$	$3.25 \pm 1.11 \times 10^{-2}$	1.64
50 min	$4.38 \times 10^{-5} \pm 5.08 \times 10^{-6}$	149.9 ± 5.10	$5.05 \times 10^{-7} \pm 4.33 \times 10^{-7}$	$3.32 \pm 4.33 \times 10^{-2}$	1.55
55 min	-	-	$1.46 \times 10^{-7} \pm 1.12 \times 10^{-8}$	$3.66 \pm 1.50 \times 10^{-2}$	1.50
60 min	-	-	$5.86 \times 10^{-9} \pm 4.84 \times 10^{-10}$	$3.82 \pm 3.48 \times 10^{-2}$	1.50
65 min	-	-	$5.86 \times 10^{-9} \pm 7.60 \times 10^{-10}$	$4.22 \pm 2.48 \times 10^{-2}$	1.57
70 min	-	-	$3.73 \times 10^{-9} \pm 4.53 \times 10^{-10}$	$4.33 \pm 2.32 \times 10^{-2}$	1.65
75 min	-	-	$3.76 \times 10^{-9} \pm 6.53 \times 10^{-10}$	$4.24 \pm 3.31 \times 10^{-2}$	1.49
80 min	-	-	$1.57 \times 10^{-9} \pm 4.56 \times 10^{-10}$	$4.31 \pm 5.53 \times 10^{-2}$	1.36
85 min	-	-	$2.42 \times 10^{-9} \pm 7.99 \times 10^{-10}$	$4.19 \pm 6.30 \times 10^{-2}$	1.35
90 min	-	-	$2.24 \times 10^{-9} \pm 7.55 \times 10^{-10}$	$4.20 \pm 6.43 \times 10^{-2}$	1.30

Table A3.36. Fitting parameters for Carb-Gly SAXS data at Position 4. From 0-50 min, the data fit a cylinder model; from 55-60 min, a power-law model; and from 65-90 min, no model. The background and length parameters are not included, as they were fixed at 0.01 cm^{-1} and 1000 Å, respectively.

	A Scale	Radius (Å)	B Scale	B Power	χ^2
0 min	$1.29 \times 10^{-4} \pm 5.11 \times 10^{-6}$	198.4 ± 2.68	$5.39 \times 10^{-6} \pm 1.23 \times 10^{-7}$	$3.28 \pm 4.39 \times 10^{-3}$	1.96
5 min	$1.45 \times 10^{-4} \pm 5.04 \times 10^{-6}$	199.7 ± 1.85	$4.62 \times 10^{-6} \pm 1.10 \times 10^{-7}$	$3.30 \pm 4.58 \times 10^{-3}$	1.78
10 min	$1.53 \times 10^{-4} \pm 5.01 \times 10^{-6}$	194.9 ± 2.18	$3.95 \times 10^{-6} \pm 1.05 \times 10^{-7}$	$3.32 \pm 5.04 \times 10^{-3}$	1.74

15 min	$1.57 \times 10^{-4} \pm 5.01 \times 10^{-6}$	190.0 ± 2.07	$3.45 \times 10^{-6} \pm 9.88 \times 10^{-8}$	$3.34 \pm 5.38 \times 10^{-3}$	1.66
20 min	$1.53 \times 10^{-4} \pm 4.88 \times 10^{-6}$	196.2 ± 1.72	$3.37 \times 10^{-6} \pm 9.76 \times 10^{-8}$	$3.33 \pm 5.49 \times 10^{-3}$	1.61
25 min	$1.52 \times 10^{-4} \pm 4.94 \times 10^{-6}$	182.8 ± 2.04	$2.68 \times 10^{-6} \pm 9.55 \times 10^{-8}$	$3.35 \pm 6.66 \times 10^{-3}$	1.61
30 min	$1.10 \times 10^{-4} \pm 4.95 \times 10^{-6}$	191.8 ± 2.84	$1.77 \times 10^{-6} \pm 6.28 \times 10^{-8}$	$3.45 \pm 6.61 \times 10^{-3}$	1.80
35 min	$1.30 \times 10^{-4} \pm 4.65 \times 10^{-6}$	189.0 ± 2.28	$1.67 \times 10^{-6} \pm 7.48 \times 10^{-8}$	$3.40 \pm 8.30 \times 10^{-3}$	1.57
40 min	$1.00 \times 10^{-4} \pm 5.34 \times 10^{-6}$	162.3 ± 2.66	$1.07 \times 10^{-6} \pm 7.69 \times 10^{-8}$	$3.44 \pm 1.31 \times 10^{-2}$	1.46
45 min	$6.93 \times 10^{-5} \pm 4.12 \times 10^{-6}$	172.8 ± 3.61	$1.21 \times 10^{-6} \pm 1.38 \times 10^{-7}$	$3.24 \pm 2.11 \times 10^{-2}$	1.40
50 min	$4.07 \times 10^{-5} \pm 4.65 \times 10^{-6}$	157.6 ± 5.10	$3.88 \times 10^{-7} \pm 1.18 \times 10^{-7}$	$3.31 \pm 5.56 \times 10^{-2}$	1.39
55 min	-	-	$1.17 \times 10^{-6} \pm 1.75 \times 10^{-7}$	$3.03 \pm 3.02 \times 10^{-2}$	1.36
60 min	-	-	$8.97 \times 10^{-8} \pm 7.76 \times 10^{-8}$	3.21 ± 0.17	1.25
65 min	-	-	-	-	-
70 min	-	-	-	-	-
75 min	-	-	-	-	-
80 min	-	-	-	-	-
85 min	-	-	-	-	-
90 min	-	-	-	-	-

Table A3.37. Fitting parameters for Carb-Gly SAXS data at Position 5. From 0-45 min, the data fit a cylinder model and from 50-90 min, no model. The background and length parameters are not included, as they were fixed at 0.01 cm^{-1} and 1000 Å, respectively.

	A Scale	Radius (Å)	B Scale	B Power	χ^2
0 min	1.88×10^{-4}	22.5 ± 3.48	1.58×10^{-6}	$3.26 \pm 1.47 \times 10^{-2}$	1.58

	$\pm 4.35 \times 10^{-5}$		$\pm 1.21 \times 10^{-7}$		
5 min	1.52×10^{-5} $\pm 3.52 \times 10^{-6}$	226.3 ± 17.5	1.83×10^{-6} $\pm 1.26 \times 10^{-7}$	3.20 $\pm 1.37 \times 10^{-2}$	1.54
10 min	1.70×10^{-5} $\pm 3.85 \times 10^{-6}$	183.6 ± 14.9	1.36×10^{-6} $\pm 1.25 \times 10^{-7}$	3.25 $\pm 1.70 \times 10^{-2}$	1.47
15 min	2.25×10^{-5} $\pm 5.13 \times 10^{-6}$	154.7 ± 2.07	8.02×10^{-7} $\pm 9.99 \times 10^{-8}$	3.37 $\pm 2.27 \times 10^{-2}$	1.44
20 min	2.96×10^{-5} $\pm 4.36 \times 10^{-6}$	169.2 ± 8.18	8.09×10^{-7} $\pm 1.03 \times 10^{-7}$	3.33 $\pm 2.33 \times 10^{-2}$	1.33
25 min	2.64×10^{-5} $\pm 4.21 \times 10^{-6}$	173.6 ± 9.12	6.79×10^{-7} $\pm 9.38 \times 10^{-8}$	3.34 $\pm 2.53 \times 10^{-2}$	1.33
30 min	3.03×10^{-5} $\pm 4.06 \times 10^{-6}$	178.4 ± 7.97	6.03×10^{-7} $\pm 8.89 \times 10^{-8}$	3.35 $\pm 2.70 \times 10^{-2}$	1.23
35 min	3.68×10^{-5} $\pm 4.20 \times 10^{-6}$	175.1 ± 6.46	4.65×10^{-7} $\pm 8.05 \times 10^{-8}$	3.38 $\pm 3.16 \times 10^{-2}$	1.28
40 min	3.40×10^{-5} $\pm 4.02 \times 10^{-6}$	179.5 ± 7.07	4.32×10^{-7} $\pm 8.10 \times 10^{-8}$	3.37 $\pm 3.42 \times 10^{-2}$	1.26
45 min	2.33×10^{-5} $\pm 3.29 \times 10^{-6}$	203.8 ± 10.1	2.88×10^{-7} $\pm 8.28 \times 10^{-8}$	3.31 $\pm 5.33 \times 10^{-2}$	1.20
50 min	-	-	-	-	-
55 min	-	-	-	-	-
60 min	-	-	-	-	-
65 min	-	-	-	-	-
70 min	-	-	-	-	-
75 min	-	-	-	-	-
80 min	-	-	-	-	-
85 min	-	-	-	-	-
90 min	-	-	-	-	-

3.8. SAXS data for Carb-Val electropolymerisation

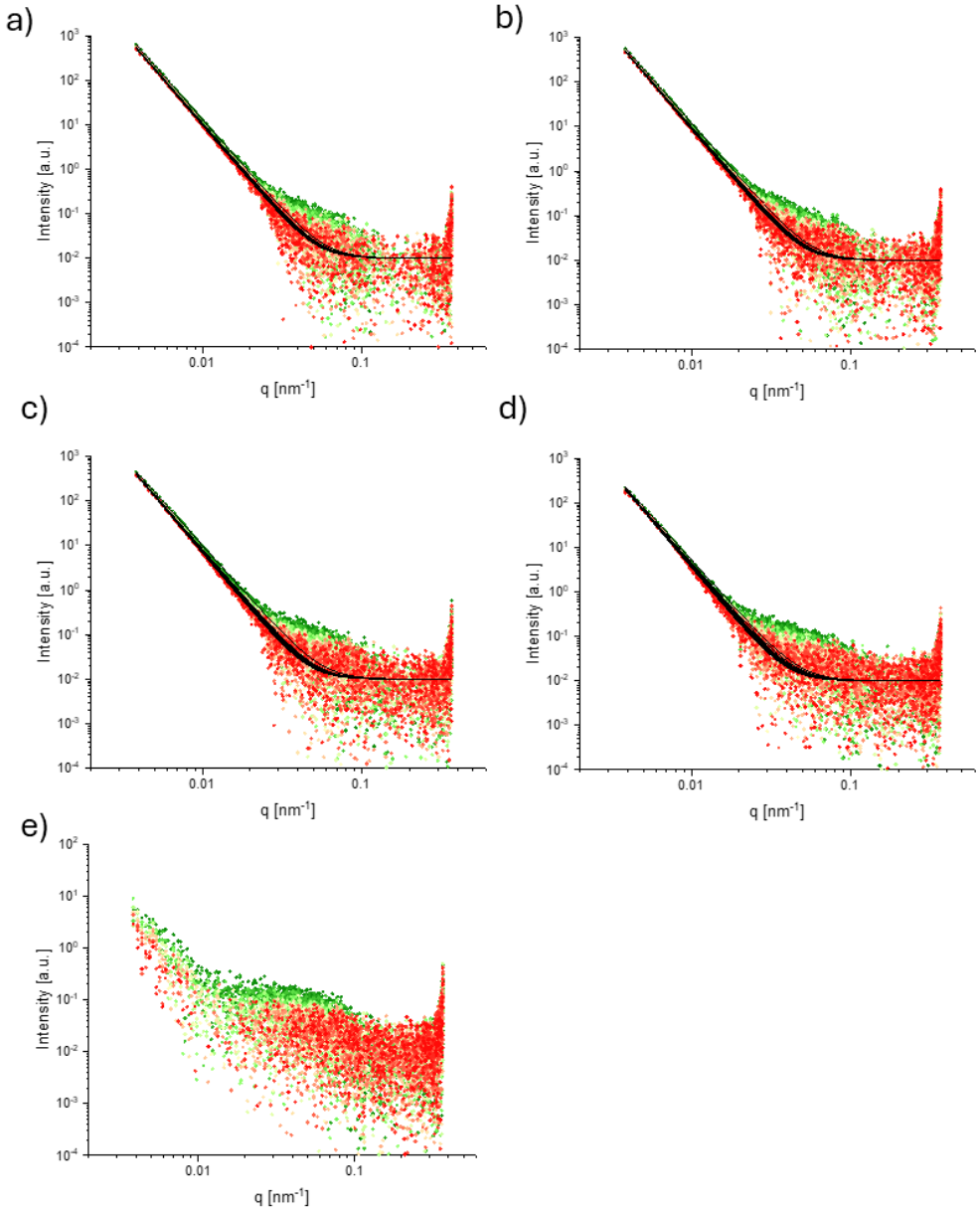

Figure A3.8. SAXS plots for Positions 1–5 (a-e) showing the attempted electropolymerisation of Carb-Val over 90 min, with scan colour progressing from light green to red, the fits are overlaid in black.

Table A3.38. Fitting parameters for Carb-Val SAXS data at Position 1. The data fit a power-law model. The background and length parameters are not included, as they were fixed at 0.01 cm^{-1} and 1000 Å, respectively.

	Scale	Power	χ^2
0 min	$1.08 \times 10^{-7} \pm 2.50 \times 10^{-9}$	$4.05 \pm 4.51 \times 10^{-3}$	5.94
5 min	$7.97 \times 10^{-8} \pm 2.16 \times 10^{-9}$	$4.08 \pm 5.25 \times 10^{-3}$	2.91
10 min	$6.88 \times 10^{-8} \pm 1.90 \times 10^{-9}$	$4.10 \pm 5.34 \times 10^{-3}$	2.74
15 min	$6.26 \times 10^{-8} \pm 1.74 \times 10^{-9}$	$4.12 \pm 5.63 \times 10^{-3}$	2.65
20 min	$5.99 \times 10^{-8} \pm 1.66 \times 10^{-9}$	$4.13 \pm 5.36 \times 10^{-3}$	2.72
25 min	$5.72 \times 10^{-8} \pm 1.60 \times 10^{-9}$	$4.14 \pm 5.41 \times 10^{-3}$	2.69
30 min	$5.38 \times 10^{-8} \pm 1.51 \times 10^{-9}$	$4.15 \pm 5.43 \times 10^{-3}$	2.68
35 min	$5.13 \times 10^{-8} \pm 1.45 \times 10^{-9}$	$4.16 \pm 5.47 \times 10^{-3}$	2.69
40 min	$5.32 \times 10^{-8} \pm 1.50 \times 10^{-9}$	$4.15 \pm 5.43 \times 10^{-3}$	2.61
45 min	$5.10 \times 10^{-8} \pm 1.45 \times 10^{-9}$	$4.16 \pm 5.49 \times 10^{-3}$	2.61
50 min	$4.76 \times 10^{-8} \pm 1.37 \times 10^{-9}$	$4.17 \pm 5.55 \times 10^{-3}$	2.49
55 min	$4.91 \times 10^{-8} \pm 1.41 \times 10^{-9}$	$4.16 \pm 5.57 \times 10^{-3}$	2.63
60 min	$4.69 \times 10^{-8} \pm 1.35 \times 10^{-9}$	$4.17 \pm 5.62 \times 10^{-3}$	2.48
65 min	$4.63 \times 10^{-8} \pm 1.35 \times 10^{-9}$	$4.17 \pm 5.64 \times 10^{-3}$	2.49
70 min	$4.81 \times 10^{-8} \pm 1.42 \times 10^{-9}$	$4.16 \pm 5.68 \times 10^{-3}$	2.40
75 min	$4.32 \times 10^{-8} \pm 1.28 \times 10^{-9}$	$4.18 \pm 5.73 \times 10^{-3}$	2.42
80 min	$4.23 \times 10^{-8} \pm 1.26 \times 10^{-9}$	$4.18 \pm 5.76 \times 10^{-3}$	2.38
85 min	$4.52 \times 10^{-8} \pm 1.36 \times 10^{-9}$	$4.17 \pm 5.79 \times 10^{-3}$	2.30
90 min	$4.54 \times 10^{-8} \pm 1.36 \times 10^{-9}$	$4.16 \pm 5.80 \times 10^{-3}$	2.36

Table A3.39. Fitting parameters for Carb-Val SAXS data at Position 2. The data fit a power-law model. The background and length parameters are not included, as they were fixed at 0.01 cm^{-1} and 1000 Å, respectively.

	Scale	Power	χ^2
0 min	$1.05 \times 10^{-7} \pm 2.64 \times 10^{-9}$	$4.03 \pm 4.87 \times 10^{-3}$	4.59
5 min	$7.17 \times 10^{-8} \pm 2.10 \times 10^{-9}$	$4.08 \pm 5.68 \times 10^{-3}$	2.72
10 min	$6.37 \times 10^{-8} \pm 1.90 \times 10^{-9}$	$4.09 \pm 5.78 \times 10^{-3}$	2.33
15 min	$5.87 \times 10^{-8} \pm 1.77 \times 10^{-9}$	$4.11 \pm 5.83 \times 10^{-3}$	2.33
20 min	$5.02 \times 10^{-8} \pm 1.52 \times 10^{-9}$	$4.14 \pm 5.84 \times 10^{-3}$	2.25
25 min	$4.74 \times 10^{-8} \pm 1.45 \times 10^{-9}$	$4.15 \pm 5.90 \times 10^{-3}$	2.22
30 min	$4.95 \times 10^{-8} \pm 1.50 \times 10^{-9}$	$4.14 \pm 5.87 \times 10^{-3}$	2.29
35 min	$4.55 \times 10^{-8} \pm 1.40 \times 10^{-9}$	$4.16 \pm 5.94 \times 10^{-3}$	2.18
40 min	$4.23 \times 10^{-8} \pm 1.30 \times 10^{-9}$	$4.17 \pm 5.96 \times 10^{-3}$	2.21
45 min	$4.07 \times 10^{-8} \pm 1.27 \times 10^{-9}$	$4.18 \pm 6.01 \times 10^{-3}$	2.15
50 min	$4.01 \times 10^{-8} \pm 1.26 \times 10^{-9}$	$4.18 \pm 6.04 \times 10^{-3}$	1.19
55 min	$4.03 \times 10^{-8} \pm 1.27 \times 10^{-9}$	$4.18 \pm 6.06 \times 10^{-3}$	2.09
60 min	$3.81 \times 10^{-8} \pm 1.21 \times 10^{-9}$	$4.19 \pm 6.11 \times 10^{-3}$	2.09
65 min	$3.88 \times 10^{-8} \pm 1.23 \times 10^{-9}$	$4.18 \pm 6.13 \times 10^{-3}$	2.04
70 min	$3.67 \times 10^{-8} \pm 1.20 \times 10^{-9}$	$4.19 \pm 6.19 \times 10^{-3}$	2.01
75 min	$3.67 \times 10^{-8} \pm 1.19 \times 10^{-9}$	$4.19 \pm 6.24 \times 10^{-3}$	2.11
80 min	$3.63 \times 10^{-8} \pm 1.18 \times 10^{-9}$	$4.19 \pm 6.28 \times 10^{-3}$	1.94
85 min	$3.64 \times 10^{-8} \pm 1.20 \times 10^{-9}$	$4.19 \pm 6.33 \times 10^{-3}$	1.96
90 min	$3.52 \times 10^{-8} \pm 1.16 \times 10^{-9}$	$4.19 \pm 6.36 \times 10^{-3}$	1.93

Table A3.40. Fitting parameters for Carb-Val SAXS data at Position 3. The data fit a power-law model. The background and length parameters are not included, as they were fixed at 0.01 cm^{-1} and 1000 Å, respectively.

	Scale	Power	χ^2
0 min	$1.17 \times 10^{-7} \pm 3.36 \times 10^{-9}$	$3.97 \pm 5.59 \times 10^{-3}$	3.57
5 min	$6.11 \times 10^{-8} \pm 2.07 \times 10^{-9}$	$4.07 \pm 6.54 \times 10^{-3}$	2.42
10 min	$5.06 \times 10^{-8} \pm 1.75 \times 10^{-9}$	$4.10 \pm 6.68 \times 10^{-3}$	2.15
15 min	$4.74 \times 10^{-8} \pm 1.65 \times 10^{-9}$	$4.11 \pm 6.74 \times 10^{-3}$	2.10
20 min	$4.09 \times 10^{-8} \pm 1.45 \times 10^{-9}$	$4.14 \pm 6.83 \times 10^{-3}$	2.08
25 min	$3.93 \times 10^{-8} \pm 1.40 \times 10^{-9}$	$4.15 \pm 6.89 \times 10^{-3}$	1.98
30 min	$3.67 \times 10^{-8} \pm 1.31 \times 10^{-9}$	$4.16 \pm 6.89 \times 10^{-3}$	2.00
35 min	$3.40 \times 10^{-8} \pm 1.23 \times 10^{-9}$	$4.17 \pm 7.00 \times 10^{-3}$	1.94
40 min	$3.55 \times 10^{-8} \pm 1.28 \times 10^{-9}$	$4.16 \pm 6.95 \times 10^{-3}$	1.92
45 min	$3.26 \times 10^{-8} \pm 1.20 \times 10^{-9}$	$4.18 \pm 7.08 \times 10^{-3}$	1.92
50 min	$2.95 \times 10^{-8} \pm 1.09 \times 10^{-9}$	$4.20 \pm 7.11 \times 10^{-3}$	1.93
55 min	$3.08 \times 10^{-8} \pm 1.14 \times 10^{-9}$	$4.19 \pm 7.16 \times 10^{-3}$	1.89
60 min	$2.70 \times 10^{-8} \pm 1.02 \times 10^{-9}$	$4.21 \pm 7.23 \times 10^{-3}$	1.91
65 min	$2.80 \times 10^{-8} \pm 1.06 \times 10^{-9}$	$4.20 \pm 7.27 \times 10^{-3}$	1.81
70 min	$2.89 \times 10^{-8} \pm 1.09 \times 10^{-9}$	$4.20 \pm 7.28 \times 10^{-3}$	1.68
75 min	$2.66 \times 10^{-8} \pm 1.02 \times 10^{-9}$	$4.21 \pm 7.39 \times 10^{-3}$	1.74
80 min	$2.61 \times 10^{-8} \pm 1.01 \times 10^{-9}$	$4.21 \pm 7.42 \times 10^{-3}$	1.77
85 min	$2.38 \times 10^{-8} \pm 9.32 \times 10^{-10}$	$4.23 \pm 7.53 \times 10^{-3}$	1.76
90 min	$2.44 \times 10^{-8} \pm 9.61 \times 10^{-10}$	$4.22 \pm 7.57 \times 10^{-3}$	1.71

Table A3.41. Fitting parameters for Carb-Val SAXS data at Position 4. The data fit a power-law model. The background and length parameters are not included, as they were fixed at 0.01 cm^{-1} and 1000 Å, respectively.

	Scale	Power	χ^2
0 min	$6.61 \times 10^{-8} \pm 3.18 \times 10^{-9}$	$3.95 \pm 9.31 \times 10^{-3}$	2.82
5 min	$4.40 \times 10^{-8} \pm 2.32 \times 10^{-9}$	$4.02 \pm 1.04 \times 10^{-2}$	2.18
10 min	$3.05 \times 10^{-8} \pm 1.71 \times 10^{-9}$	$4.08 \pm 1.08 \times 10^{-2}$	1.99
15 min	$2.79 \times 10^{-8} \pm 1.58 \times 10^{-9}$	$4.09 \pm 1.09 \times 10^{-2}$	1.98
20 min	$2.68 \times 10^{-8} \pm 1.52 \times 10^{-9}$	$4.10 \pm 1.09 \times 10^{-2}$	1.87
25 min	$2.25 \times 10^{-8} \pm 1.30 \times 10^{-9}$	$4.13 \pm 1.11 \times 10^{-2}$	1.88
30 min	$5.38 \times 10^{-8} \pm 1.51 \times 10^{-9}$	$4.15 \pm 5.43 \times 10^{-2}$	1.94
35 min	$2.34 \times 10^{-8} \pm 1.36 \times 10^{-9}$	$4.12 \pm 1.11 \times 10^{-2}$	1.80
40 min	$2.13 \times 10^{-8} \pm 1.25 \times 10^{-9}$	$4.14 \pm 1.13 \times 10^{-2}$	1.73
45 min	$2.04 \times 10^{-8} \pm 1.20 \times 10^{-9}$	$4.15 \pm 1.13 \times 10^{-2}$	1.74
50 min	$1.77 \times 10^{-8} \pm 1.07 \times 10^{-9}$	$4.17 \pm 1.15 \times 10^{-2}$	1.76
55 min	$1.69 \times 10^{-8} \pm 1.02 \times 10^{-9}$	$4.18 \pm 1.16 \times 10^{-2}$	1.81
60 min	$1.48 \times 10^{-8} \pm 9.16 \times 10^{-10}$	$4.20 \pm 1.19 \times 10^{-2}$	1.62
65 min	$1.55 \times 10^{-8} \pm 9.72 \times 10^{-10}$	$4.19 \pm 1.20 \times 10^{-2}$	1.64
70 min	$1.48 \times 10^{-8} \pm 9.33 \times 10^{-10}$	$4.20 \pm 1.21 \times 10^{-2}$	1.64
75 min	$1.43 \times 10^{-8} \pm 9.10 \times 10^{-10}$	$4.20 \pm 1.22 \times 10^{-2}$	1.64
80 min	$1.39 \times 10^{-8} \pm 8.91 \times 10^{-10}$	$4.21 \pm 1.23 \times 10^{-2}$	1.59
85 min	$1.30 \times 10^{-8} \pm 8.45 \times 10^{-10}$	$4.22 \pm 1.25 \times 10^{-2}$	1.60
90 min	$1.29 \times 10^{-8} \pm 8.52 \times 10^{-10}$	$4.22 \pm 1.26 \times 10^{-2}$	1.55

3.9. SAXS data for Carb-Leu electropolymerisation

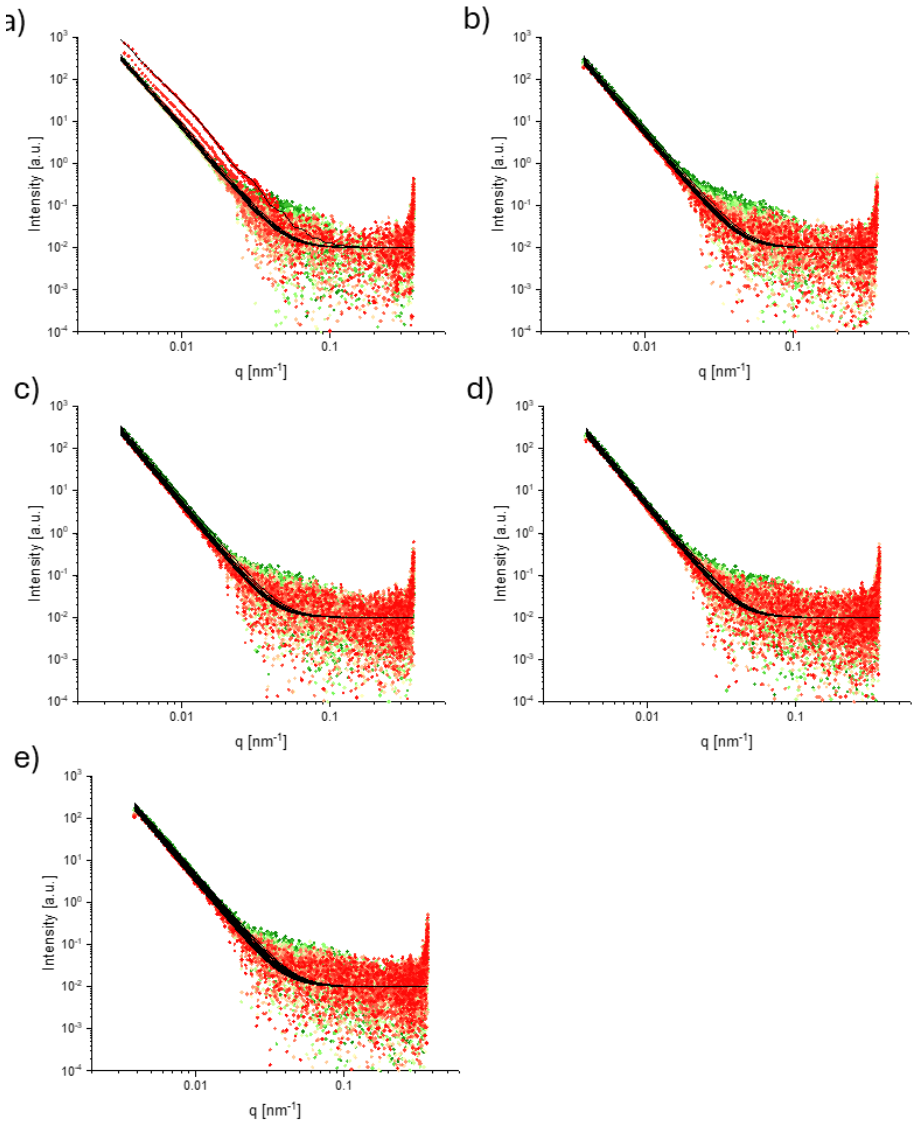

Figure A3.9. SAXS plots for Positions 1-5 (a-e) showing the attempted electropolymerisation of Carb-Leu over 90 min, with scan colour progressing from light green to red; the fits are overlaid in black.

Table A3.43. Fitting parameters for Carb-Leu SAXS data at Position 1. From 0-50 min, the data fit a power-law model, and from 55-90 min, the data fit a cylinder with a power-law model. The background and length parameters are not included, as they were fixed at 0.01 cm^{-1} and 1000 Å, respectively.

	A Scale	Radius (Å)	B Scale	B Power	χ^2
0 min	-	-	8.40×10^{-8} $\pm 2.73 \times 10^{-9}$	4.00 ± 0.06	5.79

5 min	-	-	$6.99 \times 10^{-8} \pm 2.56 \times 10^{-9}$	4.01 ± 0.07	3.57
10 min	-	-	$5.96 \times 10^{-8} \pm 2.32 \times 10^{-9}$	4.03 ± 0.08	2.95
15 min	-	-	$5.66 \times 10^{-8} \pm 2.26 \times 10^{-9}$	4.04 ± 0.08	2.70
20 min	-	-	$5.54 \times 10^{-8} \pm 2.26 \times 10^{-9}$	4.04 ± 0.08	2.48
25 min	-	-	$5.80 \times 10^{-8} \pm 2.39 \times 10^{-9}$	4.02 ± 0.08	2.38
30 min	-	-	$5.67 \times 10^{-8} \pm 2.37 \times 10^{-9}$	4.03 ± 0.08	2.32
35 min	-	-	$6.26 \times 10^{-8} \pm 2.60 \times 10^{-9}$	4.01 ± 0.08	2.27
40 min	-	-	$6.88 \times 10^{-8} \pm 2.85 \times 10^{-9}$	3.99 ± 0.08	2.34
45 min	-	-	$7.17 \times 10^{-8} \pm 2.93 \times 10^{-9}$	3.98 ± 0.08	2.26
50 min	-	-	$8.02 \times 10^{-8} \pm 3.26 \times 10^{-9}$	3.96 ± 0.08	2.34
55 min	$3.60 \times 10^{-5} \pm 4.50 \times 10^{-6}$	222.3 ± 7.05	$5.10 \times 10^{-8} \pm 4.78 \times 10^{-9}$	4.03 ± 0.02	2.24
60 min	$3.91 \times 10^{-5} \pm 4.40 \times 10^{-6}$	229.8 ± 6.72	$5.83 \times 10^{-8} \pm 5.04 \times 10^{-9}$	4.01 ± 0.02	2.16
65 min	$5.48 \times 10^{-5} \pm 4.66 \times 10^{-6}$	216.1 ± 4.57	$5.00 \times 10^{-8} \pm 4.88 \times 10^{-9}$	4.04 ± 0.02	2.21
70 min	$4.67 \times 10^{-5} \pm 4.45 \times 10^{-6}$	227.7 ± 5.65	$6.17 \times 10^{-8} \pm 5.21 \times 10^{-9}$	4.01 ± 0.02	2.26
75 min	$6.21 \times 10^{-5} \pm 4.77 \times 10^{-6}$	209.5 ± 4.02	$6.14 \times 10^{-8} \pm 5.75 \times 10^{-9}$	4.01 ± 0.02	2.19
80 min	$6.55 \times 10^{-5} \pm 5.15 \times 10^{-6}$	197.6 ± 3.73	$6.42 \times 10^{-8} \pm 5.95 \times 10^{-9}$	4.03 ± 0.02	2.22
85 min	$1.07 \times 10^{-4} \pm 5.98 \times 10^{-6}$	181.3 ± 2.34	$9.36 \times 10^{-8} \pm 6.70 \times 10^{-9}$	4.04 ± 0.01	2.70
90 min	$2.71 \times 10^{-4} \pm 6.76 \times 10^{-6}$	177.2 ± 1.09	$2.69 \times 10^{-7} \pm 1.14 \times 10^{-8}$	3.94 ± 0.01	4.14

Table A3.44. Fitting parameters for Carb-Leu SAXS data at Position 2. The data fit a power-law model. The background and length parameters are not included, as they were fixed at 0.01 cm^{-1} and 1000 Å, respectively.

	Scale	Power	χ^2
0 min	$5.27 \times 10^{-8} \pm 1.91 \times 10^{-9}$	$4.07 \pm 6.99 \times 10^{-3}$	4.75
5 min	$3.77 \times 10^{-8} \pm 1.54 \times 10^{-9}$	$4.11 \pm 7.90 \times 10^{-3}$	3.10
10 min	$3.15 \times 10^{-8} \pm 1.38 \times 10^{-9}$	$4.14 \pm 8.46 \times 10^{-3}$	2.42
15 min	$2.83 \times 10^{-8} \pm 1.29 \times 10^{-9}$	$4.15 \pm 8.81 \times 10^{-3}$	2.23
20 min	$2.41 \times 10^{-8} \pm 1.15 \times 10^{-9}$	$4.17 \pm 9.16 \times 10^{-3}$	2.05
25 min	$2.27 \times 10^{-8} \pm 1.11 \times 10^{-9}$	$4.18 \pm 9.40 \times 10^{-3}$	1.99
30 min	$2.26 \times 10^{-8} \pm 1.13 \times 10^{-9}$	$2.17 \pm 9.63 \times 10^{-3}$	1.96
35 min	$2.18 \times 10^{-8} \pm 1.10 \times 10^{-9}$	$4.18 \pm 9.73 \times 10^{-3}$	1.81
40 min	$2.39 \times 10^{-8} \pm 1.22 \times 10^{-9}$	$4.16 \pm 9.80 \times 10^{-3}$	1.84
45 min	$2.61 \times 10^{-8} \pm 1.34 \times 10^{-9}$	$4.14 \pm 9.86 \times 10^{-3}$	1.77
50 min	$2.38 \times 10^{-8} \pm 1.25 \times 10^{-9}$	$4.15 \pm 1.01 \times 10^{-2}$	1.74
55 min	$2.68 \times 10^{-8} \pm 1.42 \times 10^{-9}$	$4.12 \pm 1.02 \times 10^{-2}$	1.68
60 min	$2.78 \times 10^{-8} \pm 1.47 \times 10^{-9}$	$4.12 \pm 1.02 \times 10^{-2}$	1.60
65 min	$2.86 \times 10^{-8} \pm 1.53 \times 10^{-9}$	$4.11 \pm 1.03 \times 10^{-2}$	1.66
70 min	$2.78 \times 10^{-8} \pm 1.49 \times 10^{-9}$	$4.11 \pm 1.04 \times 10^{-2}$	1.56
75 min	$2.87 \times 10^{-8} \pm 1.54 \times 10^{-9}$	$4.10 \pm 1.03 \times 10^{-2}$	1.65
80 min	$3.17 \times 10^{-8} \pm 1.71 \times 10^{-9}$	$4.08 \pm 1.04 \times 10^{-2}$	1.52
85 min	$3.05 \times 10^{-8} \pm 1.66 \times 10^{-9}$	$4.09 \pm 1.05 \times 10^{-2}$	1.57
90 min	$2.65 \times 10^{-8} \pm 1.47 \times 10^{-9}$	$4.11 \pm 1.07 \times 10^{-2}$	1.55

Table A3.45. Fitting parameters for Carb-Leu SAXS data at Position 3. The data fit a power-law model. The background and length parameters are not included, as they were fixed at 0.01 cm^{-1} and 1000 Å, respectively.

	Scale	Power	χ^2
0 min	$3.91 \times 10^{-8} \pm 1.48 \times 10^{-9}$	$4.13 \pm 7.30 \times 10^{-3}$	3.38
5 min	$2.62 \times 10^{-8} \pm 1.12 \times 10^{-9}$	$4.18 \pm 8.22 \times 10^{-3}$	2.44
10 min	$2.19 \times 10^{-8} \pm 9.98 \times 10^{-10}$	$4.20 \pm 8.76 \times 10^{-3}$	2.04
15 min	$1.86 \times 10^{-8} \pm 8.89 \times 10^{-10}$	$4.23 \pm 9.16 \times 10^{-2}$	1.88
20 min	$1.62 \times 10^{-8} \pm 8.05 \times 10^{-10}$	$4.25 \pm 9.52 \times 10^{-3}$	1.77
25 min	$1.58 \times 10^{-8} \pm 8.05 \times 10^{-10}$	$4.24 \pm 9.80 \times 10^{-3}$	1.72
30 min	$1.44 \times 10^{-8} \pm 7.59 \times 10^{-10}$	$4.26 \pm 1.01 \times 10^{-2}$	1.59
35 min	$1.51 \times 10^{-8} \pm 8.03 \times 10^{-10}$	$4.24 \pm 1.02 \times 10^{-2}$	1.63
40 min	$1.41 \times 10^{-8} \pm 7.69 \times 10^{-10}$	$4.25 \pm 1.05 \times 10^{-2}$	1.50
45 min	$1.73 \times 10^{-8} \pm 9.48 \times 10^{-10}$	$4.21 \pm 1.05 \times 10^{-2}$	1.49
50 min	$1.53 \times 10^{-8} \pm 8.56 \times 10^{-10}$	$4.23 \pm 1.07 \times 10^{-2}$	1.51
55 min	$1.65 \times 10^{-8} \pm 9.29 \times 10^{-10}$	$4.21 \pm 1.08 \times 10^{-2}$	1.49
60 min	$1.83 \times 10^{-8} \pm 1.03 \times 10^{-9}$	$4.19 \pm 1.09 \times 10^{-2}$	1.49
65 min	$1.90 \times 10^{-8} \pm 1.08 \times 10^{-9}$	$4.18 \pm 1.09 \times 10^{-2}$	1.46
70 min	$1.68 \times 10^{-8} \pm 9.80 \times 10^{-10}$	$4.20 \pm 1.11 \times 10^{-2}$	1.35
75 min	$1.97 \times 10^{-8} \pm 1.14 \times 10^{-9}$	$4.16 \pm 1.11 \times 10^{-2}$	1.29
80 min	$1.95 \times 10^{-8} \pm 1.14 \times 10^{-9}$	$4.17 \pm 1.12 \times 10^{-2}$	1.33
85 min	$1.88 \times 10^{-8} \pm 1.11 \times 10^{-9}$	$4.17 \pm 1.13 \times 10^{-2}$	1.36
90 min	$1.90 \times 10^{-8} \pm 1.13 \times 10^{-9}$	$4.17 \pm 1.15 \times 10^{-2}$	1.29

Table A3.46. Fitting parameters for Carb-Leu SAXS data at Position 4. The data fit a power-law model. The background and length parameters are not included, as they were fixed at 0.01 cm^{-1} and 1000 Å, respectively.

	Scale	Power	χ^2
0 min	$2.81 \times 10^{-8} \pm 1.26 \times 10^{-9}$	$4.15 \pm 8.59 \times 10^{-3}$	2.68
5 min	$2.33 \times 10^{-8} \pm 1.13 \times 10^{-9}$	$4.17 \pm 9.30 \times 10^{-3}$	2.01
10 min	$1.91 \times 10^{-8} \pm 9.87 \times 10^{-10}$	$4.20 \pm 9.91 \times 10^{-3}$	1.80
15 min	$1.59 \times 10^{-8} \pm 8.54 \times 10^{-10}$	$4.23 \pm 1.03 \times 10^{-2}$	1.68
20 min	$1.41 \times 10^{-8} \pm 7.86 \times 10^{-10}$	$4.24 \pm 1.07 \times 10^{-2}$	1.67
25 min	$1.22 \times 10^{-8} \pm 7.01 \times 10^{-10}$	$4.27 \pm 1.10 \times 10^{-2}$	1.57
30 min	$1.33 \times 10^{-8} \pm 7.78 \times 10^{-10}$	$4.24 \pm 1.12 \times 10^{-2}$	1.44
35 min	$1.26 \times 10^{-8} \pm 7.55 \times 10^{-10}$	$4.25 \pm 1.15 \times 10^{-2}$	1.48
40 min	$1.39 \times 10^{-8} \pm 8.45 \times 10^{-10}$	$4.23 \pm 1.16 \times 10^{-2}$	1.45
45 min	$1.42 \times 10^{-8} \pm 8.70 \times 10^{-10}$	$4.22 \pm 1.18 \times 10^{-2}$	1.40
50 min	$1.40 \times 10^{-8} \pm 8.78 \times 10^{-10}$	$4.22 \pm 1.20 \times 10^{-2}$	1.35
55 min	$1.58 \times 10^{-8} \pm 9.97 \times 10^{-10}$	$4.19 \pm 1.21 \times 10^{-2}$	1.36
60 min	$1.65 \times 10^{-8} \pm 1.04 \times 10^{-9}$	$4.18 \pm 1.21 \times 10^{-2}$	1.27
65 min	$1.66 \times 10^{-8} \pm 1.05 \times 10^{-9}$	$4.18 \pm 1.22 \times 10^{-2}$	1.31
70 min	$1.84 \times 10^{-8} \pm 1.18 \times 10^{-9}$	$4.15 \pm 1.23 \times 10^{-2}$	1.30
75 min	$1.87 \times 10^{-8} \pm 1.18 \times 10^{-9}$	$4.15 \pm 1.22 \times 10^{-2}$	1.24
80 min	$1.85 \times 10^{-8} \pm 1.19 \times 10^{-9}$	$4.15 \pm 1.24 \times 10^{-2}$	1.23
85 min	$1.67 \times 10^{-8} \pm 1.08 \times 10^{-9}$	$4.17 \pm 1.25 \times 10^{-2}$	1.23
90 min	$1.89 \times 10^{-8} \pm 1.23 \times 10^{-9}$	$4.22 \pm 1.26 \times 10^{-2}$	1.24

Table A3.47. Fitting parameters for Carb-Leu SAXS data at Position 5. The data fit a power-law model. The background and length parameters are not included, as they were fixed at 0.01 cm^{-1} and 1000 Å, respectively.

	Scale	Power	χ^2
0 min	$4.93 \times 10^{-8} \pm 2.43 \times 10^{-9}$	$4.01 \pm 9.51 \times 10^{-3}$	2.09
5 min	$4.13 \times 10^{-8} \pm 2.15 \times 10^{-9}$	$4.03 \pm 1.01 \times 10^{-2}$	1.78
10 min	$3.33 \times 10^{-8} \pm 1.83 \times 10^{-9}$	$4.07 \pm 1.05 \times 10^{-2}$	1.65
15 min	$3.02 \times 10^{-8} \pm 1.70 \times 10^{-9}$	$4.08 \pm 1.08 \times 10^{-2}$	1.53
20 min	$2.40 \times 10^{-8} \pm 1.41 \times 10^{-9}$	$4.12 \pm 1.13 \times 10^{-2}$	1.56
25 min	$2.22 \times 10^{-8} \pm 1.34 \times 10^{-9}$	$4.13 \pm 1.16 \times 10^{-2}$	1.51
30 min	$2.07 \times 10^{-8} \pm 1.30 \times 10^{-9}$	$4.13 \pm 1.21 \times 10^{-2}$	1.41
35 min	$1/78 \times 10^{-8} \pm 1.14 \times 10^{-9}$	$4.16 \pm 1.23 \times 10^{-2}$	1.46
40 min	$1.81 \times 10^{-8} \pm 1.19 \times 10^{-9}$	$4.15 \pm 1.26 \times 10^{-2}$	1.36
45 min	$1.88 \times 10^{-8} \pm 1.26 \times 10^{-9}$	$4.14 \pm 1.29 \times 10^{-2}$	1.29
50 min	$1.89 \times 10^{-8} \pm 1.30 \times 10^{-9}$	$4.13 \pm 1.32 \times 10^{-2}$	1.29
55 min	$1.82 \times 10^{-8} \pm 1.27 \times 10^{-9}$	$4.13 \pm 1.34 \times 10^{-2}$	1.36
60 min	$1.86 \times 10^{-8} \pm 1.31 \times 10^{-9}$	$4.13 \pm 1.35 \times 10^{-2}$	1.25
65 min	$1.75 \times 10^{-8} \pm 1.26 \times 10^{-9}$	$4.13 \pm 1.38 \times 10^{-2}$	1.22
70 min	$1.68 \times 10^{-8} \pm 1.24 \times 10^{-9}$	$4.14 \pm 1.41 \times 10^{-2}$	1.16
75 min	$1.75 \times 10^{-8} \pm 1.28 \times 10^{-9}$	$4.13 \pm 1.41 \times 10^{-2}$	1.18
80 min	$1.74 \times 10^{-8} \pm 1.30 \times 10^{-9}$	$4.13 \pm 1.44 \times 10^{-2}$	1.16
85 min	$1.59 \times 10^{-8} \pm 1.21 \times 10^{-9}$	$4.14 \pm 1.46 \times 10^{-2}$	1.22
90 min	$1.42 \times 10^{-8} \pm 1.11 \times 10^{-9}$	$4.16 \pm 1.49 \times 10^{-2}$	1.20